## REVIEW

# Deep level centers in silicon carbide: A review

A. A. Lebedev

*A. F. Ioffe Physicotechnical Institute, Russian Academy of Sciences, 194021 St. Petersburg, Russia*
(Submitted March 2, 1998; accepted for publication March 26, 1998)
Fiz. Tekh. Poluprovodn. **33**, 129–155 (February 1998)

Results from current studies of the parameters of deep centers in $6H$-, $4H$-, and $3C$-SiC are analyzed. Data are presented on the ionization energy and capture cross sections of centers formed by doping SiC with different types of impurities or during irradiation, as well as of intrinsic defects. The involvement of these centers in radiative and nonradiative recombination is examined. This analysis of published data illustrates the large effect of intrinsic defects in the SiC crystal lattice both on the formation of deep centers and on the properties of the epitaxial layers themselves, such as their doping level and polytype homogeneity. © *1999 American Institute of Physics.* [S1063-7826(99)00102-7]

### INTRODUCTION

Progress in modern power generation and space technology requires the creation of semiconductor devices that are capable of operating at elevated temperatures and under high levels of ionizing radiation. One of the semiconductor materials upon which such devices can be based is silicon carbide.

The substantial advances in the development of SiC technology over the last 10–15 years have made it possible to develop almost all the basic types of semiconductor devices based on SiC, including the first integrated circuits.

Deep centers determine many of the most important parameters of semiconductor devices. Deep centers in the bulk of a semiconductor have an effect on the lifetime and diffusion mean free path of minority charge carriers, the efficiency of light emitting diodes and photodetectors, the gain of transistors, and the magnitude of and temperature coefficient for the breakdown voltage of $p-n$ junctions. Since at this time it is impossible to predict theoretically the main parameters of impurity and defect centers in the new semiconducting material, the principal source of information on deep centers is experiment.

It is evident that further advances in the technology of SiC and in creating new devices will, on one hand, require studies of the parameters of deep centers in epitaxial layers and $p-n$ junctions obtained by various techniques. On the other hand, studies of the parameters of devices that have already been created can yield additional information on the properties of the deep centers in them. In addition, the various methods for growing epitaxial layers and creating $p-n$ lead to the formation of different deep centers in the bulk of the semiconductor and on its surface, which, in turn, affect the characteristics of the devices created from them. Thus, it is possible to determine the optimum combination of technologies for creating a given type of device with the best set of operating characteristics through studies of the parameters and distributions of the deep centers.

The purpose of this review article is to generalize the currently available data on the parameters of deep centers in $6H$-, $4H$-, and $3C$-SiC and to analyze their properties from the standpoint of their possible influence on the characteristics of device structures based on silicon carbide.

### A BRIEF HISTORY OF RESEARCH ON THE SEMICONDUCTOR PROPERTIES OF SIC

At the end of the last century, Acheson proposed and patented a method for industrial production of SiC.[1] The crystals grown by this method were highly doped (up to $10^{21}\,\mathrm{cm}^{-3}$), were not of a uniform polytype, and were small, at $10\times10\times3$ mm (Ref. 2) studies of samples of this type, Round observed (1907) light associated with the passage of an electrical current through a crystal.[3] A more detailed study of the electrical luminescence of silicon carbide was made by Losev in 1923–1940 (Ref. 4). He found that one of the types of emission was associated with the presence of a special ''active layer'' on a crystal surface. Later he showed that this layer has electron conductivity and the bulk of the sample has hole conductivity. Losev also established the existence of a coupling between rectification and electrical luminescence. Thus, the two most important phenomena for semiconductor electronics, electrical luminescence and the rectifying properties of $p-n$ structures were first observed in SiC crystals. Unfortunately, at that time the electronics industry was based on using vacuum tubes and these discoveries remained unnoticed.

Industrial interest in semiconductors emerged after Shockley's discovery of the transistor effect in crystalline Ge in 1949. At about this time, Lely proposed a new method for growing SiC crystals.[5] Here, single crystals were grown by sublimation as a result of distilling SiC through a vapor phase from hotter into colder regions.

 

In the first half of the 1950s, the search began for semiconductor materials capable of operating at higher ambient temperatures than Ge. Thus, the attention of many researchers turned to silicon and silicon carbide. In the next 10–15 years many papers were published on the properties of SiC and on the development of semiconductor devices based on it.

However, in the beginning of the 1970s industrial interest in silicon carbide had again waned. Evidently, this was a result of the incomparably greater success in the development of Si and GaAs technology compared to that for SiC. The substantial technological difficulties in growing silicon carbide and fabricating devices based on it meant that the parameters of the resulting devices were far from the theoretically expected values.

The next 15 years of research on the properties of SiC were conducted by a few research groups, most of which were in the USSR. In 1970, Vodakov and Mokhov proposed a sublimation ''sandwich method'' for growing epitaxial SiC layers.[6] According to this method, the growth process took place as the vapor source and substrate were brought together.

At the end of the 1970s, Tairov and Tsvetkov also proposed a method for growing bulk SiC crystals[7] that was a modification of Lely's method. This method was based on the condensation of the vapor on a single crystal substrate. Growth took place at temperatures near 2000 °C. The diameter of the grown ingot was determined by the size of the substrate (currently about 50 mm) and its length was determined by the duration of the fabrication process. The polytype structure of the ingot was determined by the polytype of the seed.[8]

Based on these technologies and modifications of them, an entire series of SiC semiconductor devices had been developed by the mid-1980s in the laboratory of Vodakov and Chelnokov at the Ioffe Physicotechnical Institute and an extensive range of studies had been undertaken on the electrical properties of silicon carbide, including the parameters and properties of deep centers.

Finally, interest in silicon carbide as a prospective material for semiconductor electronics was revived after Nishino developed a method for the CVD epitaxy of $3C$-SiC films on silicon substrates.[9] Using standard equipment and large area substrates opened up possibilities for rapid commercial utilization of these results. Several types of field-effect transistors were quickly produced using films of this type. However, the parameters of these devices, like the quality of the films themselves, were still low. In addition, of the silicon carbide polytypes, $3C$-SiC has the lowest band gap ($E_g \sim 2.4$ eV) and, from the standpoint of peak operating temperatures, it is only slightly better than GaP. Thus, shortly afterwards the same CVD method was used to obtain films of $6H$-SiC on the basis of $6H$-SiC substrates.[10] The combination of a modified Lely method (substrate), CVD epitaxy (epitaxial layers) on the (0001) facet of Si, and plasma chemical etching (mesostructure formation) made it possible to obtain an entire series of semiconductor devices based on silicon carbide–blue light emitting diodes, ultraviolet detectors, rectifying diodes, field-effect transistors, bipolar transistors, and thyristors.[11–13]

Now the largest companies specializing in the production of semiconductor technology are engaged in the experimental production of devices based on silicon carbide, along with intense research: CREE and Westinghouse (USA), Thomson and Schneider Electrique (France), ABB (Switzerland), Siemens (Germany), and Hitachi (Japan). Unfortunately, because of the overall collapse of science and the electronics industry in the Soviet Union, the work of Russian scientists and the scientific potential they had developed in the physics of SiC have, in recent years, been ignored in their own country.

## 1. SOME FEATURES OF THE CRYSTAL STRUCTURE OF SIC

Silicon carbide is among the most striking representatives of the polytype compounds. The term ''polytypism'' was, itself, specially introduced for carborundum, because the different crystalline forms of SiC are structurally very close to one another. At present, more than 140 crystalline modifications of SiC are known.[14]

All the known polytypes of silicon carbide crystallize in accordance with the close spherical packing law and are binary structures constructed of identical layers differing both in the order of positioning of a cubic $C$ or hexagonal $H$ layer and in the number of these layers per unit cell. The polytype is usually characterized using the Ramsdell notation,[15] which consists of a natural number equal to the number of layers per period in the direction perpendicular to the basal plane and an alphabetic symbol characterizing the syngony of the Bravais lattice: $C$ for cubic, $H$ for hexagonal, and $R$ for rhombohedral. The most widespread polytypes are $6H$, $4H$, $15R$, and $3C$ (Fig. 1). Although the position of the closest of neighboring atoms is the same for each atom of silicon or carbon in all the polytypes, the position of the most distant neighbors differs, and this leads to the appearance of crystallographically nonequivalent sites in the SiC lattice ($4H$ with one cubic and one hexagonal, $6H$ with two cubic and one hexagonal).[16] At present, there is no satisfactory theory in all regards, capable of explaining why SiC crystallizes in the form of a large number of polytypes. It is also not completely clear which factors favor the formation of one or another polytype.

It is known that silicon carbide is a semiconductor with an indirect band structure. Here the width of the band gap depends substantially on the polytype and ranges from 2.39 eV for $3C$-SiC to 3.3 eV for $2H$-SiC. Experiment and theory show that the maximum of the valence band lies at the center of the Brillouin zone, while the minimum of the conduction band lies at its edge. The strong dependence of the band gap on the polytype structure is attributable to this fact. According to Hymphreys *et al.*,[17] the spin-orbit splitting of the valence band is 10 meV.

In the polytypes that are more complicated than $2H$ and $3C$, there is yet another feature of the band structure.[18,19] In the analysis of the electronic spectra, the alternation of the layers in long period polytypes can be regarded as the action

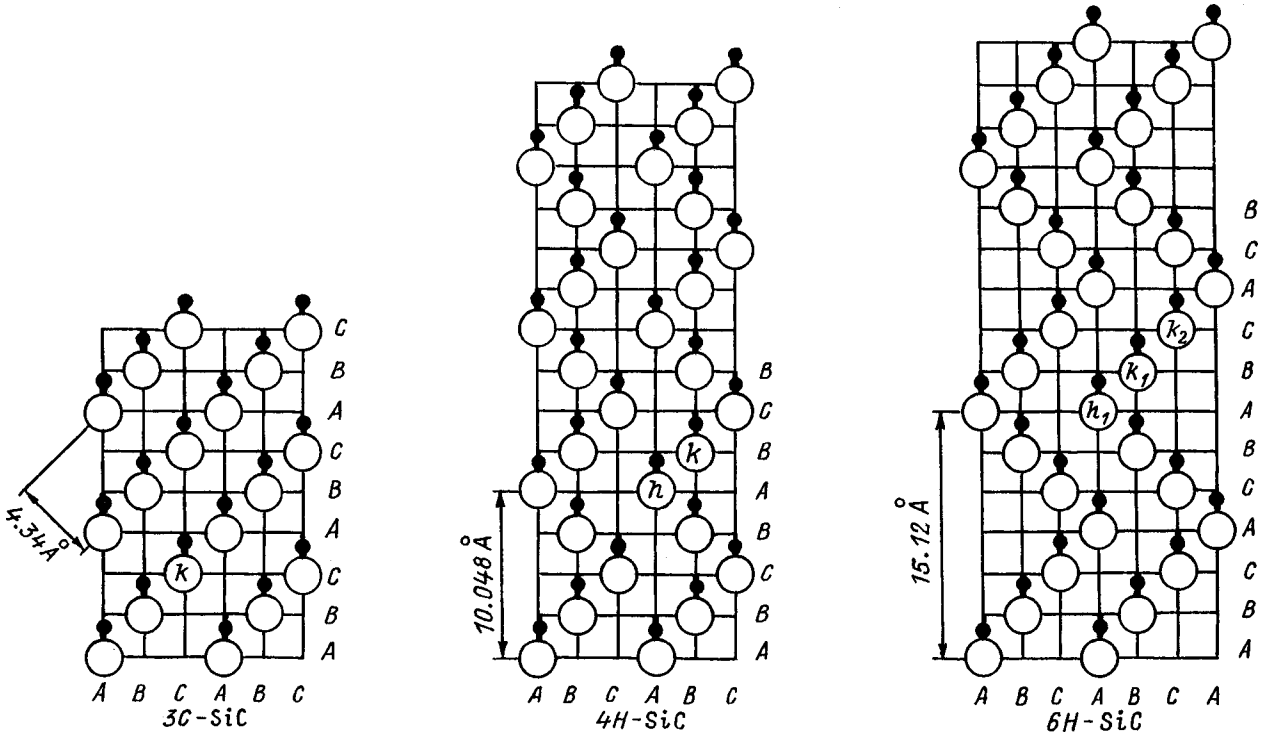


FIG. 1. The location of Si and C atoms (hollow and solid circles, respectively) in the $(11\bar{2}0)$ plane for the SiC polytypes $3C$, $4H$, and $6H$. The labels $A$, $B$, and $C$ correspond to different positions of atoms in a dense packed hexagonal structure. The symbols $h$ and $k$ denote hexagonal and cubic sites of atoms in the lattice, respectively.[135]

on an electron situated in a crystal with cubic modification by some superperiodic potential. In this treatment, the conduction band breaks up into a series of subbands. The anisotropy in the effective masses in the polytypes and its dependence on the specific structure of the crystal can be explained in terms of these ideas.

The existence of polarized absorption bands, which are attributable to transitions among minibands,[20,21] is an important feature of the electronic superlattices. These absorption bands are observed in crystals of various polytypes, and in all cases their position in the spectrum and their polarization are in agreement with calculations of the electronic spectra.[19,22,23] The basic parameters of the SiC polytypes $6H$, $4H$, and $3C$ are listed in Table I.

TABLE I. Some parameters of SiC (Refs. 135 and 209).

| Parameter | $4H$-SiC | $6H$-SiC | $3C$-SiC |
|---|---|---|---|
| Band gap, eV | 3.2 | 3.0 | 2.3 |
| Lattice constant, Å | $a=3.09$ | $a=3.09$ | 4.34 |
| | $c=10.48$ | $c=15.12$ | |
| Thermal conductivity W/cm·deg | 3–5 | 3–5 | 5 |
| Critical breakdown field strength $E_{cr}$, mV/cm | 2–3 | 2–3 | $>1.5$ |
| Electron mobility $\mu_n$, $cm^2/(V\cdot s)$ (300 K) | 800 | 200–300 | 1000 |
| Saturation rate, $10^7$ cm/s | 2 | 2 | 2.7 |
| Hole mobility $\mu_p$ $cm^2/(V\cdot s)$ (300 K) | 60 | 50 | 40 |

## 2. PARAMETERS OF DEEP CENTERS IN SIC

### 2.1. Major dopant impurities in SiC

The allowed states in the band gap of semiconductors are traditionally divided into ''shallow'' and ''deep.'' This division is extremely arbitrary and shallow states are usually assumed to be those with ionization energies $E_i<0.1$ eV and deep states, those with $E_i>0.1$ eV (Ref. 24). For silicon carbide this division is even more arbitrary, since even the ground donor and acceptor levels have ionization energies $E_i\geqslant 0.1$ eV. Thus, strictly speaking, in silicon carbide all the levels that have been studied are deep. However, in the following we shall refer to the levels which determine the resistance of the base regions as shallow compared to the deeper levels which do not make a noticeable contribution to the concentration of the majority charge carriers.

**Nitrogen.** Specially undoped SiC layers have $n$-type conductivity. This is explained by the uncontrolled doping of the growing layer by nitrogen. In addition, nitrogen has a fairly high solubility in SiC ($\approx 10^{21}\,cm^{-3}$) and the lowest ionization energy of all the impurity donor levels. By implanting N ions it is also possible to obtain thin, heavily doped layers of SiC for forming ohmic contacts.[25]

The existence of nonequivalent sites in the SiC lattice shows up most clearly in the energy position of the deep centers associated with nitrogen atoms.[26–28] In all the main polytypes of SiC, nitrogen atoms have been observed in association both with cubic ($c$) and with hexagonal ($h$) lattice sites, with the ratio of the level concentrations ($N_h/N_c$) corresponding to the ratio of the number of hexagonal and cubic

sites in the crystal lattices of the different SiC polytypes. $N_h/N_c=1:1$ for $4H$, $N_h/N_c=1:2$ for $6H$, and $N_h/N_c=2:3$ for $15R$. According to the latest studies, the ionization energies of the nitrogen levels are: [$E_c-0.081$, $E_c-0.138$, $E_c-0.142$ eV $(6H)$];[29] [$E_c-0.052$, $E_c-0.092$ eV $(4H)$].[30] Most investigators assume that nitrogen occupies a carbon site in the SiC lattice.[26,32] However, data exist, at least for $3C$-SiC and especially at concentrations $\leqslant 10^{19}\,\mathrm{cm}^{-3}$, which indicate that nitrogen also displaces silicon.[33] This contradiction may be explained by the fact that when SiC is doped with nitrogen, various complexes are formed in association with intrinsic defects of the SiC or background impurities, which have a different position in the lattice than that of single nitrogen atoms. Thus, observations of Ti–N pairs have been reported[34] in $6H$- and $4H$-SiC, which formed a donor level $E_c-0.6$ eV.

It has been reported[35] that in the purest $4H$-SiC layers the electron spin resonance (ESR) usually associated with nitrogen levels is absent. This was believed[35] to indicate a significant contribution from intrinsic defects to the conductivity of lightly doped layers of SiC. Another feature of SiC(N) samples is the formation of an exciton bound to a neutral donor level of nitrogen. The lines associated with recombination of this exciton in the luminescence spectrum of $6H$-SiC have wavelengths of 4122, 4142, and 4144 Å.[36]

**Aluminum.** The $p$-type silicon carbide is customarily obtained using Al,[37–39] which forms the shallowest acceptor levels in the lower half of the band gap and has the highest solubility ($\sim 10^{21}\,\mathrm{cm}^{-3}$).[40]

It has been shown[38] that when the Al concentration is raised from $10^{18}$ to $10^{21}\,\mathrm{cm}^{-3}$, its ionization energy decreases from 0.27 to 0.1 eV. Later, it was shown[41] that the ionization energy of the Al levels ($E_v+0.24$ eV) is independent of its concentration up to $5\times 10^{20}\,\mathrm{cm}^{-3}$ if the degree of compensation of the epitaxial layers is $k<0.01$. For $k>0.01$, the ionization energy dropped to 0.1 eV ($N_{\mathrm{Al}}\sim 5\times 10^{20}\,\mathrm{cm}^{-3}$). These results were explained in terms of percolation theory;[42] i.e., the interaction among all the forms of impurities in the compensated semiconductor gives rise to an additional potential which reduces the ionization energy of the impurity. This explanation, however, does not rule out the formation of several types of deep centers when silicon carbide is doped with aluminum.

Thus, deep level current spectroscopy of $6H$-SiC $p-n$-structures with an $n$-base doped with Al during the growth process has been used[43] to observe two deep acceptor levels which are absent in undoped samples produced by the same techniques: $HK_1$ ($E_v+0.22$ eV, $\sigma_p=3.6\times 10^{-12}\,\mathrm{cm}^2$) and $HK_2$ ($E_v+0.28$ eV, $\sigma_p=1.3\times 10^{-15}\,\mathrm{cm}^2$). The ratio of the ionization energies of the $HK_1$ and $HK_2$ centers, $E_{i2}/E_{i1}=1.27$, which is substantially greater than the energy ratio for acceptor impurity atoms lying in different nonequivalent sites of an SiC crystal lattice.[27] The concentration of the $HK_1$ center ($N_1$) remained essentially constant in all the samples that were studied, at $\sim 3\times 10^{15}\,\mathrm{cm}^{-3}$. At the same time, the concentration of $HK_2$ ($N_2$) fell sharply when the overall degree of compensation was changed slightly, so that the ratio $N_2/N_1$ changed from 7–12 to 2, although the ratio of the amount of cubic and hexagonal sites in the $6H$-SiC crystal lattice is 2:1. Thus, it is more probable that the $HK_1$ and $HK_2$ levels correspond to different types of deep centers in $6H$-SiC ⟨Al, N⟩ than to a single type of center formed in different nonequivalent sites of the SiC crystal lattice.

A photocapacitance method has been used on $p^+-n$ structures obtained by Al ion implantation[44] to observe a band of levels in the upper half of the band gap, at energies of 0.15–0.5 eV with a capture cross section $\sigma_n\sim 10^{-22}\,\mathrm{cm}^2$.

Thus far, there are no clearly determined data on the ionization energy of Al in different nonequivalent sites of the SiC lattice, although in a number of papers an energy separation has been reported.[27] In any case, the observed difference in the ionization energies was $\sim 0.03$ eV, which, as a rule, is less than the spread in energies obtained by the different authors. Based on a number of optical and electrical measurements, we may assume that at least one center with an ionization energy $E_v+0.23\pm 0.01$ eV is associated with impurity Al in SiC. For $4H$-SiC⟨Al⟩, deep level capacitive spectroscopy (DLTS) has revealed the presence of a level with $E_v+0.23$ eV.[45]

Aluminum ion implantation has been used to create heavily doped spacers for fabricating ohmic contacts to $p$-SiC. It is also possible to obtain $p-n$ structures by ion implantation of Al in epitaxial $n$-type SiC layers. Attempts have been made, although not very successfully, to obtain SiC/AlN solid solutions by implantation of large doses of Al and N.[46]

The doping of SiC with aluminum was the only method (until GaN light emitting diodes were produced) for creating light emitting diodes with peak emission in the blue region of the spectrum. Introducing aluminum also leads to the formation of a bound exciton whose presence can be traced in all the main polytypes of SiC.[47]

**Boron.** A large number of papers have been devoted to studies of the diffusion of boron in SiC.[48–63] This impurity is of interest because in SiC boron forms acceptor levels and can be used to make $p-n$ junctions. In addition, boron has a high solubility, $10^{20}\,\mathrm{cm}^{-3}$, and is one of the most rapidly diffusing impurities in SiC. One feature of the diffusion distribution of boron in SiC is the existence of surface regions (high concentration, low effective diffusion coefficients) and bulk regions (conversely, low concentrations, high diffusion coefficients).[48] This sort of distribution of the boron means that smooth $p-n$ junctions are obtained with rather extended compensated regions as a result of its diffusion into $n$-SiC. This may result in $S$-shaped current-voltage characteristics for a diode produced in this manner.[49] Another shortcoming of boron, as a shallow acceptor impurity, is its substantial ionization energy, $E_v+0.35$ eV, according to Hall measurements.[50,51] Thus, at room temperature the degree of ionization of the impurity is negligible and, despite the high concentration of uncompensated acceptors, the concentration of ionized holes is still low. Thus, efficient injection of holes from a boron doped emitter can be observed only at high temperatures. All this has meant that Al serves as the main acceptor impurity for doping SiC. However, the diffusion of boron has not lost its relevance for certain special problems

in the technology of silicon carbide. One of these applications is the production of light emitting diodes with peak emission in the yellow region of the spectrum ($6H$-SiC). It has been found that boron doping yields luminescence with $h\nu = 2.14$ eV.[52] The diffusion of boron into epitaxial $p-n$ structures makes it possible to obtain $p-i-n$ diodes.[53,54] It has been shown,[55,56] that with boron doping in SiC, in addition to a shallow boron center, a deep $D$-center is formed ($E_v + 0.58$ eV). Later, an analog of the $D$-center was observed in $4H$-SiC.[57,58] The formation of two types of levels, which are not different charge states of a single center, after diffusion of boron into SiC is evidently related to the complexity of the diffusion distribution of B in SiC. For example, it was assumed[59] that boron atoms diffuse in the form of associates with the intrinsic defects of the SiC lattice. This assumption is in agreement with a study[51] of the concentrations of shallow center boron and the $D$-center in SiC samples doped with boron using different techniques. It was shown that during diffusion mostly $D$-centers are formed, while during boron doping in the course of growing epitaxial layers, mainly shallow boron centers are formed. On the whole, it appears entirely probable to us that the surface branch of the diffusion distribution is caused by shallow boron centers, i.e., boron atoms occupying sites in the SiC crystal lattice. The volume branch, on the other hand, is formed by boron+intrinsic defect complexes.

According to the latest ESR data, the structure of the shallow boron center corresponds to a boron atom which displaces Si ($B_{Si}$), while the deep boron center is a complex of a boron atoms with a carbon vacancy.[60,61,91] Note that the $D$-center is a characteristic level for SiC and has been observed in material grown by various techniques.[62,67]

**Gallium.** Gallium is another acceptor impurity in silicon carbide, but with a lower solubility than Al ($\sim 1.2 \times 10^{19}$ cm$^{-3}$)[64,40] and a higher ionization energy [$E_v + 0.29$ eV ($6H$) and $E_v + 0.3$ eV ($4H$)],[64,65] it is essentially not used for fabricating $p-n$ structures. The ionization energy for gallium impurity has also been found to be independent of its concentration. In the different SiC polytypes, Ga has similar ionization energies, as for $3C$ ($E_v + 0.34$ eV) and $15R$ ($E_v + 0.3$ eV).[27] Just as aluminum, gallium is a substitution impurity in a silicon sublattice[29] and it can bind an exciton.[66]

**Indium.** Very little is known about the properties of indium in silicon carbide. It appears to have a low solubility ($\sim 10^{17}$ cm$^{-3}$),[40] and it has not been possible to obtain $p$-type SiC layers by implanting indium during growth.

### 2.2. Other types of impurity centers in SiC

**Beryllium.** In studies[68] of SiC⟨Be⟩ it has been found that Be is an amphoteric impurity in SiC. Photoluminescence has been observed in $n$- and $p$-type $6H$-SiC⟨Be⟩ crystals with a maximum in the red at 1.85–2.1 eV (293 K).[69] As the temperature is lowered, a band with a maximum at $\sim 2.4$ eV flares up in the photoluminescence spectrum of $p$-type samples. Beryllium has not been used to fabricate device structures based on SiC. Only recently has it been shown that Be ion implantation can be used to fabricate epitaxial $p$-type $6H$-SiC layers and produce $p-n$ structures based on them.[70] ESR spectra of an acceptor Be level have been studied.[71,72] The similarity of the structure of this center to that of the shallow boron level was noted.

**Magnesium.** The formation of two new levels has been observed (DLTS) in $n$-$6H$-SiC following implantation of Mg ions ($E_c - 0.49$ and $E_c - 0.45$ eV).[73] Annealing to temperatures of $\sim 1600\,^\circ$C leads to a rise in the concentration of these deep centers.

**Scandium.** In DLTS studies[74] of SiC⟨Sc⟩ a deep center with an energy $E_v + (0.52-0.55)$ eV has been observed; the position of its DLTS peak depends strongly on the electric field strength $E$ in the space charge layer [$E = (1-2.6) \times 10^5$ V/cm]. This was explained[74] in terms of the Poole-Frenkel effect, and the observed deep center attributed to Sc. It is also known that SiC⟨Sc⟩ samples have a photoluminescence peak in the yellow-green region of the spectrum ($6H$ polytype).[75] When SiC is doped with scandium, it is possible to obtain $p-i-n$ structures with a highly resistive $\pi$-region.[76]

**Titanium.** Of the transition metals, Ti and V have been studied in greatest detail as impurities in SiC. On the one hand, this is explained by the fact that these metals are characteristic background impurities in SiC and, on the other, by their large effect on the electrical properties of doped samples. Some time ago,[77,78] it was found that introducing Ti leads to the appearance of narrow lines at energies of 2.79–2.86 eV in the photoluminescence spectrum of $6H$-SiC. These lines were observed in $6H$-, $4H$-, $15R$-, and $33R$-SiC and the number of lines corresponded to the number of nonequivalent sites in the crystal lattice of a given polytype. At the same time, this sort of spectrum was not observed in the $21R$ and $3C$ polytypes of SiC⟨Ti⟩. The relationship of Ti atoms to the observed photoluminescence spectrum was confirmed by a study of optically detectable magnetic resonance (ODMR) in $6H$-, $4H$-, $15R$-, and $15R$-SiC⟨Ti⟩.[79] However, studies of the electron spin resonance[80,81] demonstrated the existence of centers associated with Ti only in $4H$-SiC. Similar results were obtained in DLTS-studies of SiC samples that had been ion-doped with titanium;[82,83] two deep centers associated with titanium were observed in $4H$-SiC⟨Ti⟩, $E_c - 0.12$ and $E_c - 0.16$ eV; which correspond to a hexagonal and cubic position of the impurity in the lattice. In $6H$-SiC⟨Ti⟩ there were no such centers. A general analysis of the data for SiC⟨Ti⟩ has been given by Dalibor *et al.*[82] They suggested that the empirical ''Langer-Heinrich'' (LH) rule, which had been proposed earlier for the III–V and II–VI compounds,[84] applies to the SiC polytypes. According to the LH rule, the energy location of the levels of the transition metals in a series of isovalent semiconducting compounds is unchanged with respect to some common energy level; in other words, the mutual position of the Ti levels in the SiC polytypes remains fixed and does not depend on the polytype parameters. At the same time, the possibility of observing these levels by different methods is determined by the magnitude of the band gap of a given polytype. Thus, the ground state of titanium, observed by DLTS in $4H$-SiC, will not be observed by this method in the other (narrower gap) SiC polytypes, since it is beyond the

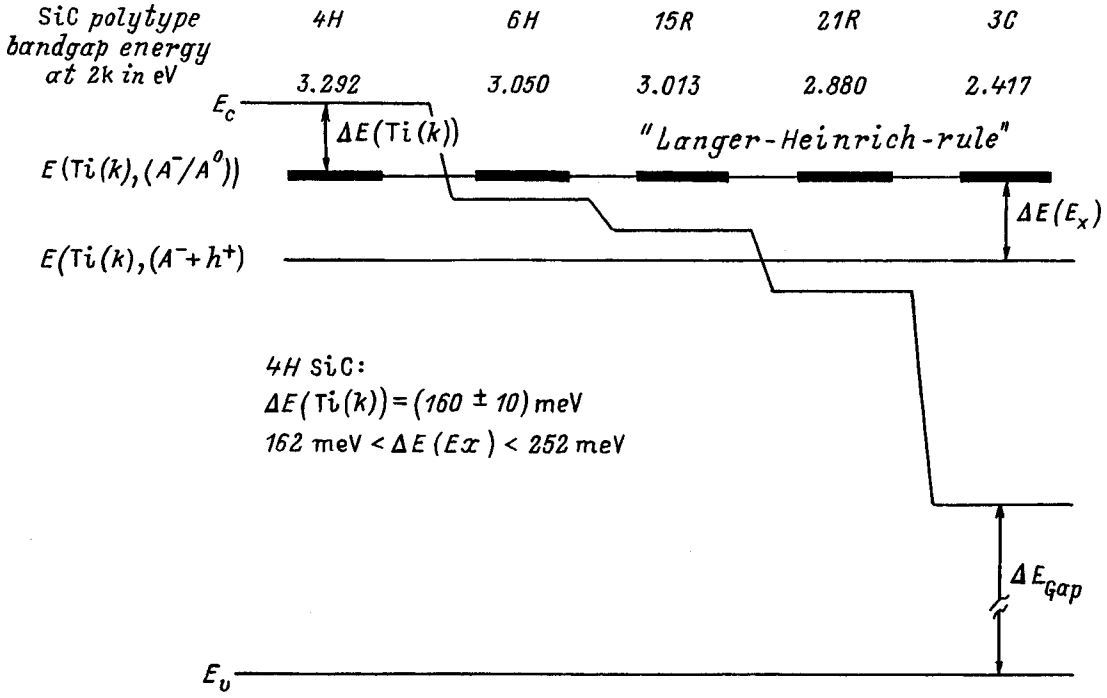


FIG. 2. A diagram illustrating the application of the Langer-Heinrich rule for an impurity Ti center in SiC.[82]

limits of the gap (see Fig. 2.) The energy of an exciton bound to a Ti atom, however, is lower. Thus, photoluminescence owing, which is attributable to recombination of this exciton, has been observed in SiC polytypes with a smaller band gap. Based on the observation of excitons bound with Ti in 4*H*-, 6*H*-, and 15*R*-SiC and their absence in the narrower-gap 21*R* and 3*C* polytypes, the binding energy $[\Delta E(Ex)]$ of this exciton was estimated[82] to be $162\,\text{meV} < \Delta E(Ex) < 252\,\text{meV}$.

**Vanadium.** Studies of the behavior of vanadium in SiC became especially relevant after it was found that doping with V leads to the formation of semi-insulating layers of silicon carbide.[85,86] Introducing vanadium during CVD growth yielded epitaxial layers of 6*H*-SiC with a resistivity of $3000\,\Omega\cdot\text{cm}$. These results were explained by the formation of a deep donor in SiC⟨V⟩ near the middle of the band gap ($E_c - 1.59\,\text{eV}$) which was overcompensated by a background acceptor impurity (boron). According to data from various sources, vanadium is an amphoteric impurity in SiC; i.e., it leads to the formation of both donor and acceptor levels.[80,81,87,88] DLTS on SiC⟨V⟩ has been used to observe yet another level with ionization energies $E_c - (0.65 - 0.75)\,\text{eV}$ and $E_c - 0.97\,\text{eV}$ for the 6*H* and 4*H* polytypes, respectively.[82,89–91,209] It has been proposed that the HL rule holds for vanadium impurity in silicon carbide.[89]

**Chromium.** As for the levels formed during doping of SiC by chromium, there is as yet no established viewpoint. In a study of 6*H*-SiC ion-doped with Cr, two levels with $E_c - 0.38$ and $E_c - 0.34\,\text{eV}$, were observed; the signals from these levels completely disappeared after the samples were annealed at $T \geqslant 1600\,^\circ\text{C}$.[73] At the same time, in SiC⟨Cr⟩ obtained by a similar technique three levels have been observed in 4*H*-SiC ($E_c - 0.15$, $E_c - 0.18$, and $E_c - 0.74$) and one in 6*H*-SiC ($E_c - 0.54\,\text{eV}$).[89,92] These results were interpreted in terms of the HL rule. The reduction in the band gap ($\Delta E \sim 0.22\,\text{eV}$) on going from 4*H* to 6*H* means that the two shallower levels lie beyond the confines of the band gap and the ionization energy of the deeper level is reduced by an amount $\Delta E$.

**Molybdenum.** A center associated with background impurity Mo has been found[93] in commercially produced (CREE) SiC epitaxial layers. It was found that Mo in 6*H*-SiC occupies a silicon site in the lattice and can coexist in two charge states, one of which forms an acceptor level in the *n*-type material near the middle of the band gap. In this regard, it was concluded that using ohmic contacts based on Mo at high temperatures may lead to diffusion of Mo into the bulk semiconductor, compensation of *n*-type material, and device degradation.

**Manganese.** An ESR spectrum has been observed[94] and attributed to a doubly charged donor state of an impurity Mn atom lying in a hexagonal site of a 6*H*-SiC lattice.

**Phosphorus.** As a group V element, phosphorus should form donor centers in SiC. However, since a shallow donor with good solubility in SiC is available (nitrogen), there has been limited interest in investigating other donor impurities in SiC. Phosphorus forms two donor levels in 6*H*-SiC, located at hexagonal ($E_c - 0.085\,\text{eV}$) and cubic ($E_c - 0.135\,\text{eV}$) lattice sites.[95] With phosphorus ion implantation it was possible to obtain $n^+$-layers of 6*H*-SiC with electrically active donor concentrations $\geqslant 3\times10^{18}\,\text{cm}^{-3}$.

**Oxygen.** By analogy with Si, it can be assumed that there will be a high concentration of background oxygen in SiC which can have a significant effect on the parameters of fabricated devices. However, because of the small number of studies on this topic, it is, as yet, difficult to judge the validity of this assumption. The effect of dopant oxygen on the intensity of blue and yellow (boron) photoluminescence in

TABLE II. Parameters and properties of some impurity centers in 6*H*- and 4*H*-SiC.

| Imp. | Energy location, eV | | Lattice site | Participation in recomb. | Other properties | Donor or acceptor |
|---|---|---|---|---|---|---|
| | 6*H*-SiC | 4*H*-SiC | | | | |
| N | $E_c-0.081$<br>$E_c-0.138$<br>$E_c-0.142$[29] | $E_c-0.052$<br>$E_c-0.092$[30] | C[26,32]<br>Si[33] | Bound exciton[31]<br>(cf. Al, Ga, B) | Heteropolytype epitaxy $6H\Rightarrow 3C$ (Refs. 136–138) | D |
| Al | $E_v+0.23$[41,43]<br>$E_v+0.1-0.27$[38] | $E_v+0.23$[45] | Si[47] | Bound exciton (Ref. 47) Al–N DAR, CA recomb.**[27] | Heteropolytype epitaxy $6H\Rightarrow 4H$ (Refs. 136–138) | A |
| B* | $E_v+0.35$[50,51] | $E_v+0.29$[123] | Si[60,61] | B–N DAR[183] | Heteropolytype epitaxy $6H\Rightarrow 4H$ (Refs. 136–138) | A |
| Ga | $E_v+0.29$[64,65] | $E_v+0.3$[64,65] | Si[64] | Bound exciton (Ref. 66), Ga–N DAR, CA recomb.**[27] | | A |
| Sc | $E_v+0.52-0.55$[74] | | Si[140] | Yellow-green PL (6*H*-SiC)[75] | Heteropolytype epitaxy $6H\Rightarrow 4H$ | A |
| Ti | $E_c-0.6$ eV, (Ti–N pairs)[34] | $E_c-0.12$,<br>$E_c-0.16$[82,83] | Si[77,79] | Bound exciton Refs. 77, 78 | | A[82] |
| Cr | $E_c-0.54$[89] | $E_c-0.15$<br>$E_c-0.18$<br>$E_c-0.74$[89] | | | | A[89] |
| V | $E_c-0.7$[209]<br>$E_v+1.6$[81] | $E_c-0.97$[82,89] | Si[88] | Radiative intracenter transition[90] | Semi-insulating layers[85,86], non-radiative recombination center[90] | D[81]<br>A[89] |

*Note:* *The properties of *D*-centers bound to boron are shown in Table III. **A conduction band–neutral acceptor radiative transition.

6*H*-SiC has been studied.[96] No correlation was observed between the oxygen concentration and the intensity of the blue luminescence, while it was found that oxygen is a coactivator of the yellow luminescence. A study of 4*H*-SiC samples that have been ion-doped with oxygen has been made.[97] Two shallower ($E_c-0.3$ and $E_c-0.44$ eV) and three deeper ($E_c-0.74$, $E_c-0.9$, and $E_c-0.95$ eV) centers were found. These centers were attributed to the formation of complexes containing oxygen atoms.

**Argon.** Argon implantation can be used to produce semi-insulating SiC layers, for example, to protect the periphery of Schottky diodes.[73,98] Argon implantation leads to the formation of a band of acceptor centers in *n*-SiC with energies $E_c-(0.2-0.8)$ eV.

**Erbium.** Erbium doping leads to the appearance of a narrow line with a wavelength of $\approx 1.54\,\mu$m in the photoluminescence spectrum of various semiconductors.[99] A radiation source in this optical band is of great interest from a practical standpoint, since it coincides with the absorption minimum of quartz optical fibers. It is assumed that this photoluminescence is associated with an intracenter transition in Er atoms which are fairly weakly bound to the surrounding semiconducting matrix. Single crystal samples of 4*H*-, 6*H*-, 15*R*-, and 3*C*-SiC that were ion-doped with erbium have been studied.[100] In the above-mentioned portion of the spectrum of these samples, a narrow photoluminescence line, whose intensity is essentially unchanged over temperatures of 2–400 K, was detected. At $T>400$ K, the photoluminescence was observed to quench rapidly. No significant differences were observed in the photoluminescence spectra of 4*H*, 6*H*, and 15*R* polytype samples, including in the fine structure of the lines associated with the existence of nonequivalent sites in the SiC lattice. Qualitatively similar results have been obtained in a study of polycrystalline SiC layers implanted with Er.[101] Evidently, the structure of an Er center in SiC and its properties are similar to the properties of erbium in other semiconducting materials.

The parameters of the impurities in SiC studied most extensively are listed in Table II. The table shows that there is a similarity in the parameters and properties of centers formed in the different polytypes of SiC when they are doped by given impurity if the given deep centers develop in the lower half of the band gap. If a given impurity forms centers in the upper half of the band gap, then the parameters (and even the number) of centers in the different polytypes can be different. This property of silicon carbide shows up even more clearly for intrinsic and radiation defects in SiC. Thus, for describing the properties of the latter, we thought it more appropriate to use the order of discussion of the material used in Sec. 2.3.

### 2.3. Intrinsic defects in silicon carbide

#### *2.3.1. Centers in the lower half of the band gap*

***L*-center.** In studies of 6*H*-SiC $p-n$-structures produced by ion implantation of Al (ID structures), deep centers with ionization energies $E_v+0.24$ eV and $\sigma_p\sim 10^{-15}$ cm$^2$ (*L*-centers) have been observed.[55] *L*-centers have also been observed in $p-n$-structures obtained by sublimation epitaxy (SE structures) and in several $p-n$-structures produced by

containerless liquid epitaxy (CLE structures). In the implantation structures their concentration increased near the metallurgical boundary of the $p-n$-junction, while in the other types of samples there was no noticeable profile in the distribution of $L$-centers.

The ionization energy of the $L$-centers was close to the data obtained by other methods for the ionization energy of an impurity Al level.[38] However, while in the case of the ID $p-n$ structures the presence of Al atoms in the base region and a drop in their concentration far from the $p$-region can be explained, for the sharp CLE and SE structures the presence of Al in the $n$-base at concentrations $\sim 10^{16}\,\mathrm{cm}^{-3}$ appears improbable. To clarify the relationship between the observed $L$-center and impurity Al atoms, a study was made of CLE and SE $p-n$ structures with a $n$-base doped with aluminum during growth of SiC⟨Al⟩.[43] Based on studies of these samples, it was concluded[102,103] that the $L$-center is a defect complex, which does not directly include an Al atom and develops both after diffusion and implantation of Al and for other reasons, as well. Later, analogs of the $L$-center were observed in 4$H$-SiC samples obtained by sublimation[104] and in 4$H$- and 6$H$-SiC samples obtained by CVD.[45,105]

***i*-center.** Besides $L$-centers, DLTS spectra of 6$H$-SiC ID structures have revealed a deep level in the lower half of the band gap (an $i$-center). Various analysis techniques have shown that the DLTS peak of the $i$-center is broadened and is not described by the classical equation for the DLTS spectrum.[55] The observed broadening of the DLTS spectra may be caused by the overlap of capacitance signals from two (or more) deep centers with ionization energies $E_1$ and $E_2$. The ionization energy of the $i$-center was found to be in the interval $E_v+(0.52-0.58)$ eV.

Analogous ID structures have been obtained on the basis of epitaxial films of 4$H$-SiC. Their DLTS spectrum was similar to the spectra of ID samples of 6$H$-SiC and an analog of the $i$-center with $E_c+0.53$ eV was observed in them.[106,107] The closeness of the parameters of the $i$-centers in 6$H$ and 4$H$ indicates that the structures of these centers are similar for these polytypes. The distribution of $i$-centers in the base region of a diode has been measured in ID structures based on 6$H$- and 4$H$-SiC.[105] When the distribution profile of $i$-centers in structures based on 4$H$-SiC was extrapolated, good agreement with the beginning of the profile in structures based on 6$H$-SiC was observed; this suggests that the character of the distribution of $i$-centers in structures based on 4$H$-SiC and 6$H$-SiC is the same (Fig. 3). A comparison of the distribution of the $i$-centers and the $N_d-N_a$ profile obtained from capacitance-voltage characteristics showed that the distributions of the compensating defects in the base are the same as the distribution of the $i$-centers.[108] Thus, compensation of the base region in ID structures is caused by an enhanced concentration of deep acceptor levels ($i$-centers) near the metallurgical boundary of the $p-n$-junction. The acceptor nature of the $i$-center is also confirmed by the ratio of the cross sections for carrier capture ($\sigma_p \gg \sigma_n$) for this deep center. It has also been found[107] that implantation of Al in the purest epitaxial layers of 4$H$-SiC leads to formation of an S-shaped current-voltage characteristic, which has been related to a high concentration of $i$-centers. In SE $p-n$ structures it has been found that the distribution of $i$-centers is essentially constant over the entire depth of the base region.[109]

It has been found[67] that both 3$C$-SiC inclusions in epitaxial 6$H$-SiC layers and activator-centers for defect electroluminescence (DEL) are formed under the influence of the same mechanisms, which must be accompanied by relaxation of stresses in the epitaxial layer. In other words, besides a realignment of the 6$H$-SiC lattice with formation of inclusions in a cubic phase, it is possible for stress relaxation to take place through merging of intrinsic defects into the more stable and more energetically favorable complexes which are activators for defect electroluminescence. Since the activator for defect electroluminescence is an $i$-center (see Sec. 4.3), this suggests that it is a complex consisting principally of intrinsic defects of the SiC crystal lattice whose concentration increases after irradiation or implantation. This assumption is in good agreement with the results of Ref. 91, where, based on experiments on the thermal stability of defect electroluminescence in SiC crystals with different concentrations of intrinsic structural defects, it was found that a carbon vacancy is included in the composition of the luminescence center-activator.

***D*-center.** Although a $D$-center is not a purely structural defect (it obviously includes a boron atom), it is a characteristic background center in 6$H$- and 4$H$-SiC grown by various technologies.[55–63] These centers were first observed in a study of DLTS spectra in SiC⟨B⟩ structures and along with $i$-centers in a study of SE samples.[55,56] The closeness of $E_T$ and $\sigma_p$ for $i$- and $D$-centers led to overlapping of their DLTS peaks in SE and ID structures. Thus, the ionization energy of the deep centers ($E^{\partial v}$) determined for structures of these types varied in the range $0.52 \leqslant E_i \leqslant 0.58$ eV. A study of the parameters of $i$- and $D$-centers for electric fields of $(1-7)\times 10^5$ V/cm yielded no noticeable dependence of the ionization energy of these deep centers on electric field strength.[110]

Although the ionization energy of a $D$-center is more than 10% greater than that of a $i$-center, the cross sections for hole capture at these centers have the opposite relation, so that the charge exchange time constants for these centers are very close at $T\sim 300$ K. Here the deeper $D$-center undergoes charge exchange at lower temperatures, so that the total DLTS peak looks like a peak from a single center (Fig. 4). In order to separate the signal from these deep centers, the current relaxation $i$-DLTS method has been used.[111,112] This method has a high resolving power, since it essentially yields the first derivative of the DLTS spectrum. In addition, the use of other temporal windows made it possible to enter a temperature region where the charge exchange time constants for the observed deep centers differ more strongly. Figure 4 shows an $i$-DLTS spectrum of an SE structure, in which the signals from the initial centers can be seen clearly.[110]

Thus, in SE structures both $i$- and $D$-centers exist. The ionization energies of these centers are independent of the electric field strength in the space charge layer in the ranges of concentrations and reverse voltages that have been studied.[55,110] Methods for resolving the DLTS signals in these structures showed that $D$-centers predominate in

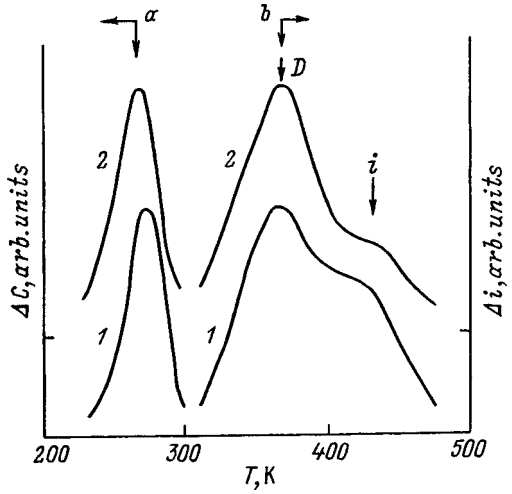


FIG. 4. DLTS (a) and *i*-DLTS (b) spectra of SE $p-n$ structures with large (*1*) and small (*2*) ratios of the concentrations of *i*- and *D*-centers. The parameters of the spectra are: $t_1=10$, $t_2=30$ ms (a) and $t_1=0.1$, $t_2=0.5$ ms (b).[110]

SiC⟨B⟩ and *i*-centers predominate in ID structures. Additional diffusion of boron into epitaxial SE layers prior to formation of the $p-n$ junction also leads to dominance of the *D*-centers. In epitaxial 4*H*-SiC layers doped with boron, an analog of the *D*-center ($E_v+0.54$ eV) has been observed during growth.[58,82]

**Other defects.** A center has been observed near the middle of the band gap ($E_v+1.41$ eV) in *p*-6*H*-SiC and attributed to an intrinsic defect.[105] SiC samples doped with Mn and V and irradiated by neutrons have been studied.[113] A comparison of photoluminescence (PL) spectra and ESR data revealed the existence of a deep acceptor which is related to the appearance of red photoluminescence. Three traps ($E_v+0.5$, $E_v+0.56$, and $E_v+0.69$ eV) were found in a study[114] of *p*-6*H*-SiC (commercial photodetectors from CREE, Inc.). The first two of these have parameters close to *i*- and *D*-centers, respectively.

#### *2.3.2. Defects in the upper half of the band gap*

**6*H*-SiC**

*R- and S-centers.* In studies of Schottky diodes based on 6*H*-SiC two deep centers have been observed: *S* ($E_c-0.35$ eV, $\sigma_p\sim10^{-15}$ cm$^2$) and *R* ($E_c-1.27$ eV).[115–117] The concentrations of these levels, $N_R$ and $N_S$, were the same to within 10–20% in all the surface-barrier structures that were studied. $N_R$ and $N_S\sim10^{15}$ cm$^{-3}$ were close to the values of $N_R$ and $N_S$ in ID and SE $p-n$-structures based on these epitaxial layers. Thus, we may conclude that during the creation of a $p-n$-junction, there was no significant change in the concentration of the *R*- and *S*-centers.

In CLE structures the concentrations of these deep centers were also the same and were, on the average, an order of magnitude lower than in SE structures. It has been shown[82] that these centers are formed after irradiation and ion implantation of 6*H*-SiC. Since these levels annealed out at different temperatures, it appears that they belong to two different centers and not to a single doubly charged center. A double center ($E_1/E_2$) ($E_c-0.34$, $E_c-0.41$), which has parameters close to an *S*-center, has been observed in substrates obtained by the Lely method[118] and subsequently in epitaxial layers grown by CVD.[119] *R*- and *S*-centers have been examined[116] as the main centers for nonradiative recombination (see Sec. 5.1).

*Z*1/*Z*2. Yet another double peak *Z*1/*Z*2 ($E_c-0.6-0.7$ eV) has been observed[118] and subsequently also found in CVD epitaxial layers.[114] ESR was used previously to study several deep centers in 6*H*-SiC substrates obtained by the Lely method.[120] One of the observed centers with an energy $\sim600$ meV was associated with a $V_C-V_{Si}$ divacancy. It was suggested[82] that this center corresponds to the *Z*1/*Z*2 center observed by DLTS.

*Other centers.* In some samples of 6*H*-SiC grown by sublimation epitaxy a center $E_c-1.06$ eV (Ref. 121) has been observed, but not an *R*-center. A level with similar parameters has also been observed in substrates obtained by a modified Lely method.[122] A somewhat deeper level (*EK*4) ($E_c-1.45$ eV) has been found in *p*-CVD-6*H*-SiC.[105]

**4*H*-SiC**

In CVD-layers of 4*H*-SiC only one background $Z_1$ level has been observed with energy $E_c-(0.63–0.68)$ eV.[82,119,124] In epitaxial layers of 4*H*-SiC obtained by SE, no centers have been observed in the upper half of the band gap.[125]

**3*C*-SiC**

Studies of background defects in 3*C*-SiC have been conducted on epitaxial layers grown on silicon substrates.[126,127] Two centers were observed in Ref. 126, *SC*1 ($E_c-0.34$ eV) and *SC*2 ($E_c-0.58$ eV), with DLTS peaks that hardly stood out against the background of a continuous relaxation band. These bands might be associated with a high density of volume defects (dislocations, etc.). After eight years the quality of the epitaxial films had improved greatly and this was reflected in the DLTS spectrum shown in Ref. 127, in which the signals from the separate levels are now fully resolvable. Three deep centers were observed there:[127] $T_1$ ($E_c-0.32$ eV), $T_2$ ($E_c-0.52$ eV), and $T_3$ ($E_c-0.56$ eV), the shallowest of which was identified with the previously observed *SC*1. The parameters of the observed centers are listed in Table III.

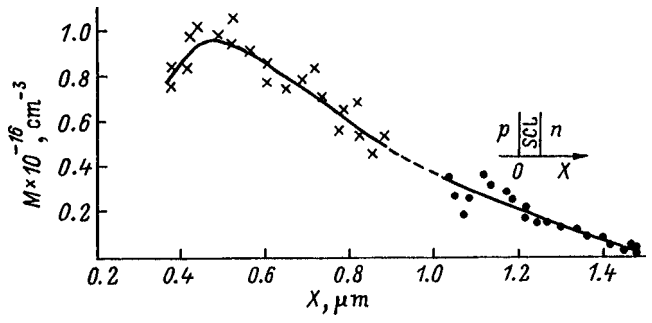


FIG. 3. The distribution of *i*-centers near the metallurgical boundary of an ID $p-n$ structure. The crosses are for 6*H*-SiC, the points, for 4*H*-SiC.[107]

TABLE III. Parameters and properties of intrinsic deep centers in $6H$- $4H$-SiC.

| Center | Energy Location, eV | | pro-posed structure | Participation in recomb. | Conc. rise after | | Donor or acceptor |
|---|---|---|---|---|---|---|---|
| | $6H$-SiC | $4H$-SiC | | | implantation | irradiation | |
| $L$ | $E_v+0.24$[55,105] | $E_v+0.24$[45,104] | $V_C+?$[146] | | | | A[55] |
| $i$ | $E_v+0.52$[55,106,107] | $E_v+0.53$[106,107] | $V_C+?$[146] | Donor EL[158] | Al[55,106,107] | $\alpha$-part.[114] | A[55,106] |
| $D$ | $E_v+0.58$[55,56] | $E_v+0.54$[58] | $B+V_C$ [60,61,146] | ''Boron'' EL[55,56] | Boron diff.[55] | $\alpha$-part.[114] | A[55,58] D[123] |
| $S$ ($E1/E2$) | $E_c-0.35$ (Refs. 115–117) $E_c-0.34/0.41$[118] | | | Nonrad. recomb.[116] | $He^{+}$[82] | Electrons [128,129] | A[82] |
| $Z1/Z2$ | $E_c-0.6/0.7$[114,118] | $E_c-0.63\ldots 0.68$[119] | $V_C+V_{Si}$ [82,120] | | $He^{+}$,$H^{+}$[82] | Electrons [128–130] | A[82] |
| | $E_c-1.06$[121,122] | | | | | Electrons[128] | |
| $EH4$ | $E_c-1.45$[105] | | | Nonrad. recomb.[105] | | | |
| $R$ | $E_c-1.27$[115–117] | | | Nonrad. recomb.[116] | $He^{+}$[82] | Electrons[129] | A[82] |

### 2.4. Radiation doping of SiC

*Electrons.* In a study of $n$-$6H$-SiC bombarded by 3.5 to 4-MeV electrons, centers were observed in the upper half of the band gap with energies of 0.35, 0.6, and 1.1 eV.[128] All these defects annealed out at temperatures up to $\sim$1300 K. According to their ionization energies, these defects can be associated with intrinsic defects: an $S$ center, $Z_1/Z_2$, and a center $E_c-1.06$ eV. These experiments were repeated later[129] using 2-MeV electrons. Besides an increase in the concentration of the background defects $E_1/E_2$ and $Z_1/Z_2$, a new center $E_3/E_4$ ($E_c-0.57$ eV) was observed. A similar increase in the concentration of the $S$ center ($E_1/E_2$) was obtained for CVD epitaxial layers bombarded by 2-MeV electrons.[119] In addition, a center ($E_c-0.51$ eV), which annealed out at temperatures $\sim$800 °C, was observed. The most stable center with respect to annealing was the $S$-center, which was maintained up to temperatures $\sim$1000 °C.

After bombardment by electrons with energies of 2–2.5 MeV, in $4H$-SiC CVD structures,[119,130] besides an increase in the concentration of the background level $Z_1$, a whole series of defects was found to be formed: $EH1$ ($E_c-0.45$ eV), $EH2$ ($E_c-0.68$ eV), $EH4$ ($E_c-0.72$ eV), $EH5$ ($E_c-1.15$ eV), and $EH6/EH7$ ($E_c-1.65$ eV). Most of these centers also appeared after implantation of He and some other ions.[82]

*Neutrons.* A number of deep centers have also been observed after bombardment of SiC by neutrons ($E_c-0.5$, $E_c-0.24$, and $E_c-0.13$ eV).[131,132] It has been proposed that, after annealing, stable vacancy complexes are formed in SiC which are not electrically active. There are several more recent papers on the effect of neutron irradiation on the properties of SiC.[133,134] Mostly the effect of a given type of radiation on the current-voltage characteristics of devices were studied. It has been reported that the rate of carrier removal for SiC is on the order of 4.5 (carriers/cm$^3$)/(neutrons/cm$^2$), which is roughly a factor of 3 lower than for silicon.[135]

*$\alpha$-particles.* It has been reported[114] that irradiation of $n$- and $p$-$6H$-SiC by $\alpha$-particles leads only to an increase in the concentration of already-existing background defects. These studies show that, in terms of radiation resistance, SiC is as good as InP, another radiation resistant semiconductor.

## 3. INFLUENCE OF IMPURITIES ON THE GROWTH OF EPITAXIAL SIC LAYERS

### 3.1. Heteropolytype SiC epitaxy

It has been found[136–138] that when certain impurities are added to the growth zone of SiC layers, it is possible to obtain epitaxial films of a different polytype than the substrate. Thus, introducing the rare-earth elements Sc and Tb, as well as Al and B, led to the growth of epitaxial $4H$-SiC films on $6H$-SiC substrate bases. The most efficient transformation of the polytype of the growing layer, $6H \Rightarrow 4H$, has been observed on introducing the group IV impurities, Sn, Pb, and Ge. Group V impurities (nitrogen and phosphorus) facilitated the growth of polytype $3C$.

It was also found that changing the ratio of the Si and C concentrations in the growth zone had a significant effect on heteropolytype epitaxy. Increasing the Si concentration, for example, leads to a rise in the probability of forming $3C$-SiC or other polytypes with a low hexagonal percentage. At the same time, introducing excess carbon made it possible to grow epitaxial layers of $4H$-SiC from melts of Gd and Dy, as well, on $6H$ substrates.[138] It has also been noted[136] that the transformation of the substrate polytype takes place especially easily during growth in the (0001)C direction. Here the temperature and growth rate had little effect on the heteropolytype epitaxy process.

Thick epitaxial layers of $4H$-SiC on a base of $15R$- and $6H$-SiC substrates have been produced and then used as seeds for growing single crystal ingots.[139,140] Growth was on the (0001)C facet with Sc added to the vapor phase. This method made it possible to obtain epitaxial layers of both $n$- and $p$-types. It was noted[140] that a high concentration of Sc ($\geqslant 10^{17}$ cm$^{-3}$) in the epitaxial films produced mechanical stresses in them. On the whole, the epitaxial layers obtained in this way had fairly high structural perfection, so that they could be used to make field-effect transistors with a gate in the form of a $p-n$-junction (JFET transistors).[141]

$3C$-SiC layers on a base of $6H$-SiC substrates can also be produced by sublimation growth in excess silicon without additional doping.[142] In this case the growth of the $3C$ films takes place with twinning, and the area of a single twin is, at most, $4-6\ \mathrm{mm}^2$ (Ref. 143). The $n$-$6H$-SiC/$p$-$3C$-SiC heterojunctions produced by a similar technology have been studied.[144,145] These studies show that in these heteropolytype $p-n$ structures, a thin $\pi$-$6H$-SiC defect layer develops between the $p$-$3C$ and $n$-$6H$, which also determines the electrical characteristics of the resulting diode structures.

Since the nature of polytypism is still unclear, it is also rather difficult to understand the nature of heteropolytype epitaxy. Besides the impurity composition of the growth zone, various other factors can affect the probability of heteropolytype epitaxy, ranging from thermodynamic (pressure, temperature) to crystallographic (orientation and the degree of imperfection of the substate). It was found,[146] for example, that if substrates of $6H$-SiC produced by the Lely method with a high density of dislocations ($\sim 10^5\ \mathrm{cm}^{-2}$) are used in the standard (for growing $6H$ layers) sublimation epitaxy process, epitaxial $3C$ layers will be grown.

Heteropolytype epitaxy processes have been linked to the stoichiometric composition of various SiC polytypes.[136,147] It had been observed earlier that the ratio of the Si and C concentrations is not constant in the different SiC polytypes, and that it decreases as the hexagonal percentage is increased. It was shown that the ratio of the Si and C concentrations was 1.046, 1.022, and 1.001 for $3C$, $6H$, and $4H$, respectively.[148] An examination[136] of data on diffusion and solubility in various SiC polytypes also indicates that the vacancy concentration $V_{\mathrm{C}}$ is also different.

The observed dependence was explained[136] by the fact that, when the stresses in the lattice rise as the concentration of carbon vacancies increases, bonds between atoms in cubic sites became more energetically favorable. This also led to a realignment of the crystal and a polytype transformation. It was also assumed[136] that the bulk of $V_{\mathrm{C}}$ is in an electrically inactive state. The formation of $3C$ inclusions in $6H$-SiC $p-n$-structures under the action of a forward current has also been reported.[149]

### 3.2. Site-competition epitaxy of SiC

Larkin *et al.*[150] have found that the concentration of electrically active impurities depends on the ratio of the concentrations of C and Si in the gaseous phase during CVD growth of epitaxial SiC layers. They referred to this effect as site-competition epitaxy (SCE).[150] The $n$-SiC epitaxial layers with uncompensated donor concentrations $N_d-N_a \sim 10^{14}\ \mathrm{cm}^{-3}$ have been obtained using SCE.[135,151] The observed dependence was explained[150] by a high concentration of C atoms on the crystal growth surface which inhibits the implantation of N atoms that occupy carbon sites in the lattice. This dependence was observed only in the case of growth on an Si-facet of the substrate. During growth on a C-facet, a change in the ratio of the C and Si concentrations had little effect on the concentration of the electrically active impurity. This model has been confirmed by secondary ion mass spectrometry (SIMS) measurements of the concentration of N atoms in SiC epitaxial layers grown with different ratios of the C and Si concentrations in the gaseous phase, although, according to Ref. 150, a change in the concentration of N atoms by a factor of 2.5–3.5 in the SIMS data corresponded to a reduction in $N_d-N_a$ by a factor of 4 or 5. In our opinion, this indicates the possible existence of another process which also affects the magnitude of $N_d-N_a$. One such process might be a dependence of the concentration of background acceptor defect centers in epitaxial layers on the ratio of the C and Si concentrations in the gaseous phase; i.e., it might be assumed that as the ratio of the C and Si concentrations is lowered, the total concentration of background acceptor levels increases. This assumption is consistent with a report[151] that lightly doped $p$-layers were obtained at the highest values of the ratio of the C and Si concentrations in the gaseous phase.

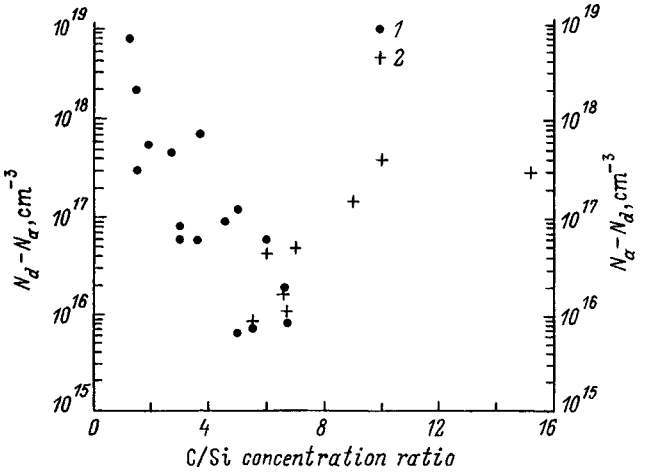


FIG. 5. The type of conductivity and $N_d-N_a$ ($N_a-N_d$) in $6H$-SiC CVD epitaxial layers grown with different ratios as functions of the concentrations of C and Si in the gaseous phase: (*1*) $n$-type, (*2*) $p$-type.

Such an effect, the overcompensation of lightly doped $n$-layers by deep background acceptors ($i$- and $D$-centers), has also been observed during growth of $6H$-SiC by sublimation epitaxy.[109] During studies of epitaxial layers grown by sublimation epitaxy, it has also been found that increasing the pressure of silicon ($P_{\mathrm{Si}}$) in the growth cell (increasing the ratio of the C and Si concentrations) leads to overcompensation of the growing layer and, then, with further increases in $P_{\mathrm{Si}}$, to the growth of ever more heavily doped layers of $p$-SiC.[152]

In studies of $6H$-SiC layers grown by CVD (in a methane+silane+$H_2$ system) in our laboratory, it has also been found that as the ratio of the concentrations of C and Si in the gaseous phase is increased, there is an initial inversion of the conductivity type followed by the growth of progressively more heavily doped $p$-layers (Fig. 5). DLTS studies of the grown $p$-layers showed that the main contribution of $N_a-N_d$ is from deep acceptor centers ($E_c+0.2\pm0.02$ eV), whose parameters are close to those of $L$-centers, the usual background center in layers grown by sublimation. The concentration of these centers increased as $N_d-N_a$ rose (i.e., as the ratio of the concentrations of C and Si, which was main-

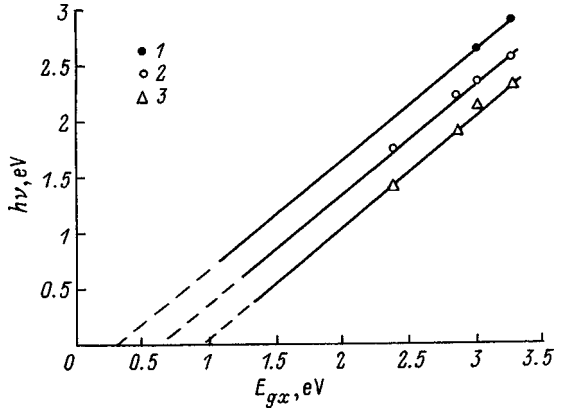


FIG. 6. The position of the maxima of several electroluminescence bands in SiC polytypes as a function of the exciton width of the band gap: (*1*) ''aluminum'' electroluminescence,[45,153] (*2*) ''defect'' electroluminescence,[154] and (*3*) ''boron'' electroluminescence.[155]

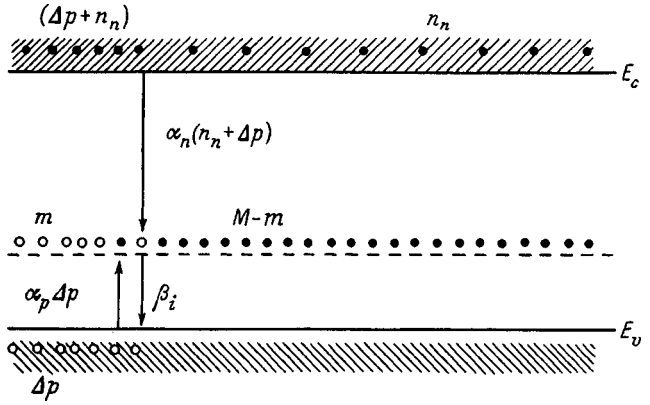


FIG. 7. A diagram of the possible electronic transitions during charge exchange by injected carriers of deep centers lying in the lower half of the band gap of an *n*-base.[159]

tained in the gas mixture during growth of the given layer, was raised).

Thus, we believe that a change in the ratio of the C and Si concentrations during growth of epitaxial SiC layers not only affects the trapping of nitrogen atoms in the SiC lattice, but also influences the concentration of the background deep acceptor levels that are formed.

## 4. RADIATIVE RECOMBINATION AND DEEP CENTERS IN SIC

### 4.1. Population statistics of deep centers in SiC

The large band gap in SiC has made it possible to fabricate light emitting devices over essentially all of the visible spectrum. The same mechanism of radiative recombination (the same technique for fabricating a light emitting diode) corresponds to different energies for the emission peak in different polytypes; i.e., compared to 6*H*-SiC the location of the electroluminescence (EL) maximum shifts to shorter wavelengths (in the case of a wider gap polytype) or to longer wavelengths (in the case of a narrower gap polytype) by an amount roughly equal to the difference between the band gaps of the given polytype and 6*H*-SiC (Fig. 6). As can be seen from this figure, the energy of the emission peaks depends linearly on the width of the band gap. The intercept formed by extrapolating these curves to zero $h\nu_{\max}$ can be used for an approximate estimate of the ionization energy of the recombination center [or the sum of the energies of two centers, in the case of donor-acceptor recombination (DAR)].

Obviously, in studying impurity luminescence bands it is important to determine the radiative recombination mechanism responsible for the given recombination. The distinctive features of donor-acceptor recombination are well known:[156] a shift of the peak to shorter wavelengths as the level of excitation is increased, nonexponential relaxation, and a shift of the peak to longer wavelengths for longer delays between detection and the end of the exciting pulse. These signs, of course, are valid for SiC, as well. However, the existence of several nonequivalent sites in the SiC lattice permits the formation of several deep centers with similar parameters by a single type of impurity or defect. A redistribution in the intensity of recombination among these deep centers as the excitation level is varied may mean that signs of donor-acceptor recombination may be observed in luminescence bands associated with other radiative processes (e.g., a radiative transition of an electron from the conduction band to a deep acceptor). Thus, formulas describing the characteristics of electroluminescence based on selected models and on the parameters of the deep centers involved in them have been derived for identifying the emission mechanisms of observed electroluminescence bands.[157–159] The calculations were then compared with experimental data.

Since this approach can be used for identifying the deep centers, we reproduce the main results of Refs. 157–159 here.

*General equations.* Let us consider the charge exchange of a deep center lying in the lower half of an *n*-base during hole injection. We shall analyze the case in which (a) the concentration of deep centers is much lower than that of shallow centers and (b) the deep center concentration is independent of position. The degree of filling of these deep centers will be determined by three processes (Fig. 7):

1) capture of an injected hole from the valence band to a level $\sim \alpha_p \Delta P(M-m)$,

2) capture of an electron from the conduction band to a level $\sim \alpha_n(N_n+\Delta P)m$, and

3) thermal ionization of a hole into the *V*-band $\sim \beta_i$,

where $\alpha_{n(p)}=\sigma_{n(p)}V_t$, $m$ is the concentration of deep centers filled by holes, $M$ is the total concentration of deep centers, $\beta_i=N_v V_t \sigma_p \exp(-E_i/kT)$, $\sigma_{n(p)}$ is the cross section for capture of an electron (hole) at a deep center, $N_n$ is the equilibrium electron concentration in the base, $V_t$ is the thermal speed of the charge carriers, $N_v$ is the density of states in the valence band, $E_i$ is the ionization energy of the deep centers, $k$ is Boltzmann's constant, $T$ is the absolute temperature, and $\Delta P$ is the concentration of injected holes.

The rate of change of the concentration of deep centers filled with holes can be written as

$$dm/dt=(M-m)\alpha_p \Delta P-(N_n+\Delta P)\alpha_n m-\beta_i m. \quad (4.1)$$

The solution of this equation for the initial conditions $t=0$, $m=0$ is

$$m = M[1-\exp(-t_i/t_0)] \times\{1+[\alpha_n(\Delta P+N_n)+\beta_i](\alpha_p\Delta P)^{-1}\}^{-1}, \quad (4.2)$$

where $t_0=[(N_n+\Delta P)\alpha_n+\alpha_p\Delta P+\beta_i]^{-1}$, and $t_i$ is the duration of the injection pulse. We shall consider the case where $t\geqslant t_0$ and $m$ goes to saturation. After the forward polarity pulse ends and the $p-n$ structure is switched to an initial reverse voltage, the deep centers undergo charge exchange which gives rise to the relaxation of the capacitance $\Delta C$. In our conditions, DLTS is used to measure the change in the deep center concentration, $m$. It is known that $\Delta P = F(I_f, X)$, where $I_f$ is the forward current, and $X$ is the distance from the $p-n$-junction. If $\Delta P > N_n$ (a high level of injection), then

$$m_1 = \alpha_p M(\alpha_p+\alpha_n)^{-1}. \quad (4.3)$$

It should be noted that the concentration measured in this fashion is not the total concentration and differs from the latter by a factor $\xi$, where $\xi=\alpha_p/(\alpha_p+\alpha_n)$. However, if $\alpha_p\gg\alpha_n$, then $\xi\approx 1$ and $\xi M\approx M$. The magnitude of $\xi$ is determined by the ratio of the cross sections for capture of carriers to a level.

*Determination of the electroluminescence characteristics in the case of a radiative transition of an electron from the conduction band to a deep acceptor.* In examining the population kinetics of deep centers in the lower half of the $n$-base during hole injection, we assume that a transition from the conduction band to an acceptor is radiative. The formula for the electroluminescence intensity per unit volume per unit time ($I_{v,t}$) can then be written in the form

$$I_{v,t} = \alpha_n(n_n+\Delta n)m. \quad (4.4)$$

The concentration of deep centers filled with holes is given by Eq. (4.2) for the case $t_i\gg\tau$ as

$$m = \frac{M}{1+\dfrac{\alpha_n(\Delta P+n_n)+\beta_i}{\alpha_p\Delta P}}. \quad (4.5)$$

To obtain an expression for the electroluminescence intensity per unit time ($I_t$), we substitute Eq. (4.5) in Eq. (4.4) and integrate over the $X$ axis (the $X$ axis is directed from the metallurgical boundary of the $p-n$ junction into the depth of the base region). Since $dV=Sdx$, $\Delta p=\Delta p_0\exp(-x/Lp)$, where $\Delta p_0$ is the concentration of injected holes in the $n$ region at the metallurgical boundary of the $p-n$ junction, $S$ is the area of the $p-n$ junction, and $L_p$ is the hole diffusion length, we obtain

$$I_t = \frac{MSL_p\alpha_p\alpha_n}{\alpha_p+\alpha_n}\left[\Delta P_0 + \frac{n_n\alpha_p-\beta_i}{\alpha_p+\alpha_n}\ln\left(\frac{\alpha_n n_n+\beta_i+(\alpha_n+\alpha_p)\Delta P_0}{\alpha_n n_n+\beta_i}\right)\right]. \quad (4.6)$$

An expression for the afterglow time constant can be obtained from Eq. (4.1) with the condition for cutoff of injection ($\Delta P=0$):

$$\tau_n = \frac{1}{\alpha_n n_n+\beta_i}. \quad (4.7)$$

An analysis of the temperature dependence of the afterglow time constant $\tau_n$ of yellow electroluminescence[53] shows that the main contribution to damping the electroluminescence at low temperatures is from recombination of holes captured at $D$-centers and of electrons in the conduction band, with $\tau_n\propto 1/\alpha_n n_n$, while at high temperatures, it is from thermal ionization of holes from $D$-centers, with $\tau_n\propto 1/\beta_i$.

We now examine the theoretical dependence $I_t = f(\Delta P_0, T)$.

I. Low-temperature region.

The thermal ionization of carriers from deep centers is negligible ($\beta_i$ is small) and the function $I_t=f(\Delta P)$ breaks up into three segments:

A. A first segment with a linear rise. The luminescence intensity is proportional to the concentration of deep centers filled with injected carriers ($m$). The quantity $m$ rises as $\Delta P_0$ is increased.

B. A sublinear segment. Since $\sigma_p\gg\sigma_n$ in our case, despite the fact that $n_n\gg\Delta P$, $\sigma_p\Delta P>\sigma(n_n+\Delta P)$. This means that essentially all of the deep centers in a given volume of the base are filled with holes. The electroluminescence intensity is determined by the term $\sigma_n(n_n+\Delta P)$ and the function $I_t=f(\Delta P_0)$ enters a sublinear segment. If $\sigma_p=\sigma_n$, then $I_t=f(\Delta P)$ would be almost completely linear.

C. A second segment with a linear rise. The electroluminescence intensity begins to rise further when $\Delta P_0\propto n_n$, i.e., in the strong injection region. Note that, because of the exponential distribution of the injected carriers, $\Delta P=\Delta P_0 e^{-x/L_p}$, even when case C occurs near the metallurgical boundary of the $p-n$ junction, in the depth of the base region there are regions where cases B and A occur. This means that in the overall dependence all the interfaces between the segments are smeared out.

II. High-temperature region.

With increasing temperature, the probability of thermal ionization of holes from deep centers increases. This means that complete filling of the deep centers in a given volume requires a high concentration of injected carriers ($\Delta P$). The low temperature boundary of segment B shifts to higher values ($\Delta P_0$) and the sublinear segment is contracted. It disappears entirely as the temperature is raised further.

**Analysis of electroluminescence spectra in the case of donor-acceptor recombination.** The following analytic expression for $I_t=f(J,T)$ can be obtained in the donor-acceptor recombination model. In the case of donor-acceptor recombination, the recombination intensity per unit volume and unit time, $I_{v,t}$ can be written as

$$I_{v,t} = M\frac{W_d W_a}{\tau_0}, \quad (4.8)$$

where $W_d$ is the probability of filling a donor level, $W_a$ is the probability of filling an acceptor level, $M$ is the number of donor-acceptor pairs, and $\tau_0$ is the radiative recombination

time constant. In general, $\tau_0$ depends on the distance between the components of a pair. We shall use the average value $\langle \tau_0 \rangle = \tau_r$, where $\tau_r$ is determined directly from experiment.

For the population statistics of the donor and acceptor levels in the base we can write

$$\frac{dn}{dt} = (N_0 - n)\alpha_n(n_n + \Delta p) - \alpha_n n \beta_n - \frac{MW_d W_a}{\tau_0},$$

$$\frac{dm}{dt} = (M_0 - m)\alpha_p \Delta p - m\alpha_p \beta_p - \frac{MW_d W_a}{\tau_0}, \qquad (4.9)$$

where $N_0 = M_0 = M$ is the total concentration of donor and acceptor levels.

For constant excitation, $dn/dt = dm/dt = 0$, the solution of this equation is

$$I_{v,t} = \frac{2AB}{A + B - \tau_0 Mab \pm \sqrt{(A + B - \tau_0 Mab)^2 - 4AB}}. \qquad (4.10)$$

In the following we consider the solution with the + in the denominator; subtraction leads to division by zero. To find the recombination intensity per unit time, $I_t$, we integrate Eq. (4.10) over the volume $V$ of the base. Since $dV = Sdx$, we obtain an expression for numerical integration:

$$I_t = SL_p M \int_0^1 \frac{\alpha_p \Delta p_0 (\Delta p_0 y + n_n) dy}{K + \sqrt{K^2 - 4\lambda(n_n + \Delta p_0 y)\Delta p_0 y}}, \qquad (4.11)$$

where

$$K = n_n + \Delta p_0 y(\lambda + 1) + \tau_0 \alpha_p (n_n + \Delta p_0 y + \beta_n)(\beta_p + \Delta p_0),$$

$$\lambda = \alpha_p / \alpha_n, \quad \text{and} \quad y = \exp(-x/L_p).$$

**Determination of the magnitude of the second cross section for capture of carriers from DLTS spectra.** The presence in the base of a diode of a deep center which undergoes charge exchange during injection makes it possible to determine the cross section for capture at this level of both the majority and minority charge carriers.

For concreteness, we consider deep centers in the lower half of the band gap of an $n$-type base. In this case the hole capture cross section can be determined directly from DLTS spectra. To determine $\sigma_n$ with DLTS, the reverse voltage is not applied instantaneously after the forward voltage pulse but after a time $t_3$ during which the reverse voltage at the $p-n$ structure equals zero. Over the time $t_3$ the deep center undergoes charge exchange by electrons from the conduction band and the amplitude of the DLTS peak, $\Delta C$, decreases. The quantity $\sigma_n$ can be determined from the tangent of the $\Delta C = f(t_3)$ curve:

$$\Delta(\Delta C) = C_0 - C_0 e^{-t_3/nV_T\sigma_n} \Rightarrow \sigma_n = \frac{\ln \dfrac{C_0 - \Delta C}{C_0}}{V_T n t_3}, \qquad (4.12)$$

where $C_0 = C$ for $t_3 = 0$. This method has been used to determine the capture cross section at $i$, $D$, and $L$ centers in $4H$- and $6H$-SiC.[58,157,158] Determining both cross sections for carrier capture at a center makes it possible to examine its contribution to radiative and nonradiative recombination in a more rigorous fashion.

### 4.2. Electroluminescence associated with impurity aluminum atoms

It has been found previously that in the short wavelength portion of the luminescence spectrum of $p-n$ structures doped with aluminum and nitrogen ($6H$-SiC⟨Al, N⟩), it is possible to distinguish four peaks,[160–163,27] which have been attributed[163,27] to phononless recombination at an Al–N donor-acceptor pair ($h\nu = 2.78$ eV) and their one-, two-, and three-phonon echoes.

The spectra in Refs. 27, 162, and 163 were analyzed taking into account the existence of nonequivalent sites for impurity atoms in the SiC crystal lattice. In a study of SiC⟨Al, N⟩ light-emitting diodes it was found that the electroluminescence spectrum depends on the concentration of the introduced aluminum. Two main peaks in the luminescence spectrum have been identified[164] (in addition to $h\nu_c \sim 2.92$ eV, which is associated with annihilation of a free exciton[165]): 2.75 eV, a conduction band-Al level transition (CA recombination), and $\sim 2.58$ eV, donor-acceptor recombination. Most other papers on the electroluminescence of SiC⟨Al, N⟩ light-emitting diodes[11,166–168] report observing a single maximum with $h\nu \sim 2.6$–$2.7$ eV, which became narrower and shifted to shorter wavelengths as the forward current density was raised.[167,168]

Although when interpreting the spectra of SiC⟨Al, N⟩, all authors have assumed that recombination proceeds with the participation of acceptor Al levels, the parameters of the latter have not been determined sufficiently unambiguously. The observed scatter in the experimental data may possibly be explained by the formation of several types of deep centers with different ionization energies during doping of SiC with aluminum. An attempt has been made[169] to interpret the electroluminescence spectra of SiC⟨Al, N⟩ $p-n$ structures using the already known spectra of deep centers.

Figure 8 shows electroluminescence spectra of $6H$-SiC samples doped with aluminum during the growth process,[169] in which $HK1$ and $HK2$ centers have been observed (see Sec. 2.1). The figure shows that the electroluminescence spectra have a maximum at $\sim 450$–$490$ nm. In addition, while the samples in which $HK2$ centers predominated had a single peak, for the samples where the concentrations of these centers were similar the peak was split into two components $\lambda_1 \sim 455$ nm (peak $C$) and $\lambda_2 \sim 480$ nm (peak $D$). As $J$ was increased, peak $D$ shifted to the other side of high energies (as is typical of donor-acceptor recombination), while peak $C$ was essentially unshifted, but its intensity increased more rapidly with $J$. All these results suggest that peaks $C$ and $D$ are caused by different recombination mechanisms.

The ratio of the amplitudes of the peaks varied nonmonotonically with $J$. At low currents their amplitudes were

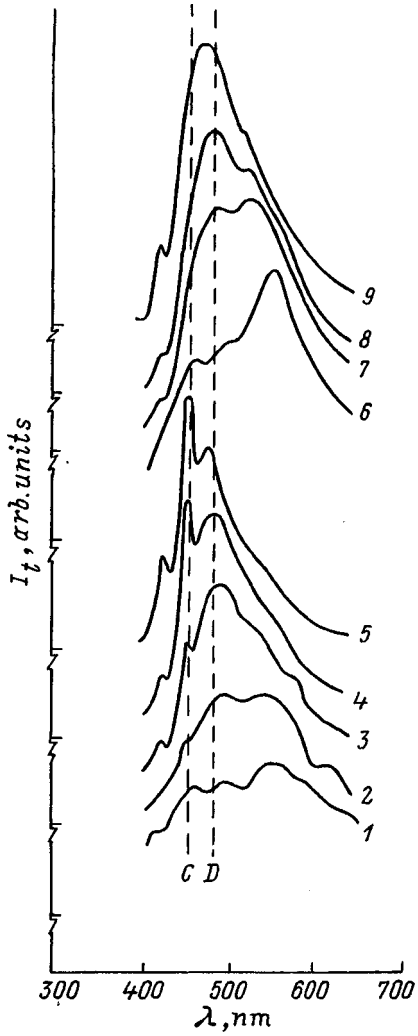


FIG. 8. Electroluminescence spectra of $6H$-SiC⟨Al⟩ samples with different forward current densities and different ratios of the concentrations of $HK1$ and $HK2$ centers (the ratio of their concentrations is denoted by $k$) at room temperature. For the sample with $k\approx 1$ $J=1.2$ (*1*), 4 (*2*), 12 (*3*), 40 (*4*), and 120 A/cm$^2$ (*5*). For the sample with $k<1$ $J=8$ (*6*), 20 (*7*), 40 (*8*), and 120 A/cm$^2$ (*9*).[169]

roughly equal, then with increasing $J$ peak $C$ essentially vanished, then it appeared anew and either exceeded peak $D$ for $J\sim 10$ A/cm$^2$ or separated from peak $D$ as a shoulder. Here the spectrum of the test samples at low currents was similar to the photoluminescence spectra of the SiC⟨Al, N⟩ samples of Refs. 161–163 and 27, while at high currents it was similar to the emission spectra of the light emitting diodes of Ref. 164 (concentrations of $HK1$ and $HK2$ are similar) and Refs. 167, 168, and 11 (concentration of $HK2$ is greater than that of $HK1$).

A comparison of the DLTS spectra and electroluminescence spectra of samples of $6H$-SiC⟨Al, N⟩ showed a unique correlation of peaks $C$ and $D$ with the presence of $HK1$ and $HK2$ deep centers in these samples. There was no correlation of these electroluminescence peaks with any other deep centers. Thus, we can say that radiative recombination of carriers involving $HK1$ and $HK2$ deep centers is responsible for the electroluminescence at energies of 2.5–1.75 eV in the emission spectrum of $6H$-SiC⟨Al, N⟩ $p-n$ structures. Here, if the $D$ peak has the characteristic features of donor-acceptor recombination, then peak $C$ is obviously caused by other recombination mechanisms, such as radiative recombination of an electron at a neutral acceptor.

A calculation of the temperature dependence of the intensity using Eq. (4.6) showed[169] that substantial agreement with experiment was obtained with the function $I_t=F(T)$ calculated using the parameters of $HK1$ centers.

As noted above, the electroluminescence spectra of SiC⟨Al, N⟩ samples differed strongly with high and low forward current densities. This may be explained by the presence of two types of spectra with different dependences of the intensity on $J$; i.e., the peaks $C$ and $D$, which depend linearly on $J$ and are coupled to $HK1$ centers, are superimposed on a ''background spectrum'' which depends weakly on the forward current density (perhaps coupled to the $HK2$ centers).

The following conclusions were reached:[169]

1. The structure of the electroluminescence spectra of SiC⟨Al, N⟩ samples depends strongly on the forward current density. The electroluminescence spectrum is evidently determined by different radiative recombination mechanisms at $J\approx 1$ A/cm$^2$ and $J\approx 100$ A/cm$^2$.

2. The electroluminescence spectrum at $J\approx 100$ A/cm$^2$ can be explained by radiative recombination involving the observed $HK1$ deep center ($E_v+0.22$ eV).

#### 4.3. ''Defect electroluminescence''

Short wavelength luminescence at energies of 2.6–2.3 eV was observed in 1966 by Makarov[170] in $n$-SiC($6H$) crystals after bombardment by K and Li ions with subsequent annealing. The luminescence spectrum consisted of two triplets of narrow lines ($H$- and $L$-lines) located near energies of 2.6 eV and a broad, structureless band with an emission peak at 2.35 eV. It was later established[171,172] that the broad band is not an extension of the fine structure and it was proposed that this band is caused by radiative recombination involving a donor nitrogen level and an acceptor center which arises during implantation. The structure of the $H$- and $L$-lines has been studied in detail with their temperature dependences[173] and the spectrum itself is designated as $D1$.

The $D1$ spectrum has been recorded in SiC after irradiation with electrons,[174] neutrons,[175] and various types of ions.[172] It has therefore been possible to fabricate efficient light-emitting diodes operating in the green region of the spectrum based on $6H$-SiC that has been ion doped with Al and Ga.[176] Irradiation has yielded luminescence with similar properties in other polytypes of SiC.[154,171] Since this sort of luminescence appears as a result of irradiation or the implantation of various kinds of ions in SiC, it was proposed that the luminescence activator-center is either a purely defect structure[177] or is a complex of an intrinsic defect with a background impurity atom.[178] No deep centers coupled to this defect have been observed.

Later, it was noted[158] that there had been some terminological confusion, since in a number of papers[172,173,178] the $D1$ spectrum was assumed to be just the $H$- and $L$-lines and their background echoes, while in others[179,180] this designa-

tion was extended to the entire spectrum of this luminescence. As a result, after it was shown[181] that the $H$- and $L$-lines can be explained by recombination of a bound exciton, some writers attributed the entire spectrum observed in Ref. 170 to this recombination mechanism. From the standpoint of the authors of Ref. 158, this is incorrect, since it contradicts the earlier results.[171,172] In Ref. 158, it was proposed that the term $D1$ be retained for the short-wavelength portion of the spectrum observed by Makarov (the $H$- and $L$-lines), while the long-wavelength portion of this spectrum (the broad, structureless band) should be called ''defect'' electroluminescence. It is possible that defect electroluminescence and the $D1$ spectrum are caused by recombination of carriers involving deep centers of similar types (or even of a single type), but the specific emission mechanisms for both parts of the spectrum may be different.

DLTS studies[158,110,182] have established an unambiguous correlation between defect electroluminescence of $6H$- and $4H$-SiC $p-n$-structures and the presence of $i$-centers in these structures.

An analysis of the characteristics of defect electroluminescence from the standpoint of the different recombination mechanisms led Andreev *et al.*[158] to the conclusion that the bulk of the recombination proceeds through donor-acceptor pairs such as $i$-center–nitrogen. Calculations based on this model using Eq. (4.1) with the parameters of these centers are in good agreement with experiment, which obviously does not exclude the possibility of bound exciton's being formed next to an $i$-center. Optical lines attributable to it would be found in another region of the spectrum. We note also that the presence of three nonequivalent sites in the SiC crystalline lattice for both donor and acceptor centers can lead to the formation of several pairs with similar parameters, each of which will contribute to the total spectrum.

### 4.4. Relationship of ''boron'' electroluminescence and *D*-centers in 6*H*- and 4*H*-SiC

A correlation between the existence of ''boron'' electroluminescence [$h\nu \sim 2.14$ eV ($6H$) and $h\nu \sim 2.14$ eV ($4H$)]in $6H$- and $4H$-SiC $p-n$ structures and the presence of $D$-centers in these structures has been found.[58,157] This correlation indicates that these centers participate in the radiative recombination process. Earlier,[27,183] it had been found that the high temperature ''boron'' electroluminescence in $6H$-, $4H$-, and $3C$-SiC is caused by conduction band-acceptor radiative transitions. Thus, in an analysis of experimental data on the dependence of the electroluminescence intensity on the forward current density and temperature and of the temperature dependence of the afterglow time, Anikin *et al.*[157] began with the idea that this electroluminescence is caused by radiative recombination of a hole trapped at a $D$-center and an electron in the conduction band. Calculations based on Eqs. (4.6) and (4.7) were in good agreement with experiment (Figs. 9 and 10) for samples of both polytypes. As the figures show, the experimental $I_t = f(\Delta P_0, T)$ and $\tau = f(T)$ curves contain all the features implied by an analysis of the corresponding expressions from Sec. 4.1. At low temperatures the $I_t = f(\Delta P_0, T$ curve breaks up into three segments and as the temperature is raised, the second (sublinear) segment vanishes (Fig. 9). The afterglow time at low temperatures was mainly determined by the time constant for capture of electrons from the conduction band and at high temperatures, by thermal ionization of holes (Fig. 10).

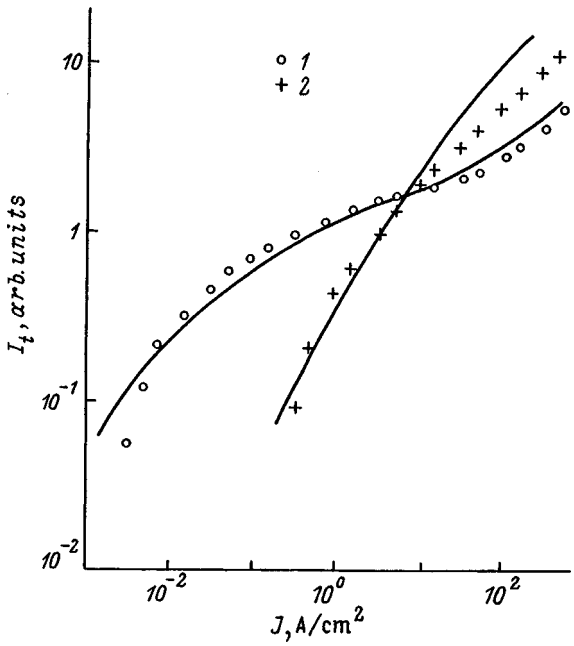


FIG. 9. The intensity of boron electroluminescence in $6H$-SiC as a function of forward current for different temperatures $T$ (K): (*1*) 300, (*2*) 630; the smooth curves are calculated.[157]

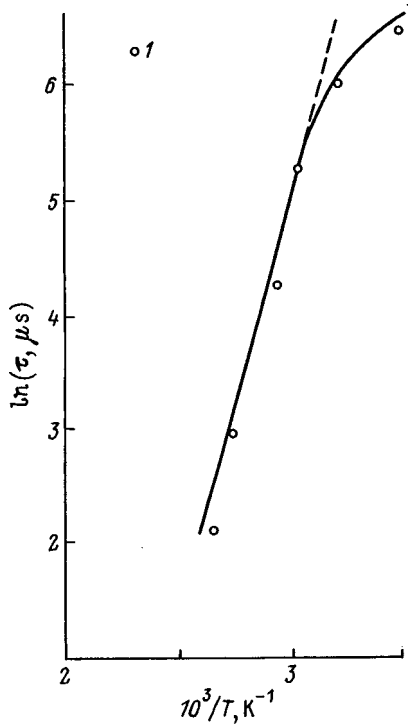


FIG. 10. The afterglow time constant of boron electroluminescence in $4H$-SiC as a function of the reciprocal of the temperature: (*1*) experiment, (*2*) calculation including only the contribution of hole thermal ionization.[58]

Note, however, that for 6*H*- and 4*H*-SiC samples the sum of the ionization energy of the *D*-center and $h\nu_{\max}$ for the electroluminescence will be less than the band gap of the corresponding polytype. It has been assumed[58,157] that, from the standpoint of the energy position of the levels, a correlation between the ''boron'' electroluminescence and a radiative transition of an electron from the conduction band to a *D*-center is possible, if the Frank-Condon shift for this center is $\leqslant 0.35$ eV. It has been proposed[184] that the hole capture cross section at a *D*-center has a strong temperature dependence, which leads to a reduction in the real ionization energy when it is determined from a DLTS spectrum. Taking into account the necessary correction, the ionization energy of the *D*-center was found[184] to be $E_v + 0.74 \pm 0.02$ eV, which eliminates the contradiction noted above.

### 4.5. Electroluminescence of 6*H*- and 4*H*-SiC $p-n$ structures when several channels for radiative recombination exist

Even in Losev's papers it was noted that when the forward current density is raised, the emission spectrum of SiC $p-n$ structures shifts to shorter wavelengths. An explanation for this effect, which is based on a tunnel mechanism for current flow in SiC $p-n$ structures, was proposed.[185] This explanation[185] is evidently not of interest for modern SiC $p-n$ structures, where the thermal injection current mechanism dominates.

Studies have been made of the location of the electroluminescence peak in 4*H*-SiC ID and SE $p-n$ structures with different concentrations of the uncompensated donor impurity in the base and different concentrations of background deep acceptors.[110,186]

It was found that in SE structures of 4*H*- and 6*H*-SiC as the forward current density is raised, there is a smooth shift of the electroluminescence peak over the approximate interval 2.14–2.35 eV (6*H*) and 2.4–2.52 (4*H*). Capacitive and current spectroscopy made it possible to detect *i*- and *D*-centers in SE. As has already been shown, these deep centers participate in various mechanisms for radiative recombination and the intensity of the electroluminescence they produce depends in different ways on the excitation level. Thus, in $p-n$ structures obtained by sublimation epitaxy the electroluminescence spectrum is a superposition of two electroluminescence bands, whose ratio of intensities (the position of the maximum $h\nu_m$ of the resulting band) depends on the forward current density, i.e., $h\nu_m = f(J)$. Calculations[110,186] of $h\nu_m = f(J)$ based on Eqs. (4.6) and (4.11) with the parameters and concentrations for *i*- and *D*-centers were in good agreement with experiment.

It has been shown[169,187] that if the concentration of deep acceptor impurities in the base of a diode is low, then for high forward current densities a peak associated with recombination of a free exciton (Fig. 11) will appear. The intensity of this band ($I_{Ex}$) increases with $J$ as $I_{Ex} = (J)^n$, where $n$ lay in the interval 2.2–2.7 for different samples. Such a rapid rise in the intensity of the exciton line may be associated with (1) temperature quenching of all the electroluminescence lines except the exciton line, or (2) an increase in the diffusion mean free path for holes as the temperature rises (see Sec. 5.1).

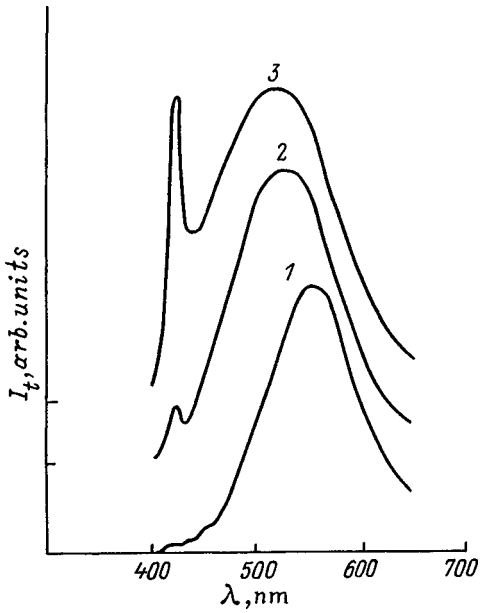


FIG. 11. Electroluminescence spectra of SE samples of 6*H*-SiC with low concentrations of deep acceptor levels for different forward current densities $J$ at room temperature (A/cm$^2$): (*1*) 4, (*2*), 40, (*3*) 120.[169]

Therefore, the $h\nu_m = f(J)$ observed in several SiC $p-n$ structures may be explained by the superposition of several independent electroluminescence lines which saturate at different forward current densities (different concentrations of the injected holes). The agreement[110,186] between experimental and theoretical dependences for $h\nu_m = f(J)$ confirms the validity of our determination of the activator centers and recombination models for defect electroluminescence and boron electroluminescence in SiC.

## 5. DEEP CENTERS AND NONRADIATIVE RECOMBINATION IN SIC

### 5.1. Influence of deep centers on the diffusion mean free path and lifetime in 6*H*-SiC $p-n$ structures

It has been found previously[188–190] that the hole lifetime in *n*-SiC lies in the range $10^{-7}$–$10^{-9}$ s, and that their diffusion mean free path is in the range 0.01–1 $\mu$m. It is clear that in SiC, as in an indirect band semiconductor, most recombination involves deep centers. However, no centers which could determine such a short lifetime have been found.

The temperature dependence of the hole diffusion length in epitaxial *n*-6*H*- and 4*H*-SiC obtained by different technologies has been studied.[191,192] It was found that the diffusion length ($L_p$) increases with rising temperature. This sort of variation $L_p = f(T)$ can be explained either by the participation of rather shallow levels in the recombination or by a negative temperature dependence for the carrier capture cross section at a deep recombination center.

It has been found[193] from an analysis of current-voltage characteristics and the magnitude of $L_p$ in 6*H*-SiC $p-n$ structures that most nonradiative recombination involves multiply charged centers whose parameters are different in

structures obtained by different techniques. These centers, however, have not been observed experimentally.

It has been predicted[90] that the major center for nonradiative recombination in SiC is vanadium. This conclusion was based on the observed inverse proportionality between the intensity of donor-acceptor recombination in Al–N and the intensity of the luminescence associated with an intracenter transition at a vanadium center, i.e., the intensity of donor-acceptor recombination was damped as the concentration of V was raised. The proofs invoked there are not exhaustive from our standpoint, since a large number of different factors, in addition to the carrier lifetime, can affect the intensity of donor-acceptor recombination. This includes the concentration of the centers, which was not determined in Ref. 90.

A complex study has been made[116] of the recombination characteristics of nonmajority current carriers and the deep center characteristics in 6*H*-SiC $p-n$ structures produced by different methods. An analysis of the experimental data showed that the relaxation lifetime of nonmajority charge carriers ($\tau_{\text{rel}}$) in SE structures is roughly 2 ns and in CLE structures $\tau_{\text{rel}}=20-30$ ns. The diffusion lengths for the minority current carriers in CLE and SE $p-n$ structures with different levels of background doping were found to lie in the intervals 0.4–1.5 and 0.05–0.4 $\mu$m, respectively.

The proposed lifetime was calculated using the parameters of the observed deep centers. The calculations showed that the only level whose parameters could explain the observed lifetime is the *S* level. A calculation using the parameters of an *R*-center yielded a value of $\tau_{\text{rel}}$ roughly an order of magnitude longer. Here the concentrations of *R*- and *S*-centers in structures of both types were the same. The previously noted long lifetime of minority charge carriers in CLE structures compared to that in SE structures was explained by a lower concentration of *S* and *R* deep centers in the CLE structures. A study of the dependence of $\tau_{\text{rel}}$ and $L_p^2$ at room temperature on the *S* and *R* concentrations showed that these quantities are inversely proportional.

The observed temperature dependence of $L_p$ could be explained only in terms of the parameters of a shallower *S*-center. A doubly charged $R-S$ center has been proposed[116] as determining the recombination parameters for the two types of 6*H*-SiC $p-n$ structures that have been studied. However, later work casts doubt on the idea that these two levels belong to a single center.[82]

After CVD technology for growing SiC epitaxial layers had been developed, studies were also made of the recombination characteristics of samples of this type.[194,195] The carrier lifetime was estimated from studies of the kinetics of low-temperature photoluminescence to be 0.45 $\mu$s, which is substantially greater than in epitaxial SiC layers grown by other technologies. *S*- and *R*-centers were also found in CVD 6*H*-SiC layers, but their concentrations were 1 or 2 orders of magnitude lower than in SE structures.[82,196]

Figure 12 shows a plot of $L_p$ as a function of the concentration of *S*- and *R*-centers[116] which we have supplemented with data from a study of CVD samples obtained during the course of this work, along with data from the purest ($\sim 10^{15}\,\text{cm}^{-3}$) SE layers. The figure shows that a reciprocal dependence of $L_p$ on the concentration of these levels is maintained for all three types of sample.

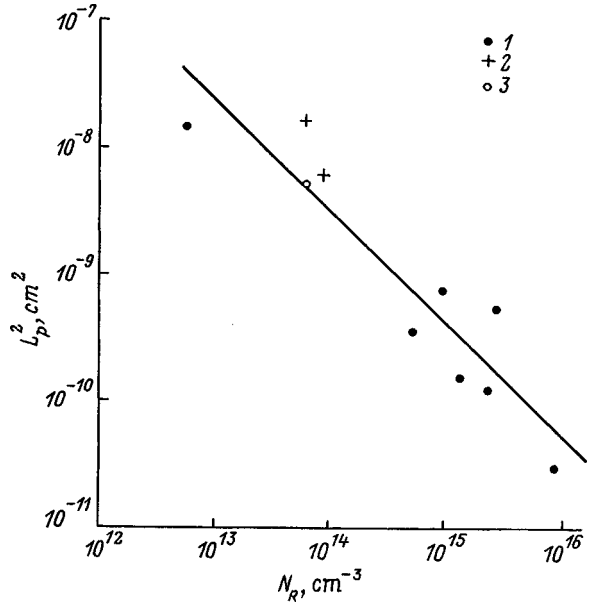


FIG. 12. The square of the hole diffusion length in 6*H*-SiC epitaxial layers grown by different technologies as a function of the *R*-center concentration: (*1*) SE $p-n$ structures, (*2*) CLE, (*3*) CVD.

Therefore, these centers are currently the most likely candidates for the role of ''killers'' of lifetime in 6*H*-SiC. Centers of this sort have not yet been observed in 4*H*-SiC.

### 5.2. Deep centers and the negative temperature coefficient for the breakdown voltage in SiC $p-n$-structures

In 6*H*-SiC $p-n$ structures where the electric field is parallel to the direction of the *C* crystal axis, the breakdown voltage generally has a negative temperature coefficient.[197] In a number of papers this has been attributed to the crystalline structure of hexagonal SiC polytypes and to the existence of a natural superlattice.[198,199] Others[200,201] have suggested that the negative temperature coefficient for the breakdown voltage may be related to charge exchange of deep centers, as has been shown for silicon,[202,203] or to the low structural perfection of SiC crystals.[204]

Studies have been made[205,206] of 6*H*-SiC $p-n$ structures obtained by sublimation epitaxy in which boron diffusion was carried out prior to formation of the mesostructures. The test structures had a negative temperature coefficient for the breakdown voltage of $-2\times10^{-3}\,\text{K}^{-1}$. The absolute magnitude of this temperature coefficient also depends on the temperature and falls by roughly an order of magnitude when the structures were heated to 600 K. In an analysis[205,206] of the experimental data following the authors of Refs. 200–203, the effect of deep centers were taken into account. The proposed model[205,206] takes into account the charge exchange of deep acceptor levels by the prebreakdown current in a lightly doped *p*-spacer near the metallurgical boundary of the $p-n$ junction.

Two assumptions were made: 1) the avalanche region lies in a lightly *p*-doped region near the metallurgical boundary of the $p-n$ junction and 2) the concentration of deep

acceptor levels in this region is comparable to that of shallow acceptors. A region of this sort may develop because of overcompensation of $n$-type material caused by diffusion of acceptor impurities (such as boron). The existence of a region of this type in the tested epitaxial-diffusion diodes was demonstrated experimentally.[54] There is a well-known expression for the breakdown voltage of a sharp $p-n$ junction:

$$U_{br}=\varepsilon_a E_{\rm cr}^2/2qN_i, \tag{5.1}$$

where $E_{\rm cr}$ is the critical electric field strength, and $N_i$ is the impurity concentration in the base.

Let us rewrite Eq. (5.1) taking into account, the presence of deep acceptors in a lightly doped $p$-base:

$$U_{br}=\varepsilon_a E_{\rm cr}^2/2q(N_s+KM)=U_{\rm bro}/(1+KM/N_s), \tag{5.2}$$

where $N_s$ is the concentration of shallow acceptor levels, $K$ is the degree of filling of the deep acceptors by electrons with $K=(M-m)/M$, where $M$ is the total concentration of deep acceptors, $m$ is the concentration of deep acceptors filled with holes, and $U_{\rm bro}$ is the breakdown strength of the $p-n$ junction in the absence of deep acceptors.

When $U\ll U_{\rm br}$, there is essentially no current through the $p-n$ junction and all the deep acceptors in the $p$-type region are filled with electrons ($K=1$). When $U\sim U_{\rm br}$, avalanche multiplication begins in the space charge region and the resulting holes are captured by deep acceptors. Since the acceptors that have captured holes are neutral, $K$ decreases and, accordingly, the electric field strength decreases. This leads to an increase in the observed value of $U_{\rm br}$. It should be noted that the degree of filling of the levels depends on the temperature and decreases upon heating. For this reason, $U_{\rm br}$ decreases with temperature and we observe a negative temperature coefficient for the breakdown voltage.

Using Eq. (4.1) for the equilibrium case ($dm/dt=0$) and noting that $\alpha_p\gg\alpha_n$, for $K$ we obtain

$$K=\beta_i(\Delta p+\beta_i)^{-1}. \tag{5.3}$$

Now we obtain an expression for $U_{\rm br}$ from Eqs. (5.2) and (5.3):

$$U_{br}=U_{\rm bro}(1+M\beta_i/N_s(\Delta p+\beta_i)). \tag{5.4}$$

We now analyze Eq. (5.4) for high and low temperatures.

In the case where $T\to 0$, $\beta_i\to 0$ and $U_{\rm br}(T_{\min})\approx U_{\rm bro}$. In the case where $T\to\infty$, $\beta_i\to 1$, and since $N_v\gg\Delta p$, we obtain $U_{\rm br}(T_{\max})/U_{\rm bro}-1=M/N_s$.

For the case examined in Refs. 205 and 206, $U_{\rm bro}$ and $M/N_s$ were given by $U_{\rm bro}=800$ V and $M/N_s=0.65$. Taking these values together with published values for $N_v$, we calculated the function $F=\{U_{\rm bro}/U_{\rm br}-1\}$.

The calculated and experimental values of $F$ are shown in Fig. 13. The figure shows that the best agreement between theory and experiment was obtained for $\Delta p$ on the order of $10^{11}-10^{12}\,{\rm cm}^{-3}$. However, the value of $\Delta p$ determined from the pre-breakdown current by $\Delta p=J/V_s q$ (where $J$ is the current density through the $p-n$ junction, and $V_s$ is the saturation rate) was $10^{10}-10^{11}\,{\rm cm}^{-3}$. This discrepancy may be explained[205,206] by the fact that breakdown in SiC usually occurs in local regions (microplasma breakdown) whose areas are more than an order of magnitude smaller than the total area of the $p-n$ junction. However, in calculating the current density through the $p-n$ junction the area of the entire structure was used; in other words, in the regions where microplasma breakdown takes place there will be a substantially higher current density and value of $\Delta p$, as required by this model.

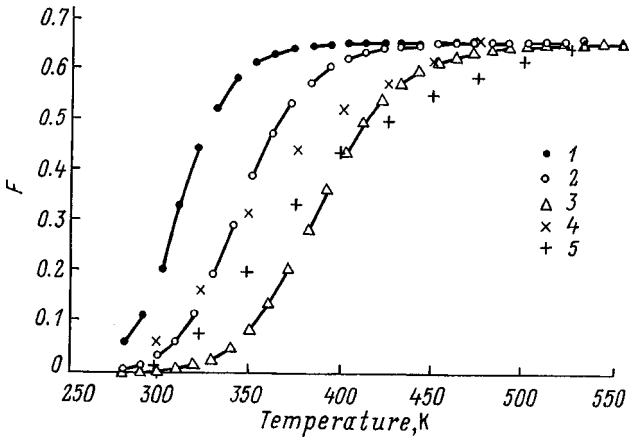


FIG. 13. Temperature variation in the calculated (*1–3*) and experimental (*4–5*) values of $F$. The calculations were done for $\Delta P=(1)\ 10^{10}$, (*2*) $10^{11}$, (*3*) $10^{12}\,{\rm cm}^{-3}$. The experimental values of $U_{\rm br}$ correspond to pre-breakdown currents of (*4*) 100 mA and (*5*) 500 mA.[205]

Therefore, the negative temperature coefficient for the breakdown voltage may be caused by charge exchange of $D$-centers ($E_v+0.58$ eV), the deepest levels which exist in boron-doped SiC. The calculations of the temperature dependence of the negative temperature coefficient based on this assumption and these parameters for the $D$-centers are in good agreement with experiment.

Since boron diffusion is often used to protect the periphery of SiC mesostructures from surface breakdown, while boron itself (a $D$-center) is a characteristic background impurity in SiC produced by various technologies,[117] we believe that the question of the sign of the temperature coefficient for breakdown can be answered definitively only when the effect of the charge exchange of $D$-centers on studies of the breakdown voltage of SiC $p-n$ structures is accounted for or excluded.

## CONCLUSIONS

If the energies of the levels in the lower half of the band gap of 4$H$- and 6$H$-SiC (Tables II and III) are compared, it will be noticed that most of the levels lie within two rather narrow bands inside the band gap: $E_v+(0.5-0.6)$ eV ($i$-band) and $E_v+0.2-0.3$ eV ($L$-band) (Fig. 14). Inside the first band lies the $D$-center, the $i$-center, and a scandium level and inside the second, a deep aluminum level, a gallium level, and the $L$-center. The boron level also lies inside (4$H$) or near the edge (6$H$) of the $L$-band. As the figure shows, in the upper half of the band gap the 4$H$- and 6$H$-SiC levels are distributed fairly uniformly and it is impossible to separate any bands which coincide for both polytypes. Since the parameters of centers of the same type formed in the lower half of the band gap of the different SiC

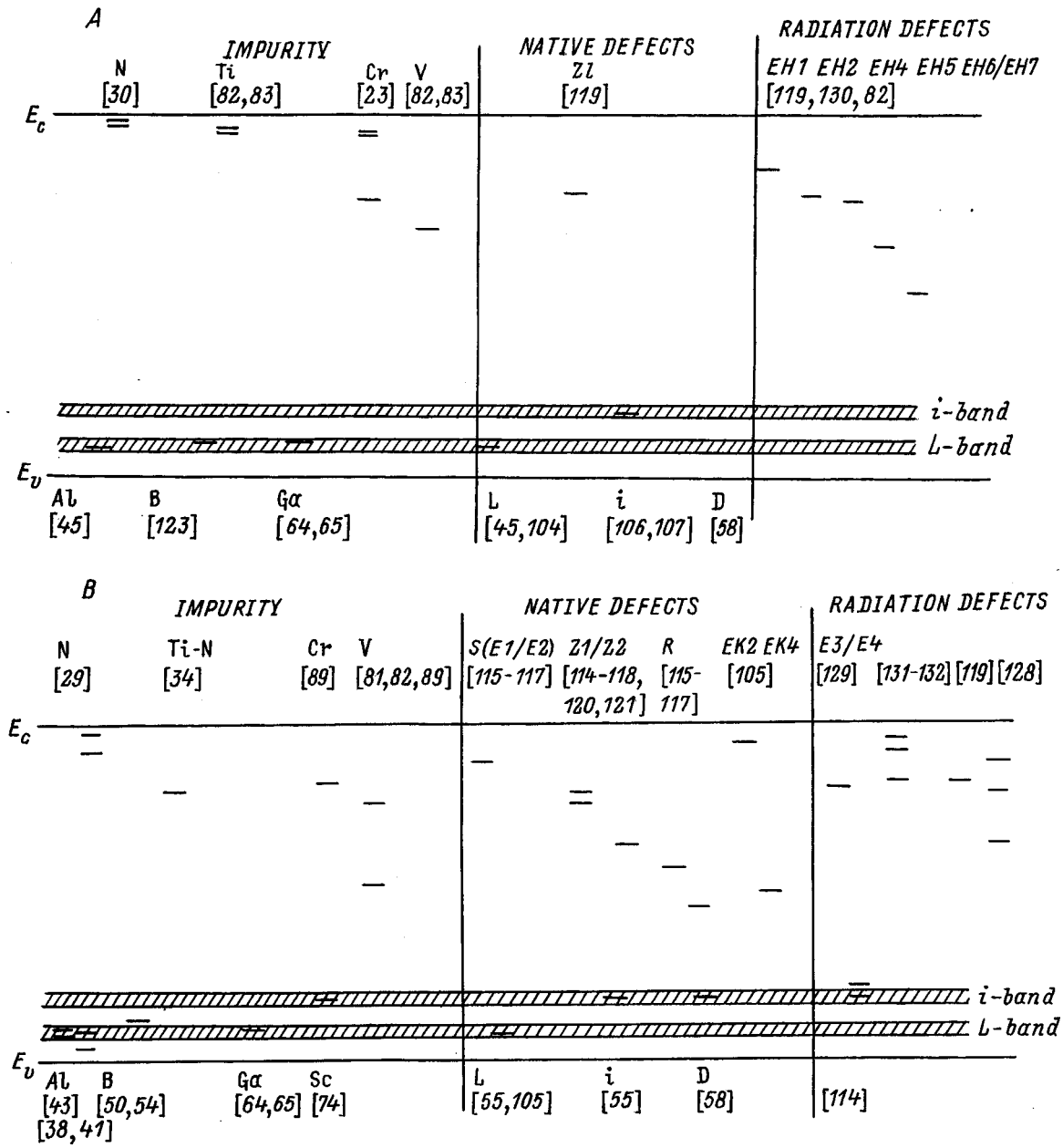


FIG. 14. A diagram of the location of the known deep centers in the band gap of silicon carbide: (*A*) 4*H*-SiC, (*B*) 6*H*-SiC. Only those deep centers are indicated which have not been identified as previously observed structural defects.

polytypes are similar, it may be assumed that such bands are present in other polytypes of silicon carbide. This is supported by the similarity of the characteristics and the shift, proportional to the band gap width, in the maxima of the main electroluminescence bands in the various polytypes of SiC (Fig. 6).

The formation of such bands inside the band gaps of different SiC polytypes indicates that centers characteristic of SiC, as such, are present and coupled to the valence band, whose structure is similar in the various polytypes. It may also be assumed that each band is coupled to some ''base'' center consisting of intrinsic defects (in the first case this is an *i*-center and in the second, an *L*-center) which can interact with atoms of an introduced impurity to form other centers with similar parameters.

What sort of intrinsic defect might be the main element in the formation of the defect complexes which produce deep centers in SiC? Figure 15 shows the average concentrations of three intrinsic defects (*i*-, *D*-, and *L*-centers) in epitaxial layers of 6*H*- and 4*H*-SiC obtained by sublimation epitaxy.[104] The figure shows that there is a fairly good correlation between the drop in concentration of carbon vacancies ($V_C$) and the increase in the percentage of hexagonal polytype and the reduction in the concentration of these centers.

That the main complex forming defect in SiC is carbon vacancies is supported by data from various papers where it has been proposed that $V_C$ participates in the formation of different centers, while isolated vacancies merge into stable clusters.[207–209] Note that the series of impurities (Sc, B, Al)

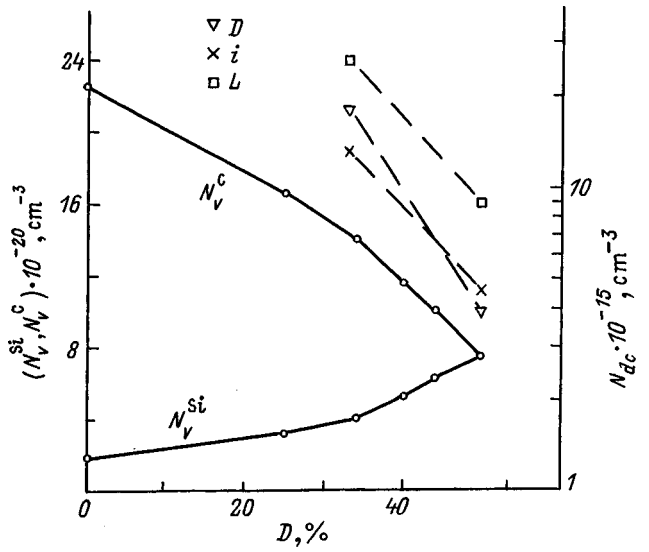


FIG. 15. The concentration of carbon ($N_V^C$) and silicon ($N_V^{Si}$) vacancies[148] and the average concentration of deep acceptor levels (*i*-, *L*-, and *D*-centers) in SE epitaxial layers as functions of the degree of hexagonality of the SiC polytype.[146]

used in heteroepitaxy of SiC[136] form deep centers which lie within the above mentioned *L*- and *i*-bands. The model of heteropolytype epitaxy proposed in Ref. 136 (see Sec. 3.1) can also be regarded as stating that each of the SiC polytypes corresponds to an equilibrium concentration of defects (carbon vacancies), which, when it is changed by adding impurities that generate excess defects or, on the other hand, bond vacancies into complexes, makes possible the heteroepitaxy of polytype films which have a lesser or greater degree of hexagonality, respectively, than the substrate.

Since an increase in the concentrations of *L*- and *i*-centers has been observed after irradiation and implantation[55,106,114] (i.e., a change in the equilibrium vacancy concentration took place), it may be assumed[104] that irradiation or implantation (or other technological actions) can cause a transformation of the polytype of already-grown epitaxial structures. This assumption is consistent with a study[149] of the degradation of 6*H*-SiC blue light-emitting diodes by a forward current, where it was found that inclusions of the 3*C* polytype appeared in the degraded structures.

This analysis of published sources, therefore, demonstrates the considerable effect intrinsic defects in the SiC crystal lattice have, both on the formation of deep centers (and, accordingly, on radiative and nonradiative recombination processes), and on the properties of the epitaxial layers, themselves (their doping level and polytype uniformity). A detailed study of the factors controlling the formation of defects and their interactions with one another and with impurity atoms will make it possible greatly to improve the parameters of SiC devices and allow SiC to occupy a central position alongside Si and GaAs in modern semiconductor electronics.

The author thanks V. V. Zelenin and N. S. Savkina for providing SiC samples for measurement, A. N. Andreev and M. G. Rastegaeva for preparing the ohmic contacts, A. M. Strel'chuk for providing data on measurements of diffusion lengths, and D. B. Davydov for help with the capacitance measurements.

This work was supported in part by Arizona University (USA) and the Schneider Group Research Center (France).

[1]E. G. Acheson, Chem. News **68**, 179 (1893).
[2]G. Pensl and R. Helbig, in *Advances in Solid State Physics*, edited by V. Rossler (Vieweg, Braunschweig, 1990).
[3]N. J. Round, Electrical World **30**, 309 (1907).
[4]O. V. Losev, Zh. Tekh. Fiz. **1**, 718 (1931).
[5]J. A. Lely, Ber. dt. keram. Ges. **32**, 229 (1955).
[6]Yu. A. Vodakov, E. N. Mokhov, M. G. Ramm, and A. O. Roenkov, Krist and Technik **14**, 729 (1979).
[7]Yu. M. Tairov and V. F. Tsvetkov, J. Cryst. Growth **43**, 209 (1978).
[8]Yu. M. Tairov and V. F. Tsvetkov, in *Problemy Fiziki i Tekhnologii Shirokozonnykh Poluprovodnikov (Problems in the Physics and Technology of Wide-gap Semiconductors)*, Leningrad (1980), p. 122.
[9]S. Nishino, J. Powell, and N. A. Will, Appl. Phys. Lett. **42**, 460 (1983).
[10]H. S. Kong, J. T. Glass, and R. F. Davis, Appl. Phys. Lett. **64**, 2672 (1988).
[11]J. A. Edmond, H. S. Kong, and C. H. Carter, Physica B **185**, 453 (1993).
[12]J. W. Palmer, J. A. Edmond, H. S. Kong, and C. H. Carter, Physica B **185**, 461 (1993).
[13]B. M. Brown, M. Chezzo, J. Kretchmen, V. Krishmuthy, and G. Michon, *Transactions Second Int. High Temp. Electron. Conf.* (Charlotte, NC, USA, 1994) V. 1, p. XI–17.
[14]A. R. Verma and P. Krishna, *Polymorphism and Polytypism in Crystals*, Wiley, N.Y. (1966).
[15]L. S. Ramsdell, Amer. Mineral **32**, 64 (1947).
[16]L. Patric, Phys. Rev. **127**, 1878 (1962).
[17]R. G. Humphreys, D. Bimberg, and W. J. Choyke, Solid State Commun. **39**, 163 (1981).
[18]G. B. Dubrovskiĭ, Fiz. Tverd. Tela **13**, 2505 (1971) [Sov. Phys. Solid State **13**, 2107 (1971)].
[19]G. B. Dubrovskii, A. A. Lepeneva, E. I. Radovanova, Phys. Status Solidi B **57**, 423 (1973).
[20]E. Bindermann, Solid State Commun. **3**, 343 (1965).
[21]G. B. Dubrovskiĭ and E. I. Raduvanova, Fiz. Tverd. Tela **11**, 680 (1969) [Sov. Phys. Solid State **11**, 549 (1969)].
[22]W. R. L. Lambrecht, S. Limpijumuong, and B. Segall, Inst. Phys. Conf. Ser. **142**, 263 (1996).
[23]W. R. L. Lambrecht and S. N. Rachkeev, *Abstracts Int. Conf. on* SiC, III *Nitrides and Related Materials* (Stockholm, Sweden, 1997), p. 263.
[24]L. S. Berman and A. A. Lebedev, *Capacitance Spectroscopy of Deep Centers in Semiconductors* [in Russian], Nauka, Leningrad (1981).
[25]M. V. Rao, J. Gardner, O. W. Holland, G. Kelner, M. Chezzo, D. S. Simons, and P. H. Chi, Inst. Phys. Conf. Ser. **142**, 521 (1996).
[26]H. H. Woodbery and G. W. Ludwig, Phys. Rev. **124**, 1083 (1961).
[27]I. Ikeda, H. Matsunami, and T. Tanaka, Phys. Rev. B **22**, 2842 (1980).
[28]A. V. Alekseenko, A. G. Zabrodskiĭ, and M. P. Timofeev, Pis'ma Zh. Tekh. Fiz. **11**, 1018 (1985) [Sov. Tech. Phys. Lett. **11**, 422 (1985)].
[29]W. Suttrop, G. Pensl, W. J. Choyke, R. Steine, and S. Leibenzeder, J. Appl. Phys. **72**, 3708 (1992).
[30]W. Gotz, A. Schoner, G. Pensl, W. Suttrop, W. J. Choyke, R. Steine, and S. Leibenzeder, J. Appl. Phys. **73**, 3332 (1993).
[31]A. O. Euwarage, S. R. Smith, and W. C. Mitchel, J. Appl. Phys. **79**, 7726 (1996).
[32]Th. Troffer, W. Gotz, A. Schoner, G. Pensl, R. P. Devaty, and W. J. Choyke, Inst. Phys. Conf. Ser. **137**, 173 (1994).
[33]A. E. Nikolaev, I. P. Nikitina, and V. A. Dmitriev, Inst. Phys. Conf. Ser. **142**, 125 (1996).
[34]V. S. Vaĭner, V. A. Il'in, V. A. Karachinov, and Yu. M. Tairov, Fiz. Tverd. Tela **28**, 363 (1986) [Sov. Phys. Solid State **28**, 201 (1986)].
[35]Yu. A. Vodakov, E. N. Kalabukhova, S. N. Lukin, A. A. Lepneva, E. N. Mokhov, and V. D. Shanina, Fiz. Tverd. Tela **20**, 448 (1978) [Sov. Phys. Solid State **20**, 258 (1978)].
[36]P. J. Dean and R. L. Hartman, Phys. Rev. B **5**, 4911 (1972).
[37]Van H. Daal, W. F. Knippenberg, and J. D. Wassher, J. Phys. Chem. Solids **24**, 109 (1963).
[38]G. A. Lamakina, Yu. A. Vodakov, E. N. Mokhov, V. G. Oding, and G. F.

Kholuyanov, Fiz. Tverd. Tela **12**, 2918 (1970) [Sov. Phys. Solid State **12**, 2356 (1970)].
[39]I. V. Kodrau and V. V. Makarov, Fiz. Tekhn. Poluprovodn. **11**, 969 (1977) [Sov. Phys. Semicond. **11**, 809 (1977)].
[40]E. N. Mokhov, M. M. Usmanov, G. F. Yuldashev, and B. S. Makhmudov, Izv. AN SSSR. Neorg. mater. **20**, 1383 (1984).
[41]A. Schoner, N. Nordell, K. Rottner, R. Helbig, G. Pensl, Inst. Phys. Conf. Ser. **142**, 493 (1996).
[42]B. I. Shklovskiĭ and A. L. Éfros, Fiz. Tekhn. Poluprovodn. **14**, 486 (1980) [Sov. Phys. Semicond. **14**, 351 (1980)].
[43]M. M. Anikin, N. I. Kuznetsov, A. A. Lebedev, N. S. Savkina, A. L. Syrkin, and V. E. Chelnokov, Fiz. Tekhn. Poluprovodn. **28**, 457 (1994) [Semiconductors **28**, 278 (1994)].
[44]P. A. Panov, Ya. V. Morozenko, and A. V. Suvorov, Fiz. Tekhn. Poluprovodn. **19**, 1430 (1985) [Sov. Phys. Semicond. **19**, 879 (1985)].
[45]N. I. Kuznetsov and A. S. Zubrilov, Mater. Sci. Eng., B **29**, 181 (1995).
[46]V. Heera, J. Pezold, X. Ning, and P. Pirouz, Inst. Phys. Conf. Ser. **142**, 509 (1996).
[47]L. L. Clemen, R. P. Devaty, W. J. Choyke, J. A. Powel, D. J. Larkin, J. A. Edmond, and A. A. Burk, Inst. Phys. Conf. Ser. **137**, 297 (1994).
[48]Yu. A. Vodakov, G. A. Lomakina, and E. N. Mokhov, Fiz. Tverd. Tela **24**, 1377 (1982) [Sov. Phys. Solid State **24**, 780 (1982)].
[49]A. N. Andreev, M. M. Anikin, A. A. Lebedev, N. K. Poletaev, A. M. Strel'chuk, A. L. Surkin, and V. E. Chelnokov, Inst. Phys. Conf. Ser. **137**, 271 (1994).
[50]A. I. Veĭnger, Yu. A. Vodakov, Yu. Kulev, G. A. Lomakina, E. N. Mokhov, V. G. Oding, and V. I. Sokolov, Pis'ma Zh. Tekh. Fiz. **6**, 1319 (1980) [Sov. Tech. Phys. Lett. **6**, 566 (1980)].
[51]V. S. Balandovich and E. N. Mokhov, *Transactions Second Int. High Temp. Electron. Conf.* (Charlotte NC, 5–10 USA, 1994) v. 2, p. 181.
[52]E. E. Violin and G. F. Kholuyanov, Fiz. Tverd. Tela **8**, 3395 (1966) [Sov. Phys. Solid State **8**, 2716 (1966)].
[53]S. Ortolland, C. Raynaunld, J. P. Chante, M. L. Locatelli, A. N. Andreev, A. A. Lebedev, M. G. Rastegaeva, A. L. Syrkin, N. S. Savkina, and V. E. Chelnokov, J. Appl. Phys. **80**, 5464 (1996).
[54]A. A. Lebedev, A. N. Andreev, A. A. Malyshev, M. G. Restegaeva, N. S. Savkina, and V. E. Chelnokov, Fiz. Tekhn. Poluprovodn. **29**, 1635 (1995) [Semiconductors **29**, 1590 (1995)].
[55]M. M. Anikin, A. A. Lebedev, A. L. Syrkin, and A. V. Suvorov, Fiz. Tekhn. Poluprovodn. **19**, 114 (1985) [Sov. Phys. Semicond. **15**, 69 (1985)].
[56]W. Suttrop, G. Pensl, and P. Laning, Appl. Phys. A: Solids Surf. **51**, 231 (1991).
[57]M. M. Anikin, A. A. Lebedev, N. K. Poletaev, A. M. Strel'chuk, A. L. Surkin, and V. E. Chelnokov, Inst. Phys. Conf. Ser. **137**, Chap. 6, 605 (1994).
[58]A. A. Lebedev and N. K. Poletaev, Fiz. Tekhn. Poluprovodn. **30**, 427 (1996) [Semiconductors **30**, 238 (1996)].
[59]A. O. Konstantinov, Fiz. Tekhn. Poluprovodn. **25**, 1175 (1991) [Sov. Phys. Semicond. **25**, 1095 (1991)].
[60]P. G. Baranov and E. N. Mokhov, Inst. Phys. Conf. Ser. **142**, 293 (1996).
[61]T. Frank, T. Troffer, G. Pensl, N. Nordell, S. Karlson, and A. Schoner, *Abstracts Int. Conf. on* SiC, III *Nitrides and Related Materials* (Stockholm, Sweden, 1997), p. 348.
[62]S. Jang, T. Kimoto, and H. Matsunami, Appl. Phys. Lett. **65**, 581 (1994).
[63]M. S. Mazzola, S. E. Saddow, P. G. Neudeck, V. K. Lakdawala, and S. We, Appl. Phys. Lett. **64**, 2730 (1994).
[64]Yu. A. Vodakov, G. A. Lomakina, E. N. Mokhov, E. I. Radovanova, V. I. Sokolov, M. M. Usmanova, G. F. Yuldashev, and B. S. Makhmudov, Phys. Status Solidi A **35**, 37 (1976).
[65]T. Troffer, G. Pensl, A. Schoner, A. Henry, C. Hallin, O. Kordina, and E. Janzen, *Abstracts Int. Conf. on* SiC, III *Nitrides and Related Materials* (Stockholm, Sweden, 1997), p. 601.
[66]A. Henry, C. Hallin, I. G. Ivanov, J. P. Bergman, O. Kordina, and E. Janzen, Inst. Phys. Conf. Ser. **142**, 381 (1996).
[67]A. A. Lebedev, M. P. Shcheglov, and T. V. Sokolova, Pis'ma Zh. Tekh. Fiz. **21**, 48 (1995) [Tech. Phys. Lett. **21**, 51 (1995)].
[68]Yu. A. Vodakov, G. A. Lomakkna, E. N. Mokhov, and V. G. Oding, Fiz. Tverd. Tela **33**, 3315 (1991) [Sov. Phys. Solid State **33**, 1869 (1991)].
[69]E. V. Violin, A. A. Kal'nin, V. V. Pasynkov, Yu. M. Tairov, and D. A. Yas'kov, Mater. Res. Bull. **4**, S231 (1969).
[70]Y. Zheng, N. Ramungul, R. Patel, V. Khemka, and T. P. Chow, *Abstracts Int. Conf. on* SiC, III *Nitrides and Related Materials* (Stockholm, Sweden, 1997), p. 71.
[71]P. G. Baranov and E. N. Mokhov, Fiz. Tverd. Tela **38**, 1446 (1996) [Phys. Solid State **38**, 798 (1996)].
[72]A. Hofstaeffer, B. K. Mayer, A. Scharmann, P. G. Baranov, I. V. Liyn, and E. N. Mokhov, *Abstracts Int. Conf. on* SiC, III *Nitrides and Related Materials* (Stockholm, Sweden, 1997) p. 294.
[73]M. B. Scott, J. D. Scofield, Y. K. Yeo, and R. L. Hengehold, *Abstracts Int. Conf. on* SiC, III *Nitrides and Related Materials* (Stockholm, Sweden, 1997), p. 389.
[74]V. S. Ballandovich, Fiz. Tekhn. Poluprovodn. **25**, 287 (1991) [Semiconductors **25**, 152 (1991)].
[75]H. Vakhner and Yu. M. Tairov, Fiz. Tverd. Tela **11**, 2440 (1969) [Sov. Phys. Solid State **11**, 1972 (1969)].
[76]D. P. Litvin, A. A. Mal'tsev, A. V. Naumov, A. D. Roenkov, and V. I. Sankin, Pis'ma Zh. Tekh. Fiz. **13**, 1247 (1987) [Sov. Tech. Phys. Lett. **13**, 523 (1987)].
[77]L. Patrick and W. J. Choyke, Phys. Rev. B **10**, 5091 (1974).
[78]A. W. C. Kemenade and S. H. Hagen, Solid State Commun. **14**, 1331 (1974).
[79]K. M. Lee, Le. Si. Dang, G. B. Watkins, and W. J. Choyke, Phys. Rev. B **32**, 2273 (1985).
[80]K. Maier, H. D. Muller, and J. Schneider, Mater. Sci. Forum **83-87**, 1183 (1992).
[81]K. Maier, J. Schneider, W. Wilkening, S. Leibenzeder, and R. Steine, Mater. Sci. Eng., B **11**, 27 (1992).
[82]T. Dalibor, G. Pensl, H. Matsunami, T. Kimoto, W. J. Choyke, A. Schoner, and N. Nordel, Phys. Status Solidi A **162**, 199 (1997).
[83]T. Dalibor, G. Pensl, N. Nordel, A. Schoner, and W. J. Choyke, *Abstracts Int. Conf. on* SiC, III *Nitrides and Related Materials* (Stockholm, Sweden, 1997), p. 55.
[84]J. M. Langer and H. Heinrich, Phys. Rev. Lett. **55**, 1414 (1985).
[85]H. McD. Hobgood, R. C. Glass, A. Augustine, R. H. Hopkins, J. Jenny, M. Skowronski, W. C. Mitchel, and M. Roth, Appl. Phys. Lett. **66**, 1364 (1995).
[86]W. C. Mitchel, M. D. Roth, A. O. Evwaraye, P. W. Yu, S. R. Smith, J. Jenny, M. Skowronski, H. McD. Hodgood, R. C. Glass, G. Augustine, and R. H. Hopkins, Inst. Phys. Conf. Ser. **142**, 313 (1996).
[87]K. F. Dombrovskii, U. Kaufman, and M. Hunzer, Appl. Phys. Lett. **65**, 184 (1994).
[88]J. Schneider, H. D. Muller, K. Maier, W. Wilkening, F. Fuchs, A. Dornen, S. Leibenzader, and S. Steine, Appl. Phys. Lett. **56**, 1184 (1990).
[89]N. Achtziger, J. Grillenberg, and W. Witthuhn, *Abstracts Int. Conf. on* SiC, III *Nitrides and Related Materials* (Stockholm, Sweden, 1997), p. 597.
[90]St. G. Muller, D. Hofmann, A. Winnacker, E. N. Mokhov, and Yu. A. Bodakov, Inst. Phys. Conf. Ser. **142**, 361 (1996).
[91]Yu. A. Vodakov, G. A. Lomakina, E. N. Mokhov, M. G. Ramm, and V. I. Sokolov, Fiz. Tekh. Poluprovodn. **20**, 2153 (1986) [Sov. Phys. Semicond. **20**, 1347 (1986)].
[92]N. Achtziger and W. Witthunh, Mater. Sci. Eng., B **46**, 333 (1997).
[93]M. Kuznser, K. F. Dombrovski, F. Fuchs, U. Kaufmann, J. Schneider, P. G. Baranov, and E. N. Mokhov, Inst. Phys. Conf. Ser. **142**, 385 (1996).
[94]M. Feege, S. Grenlich-Weber, and J.-M. Spaeth, Semicond. Sci. Technol. **8**, 1620 (1993).
[95]K. Abe, T. Ohsima, H. Iton, Y. Aoki, M. Yoshikawa, I. Nashiyama, and M. Iwami, *Abstracts Int. Conf. on* SiC, III *Nitrides and Related Materials* (Stockholm, Sweden, 1997), p. 354.
[96]G. F. Kholuyanov, Yu. A. Vodakov, and É. V. Violin, Fiz. Tekh. Poluprovodn. **5**, 39 (1971) [Sov. Phys. Semicond. **5**, 141 (1971)].
[97]T. Dalibor, G. Pensl, T. Yamamoto, T. Kimoto, H. Matsunami, S. Sridhara, D. C. Nizher, R. P. Devaty, and W. J. Choyke, *Abstracts Int. Conf. on* SiC, III *Nitrides and Related Materials* (Stockholm, Sweden, 1997), p. 599.
[98]D. Alok, B. J. Baliga, M. Kothandaraman, and P. K. McLarty, Inst. Phys. Conf. Ser. **142**, 565 (1996).
[99]H. Ennen, J. Schnider, G. Pomrenke, and A. Axmann, Appl. Phys. Lett. **43**, 943 (1983).
[100]W. J. Choyke, R. P. Devaty, L. L. Clemen, M. Yoganathan, G. Pensl, and Ch. Hassler, Appl. Phys. Lett. **65**, 1668 (1994).
[101]K. Awahara and M. Kumagai, *Abstracts Int. Conf. on* SiC, III *Nitrides and Related Materials* (Stockholm, Sweden, 1997), p. 380.
[102]M. M. Anikin, A. A. Lebedev, I. V. Popov, A. L. Syrkin, A. V. Suvorov, and G. P. Shpynev, in *Technology of Semiconductor Power Devices* [in Russian], Valgus, Tallin (1987), p. 19.

[103]N. I. Kuznetsov, A. P. Dmitrov, and A. S. Furman, Fiz. Tekh. Poluprovodn. **28**, 1010 (1994) [Semiconductors **28**, 584 (1994)].
[104]A. A. Lebedev, *Abstracts Int. Conf. on* SiC, III *Nitrides and Related Materials* (Stockholm, Sweden, 1997), p. 67.
[105]N. I. Kuznetsov and J. A. Edmond, Fiz. Tekh. Poluprovodn. **31**, 1220 (1997) [Sov. Phys. Semicond. **31**, 1481 (1997)].
[106]M. M. Anikin, A. A. Lebedev, A. L. Syrkin, and A. V. Suvorov, Fiz. Tekh. Poluprovodn. **20**, 2169 (1986) [Sov. Phys. Semicond. **20**, 1357 (1986)].
[107]M. M. Anikin, A. A. Lebedev, I. V. Popov, A. M. Strel'chuk, A. L. Syrkin, A. V. Suvorov, and V. E. Chelnokov, Fiz. Tekh. Poluprovodn. **20**, 1654 (1986) [Sov. Phys. Semicond. **20**, 1036 (1986)].
[108]A. A. Lebedev, Author's abstract of Candidate's Dissertation (Physicotechnical Institute, Leningrad, 1991).
[109]A. A. Lebedev and V. E. Chelnokov, Diamond films and Related Mater. **3**, 1393 (1994).
[110]M. M. Anikin, N. I. Kuznetsov, A. A. Lebedev, N. K. Poletaev, A. M. Strel'chuk, A. L. Syrkin, A. V. Suvorov, and V. E. Chelnokov, Fiz. Tekh. Poluprovodn. **28**, 443 (1994) [Semiconductors **28**, 609 (1994)].
[111]C. T. Sah, L. Forbes, L. L. Rossier, and A. F. Tasch, Solid-State Electron. **13**, 759 (1970).
[112]A. G. Kechek, N. I. Kuznetsov, and A. A. Lebedev, Fiz. Tekh. Poluprovodn. **21**, 2228 (1987) [Sov. Phys. Semicond. **21**, 1351 (1987)].
[113]E. N. Kolabukova, S. N. Lukin, E. N. Mokhov, J. Reinke, S. Greulich-Weber, and J.-M. Spaeth, Inst. Phys. Conf. Ser. **142**, 333 (1996).
[114]G. C. Rubicki, J. Appl. Phys. **78**, 2996 (1995).
[115]M. M. Anikin, A. N. Andreev, A. A. Lebedev, S. N. Pyatko, M. G. Rasetegaeva, N. S. Savkina, A. M. Strelchuk, A. L. Syrkin, and V. E. Chelnokov, Fiz. Tekh. Poluprovodn. **25**, 328 (1991) [Sov. Phys. Semicond. **25**, 409 (1991)].
[116]M. M. Anikin, A. S. Zubrilov, A. A. Lebedev, A. M. Strel'chuk, and A. E. Cherenkov, Fiz. Tekh. Poluprovodn. **25**, 479 (1991) [Sov. Phys. Semicond. **25**, 519 (1991)].
[117]M. M. Anikin, A. A. Lebedev, A. L. Syrkin, A. V. Suvorov, and A. M. Strel'chuk, Ext. Abstracts Electrochem. Soc. Mtg., , 708 (1989).
[118]H. Zhang, G. Pensl, A. Dorner, and S. Leibenzeder, Ext. Abstr. Electrochem. Soc. Mtg., , 699 (1989).
[119]J. P. Doyle, M. O. Adoelfotoh, B. G. Svensson, A. Schoner, and N. Nordel, Diamond Relat. Mater. , 1388 (1997).
[120]A. I. Vaĭner, V. A. Il'in, Yu. M. Tairov, and V. F. Tsvetkov, Fiz. Tekh. Poluprovodn. **15**, 1557 (1981) [Sov. Phys. Semicond. **15**, 902 (1981)].
[121]M. M. Anikin, A. A. Lebedev, I. V. Popov, V. P. Rastegaev, A. M. Strel'chuk, A. L. Syrkin, Yu. Tairov, V. F. Tsvetkov, and V. E. Chelnokov, Fiz. Tekh. Poluprovodn. **22**, 298 (1988) [Sov. Phys. Semicond. **22**, 181 (1988)].
[122]N. T. Son, E. Sorman, W. M. Chen, O. Kordina, B. Monemar, and E. Janzen, Appl. Phys. Lett. **65**, 2687 (1994).
[123]T. Troffer, Ch. Habler, G. Pensl, K. Holzlein, H. Mitlehner, and J. Volki, Inst. Phys. Conf. Ser. **142**, 281 (1996).
[124]T. Dalibor, G. Pensl, T. Kimoto, H. Matsunami, S. Shidhara, P. P. Devaty, and W. J. Choyke, Diamond Relat. Mater. **6**, 1333 (1997).
[125]A. A. Lebedev, A. N. Andreev, M. M. Anikin, M. G. Rastegaeva, N. S. Savkina, A. M. Strelchuk, A. L. Syrkin, A. S. Tregubova, and V. E. Chelnokov, *Proc. ISPSD'95* (Yokohama, Japan, 1995), p. 90.
[126]P. Zhou, M. G. Spencer, G. L. Harris, and K. Fekade. Appl. Phys. Lett. **50**, 1384 (1987).
[127]K. Zakentes, M. Kayiambaki, and G. Constantinidis, Appl. Phys. **66**, 3015 (1995).
[128]V. S. Balandovich and G. N. Violina, Cryst. Lattice Defects Amorphous Mater. **13**, 189 (1987).
[129]H. Zhang, G. Pensl, P. Glasow, and S. Leibenzeder, Ext. Abstracts Electrochem. Soc. Mtg., , 714 (1989).
[130]C. Hemmingson, N. T. Son, O. Kordina, E. Janzen, J. L. Lindstrom, S. Savarge, and N. Nordel, Mater. Sci. Eng., B **46**, 336 (1997).
[131]I. M. Pavlov, M. I. Iglitsin, M. G. Kosganov, and V. N. Solomatin, Fiz. Tekh. Poluprovodn. **9**, 1279 (1975) [Sov. Phys. Semicond. **9**, 1320 (1975)].
[132]A. I. Veigner, A. A. Lepeneva, G. A. Lomakina, E. N. Mokhov, and V. I. Sokolov, Fiz. Tekh. Poluprovodn. **18**, 2014 (1984) [Sov. Phys. Semicond. **18**, 1932 (1984)].
[133]V. V. Evstropov, A. M. Strel'chuk, A. L. Syrkin, and V. E. Chelnokov, Inst. Phys. Conf. Ser. **137**, 589 (1994).
[134]M. Okada, T. Kimura, T. Nakata, M. Watanbe, S. Kanazava, I. Kanno, K. Kamitani, K. Atobe, and M. N. Nakagawa, Inst. Phys. Conf. Ser. **142**, 469 (1996).
[135]H. Matsunami and T. Kimoto, Mater. Sci. Eng., R. **20**, 125 (1997).
[136]Yu. A. Vodakov, G. A. Lomakina, and E. N. Mokhov, Fiz. Tverd. Tela **24**, 1377 (1982) [Sov. Phys. Solid State **24**, 780 (1982)].
[137]Yu. Vakhner and Yu. M. Tairov, Fiz. Tverd. Tela **12**, 1543 (1970) [Sov. Phys. Solid State **12**, 1213 (1970)].
[138]Yu. A. Vodakov, E. N. Mokhov, A. D. Roenkov, and M. M. Anikin, Pis'ma Zh. Tekh. Fiz. **5**, 367 (1979) [Sov. Tech. Phys. Lett. **5**, 147 (1979)].
[139]A. A. Maltsev, A. Yu. Maksimov, and N. K. Yushin, Inst. Phys. Conf. Ser. **142**, 41 (1996).
[140]A. A. Maltsev, D. P. Litvin, M. P. Scheglov, and I. P. Nikitina, Inst. Phys. Conf. Ser. **142**, 137 (1996).
[141]P. A. Ivanov, A. A. Maltsev, V. N. Panteleev, T. P. Samsonova, A. Yu. Maksimov, N. K. Yushin, and V. E. Chelnokov, Inst. Phys. Conf. Ser. **142**, 757 (1996).
[142]Yu. A. Vodakov, G. A. Lomakina, E. N. Mokhov, and V. G. Oding, Fiz. Tverd. Tela **19**, 1812 (1977) [Sov. Phys. Solid State **18**, 1695 (1977)].
[143]A. N. Andreev, A. S. Tregubova, M. P. Scheglov, A. L. Syrkin, and V. E. Chelnokov, Mater. Sci. Eng., B **46**, 141 (1997).
[144]A. A. Lebedev, N. S. Savkina, A. M. Strel'chuk, A. S. Tregubova, and M. P. Scheglov, Mater. Sci. Eng., B **46**, 168 (1997).
[145]A. A. Lebedev, N. S. Savkina, A. S. Tregubova, and M. P. Shcheglov, Fiz. Tekh. Poluprovodn. **31**, 1083 (1997) [Semiconductors **31**, 906 (1997)].
[146]A. A. Lebedev, *Abstracts of the 19th International Conference Def. in Semicond.* (Aveiro, Portugal, 1997), p. 239.
[147]Yu. A. Vodakov and E. N. Mokhov, Inst. Phys. Conf. Ser. **137**, 197 (1994).
[148]N. D. Sorokin, Yu. M. Tairov, V. F. Tsvetkov, and M. A. Chernov, Kristallografiya **28**, 910 (1983).
[149]G. Zeinther and D. Theeis, IEEE Trans. Electron Devices **ED-28**, 425 (1981).
[150]D. J. Larkin, P. G. Neudeck, J. A. Powell, and L. G. Matus, Appl. Phys. Lett. **65**, 1661 (1994).
[151]E. Janzen and O. Kordina, Inst. Phys. Conf. Ser. **142**, 653 (1996).
[152]A. N. Andreev, N. Yu. Smirnova, M. P. Shcheglov, M. G. Rastegaeva, V. P. Restagaev, and V. E. Chelnokov, Fiz. Tekh. Poluprovodn. **30**, 2060 (1996) [Semiconductors **30**, 1074 (1996)].
[153]L. Hoffman, G. Zeigler, D. Theeis, and G. Wegnich, J. Appl. Phys. **53**, 6962 (1982).
[154]V. M. Gusev, K. D. Demakov, V. M. Efimov, V. N. Ionov, M. G. Kosagonova, N. K. Prokof'ev, V. G. Stolyarova, and Yu. N. Chekushkin, Fiz. Tekh. Poluprovodn. **15**, 2430 (1981) [Sov. Phys. Semicond. **15**, 1413 (1981)].
[155]R. M. Potter, Mater. Res. Bull. **4**, S223 (1969).
[156]A. Bergh and P. Dean, Proc. IEEE **60**, 156 (1972).
[157]M. M. Anikin, N. I. Kuznetsov, A. A. Lebedev, A. M. Strel'chuk, and A. L. Syrkin, Fiz. Tekh. Poluprovodn. **24**, 1384 (1990) [Sov. Phys. Semicond. **24**, 1281 (1990)].
[158]A. N. Andreev, M. M. Anikin, A. A. Lebedev, N. K. Poletaev, A. M. Strel'chuk, A. L. Syrkin, and V. E. Chelnokov, Fiz. Tekh. Poluprovodn. **28**, 729 (1994) [Semiconductors **28**, 430 (1994)].
[159]A. A. Lebedev, Fiz. Tekh. Poluprovodn. **30**, 999 (1996) [Semiconductors **30**, 531 (1996)].
[160]V. I. Pavlichenko, I. V. Ryzhikov, Yu. M. Suleĭmanov, and Yu. M. Shaĭdak, Fiz. Tverd. Tela **10**, 2801 (1968) [Sov. Phys. Solid State **10**, 2205 (1968)].
[161]S. H. Hagen, A. W. C. Kemanage, and van der Does de Bye, J. Lumin. **8**, 18 (1973).
[162]A. Suzuki, H. Matsunami, and T. Tanaka, J. Electrochem. Soc. **124**, 241 (1977).
[163]V. I. Sokolov, in *Problems in the Physics and Technology of Wide Gap Semiconductors* [in Russian], Leningrad (1979), p. 301.
[164]W. von Munch and W. Kukzinger, Solid-State Electron. **21**, 1129 (1978).
[165]M. Ikeda, T. Haykawa, S. Yamagiva, H. Matsunami, and T. Tanaka, J. Appl. Phys. **50**, 8215 (1979).
[166]V. A. Dmitriev, P. A. Ivanov, Ya. V. Morozenko, I. V. Popov, and V. E. Chelnokov, Pis'ma Zh. Tekh. Fiz. **11**, 246 (1985) [Sov. Tech. Phys. Lett. **11**, 101 (1985)].
[167]L. Hoffman, G. Zeidler, D. Theis, and G. Wegnich, J. Appl. Phys. **53**, 6962 (1982).
[168]V. I. Vishnevskaya, V. A. Dmitriev, I. D. Kovalenko, L. M. Kogan, Ya.

V. Morozenko, V. S. Rodkin, A. L. Syrkin, B. V. Tsarenkov, and V. E. Chelnokov, Fiz. Tekh. Poluprovodn. **22**, 664 (1988) [Sov. Phys. Semicond. **22**, 414 (1988)].
[169]A. A. Lebedev, N. K. Poletaev, M. G. Rastegaeva, and A. M. Strel'chuk, Fiz. Tekh. Poluprovodn. **28**, 1769 (1994) [Semiconductors **28**, 981 (1994)].
[170]V. V. Makarov and N. N. Petrov, Fiz. Tverd. Tela **8**, 1602 (1966) [Sov. Phys. Solid State **8**, 1272 (1966)].
[171]V. V. Makarov, Fiz. Tverd. Tela **9**, 596 (1967) [Sov. Phys. Solid State **9**, 457 (1967)].
[172]N. V. Kodrau and V. V. Makarov, Fiz. Tekh. Poluprovodn. **15**, 1408 (1981) [Sov. Phys. Semicond. **15**, 813 (1981)].
[173]L. Patrick and W. J. Choyke, Phys. Rev. B **5**, 3253 (1972).
[174]V. V. Makarov and N. N. Petrov, Fiz. Tverd. Tela **8**, 3393 (1966) [Sov. Phys. Solid State **8**, 2714 (1966)].
[175]V. V. Makarov, Fiz. Tverd. Tela **13**, 2357 (1971) [Sov. Phys. Solid State **13**, 1974 (1971)].
[176]V. M. Gusev, K. D. Demakov, V. M. Efimov, V. I. Ionov, M. G. Kosagonova, N. K. Prokof'eva, V. G. Stolyarova, and Yu. N. Chekushkin, Fiz. Tekh. Poluprovodn. **15**, 2430 (1981) [Sov. Phys. Semicond. **15**, 1413 (1981)].
[177]Yu. A. Vodakov, G. A. Lomakina, E. N. Mokhov, M. G. Ramm, and V. I. Sokolov, Fiz. Tekh. Poluprovodn. **20**, 2153 (1986) [Sov. Phys. Semicond. **20**, 1347 (1986)].
[178]Yu. M. Suleĭmanov, A. M. Grekhov, and V. M. Grekhov, Fiz. Tverd. Tela **25**, 1840 (1983) [Sov. Phys. Solid State **25**, 1060 (1983)].
[179]Yu. A. Vodakov, A. I. Girka, A. O. Konstantinov, E. N. Mokhov, A. D. Roenkov, S. V. Svirida, V. V. Semenov, V. I. Sokolov, and A. V. Shishkin, Fiz. Tekh. Poluprovodn. **26**, 1857 (1992) Semiconductors **26**, 1041 (1992)].
[180]Yu. A. Vodakov, A. A. Vol'fson, G. V. Zaritskiĭ, E. N. Mokhov, A. G. Ostroumov, A. D. Roenkov, V. V. Semenov, V. I. Sokolov, and V. E. Udal'tsov, Fiz. Tekh. Poluprovodn. **26**, 107 (1992) [Sov. Phys. Semicond. **26**, 59 (1992)].
[181]W. J. Choyke, in *NATO ASI Ser. Physics and Chemistry of Carbides, Nitrides and Borides*, edited by R. Freer (Manchester, 1989).
[182]A. A. Lebedev, M. P. Shcheglov, and T. V. Sokolova, Pis'ma Zh. Tekh. Fiz. **21**, 48 (1995) [Tech. Phys. Lett. **21**, 61 (1995)].
[183]H. Kuwabara and S. Yamata, Phys. Status Solidi A **30**, 739 (1975).
[184]S. E. Saddow, C. W. Tripton, and M. S. Mazzola, J. Appl. Phys. **77**, 318 (1994).
[185]H. Matsunami, M. Ikeda, and T. Tanaka, Jpn. J. Appl. Phys. **19**, 1323 (1980).
[186]M. M. Anikin, A. A. Lebedev, N. K.Poletaev, A. M. Strel'chuk, A. L. Syrkin, and V. E. Chelnokov, Fiz. Tekh. Poluprovodn. **28**, 473 (1994) [Semiconductors **28**, 288 (1994)].
[187]A. A. Lebedev and M. C. do Carmo, Mater. Sci. Eng., B **46**, 275 (1997).
[188]A. V. Naumov and V. I. Sankin, Fiz. Tekh. Poluprovodn. **23**, 1009 (1989) [Sov. Phys. Semiconductors **23**, 630 (1989)].
[189]V. I. Sankin, R. G. Verenchikova, Yu. A. Vodakov, M. G. Ramm, and A. D. Roenkov, Fiz. Tekh. Poluprovodn. **16**, 1325 (1983) [Sov. Phys. Semicond. **16**, 839 (1983)].
[190]V. S. Balandovich and G. N. Violina, Fiz. Tekh. Poluprovodn. **15**, 1650 (1981) [Sov. Phys. Semicond. **15**, 959 (1981)].
[191]M. M. Anikin, A. A. Lebedev, S. N. Pyatko, V. A. Soloviev, and A. M. Strel'chuk, Springer Proc. Phys. **56**, 269 (1992).
[192]A. M. Strel'chuk, Fiz. Tekh. Poluprovodn. **29**, 1190 (1995) [Sov. Phys. Semicond. **29**, 850 (1995)].
[193]A. M. Strel'chuk and V. V. Evstropov, Inst. Phys. Conf. Ser. **155**, 1009 (1997).
[194]O. Kordina, J. P. Bergman, A. Henry, and E. Janzen, Appl. Phys. Lett. **66**, 189 (1995).
[195]J. P. Bergman, C. Hallin, and E. Janzen, *Abstracts Int. Conf. on* SiC, III *Nitrides and Related Materials* (Stockholm, Sweden, 1997), p. 63.
[196]A. A. Lebedev and D. V. Davydov, Fiz. Tekh. Poluprovodn. **31**, 1049 (1997) [Sov. Phys. Semicond. **31**, 935 (1997)].
[197]A. O. Konstantinov, D. P. Litvin, and V. I. Sankin, Pis'ma Zh. Tekh. Fiz. **7**, 1335 (1981) [Sov. Tech. Phys. Lett. **7**, 572 (1981)].
[198]Yu. A. Vodakov, A. O. Konstantinov, D. P. Litvin, and V. I. Sankin, Pis'ma Zh. Tekh. Fiz. **7**, 705 (1981) [Sov. Tech. Phys. Lett. **7**, 301 (1981)].
[199]A. P. Dmitriev, A. O. Konstantinov, D. P. Litvin, and V. I. Sankin, Fiz. Tekh. Poluprovodn. **17**, 1093 (1983) [Sov. Phys. Semicond. **17**, 686 (1983)].
[200]M. M. Anikin, S. M. Vaĭnshteĭn, A. M. Strel'chuk, and A. L. Syrkin, Fiz. Tekh. Poluprovodn. **22**, 545 (1988) [Sov. Phys. Semicond. **22**, 307 (1988)].
[201]M. M. Anikin, M. E. Levinshteĭn, I. V. Popov, V. P. Rastegaev, A. M. Strel'chuk, and A. L. Syrkin, Fiz. Tekh. Poluprovodn. **22**, 1574 (1988) [ Sov. Phys. Semicond. **22**, 995 (1988)].
[202]A. S. Kyuregyan and P. N. Shlygin, Fiz. Tekh. Poluprovodn. **23**, 1164 (1989) [Sov. Phys. Semicond. **23**, 729 (1989)].
[203]E. V. Astrova, V. M. Volle, V. B. Voronkov, V. A. Kozlov, and A. A. Lebedev, Fiz. Tekh. Poluprovodn. **20**, 2122 (1986) [Sov. Phys. Semicond. **20**, 1326 (1986)].
[204]P. G. Neudeck and Ch. Fazi, IEEE Electron Device Lett. **18**, 96 (1997).
[205]A. A. Lebedev, A. M. Strel'chuk, S. Ortolland, C. Raynaud, M. L. Locatelli, D. Planson, and J. P. Chante, Inst. Phys. Conf. Ser. **142**, 701 (1996).
[206]A. A. Lebedev, S. Ortoland, C. Raynaud, M. L. Locatelli, D. Planson, and J. P. Chante, Fiz. Tekh. Poluprovodn. **31**, 866 (1997) [Sov. Phys. Semicond. **31**, 735 (1997)].
[207]R. N. Kyutt, A. A. Lepeneva, G. A. Lomakina, E. N. Mokhov, A. S. Tregubova, and G. F. Yuldashev, Fiz. Tverd. Tela **30**, 2606 (1988) [Sov. Phys. Solid State **30**, 1500 (1988)].
[208]A. I. Girka, V. A. Kuleshin, A. D. Mokrushin, E. N. Mokhov, S. V. Svirida, and A. V. Shishkin, Fiz. Tekh. Poluprovodn. **23**, 1270 (1989) [Sov. Phys. Semicond. **23**, 790 (1989)].
[209]V. A. Il'in and B. S. Balandovich, Defect Diffus. Forum **103–105** (Trans, Tech. publ., Switzerland, 1993), p. 633.

Translated by D. H. McNeill

# Optically active layers of silicon doped with erbium during sublimation molecular-beam epitaxy

A. Yu. Andreev, B. A. Andreev, M. N. Drozdov, Z. F. Krasil'nik, M. V. Stepikhova, and V. B. Shmagin

*Institute of Microstructure Physics, Russian Academy of Sciences, 603600 Nizhniĭ Novgorod, Russia*

V. P. Kuznetsov, R. A. Rubtsova, and E. A. Uskova

*Scientific-Research Physicotechnical Institute, Nizhniĭ Novgorod State University, 603600 Nizhniĭ Novgorod, Russia*

Yu. A. Karpov

*Institute of Chemical Problems in Microelectronics, Moscow, Russia*

H. Ellmer and L. Palmetshofer

*Institute of Experimental Physics, University of Linz, A-4040 Linz, Austria*

K. Piplits and H. Hutter

*Institute of Analytical Chemistry, Technical University of Vienna, Vienna, Austria*
(Submitted July 8, 1998; accepted for publication August 5, 1998)
Fiz. Tekh. Poluprovodn. **33**, 156–160 (February 1999)

A study is made of the electrical, optical, and structural properties of Si:Er layers produced by sublimation molecular-beam epitaxy. The Er and O contents in the layers, grown at 400–600 °C, were as high as $5\times10^{18}$ and $4\times10^{19}$ cm$^{-3}$, respectively. The electron concentration at 300 K was ~10% of the total erbium concentration and the electron mobility was as high as 550 cm$^2$/(V·s). Intense photoluminescence at 1.537 $\mu$m was observed from all the structures up to 100–140 K. The structure of the optically active centers associated with Er depended on the conditions under which the layers were grown.  [S1063-7826(99)00202-1]

## 1. INTRODUCTION

Erbium doped silicon has attracted considerable attention because the 1.54-$\mu$m $^4I_{13/2}\rightarrow{}^4I_{15/2}4f$-transition of the $Er^{3+}$ ion lies in the spectral range of the maximum transmission and minimum dispersion of quartz fibers. In order to create highly efficient light emitting structures, the erbium concentration must exceed $10^{18}$ cm$^{-3}$ (Ref. 1). One promising method for obtaining Si:Er layers is molecular-beam epitaxy (MBE), which can be used to grow highly doped structures (including multilayer ones) with a low density of structural defects that emit at a wavelength of 1.54 $\mu$m.[2–4]

Sublimation molecular-beam epitaxy (SMBE) is an interesting, new variant of MBE for this problem. In it molecular fluxes of Si and the doping impurity are produced by sublimation of a resistively heated crystalline Si source doped with a given impurity, in particular, erbium.[5–7] Direct resistive heating of the source ensures high purity of the molecular fluxes, which makes it possible to obtain silicon layers with a minimal number of defects and a long lifetime for the minority charge carriers.[6,8] We have shown previously that SMBE can be used for reproducibly growing uniformly doped, perfect, single-crystal layers of Si with concentrations of electrically active shallow impurities (P, As, Sb, B, Al) of $2\times10^{13}-4\times10^{20}$ cm$^{-3}$, as well as structures with a specified complex doping profile, including those with $\delta$-doped layers.[5,6] In this paper we use SMBE to produce efficiently radiating Si:Er layers and investigate their optical and electrical properties. There is some interest in high resolution studies of the photoluminescence spectra in order to identify the optically active centers in SMBE layers, since there are no data on MBE layers and the available spectra of Si:Er layers grown by chemical vapor deposition (CVD)[9] differ greatly from those for implanted Si.

## 2. EXPERIMENT

Si:Er structures were grown in vacuum with a residual pressure of $\sim2\times10^{-7}$ mbar on *n*- and *p*-type Si (100) substrates with resistivities of 0.005 and 10 Ω·cm. Crystalline wafers cut from ingots of Si:Er with Er and O contents of up to $\sim5\times10^{20}$ and $\sim10^{19}$ cm$^{-3}$, respectively, were used as Si and Er sublimation sources. According to infrared photoconductivity and absorption spectra, the major electrically active impurity, which determines the type of conductivity of the samples, was boron (concentration $n\sim10^{15}$ cm$^{-3}$). The source and substrate were heated resistively. The growth temperature was varied from 400 to 700 °C and the thickness of the layers, from 0.2 to 3 $\mu$m. The details of the growth

 

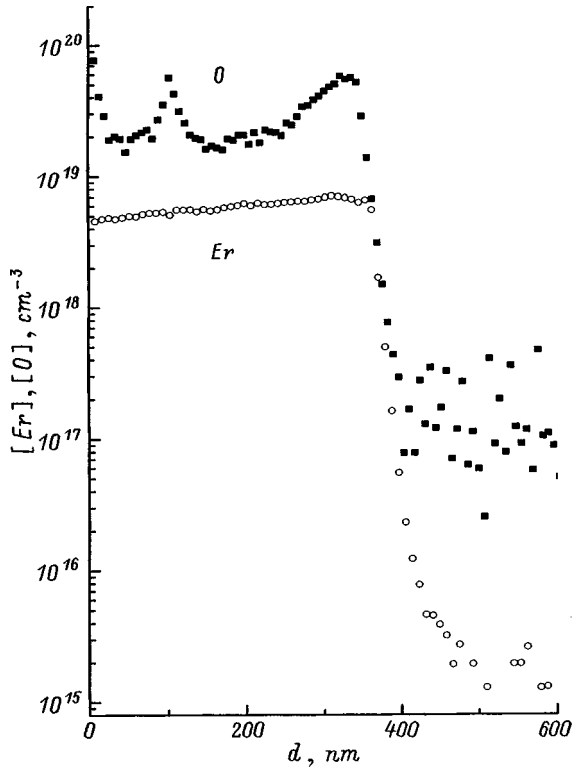


FIG. 1. Distribution of erbium and oxygen atoms (SIMS data) over the thickness $d$ of an Si layer grown on an Si (100) substrate at 600 °C. The thickness is reckoned from the free surface of the layer.

technique are discussed elsewhere.[6] The structures were subsequently annealed in vacuum or in a stream of hydrogen.

The distribution of impurity atoms over the thickness of the layers was measured by secondary ion mass spectrometry (SIMS) and Rutherford Backscatter spectroscopy (RBS). The crystalline perfection of the layers was investigated by RBS[10] and a metallographic method. The concentration of the charge carriers and their distribution over the thickness of the layers were determined by the Hall and capacitance-voltage methods. The energy levels in the band gap were studied for temperatures of 50–350 K by deep level relaxation spectroscopy (DLTS). Photoluminescence spectra were studied on a Bomem DA3.36 (InSb detector) Fourier spectrometer with a spectral resolution of up to 0.5 $cm^{-1}$. A $Kr^+$ laser was used as an excitation source (wavelength $\lambda = 647$ nm).

### 3. RESULTS AND DISCUSSION

All of the Si:Er layers that were grown had $n$-type conductivity, regardless of the substrate parameters and type of heat treatment (with and without annealing at 900 °C). The Hall electron concentration at 300 K in uniformly doped layers at 400–600 °C was $2\text{-}4\times10^{17}$ $cm^{-3}$ (after annealing at 900 °C) and the mobility was 340–550 $cm^2/(V\cdot s)$. The erbium and oxygen contents of the layers were $\sim10^{18}$ and $\sim10^{19}$ $cm^{-3}$, respectively, according to SIMS data. Thus, the electron concentration in the layers was ~10% of the total erbium concentration. This value of the degree of electrical activation is comparable to data for Er implanted Si

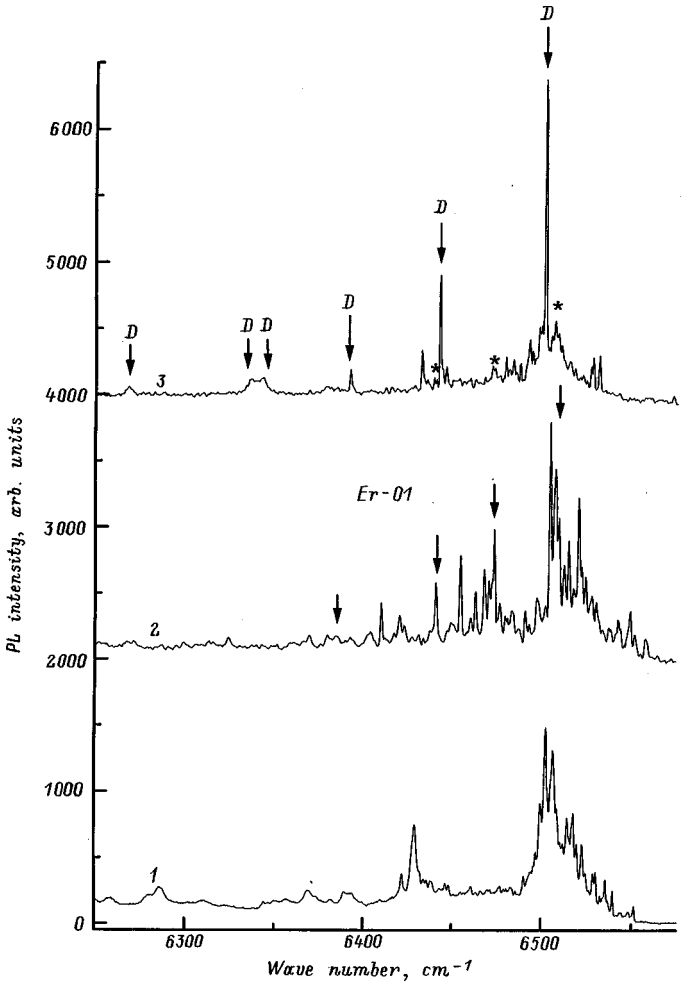


FIG. 2. Photoluminescence (PL) spectra of Si:Er layers produced by SMBE: (*1*) uniformly doped layer grown at 400 °C and vacuum annealed at 900 °C for 30 min; (*2*) uniformly doped layer grown at 500 °C without annealing; (*3*) as in curve *2*, but after annealing for 30 min in a hydrogen atmosphere at 900 °C. The arrows denote a series of lines corresponding to optically active centers associated with erbium.

layers with a similar oxygen content.[11] In the selectively doped Si:Er layers, the distributions of the electrically active centers (capacitance-voltage measurement data) correlated with the same for the total number of Er atoms (SIMS data); this confirms the coupling of the donor centers which develop in the layer to erbium atoms.

Figure 1 shows SIMS profiles of Er and O atoms in a uniformly doped (at 600 °C) Si layer. The sharpness of the film-substrate concentration transition (the Er concentration varies by two orders of magnitude over a thickness of ~35 nm) is evidence of the absence of segregation of the Er on the growth surface; this is consistent with the data of Refs. 2 and 3 for Si obtained by MBE. On the other hand, segregation of Er did occur for a substrate temperature of 700 °C. Note that oxygen could enter the epitaxial layer either from the gaseous medium within the vacuum chamber or from the Si:Er source.

This layer was also studied by RBS. The minima in the yield of scattered 400-keV $^4He^+$ ions for channelling in the directions of the $\langle100\rangle$ axis and $\{110\}$ and $\{100\}$ planes were 5, 27, and 35%, respectively, which is evidence of the crys-

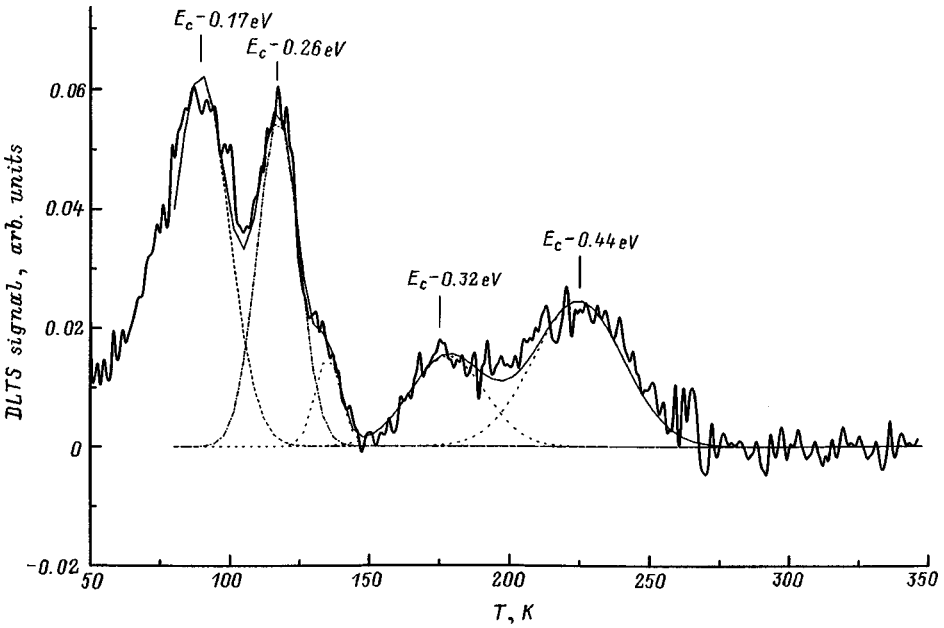


FIG. 3. Deep level spectrum in a layer of Si uniformly doped with Er to $5\times10^{17}$ cm$^{-3}$. The carrier concentration at $T=300$ K is $8\times10^{16}$ cm$^{-3}$.

talline perfection of the layer. This is also confirmed by data from the metallographic studies; no packing defects or dislocations were observed in Si:Er layers with thicknesses of $\sim 3$ $\mu$m.

Figure 2 shows photoluminescence spectra at $T=4.2$ K for two structures with uniform doping during SMBE of the Si:Er layers at 400 (*1*) and 500 °C (*2*, *3*). All of the structures manifest intense photoluminescence near 1.54 $\mu$m due to the Er and an exciton luminescence signal (not shown in Fig. 2). The photoluminescence spectrum of the sample obtained at a temperature of 400 °C has a complicated structure, even after annealing. The spectrum consists of intense lines with wave numbers of 6502.9 and 6429.2 cm$^{-1}$ (Fig. 2, spectrum *1*) and a multitude of extremely narrow lines within the interval 6506.8–6551.4 cm$^{-1}$. This is evidence of the presence of several optically active Er centers with low symmetry. The lines in the high energy region of the spectrum may be associated with complicated complexes of Er with oxygen.[12]

The photoluminescence spectrum of an unannealed sample (Fig. 2, spectrum *2*) grown at 500 °C contains a multitude of intense narrow lines in the interval 1.525–1.57 $\mu$m (6557–6369 cm$^{-1}$). The available data for implanted layers make it possible to isolate only one series of lines referring to a center denoted in Ref. 12 by Er–O1: 6508, 6474, and 6441 cm$^{-1}$. Annealing the sample in a hydrogen atmosphere at 900 °C for 30 min leads to the formation of a new dominant Er center represented by a series of narrow lines at 6502, 6443, 6393, 6342, 6337, and 6268 cm$^{-1}$ (the D series, indicated by arrows in spectrum 3) and a reduction in the relative intensity of the Er–O1 series (indicated by asterisks). Note that this spectrum contains none of the so-called dislocation luminescence, which shows up as a background signal in the neighborhood of 1.54 $\mu$m and is characteristic of layers with a large amount of structural defects.

In terms of the number of lines, their position, and their relative intensities, the D series, which reflects the splitting structure of the $^4I_{15/2}$ multiplet, has no analog among the experimental data for the well-studied ion-implanted Si layers and cannot be attributed to any of the optical centers associated with Er that have been identified in Ref. 12. On the other hand, this spectrum is extremely close to the experimental photoluminescence spectrum given in Ref. 9 for an Si:Er layer obtained by gaseous phase epitaxy. The only open question involves the nature of the broad peak at 6513 cm$^{-1}$ observed in Ref. 9. In our spectra there is no intense line at this frequency. By using a Fourier spectrometer and high-quality Si:Er layers, we have been able to attain a spectral resolution of $\leqslant 1$ cm$^{-1}$ and observe the doublet at 6337 and 6342 cm$^{-1}$ that was predicted, but not observed experimentally, in Ref. 9 for the $Er^{3+}$ ion in states with $D_{2d}$ and $C_{3v}$ point symmetry. On comparing spectrum 3 in Fig. 2 with a calculation[9] of the position and relative intensities of the photoluminescence lines, we see that the D series is closest to the transitions corresponding to a center with $D_{2d}$ point symmetry. At the same time, the observed photoluminescence spectra and RBS data on the scattering angular dependence do not uniquely determine the position (substitution or interstitial) of the Er atoms in the crystal.

The Si:Er layers deposited at a higher temperature, 600 °C, and annealed at 900 °C in vacuum, yielded a photoluminescence spectrum similar to that shown in spectrum *3* in Fig. 2. The spectra of multilayer structures consisting of thin, highly doped layers of Si:Er grown at a lower temperature (400–500 °C) and thick (of much greater thickness) undoped layers deposited at 700 °C were the same as spectrum 3 in Fig. 2 (independently of the annealing).

The temperature dependences of the photoluminescence intensity for Si:Er layers uniformly doped at temperatures of 400 and 600 °C reveal temperature quenching of the photoluminescence at temperatures of 90 and 140 K, respectively. For a sample grown at 600 °C, the temperature quenching process is well described by two segments with activation energies of $\sim 13$ and 60 meV. The first value (temperatures of 30–80 K) is close to the corresponding magnitudes for

implanted[12,13] and molecular beam epitaxial[14] layers of Si:Er. Activation energies of 80-100 meV, or somewhat greater than 60 meV, were cited in Ref. 12 for temperatures $T>80$ K.

In this paper we have, for the first time, studied the DLTS spectra of the deep levels which were produced by introducing erbium in SMBE of Si layers. A series of lines with ionization energies $E_i=0.15-0.3$ eV is observed, as in the case of implanted structures (Fig. 3). At the same time, the intense lines in the high-temperature part of the spectrum ($E_i \geqslant 0.48$ eV) characteristic of implanted Si:Er layers[12,15] are absent. Since photoluminescence is observed in both structures, we may assume that levels with $E_i \geqslant 0.48$ eV are not responsible for excitation of the photoluminescence and correspond to complicated defect-impurity complexes which develop during implantation of Er.

#### 4. CONCLUSION

Sublimation molecular-beam epitaxy has been used to fabricate Si:Er layers which radiate efficiently at a wavelength of 1.54 $\mu$m. Erbium doping levels of $5\times10^{18}$ cm$^{-3}$ are attained in these structures and the resulting electron concentration was $\sim$10% of the total erbium concentration while the electron mobility was 300–550 cm$^2$/(V·s).

The photoluminescence spectra include a series of lines belonging to the Er–O1 center observed in implanted Er layers and a new series of intense, narrow lines at 6502, 6443, 6393, 6342, 6337, and 6268 cm$^{-1}$ which may be tentatively attributed to an Er center in a state with $D_{2d}$ point symmetry.

We wish to thank A. V. Murel' for help in conducting the DLTS measurements.

This work was supported by the Russian Fund for Fundamental Research (Grants 98-02-16619, 96-02-19283, and 96-03-32581) and the Ministry of Science, Technology, and Industry through the program on Fundamental Spectroscopy (Project 08.02.043).

[1] Y.-H. Xie, E. A. Fitzgerald, and Y. J. Mii, J. Appl. Phys. **70**, 3223 (1991).
[2] J. Stimmer, A. Reittinger, J. F. Ntzel, G. Abstreiter, H. Holzbrecher, and Ch. Buchal, Appl. Phys. Lett. **68**, 3290 (1996).
[3] R. Serna, Jung H. Shin, M. Lohmeier, E. Vlieg, A. Polman, and P. F. A. Alkemade, J. Appl. Phys. **79**, 2658 (1996).
[4] W.-X. Ni, K. B. Joelsson, C.-X. Du, I. A. Buyanova, G. Pozina, W. M. Chen, G. V. Hansson, B. Monemar, J. Gardenas, and B. G. Svensson, Appl. Phys. Lett. **70**, 3383 (1997).
[5] V. P. Kuznetsov, A. Yu. Andreev, O. A. Kyznetsov, L. E. Nikolaeva, T. M. Zotova, and N. V. Gudkova, Phys. Status Solidi A **127**, 371 (1991).
[6] V. P. Kuznetsov, A. Yu. Andreev, and N. A. Alyabina, Elektronnaya promyshlennost' **9**, 57 (1990).
[7] N. G. Kalugin, V. P. Kuznetsov, A. Yu. Andreev, M. V. Stepikhova, R. A. Rubtsova, and Z. F. Krasil'nik, in *Proceedings of the International Symposium ''Nanostructures: Physics and Technology''*, (St. Petersburg, 1997), p. 310.
[8] T. N. Sergievskaya, V. P. Kuznetsov, V. G. Vasil'ev, and V. A. Tolomasov, Élektron. tekhn. Materialy, vyp. **10**, 58 (1980).
[9] D. E. Wortman, C. A. Morrison, and J. L. Bradshaw, J. Appl. Phys. **82**, 2580 (1997).
[10] H. Ellmer, W. Fischer, and A. Klose, D. Semrad, Rev. Sci. Instrum. **67**, 1794 (1996).
[11] L. Palmetshofer, Yu. Suprun-Belevich, and M. Stepikhova, Nucl. Instrum. Meth. B **127/128**, 479 (1997).
[12] H. Przybylinska, W. Jantsch, Yu. Suprun-Belevitch, M. Stepikhova, L. Palmetshofer, G. Hendorfer, A. Kozanecki, R. J. Wilson, and B. J. Sealy, Phys. Rev. B **54**, 2532 (1996).
[13] S. Coffa, G. Franzo, F. Priolo, A. Polman, and R. Serna, Phys. Rev. B **49**, 16 313 (1994).
[14] H. Efeoglu, J. H. Evans, T. E. Jackman, B. Hamilton, D. C. Houghton, J. M. Langer, A. R. Peaker, D. Perovic, I. Poole, N. Ravel, P. Hemment, and C. W. Chan, Semicond. Sci. Technol. **8**, 236 (1993).
[15] J. L. Benton, J. Michel, L. C. Kimerling, D. C. Jacobson, Y.-H. Xie, D. J. Eaglesham, E. A. Fitzgerald, and J. M. Poate, J. Appl. Phys. **70**, 2667 (1991).

Translated by D. H. McNeill

# Evidence for $\varepsilon_2$-conductivity in the magnetoresistance of multivalley semiconductors

N. V. Agrinskaya, V. I. Kozub, T. A. Polyanskaya, and A. S. Saidov

*A. F. Ioffe Physicotechnical Institute, Russian Academy of Sciences, 194021 St. Petersburg, Russia*
(Submitted September 16, 1998; accepted for publication September 17, 1998)
Fiz. Tekh. Poluprovodn. **33**, 161–169 (February 1999)

Experimental studies of the liquid-helium temperature resistivities of Ge : Sb compounds with degrees of compensation $K<0.1$, i.e., in the $\varepsilon_2$ conductivity range, reveal that the resistivity is determined by hopping of carriers activated to the upper Hubbard $D^-$ band. The experimentally observed positive magnetoresistance, which is exponential in the magnetic field, arises from field-induced changes in the occupancy of the spin subbands by electrons. Evidence for the $\varepsilon_2$-conductivity mechanism is discussed on the basis of certain features of the magnetoresistance associated with $g$-factor anisotropy of different valleys, which is therefore specific to multivalley semiconductors. © *1999 American Institute of Physics.* [S1063-7826(99)00302-6]

## 1. INTRODUCTION

It is well known[1,2] that in weakly compensated semiconductors (for which the degree of compensation $K<0.2$) there is a bounded interval of concentrations near the Mott transition for which the conductivity mechanism within the impurity band (called $\varepsilon_2$-conductivity) is different from ordinary band and hopping conductivity. This mechanism is believed to be associated with the motion of electrons activated into the upper Hubbard band (the $D^-$ band), whose state energy is $E_0+U$, where $U=e^2/\kappa a$ is the Hubbard energy, $E_0$ is the ionization energy of an isolated donor, $\kappa$ is the dielectric constant, and $a$ is the Bohr radius.

At low impurity concentrations, the $D^-$ band is separated from the usual impurity band by an energy gap of $0.9E_0 \propto U$. Note that this value usually exceeds the activation energy $\varepsilon_3$ for conduction-band hopping conductivity by a considerable amount, so that in this limit the $\varepsilon_3$ channel dominates. However, with increasing impurity concentration $N_d$ (accompanied by a decrease in the distance between impurities $R=0.6N_d^{-1/3}$) the $D^-$ band broadens, due to the increasing overlap integral between impurities [$I(R)\propto \exp(-bR/a)$, where $b$ is a numerical coefficient] and the increase in disorder (where $V=e^2/\kappa R$ is the impurity potential). For this reason, starting with a certain impurity concentration, the activation energy $\varepsilon_3$ at low degrees of compensation is observed to decrease. This can be viewed as evidence that the $\varepsilon_2$-conductivity channel has begun to contribute,[3] although another way to explain this effect is to invoke correlated hopping in the lower Hubbard band.[4]

In this connection, the work of Andreev *et al.*[5] is especially noteworthy. Andreev *et al.* investigated the thermoelectric power in the hopping conductivity range, and found an important contribution to the thermoelectric power from $\varepsilon_2$-conductivity for samples with intermediate degrees of compensation $K=0.35$.

Note that the presence of $D^-$ states can also affect variable-rangehopping conductivity as well. Specifically, Kurobe and Kanimura[6] showed that these states give rise to a positive magnetoresistance of spin origin: because the $D^-$ centers are singlets, readjustment of spins in a magnetic field contributes to the density of states in the neighborhood of the Fermi level, and hence increases the hopping range. In Ref. 7 it was shown that only this mechanism can explain certain distinctive features of the low-temperature magnetoresistance observed in CdTe in the range of comparatively weak fields. This was the first demonstration that $D^-$ states can have a role in variable-rangehopping conductivity in doped semiconductors.

Based on these results, two of us (Agrinskaya and Kozub; see Ref. 8) analyzed the behavior of the magnetoresistance in the $\varepsilon_3$- and $\varepsilon_2$-conductivity ranges. In particular, we showed that the spin correlations in the upper Hubbard band can cause the activation energy $\varepsilon_2$ to depend strongly on magnetic field, namely as

$$\varepsilon_2=\varepsilon_2^0+g\mu H \tag{1}$$

for $g\mu H \gg 2T$ and as

$$\varepsilon_2=\varepsilon_2^0+(g\mu H)^2/4T \tag{2}$$

for $g\mu H \ll 2T$. In both these cases, the universal constant $g\mu$ appears—the Bohr magneton $\mu$ multiplied by the spin-splitting factor for shallow bound states.

The magnetoresistance in the $\varepsilon_2$-conductivity regime caused by spin correlations in the $D^-$ band was first discussed by Yamanouchi in Ref. 9. However, his analysis essentially reduced to numerical calculations for the regions of weak magnetic field, leading to an interpolation expression that has been cited many times since:

$$\varepsilon_2=\varepsilon_2^0+\gamma H^2.$$

Using Eq. (2), we conclude that $\gamma \simeq g^2\mu^2/T$, i.e., $\gamma$ depends on temperature. Because it is well known that the quantity $\gamma$ lies in the range $1\times10^{-13}\,\mathrm{eV/G^2}$ to $4\times10^{-13}\,\mathrm{eV/G^2}$ for Ge : Sb in the temperature interval $T=1.7$ to 4.2 K (see, e.g., Ref. 2), we can estimate whether the experimental values of $\gamma$ correspond to reasonable values of $g$. Our estimate gives a

 

value of $g=0.6$ to 2, in good agreement with values of the $g$-factor in $n$-Ge (see Sec. 3). Now, a number of experimental papers have reported a decrease in the value of $\gamma$ with increasing impurity concentration.[2] We can explain this fact by noting that increasing the impurity concentration shifts the temperature range in which $\varepsilon_2$-conductivity is observed toward higher temperatures, while at low temperatures variable-range hopping conductivity begins to dominate. Experimental data are available for a large number of materials on how the activation energy for hopping conductivity depends on magnetic field in the strong-field range. When this data is analyzed, it is found that the activation energy increases with magnetic field, and actually follows the universal dependence $\delta\varepsilon_2=g\mu H$, where the value of $g$ is obtained from independent measurements.

We regard this result as evidence in favor of our model in Ref. 8. Note, however, that much of the existing experimental information about the dependence of $\varepsilon_2$ on magnetic field comes from the weak-field region. It is clear from Eqs. (1) and (2) given here that the field-dependent contribution to $\varepsilon_2$ is not exponentially large in this limit, which makes the analysis easier. Therefore, comparison of theoretical predictions with experiment in the weak-magnetic field range requires more care and, in particular, more detailed experimental data.

Our goal was to investigate hopping transport in the presence of weak and strong magnetic fields in samples of $n$-type Ge : Sb with degrees of compensation $K\lesssim 0.1$ and intermediate impurity concentrations corresponding to $N_d a^3 = 10^{-3}-10^{-2}$, i.e., close to the Mott transition. We assume that the dominant type of conductivity in these samples is $\varepsilon_2$-conductivity in the temperature range 1.7 to 10 K.

## 2. MAGNETORESISTANCE OF MULTIVALLEY SEMICONDUCTORS

In solving percolation problems for materials with composite (multivalley) electronic spectra a question that naturally arises is how to average over the spectrum (i.e., over the valleys). Here we will be guided by considerations analogous to those presented in Ref. 10. When the activated term can be disregarded,calculating the percolation threshold $\xi_c$ (and hence the value of the ''effective resistor'' that determines the value of the conductivity) reduces to solving the equation

$$V_{\xi_c} N = B_c ,$$

where $V_{\xi_c}$ is the spatial volume of the neighborhood near the hopping center in which the tunneling exponent does not exceed $\xi_c$, $N$ is the concentration of hopping centers, and $B_c$ is a certain number determined by the average number of random centers associated with this site.

For multivalley Ge, the volume $V$ is bounded by four intersecting ellipsoids of revolution with semi-axis ratios $(m_l/m_t)^{1/2}\equiv K^{1/2}$. For simplicity we assume that this ratio is large enough that the region of overlap of these disklike ellipsoids can be ignored, and hence the volume $V_{\xi_c}$ is a sum of independent contributions of the corresponding equal-volume ellipsoids $V_{\xi_c,\nu}$, where $\nu$ is the valley label. Accordingly, each random ''resistor'' can be associated with only one of the ellipsoids (i.e., with the corresponding center at which the hopping occurs). The connectivity condition can be written in the form

$$N\sum_{\nu} V_{\xi_c,\nu} = B_c .$$

In the presence of finite activation terms (or other corrections to $\xi$), the percolation is determined by the total exponent. If we include these corrections $\Delta\xi_{c,\nu}$ (which in our case depend on the number of valleys by virtue of the anisotropy of the $g$-factor for each of the valleys), the expression for the new percolation threshold can be written in the form

$$\xi_{ct,\nu}+\Delta\xi_{c,\nu}=\xi_c' ,$$

where $\xi_{ct,\nu}$ is the pure tunneling contribution to the exponent, which corresponds to the ''critical resistor.'' Here we include the fact that the percolation threshold is the same for the entire critical grid, whereas the critical resistor can be associated with the contribution from any of the valleys; therefore, the corresponding condition is expressed by four equations.

Note that the quantity $\xi_{ct,\nu}$ will differ, in general, from the value $\xi_c$ when these corrections are absent, and will depend on the valley number. This is because it turns out to be advantageous to decrease the volume $V_\nu$ for valleys with large values of $\Delta_{c,\nu}$ compared to those where $\Delta_{c,\nu}$ is smaller. However, if we assume that $\Delta\xi\ll\xi_c$ (which holds for nearest-neighbor hopping) we can expect that the change in the tunneling contribution due to the presence of activation corrections is not large, and carry out an expansion in terms of this change:

$$V_{\xi_{ct,\nu}} = V_{\xi_c,\nu} + \frac{\partial V_{c,\nu}}{\partial \xi_c}\Delta\xi_{ct,\nu} ,$$

where $\Delta\xi_{ct,\nu}=\xi_{ct,\nu}-\xi_c$. Since the derivatives obviously are the same for all the valleys, the connectivity condition is rewritten in the form

$$N\left( V_{\xi_c} + \frac{\partial V_{c,\nu}}{\partial \xi_c}\sum_{\nu}\Delta\xi_{c,t}\right) = B_c ,$$

from which it obviously follows that

$$\sum_{\nu}\Delta\xi_{c,t}=0. \tag{3}$$

Using the notation $\Delta\xi_c=\xi_c'-\xi_c$, we can write for each of the valleys

$$\Delta\xi_{ct,\nu}+\Delta\xi_{c,\nu}=\Delta\xi_c .$$

Summing over all the valleys and using Eq. (3), we obtain

$$\Delta\xi_c=\frac{1}{4}\sum_{\nu}\Delta\xi_{c,\nu}. \tag{4}$$

In other words, the activation energy for the effective resistor is determined by averaging the corresponding activation energies over all the valleys. It is clear that this averaging significantly decreases the anisotropy of the effective $g$-factor (which we noted in Ref. 8).

Also noteworthy, however, is the fact that in the calculations described above we have ignored the overlap region of the various ellipsoids. In this case it is obvious that for hopping pairs located in this region we must add the probabilities for hopping by way of any of the intersecting valleys, and hence, if there is a large spread in the activation energies of the valleys, the contribution of the valley with the smallest activation energy will be decisive. On the other hand, at the highest magnetic fields the contribution of only one valley can turn out to be decisive even when the anisotropy of the volume $V_{\xi_c}$ is taken into account—by analogy with the ''squeezing out'' of electrons from individual valleys when *n*-type Ge is uniaxially strained (see Refs. 10 and 11).

On the basis of the one-valley model (see Ref. 8) we obtain the following expression for the $\varepsilon_2$-conductivity, which is controlled by the occupation number $n$ of electronic states in the upper Hubbard band:

$$\sigma_{xx}(H) \propto n(H) = \left\{ \exp \frac{\varepsilon_2 + 2T \ln[2 \cosh(g\mu H/2T)]}{T} + 1 \right\}^{-1}. \tag{5}$$

In this case, when $\exp \varepsilon_2/T \gg 1$ we have

$$\frac{n(H)}{n(H=0)} = \cosh^{-2}\left(\frac{g\mu H}{2T}\right).$$

In the regions under investigation $\rho_{xy} \ll \rho_{xx}$, and hence $\rho_{xx}(H) = 1/\sigma_{xx}(H)$. Let us now extract the temperature-dependent contribution in the logarithm of the resistivity (conductivity) and denote it by $\ln_T \rho(\ln_T(\sigma))$. Taking into account the discussion given above and, in particular, Eq. (4), we obtain the following expression for a multivalley semiconductor:

$$\ln_T \frac{\rho(H)}{\rho(0)} = \frac{1}{4}\sum_\nu \ln_T \sigma^{(\nu)}(0) - \frac{1}{4}\sum_\nu \ln_T \sigma^{(\nu)}(H) = \frac{1}{4}\sum_\nu \ln_T \frac{\sigma^{(\nu)}(0)}{\sigma^{(\nu)}(H)} = \frac{1}{4}\sum_\nu \ln_T \left[\cosh^2\left(\frac{g_\nu \mu H}{2T}\right)\right], \tag{6}$$

where $g_\nu$ is the Land factor for the valley with label $\nu$, and $\sigma^{(\nu)}$ is the value of the conductivity corresponding to the critical resistor controlled by this valley.

It thus follows that the temperature-dependent contribution to the magnetoresistance depends on the ratio $H/T$ and the value of the $g$-factor in the valley, which in turn depends on the direction of the magnetic field relative to the axes of the isoenergetic surface of the valley. In a weak magnetic field, i.e., for $g_\nu \mu H \ll T$ [see Eq. (2)], we obtain:

$$\ln_T \frac{\rho(H)}{\rho(0)} \simeq \left(\frac{g_0 \mu H}{2T}\right),$$

where

$$g_0^2 = \frac{1}{4}\sum_{\nu=1}^{4} g_\nu^2. \tag{7}$$

In a strong magnetic field, i.e., for $g_\nu \mu H \gg T$, we have

$$\ln_T \frac{\rho(H)}{\rho(0)} \simeq \frac{1}{4}\sum_\nu \ln_T \exp\left[\frac{g_\nu \mu H}{T}\right] = \frac{\mu H}{T} g_{hH},$$

where

$$g_{hH} = \frac{1}{4}\sum_{\nu=1}^{4} g_\nu. \tag{8}$$

A glance at Eqs. (7) and (8) shows that experimental data for a multivalley semiconductor is more convenient to analyze when these expressions are rewritten in the form appropriate for a material with a spherical isoenergetic surface, i.e., as follows:

$$\ln \frac{\rho(H,T)}{\rho(0,T)} = \frac{(g_{\exp}\mu H)^2}{4T^2}$$

in a weak magnetic field and

$$\ln \frac{\rho(H,T)}{\rho(0,T)} = \frac{g_{\exp}\mu H}{T}$$

in a strong magnetic field, so that in a weak field $g_{\exp} \equiv g_0$ and in a strong field $g_{\exp} \equiv g_{hH}$.

## 3. EXPERIMENTAL RESULTS

We made a detailed study of the Hall effect, conductivity and magnetoresistance of three samples of Ge : Sb with degrees of compensation $K \lesssim 0.1$ in the temperature range 1.7 to 300 K. The sample parameters are listed in Table I. The

TABLE I. Parameter of Ge:Sb samples.

| Sample | Orientation **J**, **H** | $N_d$, $10^{16}$ cm$^{-3}$ | $\varepsilon_2$, meV | $\varepsilon_2'$, meV | $g$, $H<1$ T | $g$, $H>2$ T |
|---|---|---|---|---|---|---|
| | | | | | Experiment | Experiment |
| 1 | $\mathbf{J}\parallel\langle 111\rangle$, $\mathbf{H}\parallel\langle 1\bar{1}0\rangle$ | 6.6 | 0.55 | 1.2 | 2.2 | 1.6 |
| 2 | $\mathbf{J}\parallel\langle 11\bar{1}\rangle$, $\mathbf{H}\parallel\langle 110\rangle$ | 7.9 | 0.13 | 0.3 | 1.3 | 1.6 |
| 3 | $\mathbf{J}\parallel\langle 110\rangle$, $\mathbf{H}\parallel\langle 111\rangle$ | 8.8 | 0.12 | 0.31 | 0.9 | 0.8 |

*Note:* $N_d$—Donor concentration, $\varepsilon_2$—activation energy for hopping conductivity from the dependence of $\ln \rho$ on $1/T$, $\varepsilon_2'$—the same from the dependence of $\ln(\rho/T)$ on $1/T$, $g$—spin–splitting factor found form the weak ($H<1$ T) and strong ($H>2$ T) magnetic fields.

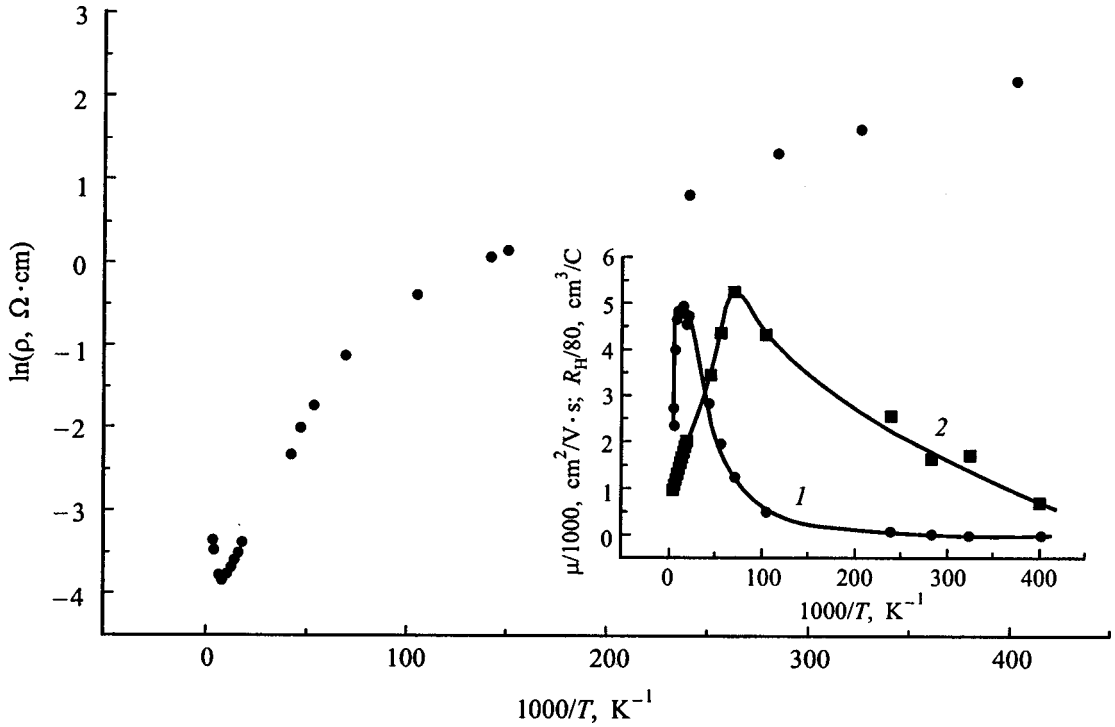


FIG. 1. Temperature dependence of the resistivity of a sample of *n*-type Ge with donor concentration $N_d = 6.6\times10^{16}\,\mathrm{cm}^{-3}$. The inset shows the temperature dependences of the Hall coefficient $R_H$ (*2*) and mobility $\mu$ (*1*) for this sample.

concentration of donors was estimated from values of the Hall coefficient at $H=0.3$ T and room temperature, taking into account the Hall factor as determined by the methods of Ref. 12. Figure 1 shows the temperature dependences of the conductivity $\sigma(T)$, the Hall coefficient $R_H(T)$, and the Hall mobility $\mu(T)$ for sample 1. We see that the function $\rho(T)$ exhibits two exponential slopes, which correspond to activation to the conduction band $\varepsilon_1$ and activation in the $D^-$ band, i.e., $\varepsilon_2$; the values of $\varepsilon_2$ are listed in Table I. The sizeable maximum in the temperature dependence of the Hall coefficient is explained by the two-band nature of the conductivity. In our samples we observe values of the Hall mobility of order 50 $\mathrm{cm}^2/(\mathrm{V}\cdot\mathrm{s})$ in the $\varepsilon_2$-conductivity range.

Figure 2 shows the dependence of the magnetoresistivity on magnetic field in the range 0 to 2.9 T for a sample in the temperature range corresponding to $\varepsilon_2$-conductivity, plotted on a scale linear with respect to magnetic field. The quadratic segment, which is shown by the solid curves, gives a good description of the experiment in the weak-field region. It is clear that for fields $H>1.5$ to 2 T we observe deviations from the quadratic dependence towards linear, which are most evident at low temperatures. Thus, for these samples

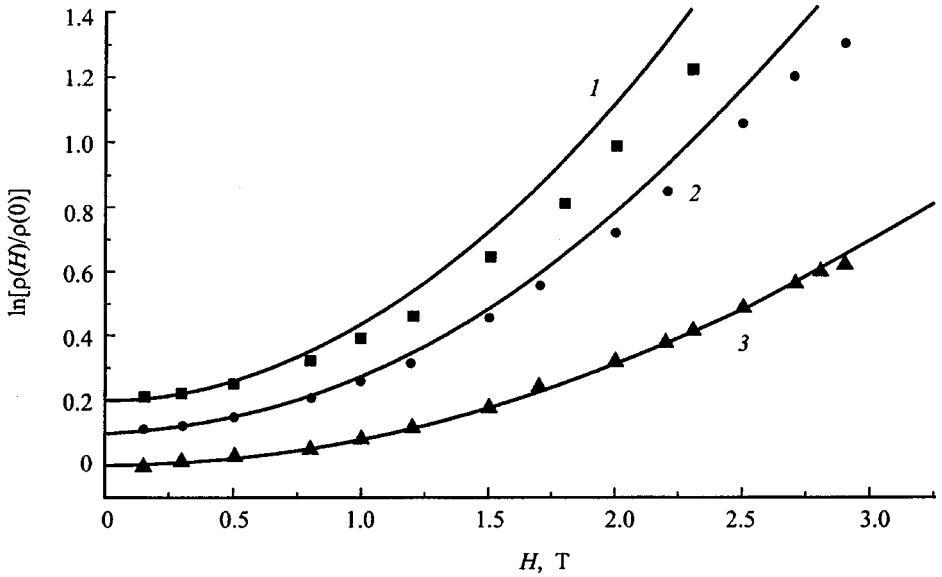


FIG. 2. Dependence of the resistivity on magnetic field for a sample of *n*-Ge ($N_d = 6.6\times10^{16}\,\mathrm{cm}^{-3}$) for the following temperatures $T$, K: *1*—2, *2*—2.5, *3*—4.2.

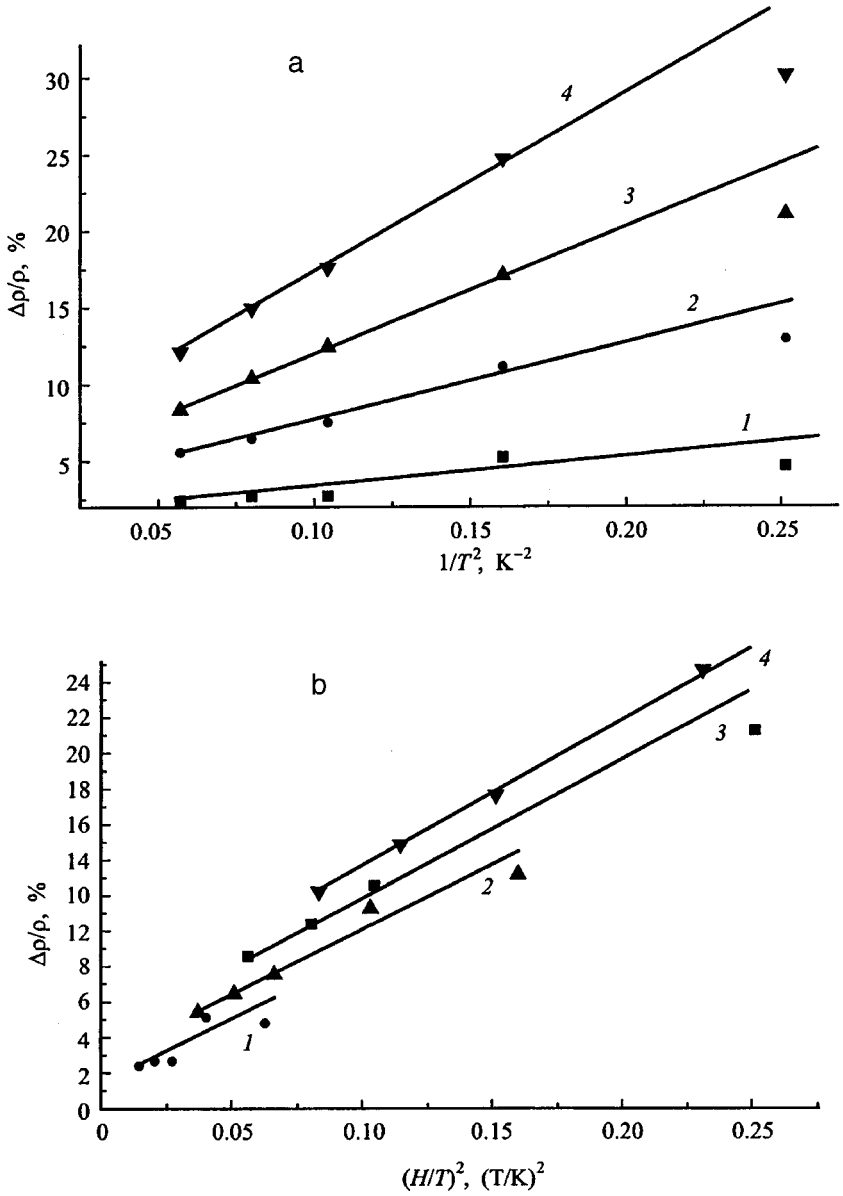


FIG. 3. Plots of the resistivity of a sample of *n*-Ge ($N_d = 6.6\times10^{16}$ cm$^{-3}$): a—versus $1/T^2$, b—versus $(H/T)^2$ for the following magnetic fields $H$, T: *1*—0.5, *2*—0.8, *3*—1, *4*—1.2.

there is a transition from quadratic to linear magnetoresistance in the magnetic field range 0 to 3 T. In order to verify the correctness of Eqs. (1) and (2), it is necessary to isolate the contribution to the magnetoresistance of the portion that depends exponentially on temperature. In order to accomplish this objective we used the following approach.

Let us write the temperature dependence of the magnetoresistance as follows:

$$\rho(H,T)=\rho_0(H,T)\exp[F(H)/T+\varepsilon_2/T], \tag{9}$$

where $F(H)$ is the correction to the activation energy $\varepsilon_2$ which is associated with spin correlations. Taking the logarithm of this equation, we obtain

$$\ln\rho(H,T)=\ln\rho_0(H,T)+F(H)/T+\varepsilon_2/T, \tag{10}$$

$$\ln[\rho(H,T)/\rho(0,T)]=\ln[\rho(H,T)/\rho(0,T)] -[F(H)-F(0)]/T. \tag{11}$$

We assume that the functions $\rho_0(H,T)$ factor out, and that $F(0)=0$. We thus have

$$\ln[\rho(H,T)/\rho(0,T)]=\ln[\tilde{\rho}_0(H)/\tilde{\rho}_0(0)]-F(H)/T. \tag{12}$$

Here the quantity $\tilde{\rho}_0$ no longer includes the temperature dependent pre-exponential factor. Thus, this procedure allows us to separate out the term $F(H)/T$ from the corrections that are temperature independent but dependent on magnetic field.

However, there is still a problem: the function $F$ has a different form for various ranges of magnetic field $H$: for small values of $H$, when $g\mu H<2T$, we have $F=(g\mu H)^2/4T$, while for large $H$ we have $F=g\mu H/T$. Therefore, we used the following procedure: for the two values $H=H_{1,2}$ in the range of sufficiently high fields we plotted the functions $\ln[\rho(H,T)/\rho(0,T)]$ versus $1/T$, so that the corresponding slope gives the value of $F(H)$. This allowed us to eliminate the temperature-independent contribution to the exponent. We then calculated the derivative

$$\frac{dF}{dH}=\frac{F(H_1)-F(H_2)}{H_1-H_2}=g\mu. \tag{13}$$

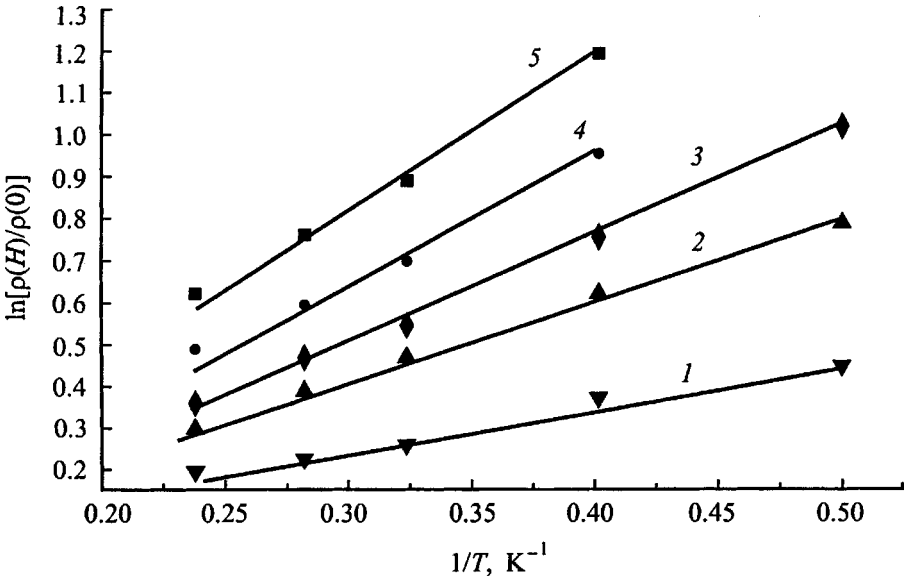


FIG. 4. Temperature dependence of the resistance of a sample of *n*-Ge ($N_d = 6.6 \times 10^{16}$ cm$^{-3}$) for the following magnetic fields $H$, T: *1*—1.5, *2*—2, *3*—2.2, *4*—2.5, *5*—2.9.

This procedure allows us to identify the asymptotic behavior at large values of $H$ more precisely than we could have done if we first had determined the slope of the linear function $\ln[\rho(H,T)/\rho(0,T)]$ versus magnetic field. In the region of weak magnetic fields, substituting in $F=(g\mu H)^2/4T$, we obtain the quadratic dependence of the magnetoresistance on inverse temperature and magnetic field, and the coefficient in front of $H^2/T^2$ has the value $g^2/4$.

Figures 3 and 4 show the temperature dependences of the magnetoresistance for sample 1 in the range of weak and strong magnetic fields. The values of $g$ obtained from the corresponding slopes are listed in Table I.

In order to compare these results with theoretical calculations we estimated the values of the effective $g$-factor in *n*-type Ge, starting from the following values of the components of the $g$-tensor (in terms of the axes of the ellipsoid): $g_\parallel = 0.63$, $g_\perp = 2$ (Ref. 11) or $g_\parallel = 0.9$, $g_\perp = 1.9$ (Ref. 13). The value of $g_\nu$ is defined as

$$g_\nu = \sqrt{g_\perp^2 \sin^2\theta + g_\parallel^2 \cos^2\theta}, \tag{14}$$

where $\cos\theta = (\mathbf{H}\cdot\boldsymbol{\nu})/\mathbf{H}\nu$; here $\boldsymbol{\nu}$ is a vector directed along the valley axis chosen. For the direction $\mathbf{H}\|\langle 100\rangle$, which is symmetric with respect to the valley axes, the value of the $g$-factorfor all the valleys is the same. For other directions of **H** listed in Table II, the valleys separate into two groups with their own values of the Land factor $g_1$ and $g_2$, which differ by factors of 1.5 to 2.

TABLE II. Computed values of the $g$-factor in valleys of the *n*- Ge conduction band for various orientations of the vector **H**.

| | $g_\parallel = 0.63$, $g_\perp = 2$ | | $g_\parallel = 0.9$, $g_\perp = 1.9$ | | Number of valleys with $g$-factor | |
|---|---|---|---|---|---|---|
| **H** | $g_1$ | $g_2$ | $g_1$ | $g_2$ | $g_1$ | $g_2$ |
| $\langle 1\bar{1}0\rangle$ | 1.26 | 2 | 1.32 | 1.9 | 2 | 2 |
| $\langle 111\rangle$ | 0.63 | 1.9 | 0.9 | 1.82 | 1 | 3 |
| $\langle 001\rangle$ | 1.67 | ⋯ | 1.64 | ⋯ | 4 | ⋯ |

## 4. DISCUSSION OF EXPERIMENTAL RESULTS

As was shown in Ref. 1, conductivity within the $D^-$ band can take place by two mechanisms: either through delocalized states (for excitation to the mobility edge $E_c$; Fig. 5), or by hopping transport along states at the bottom of the Hubbard band $E_H$. Which of these two methods occurs depends on temperature and on the density of states in the impurity band. One sign of band conduction is a large value of the Hall mobility and a large value of the thermoelectric power. The values of the Hall mobility observed in our samples—50 to 100 cm$^2$/(V·s)—did not allow us to conclude anything about the conductivity mechanism, since they could also correspond to a different mechanism. Moreover, a large value of the pre-exponential factor (which equals the value of the minimum metallic conductivity $\sigma_0 = 0.026e^2/ha$, where $a$ is the radius of a state in the $D^-$ band[1]) is characteristic of band conductivity. On the other hand, if the conductivity is attained by hopping, then if $\sigma_1 \ll \sigma_0$, the pre-exponential factor can have the form[11]

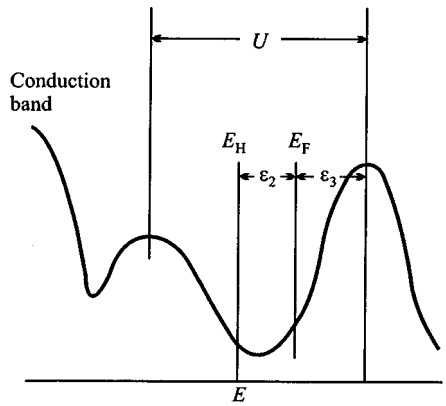


FIG. 5. Electronic density of states $N(E)$ in the neighborhood of the Hubbard bands. Notation: $E$—electron energy, $E_F$—Fermi energy, $E_H$—percolation level in the upper Hubbard band, $U$—Hubbard energy, and $\varepsilon_2$, $\varepsilon_3$—activation energies.

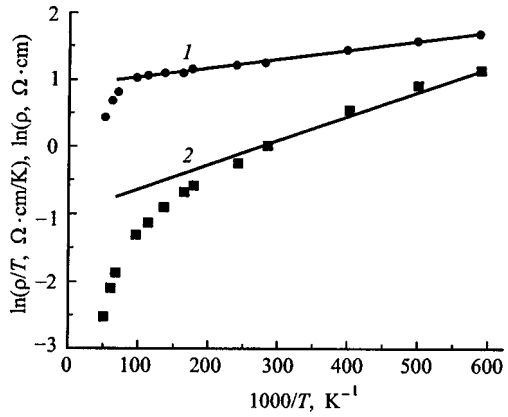


FIG. 6. Temperature dependences for a sample of *n*-Ge ($N_d=8.8\times10^{16}$ $cm^{-3}$): *1*—resistivity $\rho$, *2*—the quantity $\rho/T$.

$$\sigma_1^{-1}=C_1T\exp[1.73/(N^{1/3}a)], \tag{15}$$

where $C_1$ is a numerical coefficient. Our experiment shows that the value of the pre-exponential factor lies in the range 4 to 0.8 $(\Omega\cdot cm)^{-1}$, which is considerably smaller than $\sigma_0=30$ $(\Omega\cdot cm)^{-1}$, and in our case it is observed to increase with increasing impurity concentration. Based on these data we can argue that the transport of electrons appears to be associated with ''hopping within the tail of the $D^-$ band.'' In this case, in order to precisely calculate the activation energy it is necessary to take into account the temperature dependence of the pre-exponential factor $\sigma_1$. Curves of the temperature dependence of the resistance plotted on a scale $\ln[\rho(T)T^{-1}]$ versus $T^{-1}$ give considerably higher activation energies $\varepsilon_2'$ (see Fig. 6 and Table I). In principle, these values are in much better agreement with the calculated values of $\varepsilon_2$ for a given impurity concentration.[3]

The first report of spin subband occupation in a strong magnetic field influencing the magnetoresistance was the detailed study by Chroboczek *et al.*[11] of the magnetoresistance of Ge:P and Ge:Sb. These authors explained their data by invoking hopping accompanied by spin flip (i.e., disregarding the $D^-$ band). We analyzed their data with the help of the model of Ref. 8 for a strong magnetic field (1). The values of the *g*-factor obtained in this way are listed in Table III for various directions of the magnetic field.

It is clear that for strong magnetic fields satisfactory agreement is observed between the experimental values of the *g*-factor, both for our samples (Table I) and the Ge:P samples of Ref. 11 (Table III), with an average value for the *g*-factor of $\simeq$ 1.6.

It is also clear that for our Ge:Sb sample (Table III, $N_d=9\times10^{15}\,cm^{-3}$) the experimental values are strongly underestimated. In our view, this is explained by the sizeable contribution of $\varepsilon_3$-conductivity in this sample, due to its considerably smaller donor concentration. Let us clarify this assertion in more detail. As we showed previously in Ref. 8, when the contributions of the $\varepsilon_2$- and $\varepsilon_3$-conductivity channels are comparable and the magnetic field is capable of driving the system into a $\varepsilon_3$ regime by weakening the contribution of the $\varepsilon_2$-channel (when the activation energy does not depend on field), the expression for the conductivity can be cast in the form

$$\sigma\propto\exp\left[-\frac{\varepsilon_3}{T}+\frac{C_1}{C_2}\exp\left(-\frac{g\mu H}{T}+\frac{\varepsilon_3-\varepsilon_2}{T}\right)\right]$$

(where the second term in the exponent is assumed to be less than 1). Thus, in accordance with this expression, we can write

$$F=T\frac{C_1}{C_2}\exp\left(-\frac{g\mu H}{T}+\frac{\varepsilon_3-\varepsilon_2}{T}\right).$$

Following the procedure used in the calculation, the value of $g$ found from experiment is

$$g_{\exp}=\mu^{-1}\frac{\partial F}{\partial H}=g\frac{C_1}{C_2}\exp\left(-\frac{g\mu H}{T}+\frac{\varepsilon_3-\varepsilon_2}{T}\right),$$

so that the calculated value $g_{\exp}$ in the strong-field (saturation) limit turns out to be exponentially small. This expression, in general, cannot be used in the range of intermediate values of $H$; however, it clearly demonstrates a tendency to underestimate the values of $g$ found by our method when the contribution of the $\varepsilon_3$-channel is important, which does in fact happen for a Ge:Sb sample with concentration $N_d=9\times10^{15}\,cm^{-3}$, according to Ref. 11.

We now turn to a discussion of the role of anisotropy. It is not difficult to see that the values $g_0$ in (7) and $g_{hH}$ in (8) that follow from the values of $g_1$ and $g_2$ lie in the range 1.6 to 1.7 for all the directions of **H** and initial values of the components of the *g*-tensor that we investigated; in this case $g_0>g_{hH}$. Thus, within the framework of our simple theoretical model, we should not observe appreciable anisotropy of the magnetoresistance. However, experimentally this anisotropy is indeed substantial (see Table I) and correlates with values of $g_1$ belonging to valleys with the lowest spin splitting for a given direction of **H**.

This discrepancy can be explained by the simplifications used in designing the model. In particular, we assumed that

TABLE III. Parameters of Ge:P and Ge:Sb samples (see Ref. 11).

| Sample | Orientation | $n_{300\,K}$, $10^{16}\,cm^{-3}$ | $\varepsilon_2$, meV | $g$,$H$=10 to 14 T |
|---|---|---|---|---|
| Ge:P | $\mathbf{J}\parallel\langle1\bar{1}0\rangle$, $\mathbf{H}\parallel\langle\bar{1}10\rangle$ | 2 | 1.88 | 1.1 |
| Ge:P | $\mathbf{J}\parallel\langle1\bar{1}0\rangle$, $\mathbf{H}\parallel\langle00\bar{1}\rangle$ | 2 | 1,88 | 1.8 |
| Ge:Sb | $\mathbf{J}\parallel\langle1\bar{1}0\rangle$, $\mathbf{H}\parallel\langle110\rangle$ | 0.9 | 1.25 | 0.4 |
| Ge:Sb | $\mathbf{J}\parallel\langle110\rangle$, $\mathbf{H}\parallel\langle001\rangle$ | 0.9 | 1.25 | 1.4 |

*Note*: $n_{300\,K}\approx N_d$—donor concentration, $\varepsilon_2$—activation energy for hopping conductivity; the values of the *g*-factor in the range $H$=10 to 14 T were obtained from magnetoresistance experiments.

the magnetic field-dependent activation term was in every case small enough compared to the tunneling contribution $\xi_{ct}$ to make it possible to linearize the effective volume available for hopping with respect to these activation terms. At the same time, as we noted above, in strong magnetic fields the increased activation energy in valleys with large values of the $g$-factor can make hops by way of these valleys advantageous, despite the additional phase volume connected with them. In other words, the contributions from the corresponding valleys are ''squeezed out.'' In this connection, we note, in particular, the considerable anisotropy of the $g$-factor implied by the results of Ref. 11, which we explained in Ref. 8 by invoking this same tendency for the contribution from the valley with the lowest $g$-factor to dominate. In fact, the magnetic fields used in the experiments of Ref. 11, which were on the order of 10 T, generated an activation contribution of roughly 2 meV, which can in no way be considered infinitesimal.

Although the magnetic fields used in our experiments were considerably weaker than 10 T, we note that our samples were considerably closer to the metal-insulator transition than the samples investigated in Ref. 11, for which both the tunneling and activation contributions to the hopping probability were small. Therefore, we can assume that the squeezing out of valleys with large values of $g$ begins to manifest itself in these samples at weaker magnetic fields. Finally, we note a possible role for the region of spatially overlapping contributions from individual valleys, which we ignored in our calculations. Since for hopping centers that belong to this region the probabilities for hopping by way of the individual valleys are summed, the contributions of valleys with smaller values of $g$ will be emphasized in this case as well. These facts at least allow us to explain the anisotropy observed in the range where the activation energy depends linearly on $H$.

## 5. CONCLUSIONS

Our experiments and their analysis demonstrate that in moderately doped germanium in the temperature range from 1.7 to 10 K the dominant conductivity mechanism is hopping by carriers activated to the $D^-$ band. The primary indicator of this conductivity is an exponential positive magnetoresistance caused by the increase in the corresponding activation energy associated with the need for one of the electrons that makes up a $D^-$ center to have its spin directed opposite to the field. We have discussed distinctive features, which were connected with anisotropy of the $g$-factor for the individual valleys, of the way this mechanism manifests itself in multivalley materials.

This work was carried out with the support of the Russian Fund for Fundamental Research from Projects 97-02-18280a and 98-02-18396, and also the INTAS-RFFR fund, Project 95-0553.

[1] N. F. Mott and G. A. Davis, *Electronic Processes in Non-Crystalline Materials* (Oxford, 1979).
[2] E. M. Gershenson, A. P. Mel'nikov, and R. I. Rabinovich, in *Electron-Electron Interactions in Disordered Systems*, A. L. Efros and M. Pollak, Eds. (North-Holland, Amsterdam, 1985), p. 483.
[3] H. Nishimura, Phys. Rev. A **138**, 815 (1965).
[4] M. L. Knotek, Phys. Rev. B **16**, 2629 (1977).
[5] A. G. Andreev, A. G. Zabrodskiy, I. P. Zvyagin, and S. V. Egorov, Fiz. Tekh. Poluprovodn. **31**, 1174 (1997) [Semiconductors **31**, 1050 (1997)].
[6] A. Kurobe and H. Kamimura, J. Phys. Soc. Jpn. **51**, 1904 (1982).
[7] N. V. Agrinskaya, V. I. Kozub, R. Rench, M. Li, and P. Fozoli, Zh. Éksp. Teor. Fiz. **111**, 1477 (1997) [JETP **84**, 814 (1997)].
[8] N. V. Agrinskaya and V. I. Kozub, Solid State Commun. **108**, 355 (1998).
[9] C. Yamanouchi, J. Phys. Soc. Jpn. **18**, 1775 (1963).
[10] A. L. Efros and B. I. Shklovskii, *Electronic Properties of Doped Semiconductors* (Springer-Verlag, 1984).
[11] J. A. Chroboczek, E. W. Prohovsky, and R. J. Sladek, Phys. Rev. **169**, 593 (1968).
[12] A. G. Samoilovich, I. V. Dakhovskiy, D. I. Levinzon, Yu. I. Sterlikov, and V. A. Shershel', Fiz. Tekh. Poluprovodn. **1**, 1007 (1967) [Sov. Phys. Semicond. **1**, 842 (1967)].
[13] K. Sugiyama, J. Phys. Soc. Jpn. **22**, 109 (1967).

Translated by Frank J. Crowne

# Hot-carrier far infrared emission in silicon

L. A. Kosyachenko* and M. P. Mazur

*Chernovtsy State University, 274012 Chernovtsy, Ukraine*
(Submitted March 16, 1998; accepted for publication August 6, 1998)
Fiz. Tekh. Poluprovodn. **33**, 170–173 (February 1999)

This paper describes studies of hot electroluminescence from silicon transistor structures in the photon energy range 0.25 to 0.8 eV. The transistor structures $n-p-n$ and $p-n-p$ used to obtain the emission spectra generated at accelerating voltages low enough that only one kind of carrier was involved in the excitation. Participation of hot carriers both in direct intersubband and indirect intraband radiative transitions is discussed. © *1999 American Institute of Physics.* [S1063-7826(99)00402-0]

## 1. INTRODUCTION

A rather large number of papers have been written about hot electroluminescence in silicon diodes, starting in the 1950s,[1,2] when it was shown that this phenomenon is due to high-energy charge carriers excited by the strong electric field in the barrier structure. In addition to a recombination band with a maximum in the range of photon energies $h\nu$ close to the width of the band gap of the semiconductor $E_g \cong 1.1$ eV (which can be viewed as a consequence of collisional ionization of atoms), the electroluminescence spectrum also exhibits wideband emission in the range 1 to 3 eV. There are different opinions regarding the mechanism for this component of the electroluminescence: many authors explain it by starting from the model proposed in Ref. 3, according to which optical emission is generated by the braking of hot carriers at a charged center, while others base their explanation on a model of direct radiative transitions of carriers between different subbands of the conduction or valence band (intersubband transitions),[4] or on a model of indirect transitions within the same subband with the participation of phonons.[5] This ambiguity has never been completely resolved, even in a series of studies that appeared at the end of the 1980s.[6–10] The principal difficulty is that both direct intersubband and indirect intraband transitions (including bremsstrahlung) lead to emission spectra with the same shape, namely, a monotonic decrease with increasing $h\nu$. Another complication is the fact that hot electroluminescence is observed at high excitation voltages, where avalanche processes develop and carriers of both signs participate in generating the radiation. Finally, the emission spectra presented in the literature lie in the range $h\nu > E_g$, where they are distorted by self-absorption.

In this paper we report the results of an experimental study of hot electroluminescence by silicon $p-n$ junctions in the range $h\nu < E_g$. The bipolar transistor structures were used to obtain emission spectra in the range of $h\nu$ from $<0.8$ eV down to 0.25 to 0.3 eV (1.5 to 5 $\mu$m), since they give rise to accelerating biases so low that only one kind of carrier—electrons or holes—can take part in generating the radiation. The parameters of these structures, which are listed below, were chosen so that no quantum-well effects appear in the observed electroluminescence. Their use leads to generation of high-power emission in the required spectral range, but with a characteristic dependence of the emission spectra on the concentration and doping profile of the structure, along with a pronounced threshold dependence for the emission power versus current.[11,12]

## 2. SAMPLES AND EXPERIMENTAL METHOD

Our measurements were made on microwave $n-p-n$ and $p-n-p$ transistors with the same topology and construction (an opening was cut in the ceramic package in order to extract radiation). In microwave transistors, the base is made as thin as possible (in this case, about 1 $\mu$m); therefore, because of the voltage drop across the base, current flows primarily along the periphery of the emitter (the so-called emitter leakage current effect) which is not shadowed by the metal electrode.[13] Since the base is rather strongly doped ($\sim 10^{17}$ cm$^{-3}$), and since the emitter is even more strongly doped ($10^{19}-10^{20}$ cm$^{-3}$ or higher for an emitter layer thickness of 1.5 to 2 $\mu$m), the electric field intensity in the $p-n$ junction of the reverse-biased emitter turns out to be higher than $10^5$ V/cm. Thus, by switching on the microwave transistor backwards (i.e., with the collector junction in forward bias and the emitter junction in reverse bias) we create favorable conditions both for excitation of hot carriers and emission of radiation from the device. Once these carriers are injected from the collector through the base into the emitter junction, they are accelerated by the high electric field there and generate light. In this arrangement we can obtain sizeable hot-carrier fluxes (electrons or holes in $n-p-n$- or $p-n-p$-structures, respectively), due to an increased injection current that nevertheless does not cause electrical breakdown of the $p-n$ junction. The radiation generated includes visible light, which is perceived by the eye as a band encircling the emitter region. The spectrum contains a relatively narrow band with a maximum near 1.1 eV, caused by interband recombination of hot carriers in the base.[14,15] In the range $h\nu \lesssim 0.8$ eV of interest to us, the contribution from this band is negligible compared to a wideband structureless

 

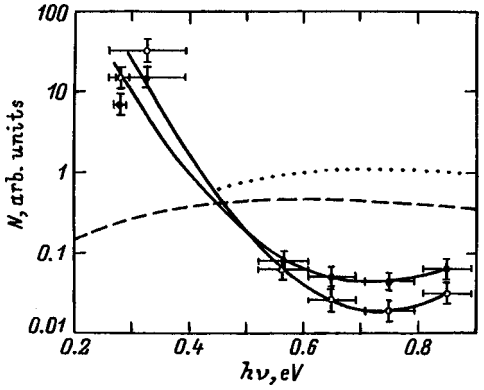


FIG. 1. Spectral distribution of the number of photons $N(h\nu)$ radiated by $n-p-n$ and $p-n-p$ transistors (the filled and empty circles, respectively) for an accelerating voltage of 4 V and injected current of 100 mA. The dashed and dotted curves are spectral distributions for the radiative electron intersubband transition rate, calculated in Refs. 9 and 10, respectively.

emission which for strong carrier heating (large accelerating voltages across the emitter $p-n$ junction) can extend up to $h\nu=3.5$–4 eV.

Measurements in the range $h\nu\lesssim 0.8$ eV are complicated by the low sensitivity of available photodetectors. A cooled PbS photoresistor in combination with a DMR-4 prism monochromator will not allow us to record photons with energies below 0.5–0.6 eV. The sensitivity spectrum of a cooled PbSe photoresistor extends down to $h\nu=0.2$–0.25 eV, but its detection capability is more than an order of magnitude lower than that of a PbS photoresistor. Therefore, in the range $h\nu<0.6$ eV we used PbSe photoresistors combined with filters—single-crystal films of CdSb with multilayer coatings made of ZnS, SiO, and Ge. These ''photoresistor-filter'' pairs were calibrated with respect to wavelength by an IR spectrophotometer, and with respect to sensitivity by a ribbon nickel emitter with known color temperature (1150 K), whose emissivity differed from that of an absolute blackbody by no more than 10–20% in the spectral range under study. The transistor was fed by rectangular voltage pulses with an off-duty factor equal to 2. Standard synchronous detection was used to record the signal, thereby ensuring a suitable ''signal-to-noise'' ratio.

### 3. EXPERIMENTAL RESULTS AND DISCUSSION

Figure 1 shows emission spectra from $n-p-n$- and $p-n-p$ transistors for which the current in the emitter junction was 100 mA and the accelerating voltage was 4 V. Judging by the behavior of photocurrents excited by external illumination,[15] this accelerating voltage gives rise to virtually no carrier multiplication; hence, we may assume that light is generated only by hot electrons in the $n-p-n$- transistor, and only by hot holes in the $p-n-p$-transistor. Of course, hot carriers of the opposite sign (minority carriers in the emitter) are injected into the base under these circumstances; however, at these low voltages, when collisional ionization does not occur ($\lesssim 4$ V), their fluxes are many orders of magnitude lower than the hot-carrier current injected into the emitter.

It is clear from Fig. 1 that the emission spectra of $n-p-n$- and $p-n-p$ structures are similar in shape, consisting of functions that are monotonically decreasing with increasing $h\nu$ (the increase that is just beginning to show for $h\nu>0.8$ eV is caused by the recombination in the base we mentioned above, and the somewhat lower position of the point $h\nu\approx 0.28$ eV is due to the fact that the transmission band of the filter used overlaps somewhat with an absorption line of $CO_2$ in the atmosphere). Figure 1 also shows the emission spectrum of silicon calculated in Ref. 9 (the dashed curve) for direct intersubband transitions with strict inclusion of the energy structure of the bands under the assumption of a Boltzmann energy distribution $\exp(-E/kT_c)$ with a carrier temperature $T_c=1500$ K. The detailed calculations of Ref. 10 showed that if we assume indirect intraband transitions via scattering by phonons or isolated impurities it is impossible to explain the falloff in the emission in the range $h\nu<0.8$ to 1 eV shown on the experimental curves from Refs. 4 and 8. This falloff is obtained if we postulate a decisive role for direct intersubband transitions, and also replace the Boltzmann carrier energy distribution by a Gaussian distribution of the form $\exp(AE-BE^2)$, where $A$ and $B$ are positive constants (the dashed curve in Fig. 1). Our experimental data, shown in Fig. 1, indicate that there is no maximum in the emission in the range $h\nu=0.5$–0.8 eV, which is characteristic of direct intersubband transitions of carriers. It is worth noting, however, that the maxima exhibited by the experimental curves in Refs. 8 and 9 lie at the long-wavelength edge of the sensitivity spectrum of the Pbs- and Ge- photoresistors used in these papers (the former in Ref. 8, the latter in Ref. 9). The sensitivity of the PbSe photoresistor we used in the range 0.25–0.6 eV is sufficiently uniform that it can ensure smaller errors in the measurements.

For this regime of excitation, the effective electrical power generated excludes significant heating of a transistor placed on a radiative heat sink (the maximum achievable emitter current for devices of this type is 1 A). The effect of heating is also lessened by the fact that the synchronous detection system used by us does not record the dc component of the signal. However, the temperature of the emitter $p-n$ junction itself and the regions immediately adjacent to it can be pulsed, leading to higher values as the frequency of the excitation pulses is decreased. With this in mind, we measured the dependence of the recorded signal on the pulse frequency, using a very long-wavelength optical filter to separate out the longest wavelengths in the emission range of interest (3.8–4.4 $\mu$m), which are obviously most subject to the influence of thermal radiation. In Fig. 2a we plot these dependences for various values of the emitter current. It is clear that as the pulse frequency $f$ increases from 20 to 1000 Hz, the signal recorded at the highest current decreases by almost an order of magnitude, whereas for a current of 100 mA it is only slightly dependent on frequency (the sensitivity of the PbSe photodetector in this frequency range is constant). This is naturally explained by the fact that at high excitation currents thermal radiation makes a significant contribution to the recorded signal; moreover, at low frequencies its role is decisive (note the almost horizontal portions of the

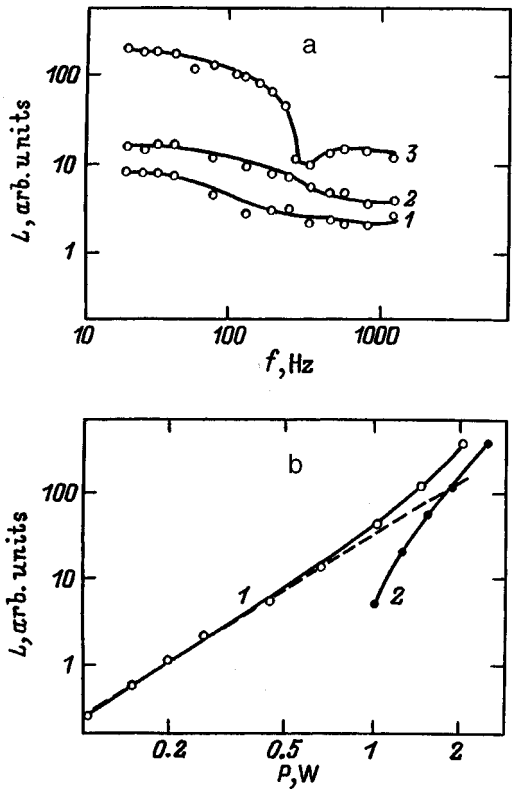


FIG. 2. Dependence of the value of the detected signal $L$: a — on frequency $f$ for currents in a reverse-biased $p-n$ junction. $I$, A: *1*—0.1, *2*—0.2, *3*—0.4; b—on the power $P$ drawn by the transistor at constant accelerating voltage (4 V) and variable current (curve *1*), and also a constant current (0.5 A) and variable accelerating voltage (curve *2*).

curves in the frequency range $f<40-50$ Hz). However, as the frequency increases, thermal emission ceases to ''keep up'' with the current pulses and ultimately its contribution to the signal detected becomes negligible compared to the electroluminescence emission, which is characterized by high speed (the horizontal portions at frequencies $f>400-500$ Hz). For low excitation currents, when the thermal emission is insignificant, the signal should not depend on the repetition rate of the pulses, which is observed in the experiments. The correctness of this interpretation of the frequency dependences is confirmed by the fact that for large excitation currents, as we go from low frequencies to high frequencies, the phase of the synchronous detector changes (at a certain frequency, the ratio of phases is such that signals excited by electroluminescence and thermal radiation mutually compensate one another, which causes the ''dip'' in the uppermost curve in Fig. 2a).

Thus, the data shown in Fig. 2a indicate that for excitation currents of the order of 100 mA thermal emission makes a negligible contribution to the detected signal over the entire band of signal modulation frequencies (20–1000 Hz), and is negligible at frequencies higher than roughly 400 Hz for currents of 0.6 to 0.8 A.

This conclusion is corroborated by the observed dependence of the emission intensity $L$ on the electric power drawn by the transistor $P$. Figure 2b shows these dependences for a pulse repetition rate of 33 Hz. Curve *1* is plotted at constant accelerating voltage and variable injection current. In this case the intensity of the electroluminescence obviously should depend linearly on current (which in our case means that for a constant accelerating voltage it should also depend linearly on $P$), which is observed experimentally for $P<0.5$-0.6 W. If, however, the power drawn by the transistor varies for a constant injection current but increasing accelerating voltage, we obtain the function $L(P)$ shown by curve *2*. If the recorded emission were thermal, the functions $L(P)$ would be identical for this and the other case. In fact, however, curves *1* and *2* differ significantly at small $P$, and only merge at large $P$, as we might expect, since in this case, according to the data of Fig. 2a, the contribution of thermal emission is important.

Thus, these measurements show that the thermal emission does not give rise to any appreciable distortion to the measured spectra shown in Fig. 1. The monotonic character of the spectral dependence of the rate of radiative electronic transitions casts doubt on the model of direct intersubband transitions,[9,10] and argues in favor of indirect transitions as the dominant mechanism for electroluminescence of these silicon structures.

In light of the strong emitter doping, we should probably assign an important role to scattering by ionized impurities rather than just phonons. Intraband radiative transitions are inverse processes to absorption of a photon by a free carrier. The cross section for absorption via scattering by charge impurities is a stronger function of the value of $h\nu$ (proportional to $h\nu^{-7/2}$ for a simple band) than the cross section for scattering via the deformation potential (proportional to $h\nu^{-3/2}$; see Ref. 16). Therefore, as the energy $h\nu$ decreases, the role of bremsstrahlung increases, which probably can give rise to the more abrupt increase in the radiative intensity observed in the region $h\nu<0.6$ eV.

In conclusion, we note that for direct transitions between light- and heavy-hole subbands the theory predicts a maximum in the emission spectrum of silicon located at the very edge of the spectral region we are studying ($\sim$0.3 eV; see Ref. 9). However, the similar characters of the spectral curves obtained for $n-p-n$- and $p-n-p$-structures, and also the similar quantum efficiencies for radiation in both cases, indicate that our conclusions regarding the emission mechanism apply not only to electrons but to holes as well.

## 4. CONCLUSION

By using bipolar transistor structures we were able to study hot electroluminescence of silicon in the photon energy range 0.25–0.8 eV at low accelerating voltages, when collisional ionization is not operating and only one kind of carrier participates in generating the light. Both for electrons and for holes, the emission spectra obtained consist of monotonically decreasing functions as the photon energy increases, which disagrees with the results of theories involving direct intersubband electronic transitions (which lead to a maximum in the range 0.5–0.8 eV) and agrees with the model of indirect intraband transitions with participation of phonons or impurities.

We are deeply grateful to S. M. Kulikovskaya for help in carrying out these experiments.

*E-mail: lakos@unicom.chernovtsy.ua

[1] R. Newmann, Phys. Rev. **100**, 700 (1955).
[2] A. G. Chynoweth and K. G. Mckay, Phys. Rev. **102**, 369 (1956).
[3] T. Figielski and A. Torun, in *Proceedings Int. Conf. Phys. Semicond.* (Exeter, UK, 1962), p. 853.
[4] W. Haeker, Solid State Phys., Adv. Res. Appl. **25**, 301 (1974).
[5] L. A. Kosyachenko, E. F. Kukhto, and V. M. Sklyarchuk, Fiz. Tekh. Poluprovodn. **18**, 426 (1984) [Sov. Phys. Semicond. **18**, 266 (1984)].
[6] A. Toriumi, M. Yoshimi, M. Iwose, Y. Akijama, and K. Taniguchi, IEEE Trans. Electron Devices **34**, 1501 (1987).
[7] M. Herzog and F. Koch, Appl. Phys. Lett. **53**, 2620 (1988).
[8] N. C. Dass and B. M. Arora, Appl. Phys. Lett. **56**, 1152 (1990).
[9] L. Carbone, R. Brunetti, C. Jacoboni, A. Lacaita, and M. Fishetti, Semicond. Sci. Technol. **9**, 674 (1994).
[10] J. Bude, N. Sano, and A. Yoshi, Phys. Rev. B **45**, 5848 (1992).
[11] N. T. Bagraev, L. E. Klyachkin, and E. I. Chaĭkina, JETP Lett. **58**, 598 (1993).
[12] N. T. Bagraev, E. V. Vladimirskaya, V. E. Gasumyants, V. I. Kaĭdanov, V. V. Kveder, L. E. Klyachkin, A. M. Malyarenko, and E. I. Chaĭkina, Fiz. Tekh. Poluprovodn. **29**, 2133 (1995) [Semiconductors **29**, 1112 (1995)].
[13] S. Sze, *Physics of Semiconductor devices* (Mir, Moscow, 1984).
[14] L. A. Kosyachenko, E. F. Kukhto, and V. M. Sklyarchuk, Pis'ma Zh. Tekh. Fiz. **11**, 1437 (1985) [Sov. Tech. Phys. Lett. **11**, 593 (1985)].
[15] L. A. Kosyachenko, M. P. Mazur, and V. M. Sklyarchuk, Ukr. Fiz. Zh. **42**, 846 (1997).
[16] K. Seeger, *Semiconductor Physics* (Mir, Moscow, 1977).

Translated by Frank J. Crowne

## SEMICONDUCTOR STRUCTURES, INTERFACES AND SURFACES

# Bragg reflectors for cylindrical waves

V. V. Nikolaev, G. S. Sokolovskiĭ, and M. A. Kaliteevskiĭ

*A. F. Ioffe Physicotechnical Institute, Russian Academy of Sciences, 194021 St. Petersburg, Russia*
(Submitted June 6, 1998; accepted for publication June 7, 1998)
Fiz. Tekh. Poluprovodn. **33**, 174–179 (February 1999)

A transfer-matrix method has been developed for cylindrical waves. Expressions are obtained for reflection and transmission coefficients of cylindrical light waves by an isolated cylindrical boundary that separates two media and a cylindrical layered medium. A construction is proposed for optimized ''Bragg'' reflectors for cylindrical waves and the properties of these reflectors are investigated. © *1999 American Institute of Physics.* [S1063-7826(99)00502-5]

### 1. INTRODUCTION

Bragg reflectors,[1] i.e., periodic sequences of pairs of quarter-wave layers, are part of the various optoelectronic devices, e.g., vertical-emission lasers.[2] A further example of the use of Bragg reflectors is in distributed-feedback lasers, where a diffraction grating serves as the Bragg reflector for a waveguide mode.[3]

When the index of refraction of the medium is periodically modulated, the propagation of photons is forbidden in a certain range of frequencies (for the Bragg reflector this region corresponds to the reflection band).[4] In these constructions, Bragg reflectors localize light in one direction, i.e., they act like a material with a one-dimensional photon band gap.

In recent years there has been a steady increase in interest in materials with two-dimensional photon band gaps, for example, two-dimensional photonic crystals of honeycomb type.[5]

Cylindrical coaxial structures, in which the index of refraction of the medium is varied periodically as a function of distance from the axis of symmetry of the system (Fig. 1) make up an alternative and promising class of structures that ensure two-dimensional confinement of an optical field.

In order to describe the propagation of light in a linear layered medium it is convenient to use the transfer matrix method.[6]

Our task was to develop a transfer matrix method for cylindrical waves that propagate in media with cylindrical symmetry [which we will henceforth refer to as cylindrical layered media (see Fig. 1)], find parameters of the structures that most efficently reflect cylindrical waves, and study the properties of these structures.

Interest in describing the propagation of light in cylindrical systems is motivated by, among other things, problems in generating nondiverging Bessel beams[7] and calculating mode structures for a cylindrical laser.[8]

### 2. BASIC EQUATIONS

#### 2.1. Transfer matrix for a basis formed by the components of electric and magnetic field tangential to a boundary between media

We start with Maxwell's equations for a monochromatic wave

$$\nabla\times\mathbf{E}=i\mu\frac{\omega}{c}\mathbf{H}, \tag{1}$$

$$\nabla\times\mathbf{H}=-i\varepsilon\frac{\omega}{c}\mathbf{E}. \tag{2}$$

In a cylindrical coordinate system Eq. (1) can be expanded into three equations

$$\frac{1}{\rho}\frac{\partial E_z}{\partial\varphi}-\frac{\partial E_\varphi}{\partial z}=i\mu\frac{\omega}{c}H_\rho, \tag{3a}$$

$$\frac{\partial E_\rho}{\partial z}-\frac{\partial E_z}{\partial\rho}=i\mu\frac{\omega}{c}H_\varphi, \tag{3b}$$

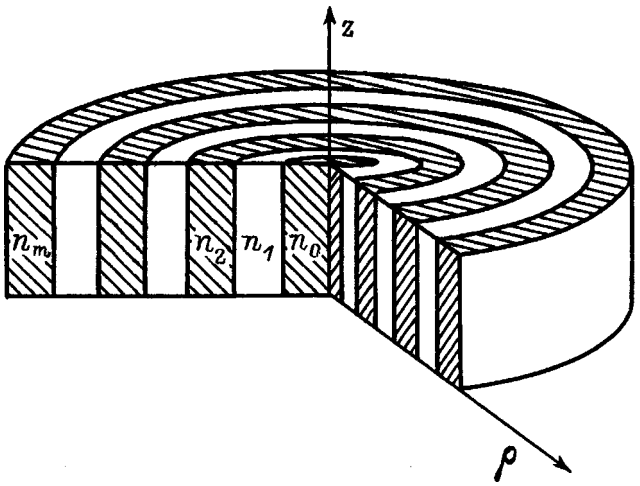


FIG. 1. Sketch of the structure.

 

$$\frac{1}{\rho}\left[\frac{\partial(\rho E_\varphi)}{\partial\rho}-\frac{\partial E_\rho}{\partial\varphi}\right]=i\mu\frac{\omega}{c}H_z, \tag{3c}$$

and Eq. (2) can also be expanded into three equations

$$\frac{1}{\rho}\frac{\partial H_z}{\partial\varphi}-\frac{\partial H_\varphi}{\partial z}=-i\varepsilon\frac{\omega}{c}E_\rho, \tag{4a}$$

$$\frac{\partial H_\rho}{\partial z}-\frac{\partial H_z}{\partial\rho}=-i\varepsilon\frac{\omega}{c}E_\varphi, \tag{4b}$$

$$\frac{1}{\rho}\left[\frac{\partial(\rho H_\varphi)}{\partial\rho}-\frac{\partial H_\rho}{\partial\varphi}\right]=-i\varepsilon\frac{\omega}{c}E_z. \tag{4c}$$

Consider the layered cylindrical coaxial system shown in Fig. 1. We will describe the propagation of cylindrical waves in this medium as either diverging from the point $\rho=0$ or converging to it with respect to the normal to the symmetry axis of the system $z$. This implies that the derivative $\partial/\partial z=0$. Equation (3) in this case takes the form

$$\frac{1}{\rho}\frac{\partial E_z}{\partial\varphi}=i\mu\frac{\omega}{c}H_\rho, \tag{5a}$$

$$\frac{\partial E_z}{\partial\rho}=-i\mu\frac{\omega}{c}H_\varphi, \tag{5b}$$

$$\frac{1}{\rho}\left[\frac{\partial(\rho E_\varphi)}{\partial\rho}-\frac{\partial E_\rho}{\partial\varphi}\right]=i\mu\frac{\omega}{c}H_z, \tag{5c}$$

and Eq. (4) will have the form

$$\frac{1}{\rho}\frac{\partial H_z}{\partial\varphi}=-i\varepsilon\frac{\omega}{c}E_\rho, \tag{6a}$$

$$\frac{\partial H_z}{\partial\rho}=i\varepsilon\frac{\omega}{c}E_\varphi, \tag{6b}$$

$$\frac{1}{\rho}\left[\frac{\partial(\rho H_\varphi)}{\partial\rho}-\frac{\partial E_\rho}{\partial\varphi}\right]=-i\varepsilon\frac{\omega}{c}E_z. \tag{6c}$$

Arbitrarily polarized cylindrical waves can be separated into waves with either the electric vector **E** ($E$-type waves) or the magnetic vector **H** ($H$-type waves) parallel to the symmetry axis. This is clear from the fact that the field components ($E_z$, $H_\varphi$, $H_\rho$) and ($H_z$, $E_\varphi$, $E_\rho$) enter into Eqs. (5) and (6) independently, and the independence of the boundary conditions for tangential and normal components of the field at the surface separating the cylindrical layers.

Let us consider the case of $E$-polarization, i.e., $E_\rho=0$, $E_\varphi=0$. (The results for $H$ polarization are obtained from those for $E$-polarization in accordance with the substitution rule of Ref. 6, i.e., replacement of the electric field by the magnetic field with simultaneous replacement of $\varepsilon$ by $-\mu$.) For this case, the electromagnetic field is described by the set of components ($E_z$, $H_\varphi$, $H_\rho$), which are interrelated by the system of equations:

$$\frac{\partial E_z}{\partial\varphi}=i\mu\frac{\omega}{c}\rho H_\rho, \tag{7a}$$

$$\frac{\partial E_z}{\partial\rho}=-i\mu\frac{\omega}{c}H_\varphi, \tag{7b}$$

$$\frac{\partial(\rho H_\varphi)}{\partial\rho}-\frac{\partial H_\rho}{\partial\varphi}=-i\varepsilon\frac{\omega}{c}\rho E_z. \tag{7c}$$

Eliminating $H_\varphi$ and $H_\rho$ from Eq. (7), we obtain the equation for $E_z$:

$$\rho\frac{\partial}{\partial\rho}\rho\frac{\partial E_z}{\partial\rho}+\frac{\partial^2E_z}{\partial\varphi^2}-\rho^2\frac{1}{\mu}\frac{\partial\mu}{\partial\rho}\frac{\partial E_z}{\partial\rho}+\varepsilon\mu\frac{\omega^2}{c^2}\rho^2E_z=0. \tag{8}$$

Equation (8) can be solved by separation of variables. Setting $E_z=V(\rho)\Phi(\varphi)$ and substituting into Eq. (8), and also taking into account the single-valuedness of the function $E_z(\varphi)$ along with Eq. (7), we obtain the fields in the form

$$E_z=V(\rho)\exp(im\varphi), \tag{9a}$$

$$H_\rho=\frac{m}{\mu}\frac{c}{\omega}\frac{V(\rho)}{\rho}\exp(im\varphi), \tag{9b}$$

$$H_\varphi=U(\rho)\exp(im\varphi), \tag{9c}$$

where $m$ is an integer, and $U(\rho)$ is a certain function that is linearly independent of $V(\rho)$.

It is clear that for $m\neq0$ the component of magnetic field $H_\rho$ will be nonzero. This implies that for modes with nonzero value of angular momentum $m$ we must add to the energy flux in the radial direction a circulating energy flux that propagates around the structure.

Substituting Eqs. (9) into Eq. (7), we obtain a system of two linear differential equations with respect to $V$ and $U$:

$$\frac{\partial V}{\partial\rho}=-i\mu\frac{\omega}{c}U, \tag{10a}$$

$$\frac{\partial(\rho U)}{\partial\rho}=-i\frac{1}{\mu}\frac{c}{\omega}\frac{1}{\rho}\left[n^2\frac{\omega^2}{c^2}\rho^2-m^2\right]V. \tag{10b}$$

From the system (10) we obtain two second-order equations for the functions $V$ and $U$:

$$\rho\frac{\partial}{\partial\rho}\left[\rho\frac{\partial V}{\partial\rho}\right]+\left[\frac{\omega^2}{c^2}n^2\rho^2-m^2\right]V=0, \tag{11a}$$

$$\rho\frac{\partial^2}{\partial\rho^2}(\rho U)+\left[\frac{\omega^2}{c^2}n^2\rho^2-m^2\right]U=0. \tag{11b}$$

Since the functions $V$ and $U$ satisfy linear differential equations of second order, each of them can be written in the form of a linear combination of two partial solutions, e.g., $V_1$, $V_2$ and $U_1$, $U_2$. Let us consider the solution of Eq. (11) with the following values specified at a certain point $\rho_0$:

$$\begin{pmatrix}V_1(\rho_0)\\U_1(\rho_0)\end{pmatrix}=\begin{pmatrix}1\\0\end{pmatrix}, \tag{12a}$$

$$\begin{pmatrix}V_2(\rho_0)\\U_2(\rho_0)\end{pmatrix}=\begin{pmatrix}0\\1\end{pmatrix}. \tag{12b}$$

In order to obtain values of the functions $(U,V)$ at an arbitrary point $\rho$ it is sufficient to multiply the matrix consisting of the solutions (12) by a column of initial values at the point $\rho_0$,:

$$\begin{pmatrix} V(\rho) \\ U(\rho) \end{pmatrix} = \hat{M} \begin{pmatrix} V(\rho_0) \\ U(\rho_0) \end{pmatrix}, \tag{13}$$

where $\hat{M}$ is the transfer matrix through a uniform layer from point $\rho_0$ to $\rho$:

$$\hat{M} = \begin{pmatrix} V_1 V_2 \\ U_1 U_2 \end{pmatrix}. \tag{14}$$

Let us find the transfer matrix through a cylindrical layer with a constant refractive index. The solution of Eq. (11) that satisfies relations (10) has the form

$$V = AJ_m(k\rho) + BY_m(k\rho), \tag{15a}$$

$$U = ip[AJ'_m(k\rho) + BY'_m(k\rho)], \tag{15b}$$

where $J_m$ and $Y_m$ are cylindrical Bessel and Weber functions, respectively; $k = \sqrt{\varepsilon\mu}(\omega/c)$, $p = \sqrt{\varepsilon/\mu}$, and $A$ and $B$ are certain constants. We note that the sign of the derivative denotes differentiation with respect to the entire argument of the function, and not just with respect to $\rho$.

Using the identity $J_m(x)Y'_m(x) + J'_m(x)Y_m(x) = 2/\pi x$, we obtain expressions for the functions $U$ and $V$ that satisfy relation (12). These solutions are elements of the transfer matrix:

$$M_{11} = \frac{\pi}{2} k\rho_0 [Y'_m(k\rho_0)J_m(k\rho) - J'_m(k\rho_0)Y_m(k\rho)],$$

$$M_{21} = i\frac{\pi}{2} kp\rho_0 [Y'_m(k\rho_0)J'_m(k\rho) - J'_m(k\rho_0)Y'_m(k\rho)],$$

$$M_{22} = \frac{\pi}{2} k\rho_0 [J_m(k\rho_0)Y'_m(k\rho) - Y_m(k\rho_0)J'_m(k\rho)],$$

$$M_{12} = -i\frac{\pi}{2}\frac{k}{p}\rho_0 [J_m(k\rho_0)Y_m(k\rho) - Y_m(k\rho_0)J_m(k\rho)]. \tag{16}$$

The transfer matrix for $H$-polarized waves has an analogous form for $p = \sqrt{\mu/\varepsilon}$.

The determinant of the transfer matrix for both cases is determined by the ratio of the initial to final radii:

$$|\hat{M}| = \rho_0/\rho, \tag{17}$$

which illustrates the conservation of total energy transported by a cylindrical wave whose amplitude decreases with increasing radius.

The transfer matrix through a layered structure gives transfer matrix products of each uniform layer. This follows from the continuity of the field components $E_z$, $H_\varphi$ at cylindrical surfaces between uniform layers. Because of this circumstance, the determinant of the transfer matrix through a layered structure will equal the ratio of initial and final radii of the entire structure.

### 2.2. Transfer matrix in a traveling-wave basis

It is often convenient to consider the field within a structure as a sum of waves traveling in opposite directions. A field that possesses cylindrical symmetry must be treated as a superposition of diverging and converging waves. A monochromatic cylindrical wave propagating in the direction of increasing $\rho$ has the following form for the case of $E$-polarization:

$$\begin{cases} E_z = AH_m^{(1)}(k\rho)\exp(im\varphi) \\ H_\varphi = ipAH_m^{(1)\prime}(k\rho)\exp(im\varphi) \end{cases}, \tag{18}$$

where $H_m^{(1)}$ is a Hankel function of the first kind. A converging wave is given by replacing the Hankel functions of the first kind by functions of the second kind:

$$\begin{cases} E_z = AH_m^{(2)}(k\rho)\exp(im\varphi) \\ H_\varphi = ipAH_m^{(2)\prime}(k\rho)\exp(im\varphi) \end{cases}. \tag{19}$$

Denoting the amplitudes of the electric field for diverging and converging waves as $E^+$ and $E^-$, respectively, we can write

$$E_z = E^+ + E^-, \tag{20a}$$

$$H_\varphi = ip[C_m^{(1)}E^+ + C_m^{(2)}E^-], \tag{20b}$$

where $C_m^{(1,2)} = H_m^{(1,2)\prime}(k\rho)/H_m^{(1,2)}(k\rho)$. Where necessary, we will label a given layer with a second subscript: $C_{ml}^{(1,2)} = H_m^{(1,2)\prime}(k_l\rho)/H_m^{(1,2)}(k_l\rho)$. Transforming from the $(E^-, E^+)$ to the $(E_z, H_\varphi)$ basis, we can write in matrix form

$$\begin{pmatrix} E_z \\ H_\varphi \end{pmatrix} = \hat{W} \begin{pmatrix} E^+ \\ E^- \end{pmatrix}, \tag{21}$$

where the transformation matrix is

$$\hat{W} = \begin{pmatrix} 1 & 1 \\ ipC_m^{(1)} & ipC_m^{(2)} \end{pmatrix}.$$

The determinant of the transformation matrix is

$$|\hat{W}| = \frac{4}{\pi}\frac{1}{k_0\rho}\frac{1}{H_m^{(1)}(k\rho)H_m^{(2)}(k\rho)}. \tag{22}$$

The matrix of the inverse transformation is given by the expression

$$\hat{W}^{-1} = \frac{\pi}{4} k_0\rho H_m^{(1)}(k\rho)H_m^{(2)}(k\rho) \begin{pmatrix} ipC_m^{(2)} & -1 \\ -ipC_m^{(1)} & 1 \end{pmatrix}. \tag{23}$$

Let us consider how the field transforms when we pass through a boundary between two uniform concentric layers. The traveling-wave amplitude will change due to reflection from the boundary. The condition for continuity of the tangential components of the field at the boundary is written in the form

$$\hat{W}_1 \begin{pmatrix} E_1^+ \\ E_1^- \end{pmatrix} = \hat{W}_2 \begin{pmatrix} E_2^+ \\ E_2^- \end{pmatrix}. \tag{24}$$

It thus follows

$$\begin{pmatrix} E_2^+ \\ E_2^- \end{pmatrix} = \hat{W}_2^{-1} \times \hat{W}_1 \begin{pmatrix} E_2^+ \\ E_2^- \end{pmatrix}. \tag{25}$$

Thus, the transfer matrix through the boundary separating the first and second layers $\hat{N}$ is a product of the direct and inverse transformation matrices $\hat{N}=\hat{W}_2^{-1}\times\hat{W}_1$, with components

$$N_{11}=i\frac{\pi}{4}k_0\rho H_m^{(1)}(k_2\rho)H_m^{(2)}(k_2\rho)[p_2C_{m1}^{(2)}-p_1C_{m2}^{(1)}],$$

$$N_{21}=i\frac{\pi}{4}k_0\rho H_m^{(1)}(k_2\rho)H_m^{(2)}(k_2\rho)[p_1C_{m1}^{(1)}-p_2C_{m2}^{(1)}],$$

$$N_{12}=i\frac{\pi}{4}k_0\rho H_m^{(1)}(k_2\rho)H_m^{(2)}(k_2\rho)[p_2C_{m2}^{(2)}-p_1C_{m1}^{(2)}],$$

$$N_{22}=i\frac{\pi}{4}k_0\rho H_m^{(1)}(k_2\rho)H_m^{(2)}(k_2\rho)[p_1C_{m1}^{(2)}-p_2C_{m2}^{(1)}]. \tag{26}$$

The transfer matrix through a uniform layer from $\rho_0$ to $\rho$ will obviously have the form

$$\hat{T}=\begin{pmatrix} \dfrac{H_m^{(1)}(k\rho)}{H_m^{(1)}(k\rho_0)} & 0 \\ 0 & \dfrac{H_m^{(2)}(k\rho)}{H_m^{(2)}(k\rho_0)} \end{pmatrix}. \tag{27}$$

### 2.3. Reflection and transmission coefficients for cylindrical surfaces

Let us consider the arrival of a diverging wave on a cylindrical boundary between medium 1 and medium 2. The amplitudes of the incident, reflected, and transmitted waves—1, $r_d$ and $t_d$, respectively—are related by

$$\begin{pmatrix} 1 \\ r_d \end{pmatrix}=\hat{N}\begin{pmatrix} t_d \\ 0 \end{pmatrix}, \tag{28}$$

where $\hat{N}$ is the transfer matrix from the second medium to the first. The amplitude coefficients for reflection and transmission of light are given by the expressions

$$r_d=\frac{N_{21}}{N_{11}}=\frac{p_2C_{m2}^{(1)}-p_1C_{m1}^{(1)}}{p_1C_{m1}^{(2)}-p_2C_{m2}^{(1)}}, \tag{29a}$$

$$t_d=\frac{1}{N_{11}}=\frac{4i}{\pi k_0\rho H_m^{(1)}(k_1\rho)H_m^{(2)}(k_1\rho)[p_2C_{m2}^{(1)}-p_1C_{m1}^{(2)}]}. \tag{29b}$$

Analogously, we can obtain the amplitude coefficients for reflection and transmission $r_c$ and $t_c$ for a converging wave

$$r_c=\frac{p_2C_{m2}^{(2)}-p_1C_{m1}^{(2)}}{p_1C_{m1}^{(2)}-p_2C_{m2}^{(1)}}, \tag{30a}$$

$$t_c=\frac{4i}{\pi k_0\rho H_m^{(1)}(k_2\rho)H_m^{(2)}(k_2\rho)[p_2C_{m2}^{(1)}-p_1C_{m1}^{(2)}]}. \tag{30b}$$

### 2.4. Reflection and transmission coefficients for cylindrical layered structures

Let us consider a cylindrical layered structure located between media with indices of refraction $n_f$ and $n_l$. Let a diverging cylindrical wave fall on the boundary of this layered structure from the medium with index of refraction $n_f$. The amplitudes of the electric and magnetic fields at the inner and outer boundaries of the structure are related to one another by the transfer matrix through the layered structure $\hat{M}$ as follows:

$$\begin{pmatrix} 1+r_d \\ ip_fC_{mf}^{(2)}r_d+ip_fC_{mf}^{(1)} \end{pmatrix}=\hat{M}\begin{pmatrix} t_d \\ ip_lC_{ml}^{(1)}t_d \end{pmatrix}, \tag{31}$$

from which it is not difficult to obtain the amplitude reflection ($r_d$) and transmission ($t_d$) coefficients:

$$r_d=\frac{(M_{21}-ip_fC_{mf}^{(1)}M_{11})+ip_lC_{ml}^{(1)}(M_{22}-ip_fC_{mf}^{(1)}M_{12})}{(ip_fC_{mf}^{(2)}M_{11}-M_{21})+ip_lC_{ml}^{(1)}(ip_fC_{mf}^{(2)}M_{12}-M_{22})}, \tag{32a}$$

$$t_d=\frac{4}{\pi\rho H_m^{(1)}(k_f\rho)H_m^{(2)}(k_f\rho)}\times\frac{1}{[(in_fC_{mf}^{(2)}M_{11}-M_{21})+in_lC_{mf}^{(1)}(in_fC_{mf}^{(2)}M_{12}-M_{22})]}. \tag{32b}$$

Analogously, we can obtain expressions for the reflection and transmission coefficients of a converging wave.

### 2.5. Cylindrical Bragg reflector

Let us determine the parameters of a layered structure in which layers with two different indices of refraction alternate, which is also an effective reflector for a cylindrical wave with frequency $\omega$. For a plane wave, such a structure is a Bragg reflector— a periodic sequence of pairs of layers whose thicknesses satisfy the condition $d_i=\pi c/2n_i\omega$ (here $c$ is the velocity of light and the $n_i$ are refractive indices of the layers).

The layered structure with the maximum reflection coefficient is one in which the boundaries between layers are at distances such that a wave reflected from the first boundary and a wave reflected from all subsequent boundaries and returning to the first boundary are in phase. Since the phase of the reflection coefficients from the cylindrical boundaries (see the expressions) and the choice of the phase of a cylindrical wave moving within a layer depend on the distance from the symmetry axis of the structure, the thicknesses of the layers will depend on the coordinate $\rho$.

Assume that a diverging cylindrical wave arrives from the inside at a surface with coordinate $\rho_0$ with amplitude unity. Let us determine the coordinate of the next boundary $\rho_1$, assuming that the wave vector in this layer equals $k$. Denoting the reflection coefficients of waves incident from inside on the first and second boundaries and from outside on the first boundary by $r_{0d}$, $r_{1d}$ and $r_{0c}$, and the transmission coefficients of the first boundary ''toward the outside'' and

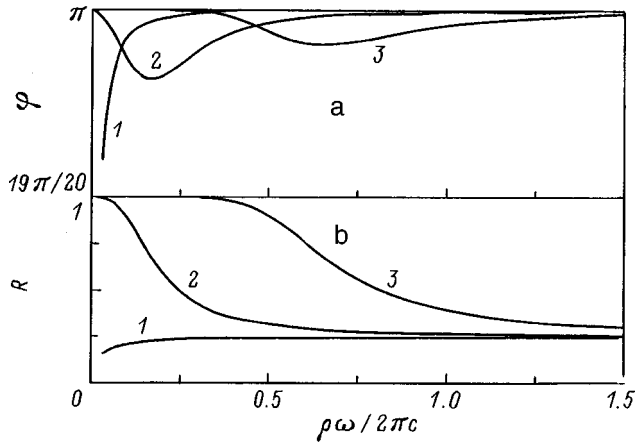


FIG. 2. Dependence of the phase (a) and squared modulus (b) of the amplitude reflection coefficient of a cylindrical wave diverging from a cylindrical boundary between two media with indices of refraction 1 (inner layer) and 3 (outer layer) versus the radius of the boundary for various values of the angular momentum $m$: *1*—$m=0$, *2*—$m=2$, *3*—$m=5$.

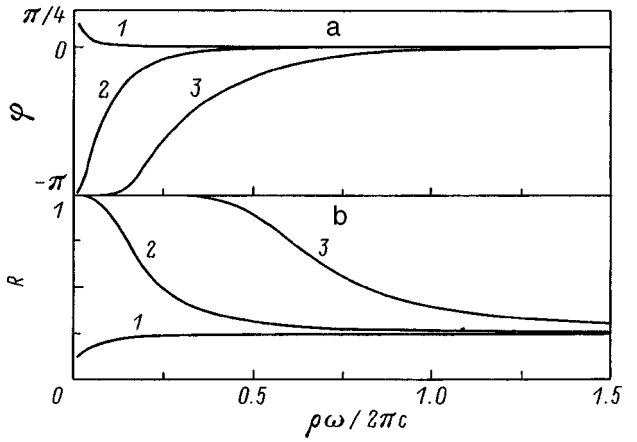


FIG. 3. Dependence of the phase (a) and squared modulus (b) of the amplitude reflection coefficient of a cylindrical wave diverging from a cylindrical boundary between two media with indices of refraction 3 (inner medium) and 1 (outer medium) versus the radius of the boundary for various values of the angular momentum $m$: *1*—$m=0$, *2*—$m=2$, *3*—$m=5$.

''toward the inside'' as $t_{0d}$ and $t_{0c}$, we find that the reflection coefficient from a cylindrical layer located between $\rho_0$ and $\rho_1$ is determined by the expression

$$r=\frac{r_{0d}+(t_{0c}t_{0d}-r_{0c}r_{1d})r_{1d}\Theta}{1-r_{0c}r_{1d}\Theta}, \tag{33a}$$

while the transmission coefficient is determined by the expression

$$t=\frac{t_{0d}t_{1d}}{1-r_{0c}r_{1d}\Theta}\frac{H_m^{(1)}(k\rho_1)}{H_m^{(1)}(k\rho_0)}, \tag{33b}$$

where

$$\Theta=\frac{H_m^{(2)}(k\rho_0)}{H_m^{(1)}(k\rho_0)}\frac{H_m^{(1)}(k\rho_1)}{H_m^{(2)}(k\rho_1)}.$$

The coordinate $\rho_1$ we are looking for is determined by the maximum of Eq. (33), which will occur when the phases of the two terms in the numerator are matched.

Repeating this procedure numerically, we can obtain the coordinates of all the subsequent boundaries. When the distance from the symmetry axis of the structure is large, we find that these are quarter-wave thicknesses.

### 3. A FEW RESULTS AND DISCUSSION

Figures 2 and 3 show the dependence of the square of the modulus ($R$) and phase ($\varphi$) of the amplitude reflection coefficient of a diverging wave incident on a cylindrical boundary between two media with refractive indices 1 and 3 versus the radius of the boundary. The situations described by these two figures differ only in the order of placement of the layers: Figure 2 corresponds to a case where light is incident from the less optically dense medium to the more optically dense medium, while Fig. 3 corresponds to the opposite situation. It is clear that as $\rho$ increases, the values of the phase and squared modulus of the reflection coefficient asymptotically approach values characteristic of reflection of a plane wave from a planar boundary between the media (25% for the squared modulus and $\pi$ or zero for the phase). It is also clear that the dependence of the squared modulus of the reflection coefficient on radius for both figures are identical: the energy reflection coefficients cannot depend on whether the light is incident from the optically more dense on the optically less dense medium or conversely. It is necessary to discuss this fact in more detail, since it gives rise to an important difference between reflections of cylindrical waves and reflections of plane waves.

For angular momentum $m$ equal to zero, the energy flux transported by an optical cylindrical wave is directed along the radius, i.e., we can say that the wave is incident normal to the cylindrical boundary between the two media. For nonzero $m$, the Poynting vector of a cylindrical wave has a component parallel to $\mathbf{e}_\varphi$ and proportional to the quantity $mc/n\omega\rho$; i.e., the energy propagates in a spiral. The arrival of such a cylindrical wave on a cylindrical boundary between two media can be likened to incidence of a plane wave on a planar boundary at an angle $\theta$ that satisfies the relation

$$\sin\theta=mc/n\omega\rho. \tag{34}$$

As $\rho$ goes to infinity, the incidence becomes normal, and the curvature of the surface reduces to zero. It thus follows that the reflection and transmission coefficients for light (29), (30) for large $\rho$ should correspond to the case of normal incidence of a plane wave on a planar boundary (Figs. 2 and 3).

For small $\rho$ this situation changes: a nonzero imaginary part appears in the reflection and transmission coefficients; as $\rho$ reduces to zero, the reflection coefficient reduces to unity, which corresponds to total internal reflection.

There are significant differences in the phenomenon of total internal reflection for the cylindrical and planar cases: for cylindrical waves and boundaries, the reflection coefficient is determined by the refractive indices of the bounding layers, the angular momentum of the wave $m$, and the boundary coordinate $\rho$, but does not depend on the order of alternation of the layers (!). This result, which at first glance is unexpected, follows from the fact that the angle between

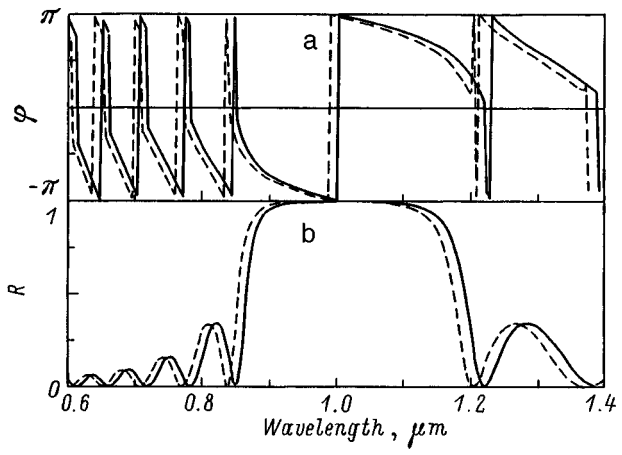


FIG. 4. Spectral dependence of the phase (a) and modulus square (b) of the amplitude reflection coefficient of a cylindrical Bragg reflector formed by quarter-wave layers (dashed curve) and a cylindrical reflector optimized in accordance with the procedure described in paragraph 2.5 (solid curve). The angular momentum of the incident wave equals zero. The indices of refraction of the materials that make up the reflector equal 1 and 3.

the Poynting vector for a cylindrical wave and the normal to the plane tangent to the cylindrical boundary (34) does not depend on the values of refractive index of all of the preceding layers. Using Eq. (29a), we can also show analytically that the relation between values of the amplitude reflection coefficients corresponding to the two different types of alternation of layers equals $-1$.

We can also assume that for cylindrical waves an effect analogous to the Brewster effect will occur.

Figure 4 shows the reflection spectra of a cylindrical wave diverging from of two different types of cylindrical Bragg reflectors: a quarter-wave reflector, the thickness of whose layers is constant, and an optimized reflector, the thickness of whose layers varies in accordance with the distance to the symmetry axis of the structure $\rho$. The layer thicknesses of the reflectors are chosen in such a way that the ''Bragg'' wavelength equals 1 $\mu$m. As in the linear case, a periodic sequence of pairs of cylindrical layers with quarter-wave thicknesses ensures efficient reflection of cylindrical waves. However, the maximum of the reflection coefficient for the quarter-wave structure is shifted relative to the prespecified (design) value of wavelength, as is true of the break in the spectral dependence of the reflection coefficient phase corresponding to it. This is because the phases of waves reflected from the various boundaries and returning to the first boundary are not matched among themselves. Conversely, the maximum in the reflection spectrum from the optimized structure occurs at the prespecified (design) value of the wavelength, due to matching of the wave phases reflected from all the boundaries in the structure.

As the radius of the first boundary increases, this mismatch decreases; however, we must take into account its effect on the frequency of the intrinsic optical modes of such a structure.[9]

The transfer matrix method which we have developed for cylindrical waves is simple and effective for calculating electromagnetic fields in cylindrical structures. This method allows us to study the passage of light through cylindrical boundaries, cylindrical layered structures, and to construct cylindrical structures with predetermined properties. Using this method we can also create methodologies for designing optical fibers and cylindrical lasers.[9]

The authors are grateful to E. L. Portnoi for useful discussions.

This work was supported by the Russian Fund for Fundamental Research.

[1] M. A. Kaliteevski and A. V. Kavokin, Fiz. Tverd. Tela (St. Petersburg) **37**, 2721 (1995) [Phys. Solid State **37**, 1497 (1995)].
[2] Kawaguchi, IEE Proc.: Optoelectron. **140**, 3 (1993).
[3] H. Kogelnik and C. V. Shank, J. Appl. Phys. **43**, 2327 (1972).
[4] E. Yablanovich, Phys. Rev. Lett. **58**, 2059 (1987).
[5] T. F. Krauss, R. M. De La Rue, and S. Brandt, Nature (London) **383**, 699 (1996).
[6] M. Born and E. Wolf, *Principles of Optics* (Nauka, Moscow, 1970), p. 77.
[7] J. Durbin, J. J. Miceli, and J. H. Eberly, Phys. Rev. Lett. **58**, N15, 1499 (1987).
[8] A. A. Tovar and G. H. Clark, J. Opt. Soc. Am. A **12**, N14, 3333 (1997).
[9] A. V. Kavokin and M. A. Kaliteevski, Solid State Commun. **95**, N12, 859 (1995).

Translated by Frank J. Crowne

## LOW-DIMENSIONAL SYSTEMS

# Photo- and electroluminescence in the 1.3-$\mu$m wavelength range from quantum-dot structures grown on GaAs substrates

A. E. Zhukov, A. R. Kovsh, A. Yu. Egorov, N. A. Maleev, V. M. Ustinov, B. V. Volovik, M. V. Maksimov, A. F. Tsatsul'nikov, N. N. Ledentsov, Yu. M. Shernyakov, A. V. Lunev, Yu. G. Musikhin, N. A. Bert, P. S. Kop'ev, and Zh. I. Alferov

*A. F. Ioffe Physicotechnical Institute, Russian Academy of Sciences, 194021 St. Petersburg, Russia*
(Submitted June 14, 1998; accepted for publication June 28, 1998)
Fiz. Tekh. Poluprovodn. **33**, 180–183 (February 1999)

A method is proposed to increase the emission wavelength from structures grown on GaAs substrates by inserting a strained InAs quantum dot array into an external InGaAs quantum well. The dependence of the luminescence peak position on the active region design was investigated for structures grown by this method. Room-temperature photo- and electroluminescence spectra in the 1.3-$\mu$m wavelength range are compared. © *1999 American Institute of Physics.* [S1063-7826(99)00602-X]

A problem of current interest is to extend the band of optical wavelengths accessible to light-emitting devices grown on GaAs substrates out to 1.3 $\mu$m, which corresponds to the maximum transmission of an optical fiber. Much of this interest is motivated by the need to find an alternative to laser diodes made from InGaAsP heterostructures, since these diodes suffer from a fundamental shortcoming: they do not confine electrons to the active region very well, which leads to a strong temperature dependence of the threshold current density.[1] In addition, if light emitters at 1.3 $\mu$m could be fabricated on GaAs substrates, they could be used as components of integrated-optics devices in the long-wavelength region along with transistors based on GaAs, whose technology is well developed, thereby obviating the need to use other substrates such as InP.

Strained InGaAs/GaAs quantum wells cannot be used to obtain the required range of wavelengths, due to bounds on the quantum-well width imposed by the limitations of pseudomorphic growth.[2] However, in Ref. 1 it was shown that adding a rather small amount of nitrogen (a few percent) to an InGaAs layer leads to a strong decrease in the width of the gap gap, making structures that emit at 1.3 $\mu$m possible.

Deposition of strongly strained layers of $In_xGa_{1-x}As$ ($x \geqslant 0.5$) is known to lead to spontaneous formation of collections of quantum dots. This process also gives rise to a considerable long-wavelength shift in the luminescence line compared to strained InGaAs quantum wells.[3] In this paper we propose and implement an approach that could serve as an alternative to using nitrogen-containing compounds, and which allows us to greatly extend the range of emission wavelengths in structures grown on GaAs substrates. This method is based on decreasing the level of size quantization in the quantum dots as the width of the band gap of the host material is decreased; this is achieved by placing the aggregate of quantum dots into an external InGaAs quantum well. Such structures make it possible to reach luminescence wavelengths of 1.3 $\mu$m at room temperature by both optical and injection pumping. In addition, optical devices based on quantum dots may possibly allow us to realize the theoretically predicted advantages of systems with size quantization in three directions.[4]

Our structures, which are shown schematically in Fig. 1a, were grown by molecular-beam epitaxy (MBE) on (100) GaAs substrates in a Riber-32P machine with a solid-state $As_4$ source. The device active layer, consisting of a collection of InAs quantum dots embedded in an external $In_xGa_{1-x}As$ quantum well, was located in the middle of a GaAs layer with thickness 0.12 $\mu$m bounded on its substrate and surface sides by short-period AlAs (2 nm)– GaAs (2 nm) superlattices. The mole fraction of InAs and width of the quantum well were varied in the ranges 0.1–0.3 and 10–4 nm, respectively, in such a way that the total stress caused both by the collection of quantum dots and the InGaAs quantum well did not exceed the critical value for forming misfit dislocations. The growth was carried out under arsenic-rich conditions at a substrate temperature of 485 °C for deposition of the active region and 600 °C for the rest of the structure. The formation of the collection of quantum dots was monitored *in situ* based on the observed change in the reflected high-energy electron diffraction (RHEED) pattern.

The photoluminescence, which we investigated from 15 to 300 K, was excited by light from an $Ar^+$-laser (with wavelength 514.5 nm) and recorded by a Ge photodiode. The excitation power density was 100 W/cm$^2$. Transmission electron microscopy (TEM) studies were carried out using a Philips-EM-420 electron microscope operated with an accelerating voltage of 100 to 120 kV. The MBE samples were prepared in a planar geometry using chemical etching in a solution of $H_2SO_4:H_2O_2:H_2O$ (5 : 1 : 1).

The photoluminescence wavelength of a collection of quantum dots grown on a GaAs substrate is sensitive to changes in the width of the host bandgap. In Ref. 5 it was

 

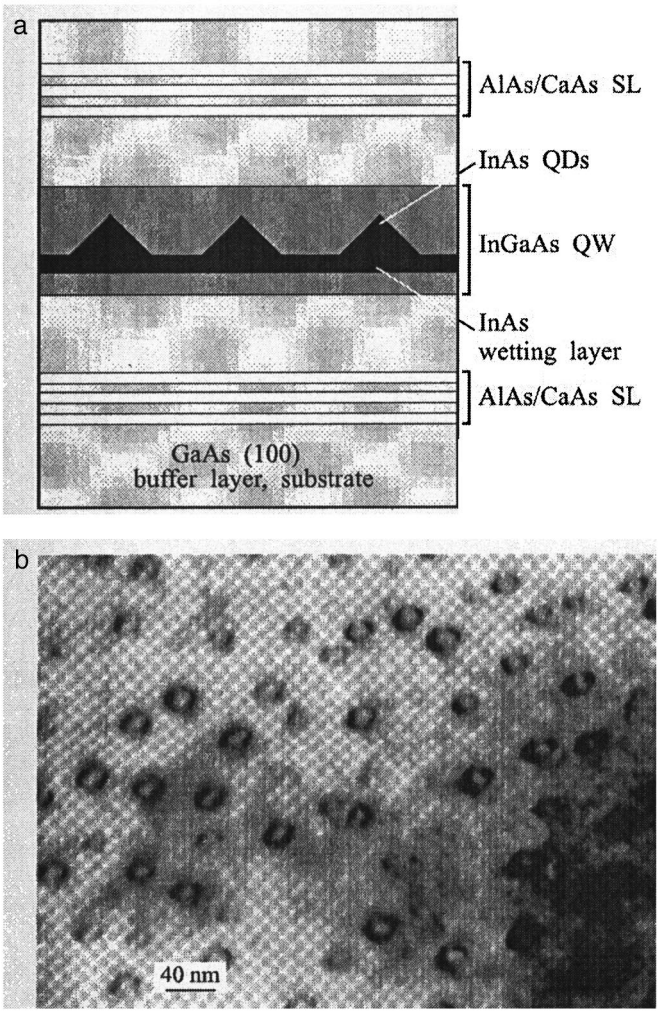


FIG. 1. Schematic illustration of structures under study containing collections of InAs quantum dots in an external InGaAs quantum well with two bounding superlattices grown on a (100) GaAs substrate (a) and an electron-microscope image obtained in the bright-field regime along the [100] axis of a structure with a collection of quantum dots in an $In_{0.12}Ga_{0.88}As$ quantum well of width 10 nm (b).

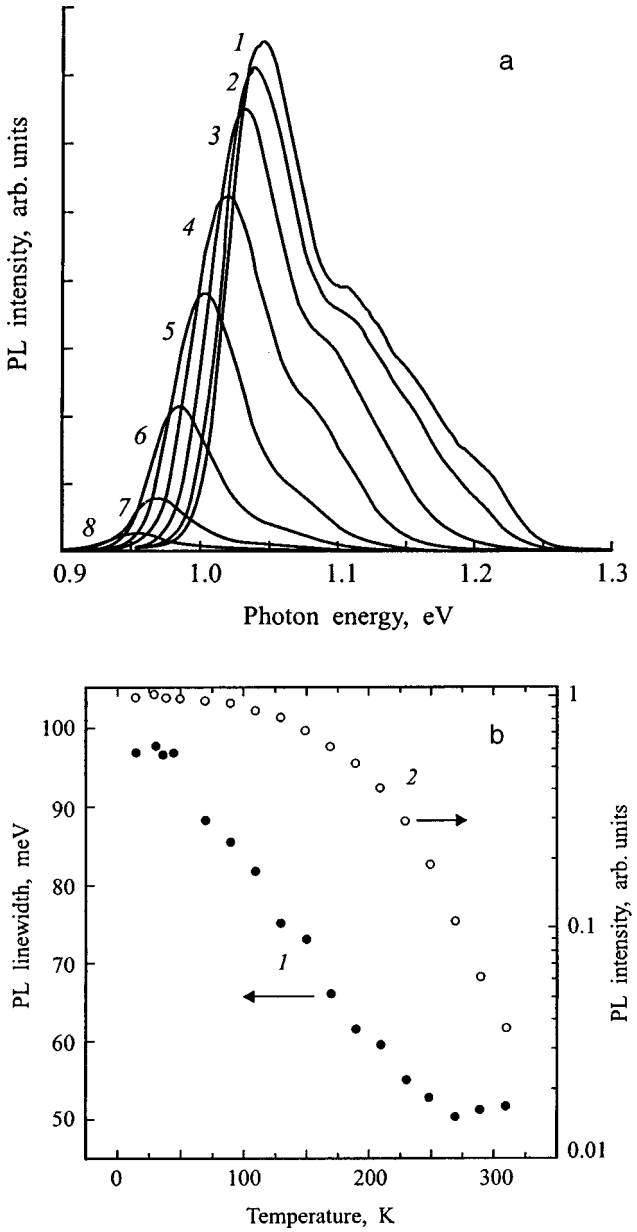


FIG. 2. a—Photoluminescence spectrum at temperatures $T$, K: *1* — 30, *2* — 70, *3* — 110, *4* — 150, *5* —190, *6* — 230, *7* — 270, *8* — 300. b—Temperature dependence of the linewidth (*1*) and intensity (*2*) of photoluminescence from a structure containing a collection of quantum dots in an $In_{0.3}Ga_{0.7}As$ quantum well of width 4 nm.

shown that replacing a GaAs host by the wider-gap three-component compound AlGaAs strongly shifts the photoluminescence line for the collection of quantum dots to shorter wavelengths. In contrast, the method we propose in this paper to increase the emission wavelength of structures grown on GaAs substrates is based on decreasing the amount of size quantization in the quantum dots by decreasing the width of the host bandgap. To do this, we propose to use a narrow-gap strained InGaAs quantum well as the host material surrounding the collection of quantum dots.

Figure 1b shows a TEM microphotograph (planar image) of a sample containing a collection of quantum dots located in an $In_{0.12}Ga_{0.88}As$ quantum well with width 10 nm. Since both the quantum dots and the quantum well on the GaAs substrate consist of material under strain, there is a risk of the appearance of misfit dislocations which would remove the mismatch stress. Analysis of the TEM data allow us to conclude that there was no formation of misfit dislocations in these samples, which is a result of our careful choice of the width of the quantum well for the amount of InAs used to form the collection of quantum dots and the mole fraction of InAs in the surrounding quantum well.

Figure 2a shows the temperature dependence of the photoluminescence for a structure containing a collection of InAs quantum dots placed in an $In_{0.3}Ga_{0.7}As$ quantum well with width 4 nm. Changing the temperature from 30 to 310 K causes shift of the photoluminescence line by 85 meV to longer wavelengths, and at room temperature the photoluminescence maximum has moved to a wavelength of 1.3 $\mu$m for a linewidth of 50 meV.

The dependence of the width of the photoluminescence band on the observation temperature, which is shown in Fig. 2b, is nonmonotonic in character: as the temperature in-

creases from 15 to 270 K, the linewidth decreases, while for temperatures above 270 K an increase in linewidth is observed. This behavior is uncharacteristic of luminescence from bulk material or quantum wells, where we typically observe a regular increase in the linewidth with increasing observation temperature, due to population of higher-lying states.

A similar anomalous temperature dependence of the photoluminescence linewidth was observed previously in structures based on quantum dots.[5–7] As shown in Refs. 7 and 8, this behavior can lead to a negative characteristic temperature, i.e., the decrease observed in the threshold current density with increasing temperature when collections of quantum dots are used as the active region of an injection laser. A distinctive feature of our results is the fact that the range in which the photoluminescence linewidth decreases extends to such high observation temperatures. We are the first to report such behavior, which could be due to the considerable increase in localization energy of the ground state of the quantum dots compared to states of bulk GaAs, which in turn comes from placing the collection of quantum dots in the external InGaAs quantum well.

It has already been reported in the literature that photoluminescence has been obtained at a wavelength of 1.3 $\mu$m in structures based on collections of InGaAs quantum dots grown both by MBE (Ref. 6) and by MOVPE-hydride epitaxy (metallorganic vapor-phase epitaxy)[9] on GaAs substrates. In both of these cases, the active region was grown by alternating depositions of indium and gallium atoms, as a result of which local regions (islands) were formed with increased In content. The process of forming these islands, and therefore the photoluminescence wavelength, are sensitive to such kinetic parameters as the arsenic pressure, the rate of growth, and the deposition temperature, which are usually difficult to control reliably during the growth process.

Our approach differs in that, as we will show below, it is possible to reliably control the emission wavelength over wide limits by choosing the effective width of the host bandgap, since the host is an InGaAs quantum well. Moreover, the photoluminescence intensity (both integrated and peak) falls off as the temperature increases from 77 to 300 K by only a factor of 10 to 30 in all (Fig. 2b), which is smaller by an order of magnitude than the values reported in Ref. 6.

Figure 3a shows photoluminescence spectra of samples which contain collections of InAs quantum dots and which differ from one another by In content in the quantum well. For comparison, we also show the photoluminescence spectrum of a collection of quantum dots in a GaAs host (no quantum well). It is clear that decreasing the width of the bandgap of the host material by increasing the In content in the quantum well leads to a regular shift in the photoluminescence line to longer wavelengths. As we have noted above, the position of the photoluminescence maximum occurs at 1.3 $\mu$m when an $In_{0.3}Ga_{0.7}As$ quantum well of width 4 nm is used.

To the best of our knowledge, there have heretofore been no reports in the literature on the observation of lasing or even electroluminescence in the wavelength range near 1.3 $\mu$m from collections of quantum dots grown on GaAs substrates. We assume that this is because structures that use injection pumping are more sensitive to crystallographic perfection both of the active region itself, based on quantum dots, and in the layers of subsequent overgrowth.

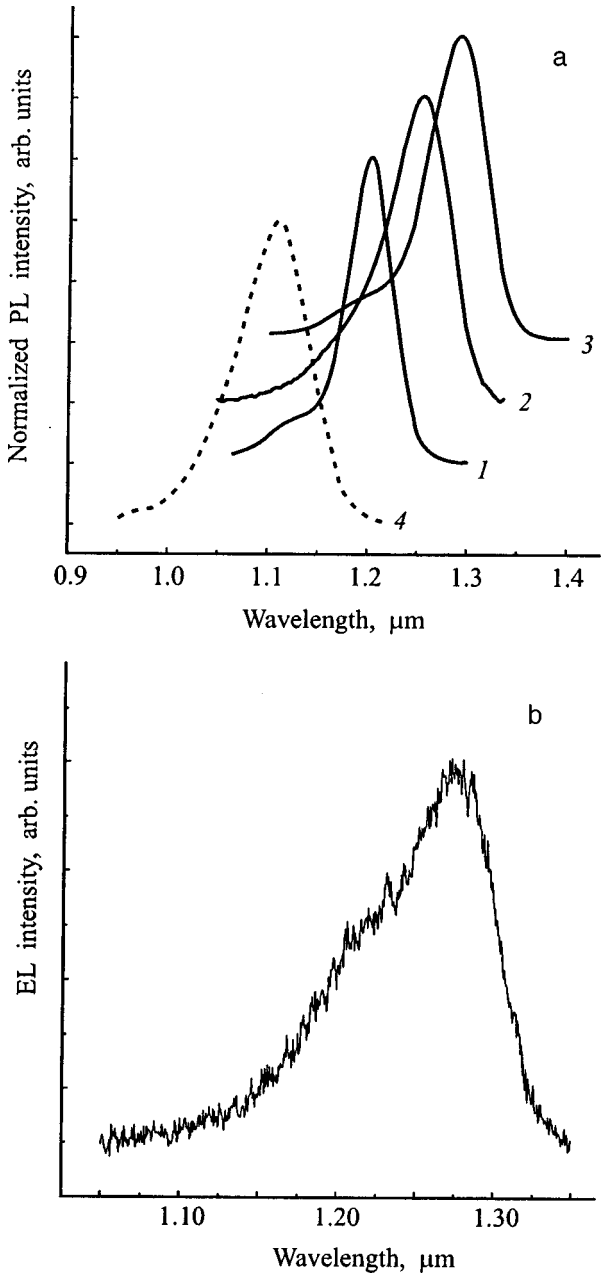


FIG. 3. a—300-K photoluminescence spectra of samples containing collections of InAs quantum dots. Indium content $x$ in the quantum well: 0.12 (*1*), 0.2 (*2*), and 0.3 (*3*). Curve *4*— photoluminescence spectrum of a collection of quantum dots in a GaAs host (no quantum well). b—Electroluminescence spectrum at room temperature of a sample containing a collection of InAs quantum dots in an InGaAs quantum well placed in the middle of a $p-i-n$ structure.

In order to investigate the possibility of making lasers at a wavelength of 1.3 $\mu$m based on the approach described in this paper, we grew a laser structure on a (100) $n^+$-type GaAs substrate. The active region, which consisted of a collection of InAs quantum dots in an InGaAs quantum well, was placed in the middle of a $p-i-n$ region consisting of

doped layers of $Al_{0.3}Ga_{0.7}As$ with *n*- and *p*-conductivity and an undoped layer of GaAs.

Figure 3b shows the electroluminescence spectrum of this sample, plotted for a pumping current of 0.1 A (current density 70 A/cm$^2$) at room temperature. The maximum of the electroluminescence line is located at 1.276 $\mu$m, which is, as far as we know, the largest wavelength attained in an injection-pumped structure with quantum dots. The electroluminescence maximum shifted toward longer wavelengths by only 24 nm relative to the photoluminescence line of a structure with a nominally identical active region but no thick, doped AlGaAs layers. This indicates that the shapes, dimensions, and chemical composition of the quantum dots placed within the external quantum well are highly stable against high-temperature annealing,[10] due to the lengthy overgrowth of the active region.

Thus, we have shown that placing a collection of InAs quantum dots in a strained InGaAs quantum well can greatly extend the range of emission wavelengths from structures grown on GaAs substrates on the long-wavelength end. Wavelengths for photo- and electroluminesence can be varied controllably over a wide range by varying the indium content of the exterior quantum well, even out to 1.3 $\mu$m at room temperature.

This work was carried out with the support of the Russian Fund for Fundamental Research (Grant 96-02-17824) and the Volkswagen Fund.

[1] M. Kondow, K. Uomi, A. Niwa, T. Kitatani, S. Watahiki, and Y. Yazawa, Jpn. J. Appl. Phys. **35**, 1273 (1996).
[2] J. W. Matthews and A. E. Blakeslee, J. Cryst. Growth **27**, 118 (1974).
[3] A. Yu. Egorov, A. E. Zhukov, P. S. Kop'ev, N. N. Ledentsov, M. V. Maksimov, V. M. Ustinov, A. F. Tsatsul'nikov, Zh. I. Alferov, D. L. Fedorov, and D. Bimberg, Fiz. Tekh. Poluprovodn. **30**, 1345 (1996) [Semiconductors **30**, 1376 (1996)].
[4] Y. Arakawa and H. Sakaki, Appl. Phys. Lett. **40**, 939 (1982).
[5] A. E. Zhukov, A. Yu. Egorov, A. R. Kovsh, V. M. Ustinov, N. N. Ledentsov, M. V. Maksimov, A. F. Tsatsul'nikov, S. V. Zaĭtsev, N. Yu. Gordeev, P. S. Kop'ev, D. Bimberg, and Zh. I. Alferov, Fiz. Tekh. Poluprovodn. **31**, 483 (1997) [Semiconductors **31**, 411 (1997)].
[6] R. P. Mirin, J. P. Ibbetson, K. Nishi, A. C. Gossard, and J. E. Bowers, Appl. Phys. Lett. **67**, 3795 (1995).
[7] D. I. Lubyshev, P. P. Gonzalez-Borrero, E. Marega, Jr., E. Petitprez, N. La Scala, Jr., and P. Basmaji, Appl. Phys. Lett. **68**, 205 (1996).
[8] A. E. Zhukov, V. M. Ustinov, A. Yu. Egorov, A. R. Kovsh, A. F. Tsatsul'nikov, N. N. Ledentsov, S. V. Zaitsev, N. Yu. Gordeev, P. S. Kop'ev, and Zh. I. Alferov, Jpn. J. Appl. Phys. **36**, 4216 (1997).
[9] K. Mukai, N. Ohtsuka, M. Sugawara, and S. Yamazaki, Jpn. J. Appl. Phys. **33**, L1710 (1994).
[10] A. E. Zhukov, A. Yu. Egorov, A. R. Kovsh, V. M. Ustinov, M. V. Maksimov, A. F. Tsatsul'nikov, N. N. Ledentsov, N. Yu. Gordeev, S. V. Zaĭtsev, P. S. Kop'ev, Zh. I. Alferov, and D. Bimberg, Fiz. Tekh. Poluprovodn. **31**, 105 (1997) [Semiconductors **31**, 145 (1997)].

Translated by Frank J. Crowne

# Capacitance spectroscopy of deep states in InAs/GaAs quantum dot heterostructures

M. M. Sobolev, A. R. Kovsh, V. M. Ustinov, A. Yu. Egorov, A. E. Zhukov, and Yu. G. Musikhin

*A. F. Ioffe Physicotechnical Institute, Russian Academy of Sciences, 194021 St. Petersburg, Russia*
(Submitted July 23, 1998; accepted for publication July 28, 1998)
Fiz. Tekh. Poluprovodn. **33**, 184–193 (February 1999)

The results of a study of a structure with a single array of InAs quantum dots in a GaAs matrix using capacitance-voltage measurements, deep-level transient spectroscopy (DLTS), photoluminescence spectroscopy, and transmission electron microscopy are reported. Clusters of interacting bistable defects are discovered in GaAs layers grown at low temperature. Controllable and reversible metastable populating of quantum-dot energy states and monoenergetic surface states, which depends on the temperature and conditions of a preliminary isochronal anneal, is observed. This effect is associated with the presence of bistable traps with self-trapped holes. The DLTS measurements reveal variation of the energy for the thermal ionization of holes from surface states of the InAs/GaAs heterointerface and the wetting layer as the reverse bias voltage is increased. It is theorized that these changes are caused by the built-in electric field of a dipole, which can be formed either by wetting-layer holes or by ionized levels located near the heterointerface.  [S1063-7826(99)00702-4]

## 1. INTRODUCTION

Semiconductor heterostructures with spatial confinement of carriers in three dimensions are presently one of the most promising objects of investigation because of the extensive possibilities of their employment in optoelectronics and as memory elements.[1,2] The greatest advances in creating quantum dots (QD's) have been achieved by utilizing the self-organization of nanostructures in heteroepitaxial semiconductor systems. The electronic spectrum of such QD's is similar to the spectrum of a single atom.[2] Lasing on the ground state of a QD has been achieved at room temperature and a threshold current density of 65 A/cm$^2$ in injection heterolasers with an active region based on vertically coupled (In, Ga)As/GaAs QD's.[2] At the same time, specific conditions for growing QD's: low deposition and capping temperatures, stimulate the generation of point defects near the QD's and on the wetting-layer/matrix heterointerface, which act as centers for the trapping and nonradiative recombination of nonequilibrium carriers and thereby lower the radiative-recombination quantum efficiency. It was shown in Ref. 3 that only 40% of the carriers in these lasers take part in radiative recombination and 65% of them participate in stimulated emission. The remaining 35% of the carriers recombine spontaneously through excited QD states and wetting-layer states. Deep-level transient spectroscopy (DLTS) is the most effective method for the spectroscopy of defects and impurities with deep states.[4] This method has been successfully applied to the spectroscopy of states bound to a heterointerface[5] and of quantum wells,[6,7] as well as both isolated QD's[8] and arrays of vertically coupled InAs/GaAs QD's.[9,10] Another method which has been successfully employed in the determination of the effective carrier distribution profile in structures containing QD's is capacitance-voltage ($C-V$) spectroscopy.[10,11] Formidable problems arise in the treatment of the results of $C-V$ and DLTS investigations of real structures when there is a wetting layer in addition to QD's and there are defects and surface states on the heterojuntion. In particular, it is known[12] that plots of the variation of the radio-frequency (rf) capacitance as a function of voltage for heterostructures with a monoenergetic surface level and with a well or dot quantum state are similar. DLTS measurements of such structures also raise questions regarding the origin of the DLTS signals, which can be assigned to emission from the wetting layer, QD's, or surface states, as well as to deep levels of defects. It was shown in Refs. 5–10 that DLTS measurements performed as a function of the reverse bias voltage and the filling pulse height permit establishment of the nature of a DLTS signal. A strong influence of the electric field in the space-charge region on carrier emission was discovered. The potential barrier in a quantum well[7] and a quantum dot[9,10] was lowered in a strong electric field with resultant displacement of the maximum of the DLTS signal toward lower temperatures with increasing reverse bias voltage. At the same time, displacement of the maximum of the DLTS signal toward higher temperatures with increasing reverse bias voltage was discovered for a monoenergetic surface state, and this effect was attributed to spatial variations of the misalignment voltages near the heterojunction.[5] When the filling pulse height was increased, it was found that the positions of DLTS peaks caused by emission from quantum dots[8–10] shift toward lower temperatures. The observed decrease in the activation energy for carrier emission from quantum dots was associated in Ref. 8 with the increase in the energy of the Coulomb charge in quantum dots as the carrier concentration in them rises. It was found in Refs. 9 and 10 for structures with vertically coupled InAs/GaAs QD's that if the defect density near the QD's is comparable to the density of the dots themselves, the Coulomb interaction of charged defects with carriers local-

 

ized by QD's can lead to the formation of an electric domain, as well as to tunneling of the carriers between the deep states and quantum states. However, despite the existence of numerous publications, there is presently a lack of detailed information on the features of $C-V$ and DLTS measurements of real structures which have not only QD's but also a wetting layer, as well as defects and deep surface states on the heterojunction. The problems then arising in assigning the DLTS signals to emission from a particular state can be solved by a combined approach involving comparison of the results from photoluminescence spectroscopy, transmission electron microscopy (TEM), and $C-V$ and DLTS measurements.

In this article we report the results of an experimental study of a structure containing one array of InAs QD's in a GaAs matrix using $C-V$, DLTS, and photoluminescence (PL) measurements, as well as TEM. We found that the DLTS spectra contain peaks assigned to deep states of known defects and a monoenergetic surface state at the heterojunction between the InAs wetting layer and the GaAs matrix and peaks of QD energy states. Controllable and reversible metastable populating of the quantum-dot energy states and the monoenergetic surface state, which depends on the temperature and conditions for the preliminary isochronal anneal, was observed.

## 2. SAMPLES AND METHODS OF INVESTIGATION

The structure investigated in this work was obtained by molecular-beam epitaxy. It contained a single plane of QD's built-in as a result of the deposition of three monolayers of InAs in the middle of a $p$-GaAs epitaxial layer ($p=3\times10^{16}$ cm$^{-3}$) of thickness 0.9 $\mu$m grown on a $p^+$-GaAs $\langle100\rangle$ substrate. The $p$-GaAs epitaxial layer was covered by a $n^+$-GaAs overlayer to create a $p-n$ junction. At liquid-nitrogen temperature the photoluminescence spectra of such structures display a line at $h\nu=1.19$ eV,[13,14] which is produced by the electron and hole ground states in the QD plane. The quantum states of the dots, the deep levels of the defects and impurities, and the carrier distribution profile in the heterostructures were investigated by $C-V$ measurements and DLTS using a Bio-Rad DL4600 spectrometer operating in the dual-gate integration mode. A Boonton-72B bridge operating at 1 MHz was used to measure the capacitance. The sensitivity of this instrument is $\Delta C/C_0\approx10^{-4}$. Ohmic contacts were thermally deposited on the $p^+$-GaAs substrate and the $n^+$-GaAs layer to perform the DLTS and $C-V$ measurements. Before each DLTS and $C-V$ measurement, the sample was annealed isochronally for 1 min at a fixed temperature. The sample was preliminarily heated to 450 K and held for 1 min with the reverse bias voltage $U_r=0$ if the annealing was carried out at $U_r<0$, and it was then cooled to the annealing temperature. For annealing with $U_r=0$ the sample was preliminarily held with $U_r<0$. The annealing temperature was varied in the range 80–450 K. Thereafter, the sample was cooled to $T=80$ K either with an applied reverse bias voltage $U_r<0$ or with $U_r=0$. The DLTS or $C-V$ measurement process was then begun. In addition, unless indicated otherwise, all the measurements were performed in the dark, and the sample was cooled under the condition $U_r<0$ before the DLTS measurements. The thermal activation energy $E_a$ and the carrier trapping cross section $\sigma_p$ were determined from an Arrhenius plot.

The investigations of the InAs/GaAs QD structure using a Philips EM420 transmission electron microscope operating at an accelerating voltage of 100 kW were performed in a planar geometry and in a transverse-section geometry. The samples were prepared in the cross-sectional geometry according to a standard procedure including finishing by 4-kW argon ions at a grazing angle of incidence on a Gatan Duo-Mill 600 machine. For investigations in the planar geometry the samples were prepared by chemical etching in a $H_2SO_4$:$H_2O_2$:$H_2O$ (5:1:1) solution after preliminary removal of the upper layer of the material.

## 3. RESULTS

Figures 1a and 1b show images of InAs QD's in a GaAs matrix in the structure that we investigated in the light-field regime and cross-sectional geometry, which were obtained using a transmission electron microscope. The dot concentration was estimated to be $(2-3)\times10^9$ cm$^{-2}$ on the basis of a light-field image obtained in the (220) reflection from a sample of planar geometry. The dominant factor shaping the image in this regime is the deformation component. It includes the deformation of the quantum dot itself and the GaAs matrix in the immediate vicinity of the dot. Therefore, the dot diameter determined on the basis of such an image, which equals $17\pm3$ nm, is an upper bound. The actual QD diameter is overestimated by 25–30%. Linear defects were also discovered with a density of $2\times10^6$ cm$^{-2}$ in the structures. The investigations showed that there are two types of linear defects: dislocations in stressed islands formed as a result of a relaxation process, as well as stacking defects in the upper layer, which are bounded by partial dislocations and appear because of the presence of the stressed layer of quantum dots. It can also be seen from the image of the QD layer in the planar geometry (Fig. 1b) that these partial dislocations terminate on one another.

Figure 2b shows distribution profiles of the effective hole concentration $[p^*(U_r)]$ determined from the $C-V$ characteristics of the InAs/GaAs QD $p-n$ structure (Fig. 2a). The $C-V$ characteristics were measured at 82 K after an isochronal anneal under various conditions. It is seen from Fig. 2b that the $p^*(U_r)$ curve has two peaks in hole accumulation regions. One of them is narrow, and the amplitude of the other is five times smaller. In addition, there is a depletion region located between the two peaks. The $C^{-2}(U_r)$ characteristic (Fig. 2a) has one extended plateau with a small gradient and another less pronounced plateau. The existence of such plots of the capacitance as a function of voltage is characteristic of structures with quantum dots, quantum wells, and monoenergetic surface states on the heterointerface. The first $p^*(U_r)$ peak is at a depth of 0.38 $\mu$m, and the second peak is at 0.46 $\mu$m. The positions of the $p^*(U_r)$ peaks coincide with the calculated positions of the quantum dots and the wetting layer. A decrease in the measurement temperature led to narrowing and an increase in the

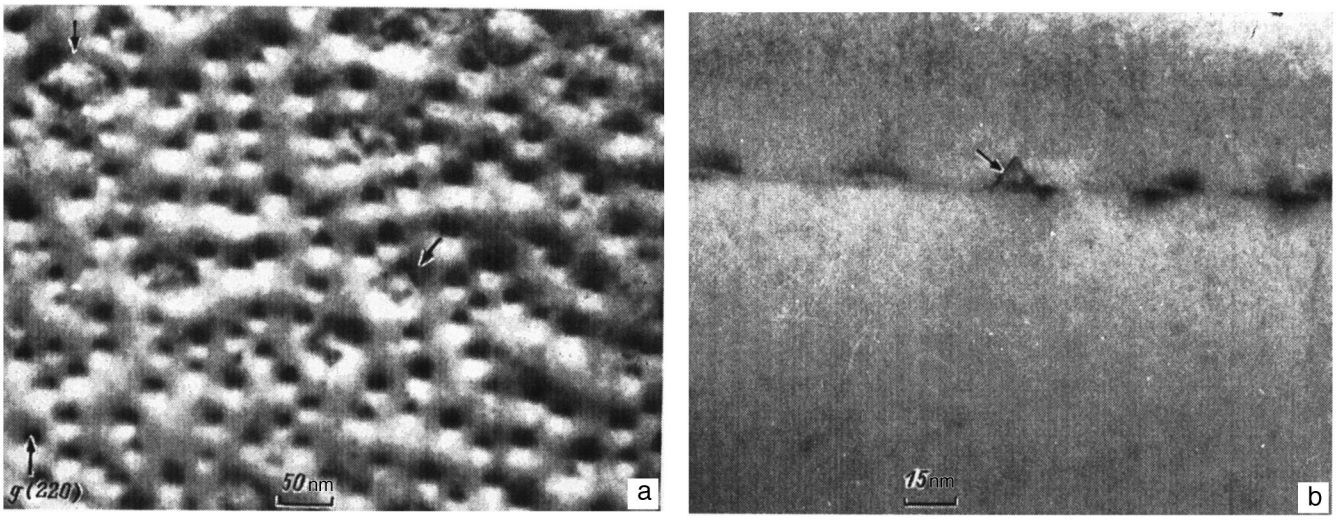


FIG. 1. Electron-microscopic images of InAs quantum dots in a GaAs matrix: a — in the (220) light-field regime (the arrows mark extended defects); b — transverse section of a layer of quantum dots (the arrow marks a packing defect).

amplitude of the peaks on the distribution of the effective hole concentration. Appreciable variations in the $p^*(U_r)$ profile were observed as a function of the conditions of the isochronal anneal ($U_r=0$ and $U_r<0$) (Fig. 2). The heights of the peaks at the maxima of the effective hole concentration $p^*(U_r)$ rose in the case of annealing with $U_r<0$. In this case the width of the first peak increased with a shift toward the second depletion region, while the second peak narrowed. The width of the depletion region remained unchanged. An even greater increase in the effective hole concentration was observed when the $C-V$ measurements were performed with illumination of the sample by white light (Fig. 2b).

The $C-V$ measurements permitted determination of the region of spatial localization of the QD's and the conditions under which the DLTS spectra should display signals associated with carrier emission from the QD's, the wetting layer, and the defects located in their vicinity. The spectra shown in Fig. 3a were measured at a constant value of the filling pulse height $U_f$ and for various values of the reverse bias pulse voltage $U_r$. To determine the spatial localization of the DLTS signals, measurements were performed with simultaneous variation of $U_f$ and $U_r$, but with a fixed difference between $U_r$ and $U_f$ [$\Delta U=(U_r-U_f)=0.8$ V] (Fig. 3b). When $U_r<1.5$ V, no DLTS signal was observed. When $U_r$ was varied in the range 1.5–3.0 V, which corresponds to the first hole accumulation peak on the $p^*(U_r)$ profile, two broad peaks appeared in the DLTS spectra. The low-temperature $H2$ peak increased with increasing $U_r$, and its maximum shifted slightly toward lower temperatures with simultaneous broadening in the same direction (Fig. 2a). The thermal activation energy determined from the Arrhenius plot for the level corresponding to this peak varied in the range $E_a=(225-240)$ meV, and the trapping cross section varied in the range $\sigma_\rho=(3.3-8.3)\times10^{-19}$ cm$^2$ as $U_r$ was increased (see Table I). The position of the maximum of the DLTS signal did not vary in response to the simultaneous variation of $U_f$ and $U_r$ (Fig. 3b). When $U_r$ was increased further in the range 3.0–3.6 V, an increase in the amplitude of the signal of the first DLTS peak and further displacement toward lower temperatures were observed. The thermal activation energy and the trapping cross section determined for this DLTS peak varied in the ranges $E_a=(314-360)$ meV and $\sigma_\rho=(0.10-3.0)\times10^{-15}$ cm$^2$. The values of $E_a$ and $\sigma_\rho$ determined by us show that another level, $H3$, with parameters differing from the preceding level is observed in this range of values of $U_r$. In this same range of values of $U_r$ the effective hole concentration on the $p^*(U_r)$ distribution profile increased from its minimum value in the depletion region to the second maximum in a hole accumulation region (Fig. 2b). In the third range $U_r=(3.6-4.4)$ V there was a shift of the position of the maximum of the first DLTS peak toward higher temperatures with little variation of its height. The thermal activation energy and the trapping cross section varied up to $E_a=293$ meV and $\sigma_\rho=2.6\times10^{-18}$ cm$^2$ (the $H4$ level). In addition, another low-temperature DLTS peak appeared, and it moved into the high-temperature portion of the spectrum as $U_r$ was increased. The thermal activation energy of the level associated with the $H1$ peak was 95 meV. In the fourth range $U_r=(4.4-6.0)$ V an increase in the height of the first DLTS peak and displacement of the position of its maximum toward higher temperatures were observed

TABLE I.

| Name of levels | Energy $E_a$, meV | Trapping cross section, $\sigma$ cm$^2$ | Corresponding levels in other studies |
|---|---|---|---|
| $H1$ | 95 | $7.2\times10^{-20}$ | |
| $H2$ | 225 | $2.7\times10^{-19}$ | |
| $H3$ | 360 | $3.0\times10^{-15}$ | $HL5$, $HL11$ (Ref. 21) |
| $H4$ | 293 | $2.6\times10^{-18}$ | |
| $H5$ | 314 | $7.9\times10^{-18}$ | |
| $H5$* | 397 | $2.6\times10^{-16}$ | $HL4$ (Cu), $H2$ (Refs. 21 and 23) |
| $H6$ | 454 | $5.2\times10^{-16}$ | |
| $H7$ | 562 | $1.9\times10^{-15}$ | $HL8$ (Fe) (Ref. 21) |
| $H8$ | 776 | $1.9\times10^{-15}$ | $H5$ (Ref. 23) |

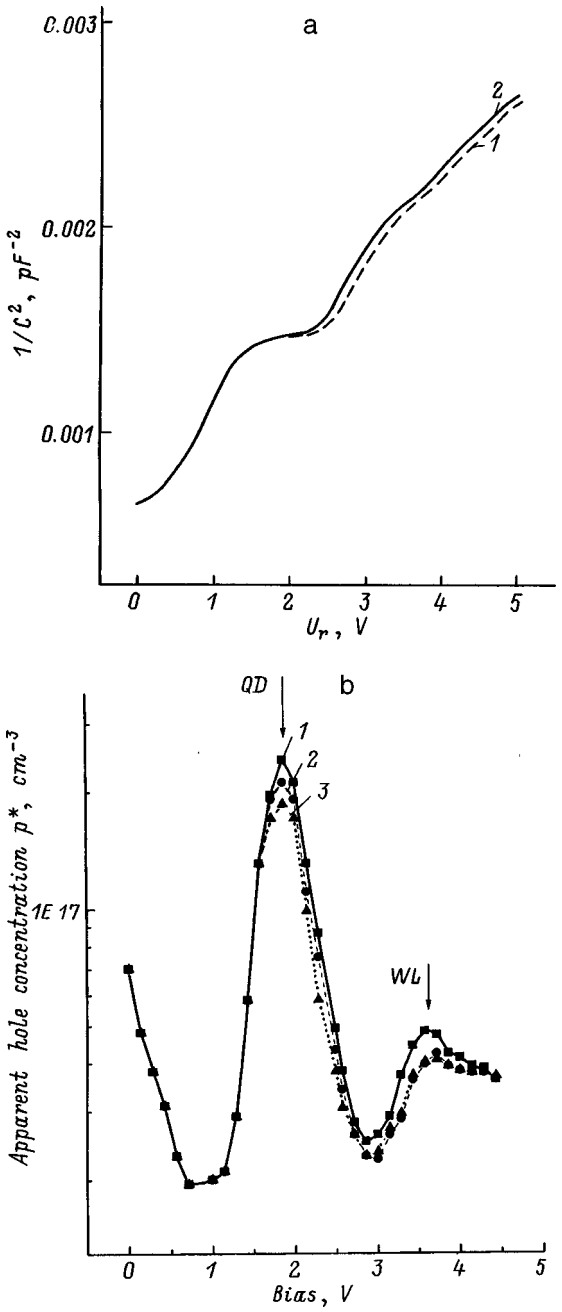


FIG. 2. $C^{-2}(V_r)$ (a) and $p^*(U_r)$ (b) characteristics of a $p-n$ heterojunction with a single array of InAs quantum dots in a GaAs matrix measured with illumination by white light (*1*), with $U_r<0$ (*2*), and with $U_r=0$ without light (*3*) after an isochronal anneal at $T_a=450$ K and preliminary deposition with $U_r<0$.

(Fig. 3). When we measured the DLTS spectra with various values of $U_f$ and $U_r$ and a fixed value of the difference between them, $\Delta U$, on a series of samples cleaved from different parts of a slab, we observed the same variations of the DLTS signal with increasing $U_r$ (Fig. 3b) as at a fixed value of $U_f$. A sharp decrease in the amplitude of the DLTS signal was discovered on other samples. The parameters of the levels are listed in Table I. The concentration of these levels determined for $U_r=5$ V was $N_t=4.5\times10^{14}$ cm$^{-3}$.

Investigations of the dependence of the DLTS spectra on the temperature and conditions of the preliminary isochronal anneal (with $U_r<0$ or $U_r=0$), as well as at four different values of $U_r$, were performed. The values of $U_r$ correspond to the values at which the previously noted characteristic changes in the behavior of the DLTS spectra were observed. Figure 4a presents the DLTS spectra measured with various values of $U_r$ after preliminary isochronal annealing of the sample at $T_a=450$ K with an applied reverse bias voltage $U_r<0$ or $U_r=0$. These measurements showed that following isochronal annealing with $U_r=0$ and $T_a=450$ K the amplitudes of the low-temperature $H2^*$, $H3^*$, and $H4^*$ DLTS peaks measured with $U_r=3.0$, 3.5, and 4.0 V are smaller than the amplitudes observed following annealing with $U_r<0$. A transformation from the state with $H2^*$, $H3^*$, and $H4^*$ to the state with $H2$, $H3$, and $H4$ and in the reverse direction took place at an annealing temperature of about 250 K. Similar changes were also noted for the first hole accumulation peak on the $p^*(U_r)$ profile. In the DLTS spectrum measured with $U_r=5$ V the $H5$ vanished, and a new peak, $H5^*$, formed. Its amplitude increased with displacement toward higher temperatures, and it thus exhibited properties which are usually observed for a bistable defect.[15–17] Optical illumination during measurement of the DLTS spectrum led to enhancement of the DLTS signal in the region of the low-temperature maximum (Fig. 4b).

## 4. DISCUSSION OF RESULTS

The measurements of the DLTS spectra (Figs. 3 and 4) as functions of $U_r$ and $U_f$ showed that four ranges of $U_r$, in which significant changes in the DLTS spectra occur, can be identified. The same ranges of $U_r$ during the measurements specify four characteristic regions on the hole distribution profile $p^*(U_r)$. The measurements of the DLTS spectra following preliminary isochronal annealing under two conditions (with $U_r<0$ or $U_r=0$), in turn, demonstrated that the first three ranges of $U_r$, in which there was a decrease in the amplitude of the DLTS peak following annealing with $U_r=0$, can be combined to form a single range. Accumulation and depletion regions associated with the quantum dots and the wetting layer were observed on the $p^*(U_r)$ distribution profile at these values of $U_r$ (Fig. 2b). The fourth range, where an increase in $U_r$ was accompanied by an increase in the width of the DLTS peak with a simultaneous increase in the amplitude of its maximum and displacement of its position toward higher temperatures, is characterized by a manifestation of bistability of the DLTS spectrum (Fig. 4). In this range of $U_r$ the hole concentration varies only slightly on the $p^*(U_r)$ distribution profile, and this GaAs region is directly adjacent to the InAs wetting layer (Fig. 2b). The variations in the DLTS spectra of the QD structures as a function of the applied bias voltage and the conditions of the isochronal anneal (Fig. 4) were similar to those previously observed in radiation-treated GaAs.[18,19] The DLTS spectra of GaAs displayed a broad band, which was assigned to clusters of closely arranged defects formed when it was irradiated. Carrier emission from a deep state of one of the defects in such a cluster could take place through shallower levels of another defect by means of a multiphonon tunneling hopping transition. In addition, it was found in Refs. 15 and 20 that the

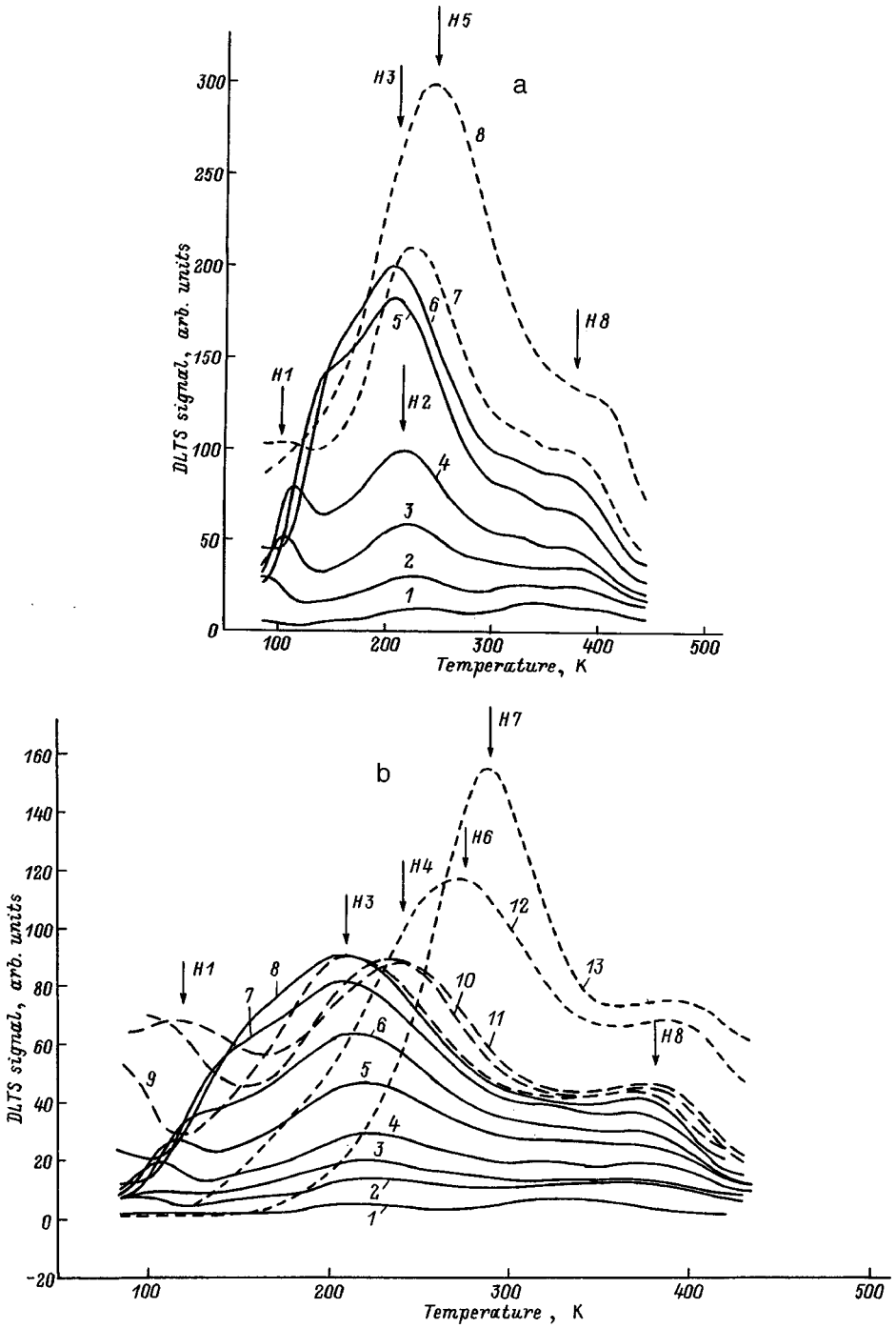


FIG. 3. DLTS spectra of a $p-n$ heterostructure with a single array of InAs quantum dots in a GaAs matrix measured under the following conditions: a — with a filling pulse height $U_f=1$ V and a reverse bias pulse height $U_r$ equal to 2 (*1*), 2.5 (*2*), 2.8 (*3*), 3.0 (*4*), 3.3 (*5*), 3.5 (*6*), 4.0 (*7*), and 5.0 V (*8*); b — for various values of $U_f$ and $U_r$, but with the fixed value $\Delta U=(U_r-U_f)=0.8$ V and $U_r$ equal to 1.8 (*1*), 2.4 (*2*), 2.6 (*3*), 2.8 (*4*), 3.0 (*5*), 3.2 (*6*), 3.4 (*7*), 3.6 (*8*), 3.8 (*9*), 4.2 (*10*), 4.4 (*11*), 5.4 (*12*), and 6.0 V (*13*).

clusters formed in GaAs either as a result of radiation treatment or during epitaxial growth from a Ga melt at high crystallization onset temperatures can exhibit the properties of configurational bistability. The DLTS measurements also revealed the formation of defect clusters in GaAs grown at low crystallization onset temperatures from a Ga melt. The results of our investigations thus show that the formation of a cluster, which is composed of defects characteristic of GaAs grown from a Ga melt (see Figs. 3 and 4, and Table I) and which displays bistability properties, takes place in low-temperature GaAs layers directly adjacent to the QD's and the InAs wetting layer. This is consistent with the results of the TEM investigations (Fig. 1), which show that the growth of the QD's is not absolutely coherent and that there are regions clearly containing dislocations in stressed islands and stacking defects in the upper layer.

The bistability of the structures investigated is also manifested by the dependence of the $p^*(U_r)$ distribution profile on the conditions of the preliminary isochronal anneal and the employment of optical illumination during the $C-V$ measurements (Fig. 2). These effects are similar to the phenomena observed for the $DX$ center in AlGaAs, whose concentration is comparable to the concentration of the donor impurity.[22] The $DX$ center is characterized by the existence of two configurations. In one configuration it is a trap with a deep level, in which a carrier can be trapped at temperatures

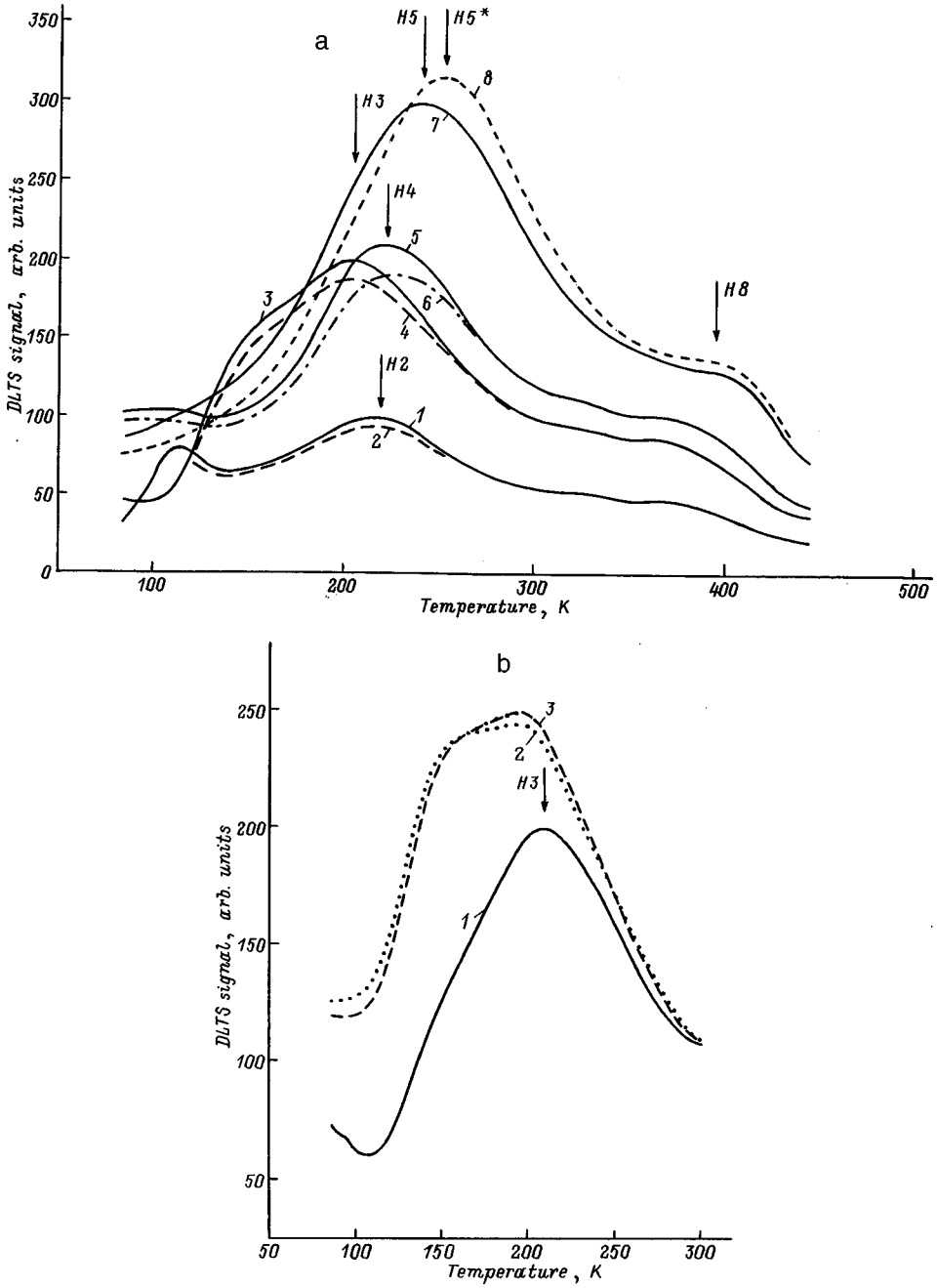


FIG. 4. DLTS spectra of a $p-n$ heterostructure with a single array of InAs quantum dots in a GaAs matrix measured with a filling pulse height $U_f=1$ V after an isochronal anneal at $T_a=450$ K and preliminary deposition with $U_r<0$ ($U_r$ during measurements, V: *1* — 3.0, *3* — 3.5, *5* — 4.0, *7* — 5.9) and $U_r=0$ ($U_r$ during measurements, V: *2* — 3.0, *4* — 3.5, *6* — 4.0, *8* — 5.9) (a) and measured with $U_r=3.6$ (*1* — without light, *3* — with illumination by white light) and $U_r=0$ (*2* — with illumination by white light during the measurements of the DLTS spectrum) (b).

sufficient for overcoming the potential barrier. A fairly high temperature is also needed for reverse emission from this self-trapping level. In the other configuration it is a shallow donor. When the *DX* center takes on the configuration with a shallow donor level, the conductivity of the sample rises. The transformation of the *DX* center from the configuration with a deep level to the configuration with a shallow level can be induced by optical excitation or by heating the sample. A preliminary isochronal anneal under appropriate conditions (with $U_r<0$ or $U_r=0$) can also transform the defect from one configuration to the other. In our case the increase in the hole concentration during annealing with $U_r<0$, during which the defect like the *DX* center transforms into a configuration with a shallow level, should occur with displacement of the position of the Fermi level closer to the valence band. As a result, the occupancy of the spatially localized quantum or surface states by holes should increase. We also observed an increase in the hole concentration in such states as a function of the conditions of the isochronal anneal when we determined the $p^*(U_r)$ distribution profile (Fig. 2b). In the case of spatially localized states this should also lead to an increase in the height of the peak of the DLTS signal. In the case of a quantum well, for example, it is known that the DLTS signal is specified by the relation[7]

$$\Delta C/C=p_wL/(2N_aW^2), \tag{1}$$

where $C$ is the capacitance of the space-charge layer for the reverse bias voltage at which the DLTS signal is measured, $p_w$ is the surface concentration of holes trapped in a well, $L$ is the depth of the quantum-well layer, $W$ is the width of the space-charge region, $\varepsilon$ is the dielectric constant, $q$ is the charge of an electron, and $N_a$ is the concentration of accep-

tors in the GaAs layer. Since $W^2=(2\varepsilon/qN_a)$, we can reduce Eq. (1) to the form $\Delta C/C\approx p_w L$. Hence it follows that enhancement of the DLTS signal should be observed as the population of the localized states ($p_w$) increases. At the same time, for defects distributed across the entire thickness of the semiconductor layer, the DLTS signal is specified by the relation[4]

$$\Delta C/C\approx N_t/2N_a \tag{2}$$

and its amplitude decreases as the concentration of the deep levels of the bistable defect $N_t$ falls and the concentration of the shallow acceptors $N_a$ rises. The increase in the amplitude of the signal in the DLTS spectra observed in response to optical illumination was also a manifestation of an effect associated with the presence of traps with a self-trapping level in the structure (Fig. 4b).

The DLTS spectra measured with various values of $U_r$ from the first three ranges contained the $H2$, $H3$, and $H4$ peaks, whose amplitudes rose as a result of isochronal anneals with $U_r<0$ and declined as a result of anneals with $U_r=0$ (Figs. 3 and 4). It follows from the foregoing material that all three levels associated with these peaks are spatially localized states. Let us consider each of them individually. The $H2$ peak was observed in the DLTS spectra measured with values of $U_r$ from the first range. The thermal activation energy corresponding to this peak varied in the range $E_a=225-240$ meV. The spatial localization of the $H2$ peak (Figs. 3 and 4) coincided with the first hole accumulation peak on the $p^*(U_r)$ profile (Fig. 2b) and with QD's, which were determined from the TEM investigations. The PL investigations revealed the presence of a band for the QD exciton ground state with an energy of 1.19 eV and a width of 110 meV in the luminescence spectra. In addition, taking into account the results in Refs. 13 and 14, we estimated the electron ground-state energy, which was found to be $\approx 100$ meV. Summing the values of the hole energy and the electron ground-state energy with the QD exciton ground-state energy, we obtain a total value of 1.515 meV, which roughly coincides with the gap width of GaAs. All these results, taken collecively, provide some basis to assume that the $H2$ level observed in the DLTS spectra is the quantum-dot hole ground state. Equation (1) was used to estimate the maximum surface concentration of holes $p_d$ in a quantum dot, which was found to be equal to $9.4\times 10^9$ cm$^{-2}$. This value is in good agreement with the value of the dot concentration determined using TEM, if it is assumed that each ground quantum state contains two holes with opposite spins. We also estimated the hole concentration in a quantum dot from the results of the $C-V$ measurements (Fig. 2a) using the relation $p_d=C^*(U_{r2}-U_{r1}/Aq)$, where $C^*$ is the capacitance on the plateau of the $C-V$ characteristic, $U_{r1}$ and $U_{r2}$ are the values of the bias voltage at the beginning and end of the plateau, and $A$ is the area of the diode. It was equal to $1.4\times 10^{11}$ cm$^{-2}$, which is significantly greater than the concentration estimated from the height of the DLTS peak. These discrepancies are possibly attributable to the fact that the $C-V$ measurements give the total value of the concentration of ground- and excited-state holes in a quantum dot, since the spatial resolution of our capacitance bridge may be insufficient for distinguishing between them, and we observe one long plateau with a gently increasing capacitance instead of two or three shorter plateaus. The DLTS spectra for different values of $U_r$ in the second range display the $H3$ peak, whose spatial localization region coincides with the depletion region and the position of the maximum of the second peak on the hole distribution profile $p^*(U_r)$. The thermal activation energy of the level associated with this peak varied in the range 314–360 meV as $U_r$ was increased. These values significantly exceed the values which we estimated in Refs. 13 and 14 for the quantum states of a dot and for the wetting layer. Therefore, the spatially localized $H3$ level can be a surface state of the GaAs/InAs wetting layer interface. This, in turn, allows us to assign the second peak on the hole distribution profile $p^*(U_r)$ (Fig. 2b) to a surface state of the GaAs/InAs interface or to the wetting-layer quantum well. A comparison of the parameters of the $H3$ level with the known parameters for GaAs revealed that at large values of $U_r$ its parameters approximate those of the $H2$ level[23] and the $HL11$ and $HL5$ levels.[21] As was established in Ref. 24, the last of these levels forms when GaAs is grown from a Ga melt and is associated with a complex containing $V_{\mathrm{As}}$. The surface concentration of the $H3$ level, like that of the $H2$ level, was estimated using Eq. (1) and was found to be equal to $2.0\times 10^{10}$ cm$^{-2}$, which is twice as large as the hole concentration in quantum dots. Finally, let us consider the last spatially localized peak, i.e., the $H4$ peak, which appears in the DLTS spectra measured with various values of $U_r$ in the fourth range. The spatial localization region of this DLTS peak coincides with the second maximum on the hole distribution profile $p^*(U_r)$. The position of the $H4$ DLTS peak shifts toward higher temperatures as $U_r$ is increased and the filling pulse height $U_f$ is diminished. It may be identical to the $H3$ surface level localized at the GaAs/InAs interface. One of the causes of the observed changes in the position of the $H4$ peak can be the Coulomb interaction between holes localized in the wetting-layer quantum well and ionized acceptor surface states of the GaAs/InAs interface, which leads to the formation of a dipole and alteration of the energy for the thermal ionization of holes from this level. At relatively small values of $U_r$ in the second range, penetration of the field of the space-charge layer is screened by carriers of localized surface states, and emission takes place from a narrow region in the vicinity of the point where the Fermi level intersects the deep state. When $U_r$ is increased, hole emission from the narrow region will progressively increase and begin to significantly exceed the hole emission from the $H3$ quantum level. This process also determines the observed growth and displacement of the $H3$ peak toward the low-temperature portion of the DLTS spectrum in the second range of $U_r$ values (Fig. 3). When $U_r=3.6$ V, the bias voltage $U_r$ becomes such that all the surface states are completely emptied in the field of the space-charge layer and saturation of the $H3$ peak is observed in the DLTS spectrum. A further increase in the value of $U_r$ initiates a penetration of the space-charge field into the quantum well. When a filling pulse of height $U_f$ is applied, the quantum well and the surface states are populated. After a reverse bias pulse is applied, hole emission from the quantum state begins at low

temperatures. When the temperature rises, a two-stage transition consisting of the emission of holes into freed states of the InAs quantum well followed by their emission into the GaAs valence band becomes likely for holes that populate surface states of the GaAs/InAs interface.[18] The rate of emission $e_i$ in the two-stage transition depends on the rates of emission from the surface level ($e_s$) and the quantum well ($e_w$) and the rates of jumps between them $R_{sw}$ and $R_{ws}$. As was found in Ref. 18, if $R_{ws} > e_w$, the emission rate is specified by the relation

$$e_i = e_s + (\exp(E_s - E_w)/kT)/e_w, \quad (3)$$

where $E_s$ is the energy of the surface level, $E_w$ is the position of the Fermi level in the quantum well, and $k$ is Boltzmann's constant. It follows from Eq. (3) that the position of the DLTS peak associated with surface transitions will differ from that for direct hole emission from a surface level. These transitions are responsible, in particular, for the appearance of the broad low-temperature band in the DLTS spectra (Fig. 3). The simultaneous existence of ionized acceptor surface states and holes in a quantum well, which leads to the formation of a dipole,[25,26] becomes possible in a thin layer on both sides of the interface. The formation of dipoles[9,10] is also possible between quantum-well holes and ionized levels of $Ga_{As}$, which is a double acceptor with 77 and 230 meV levels.[27] The electrostatic potential of such dipoles can lead to alteration of the band-discontinuity potential barrier on the heterojunction and the ionization energy of the levels, as well as the trapping cross sections for carriers on them, whose values depend on the values of the applied bias voltage $U_r$ and the filling pulse height $U_f$. The changes occurring in response to an increase in $U_r$ also cause displacement of the $H4$ peak into the high-temperatures region of the DLTS spectrum and the appearance of the $H1$ peak, which emerges from the region below 80 K (Fig. 3b). The $H1$ peak is probably attributable specifically to hole emission from the wetting-layer quantum well.

## 5. CONCLUSIONS

We have carried out detailed $C-V$ and DLTS measurements of InAs/GaAs $p-n$ structures that contain a single array of InAs QD's in a GaAs matrix with the employment of such methods as transmission electron microscopy and photoluminescence spectroscopy. The presence of a cluster of interacting bistable defects has been discovered in GaAs layers grown at low temperature. We have also discovered controllable and reversible metastable population of quantum-dot energy states and monoenergetic surface states, which depends on the temperature and conditions of the preliminary isochronal anneal. This effect is associated with the presence of bistable traps with self-trapped holes. The DLTS measurements have revealed variation of the energy for the thermal ionization of holes from surface states of the InAs/GaAs heterojunction and the wetting layer as the reverse bias voltage is increased. It has been theorized that these changes are caused by the built-in electric field of a dipole, which can be formed either by wetting-layer holes or by ionized levels located near the heterojunction.

[1] Y. Arakawa and A. Yariv, IEEE J. Quantum Electron. **QE-22**, 1887 (1986).
[2] V. M. Ustinov, A. Yu. Egorov, A. R. Kovsh, A. E. Zhukov, M. V. Maksimov, A. F. Tsatsulńikov, N. Yu. Gordeev, S. V. Zaitsev, Yu. M. Shernyakov, N. A. Bert, P. S. Kopév, Zh. I. Alferov, N. N. Ledentsov, J. Bohrer, D. Bimberg, A. O. Kosogov, P. Werner, and U. Gosele, J. Cryst. Growth **175/176**, 689 (1997).
[3] S. V. Zaitsev, N. Yu. Gordeev, V. I. Kopchatov, V. M. Ustinov, A. E. Zhukov, A. Yu. Egorov, N. N. Ledentsov, M. V. Maximov, P. S. Kopév, A. O. Kosogov, and Zh. I. Alferov, Jpn. J. Appl. Phys. **36**, 4219 (1997).
[4] D. V. Lang, J. Appl. Phys. **45**, 3023 (1974).
[5] T. Matsumoto, Y. Ito, and T. Ishida, J. Appl. Phys. **28**, L541 (1989).
[6] K. L. Jiao and W. A. Anderson, J. Appl. Phys. **73**, 271 (1993).
[7] K. Schmalz, I. N. Yassievich, H. Rücker, H. G. Grimmeiss, H. Frankenfeld, H. J. Osten, P. Schley, and H. P. Zeindl, Phys. Rev. B **50**, 14 287 (1994).
[8] S. Anand, N. Carlsson, M.-E. Pistol, L. Samuelson, and W. Seifert, Appl. Phys. Lett. **67**, 3016 (1995).
[9] M. M. Sobolev, A. R. Kovsh, V. M. Ustinov, A. Yu. Egorov, A. E. Zhukov, M. V. Maximov, and N. N. Ledentsov, in *Proceedings of the 19th International Conference on Defects in Semiconductors, July 21–25, 1997, Aveiro, Portugal* [Mater. Sci. Forum **258–263**(3), 1619 (1997)].
[10] M. M. Sobolev, F. V. Kovsh, V. M. Ustinov, A. Yu. Egorov, A. E. Zhukov, M. V. Maksimov, and N. N. Ledentsov, Fiz. Tekh. Poluprovodn. **31**, 1249 (1997) [Semiconductors **31**, 1074 (1997)].
[11] P. N. Brunkov, S. G. Konnikov, V. M. Ustinov, A. E. Zhukov, A. Yu. Egorov, M. V. Maksimov, N. N. Ledentsov, and P. S. Kopév, Fiz. Tekh. Poluprovodn. **30**, 924 (1996) [Semiconductors **30**, 492 (1996)].
[12] R. A. Suris, in *Proceedings of the 7th Winter School on Semiconductor Physics* [in Russian], Leningrad (1975), p. 245.
[13] M. Grundmann, N. N. Ledentsov, O. Stier, D. Bimberg, V. M. Ustinov, P. S. Kopév, and Zh. I. Alferov, Appl. Phys. Lett. **68**, 979 (1996).
[14] N. N. Ledentsov, V. M. Ustinov, V. A. Shchukin, P. S. Kop'ev, Zh. I. Alferov, and D. Bimberg, Fiz. Tekh. Poluprovodn. **32**, 385 (1998) [Semiconductors **32**, 343 (1998)].
[15] P. N. Brunkov, S. G. Konnikov, M. I. Papentsev, M. M. Sobolev, and M. N. Stepanova, Fiz. Tekh. Poluprovodn. **23**, 1689 (1989) [Sov. Phys. Semicond. **23**, 1044 (1989)].
[16] M. M. Sobolev, M. I. Papentsev, and I. V. Kochnev, Fiz. Tekh. Poluprovodn. **28**, 663 (1994) [Semiconductors **28**, 397 (1994)].
[17] M. M. Sobolev, I. V. Kochnev, M. I. Papentsev, and V. S. Kalinovsky, Semicond. Sci. Technol. **11**, 1692 (1996).
[18] Sh. Makram-Ebeid and P. Boher, Rev. Phys. Appl. **23**, 847 (1988).
[19] P. N. Brunkov, V. S. Kalinovsky, V. G. Nikitin, and M. M. Sobolev, Semicond. Sci. Technol. **7**, 1237 (1992).
[20] P. N. Brunkov, V. S. Kalinovskiĭ, S. G. Konnikov, M. M. Sobolev, and O. V. Sulima, Fiz. Tekh. Poluprovodn. **24**, 1320 (1990) [Sov. Phys. Semicond. **24**, 830 (1990)].
[21] A. Mitonneau, G. M. Martin, and A. Mircea, Electron. Lett. **13**, 666 (1977).
[22] P. J. Mooney, Appl. Phys. **67**, R1 (1990).
[23] D. Steivenard, J. C. Bourgoin, and D. Pons, Phys. Rev. B **34**, 4048 (1986).
[24] P. N. Brunkov, S. Gaĭbullaev, S. G. Konnikov, V. G. Nikitin, M. I. Papentsev, and M. M. Sobolev, Fiz. Tekh. Poluprovodn. **25**, 338 (1991) [Sov. Phys. Semicond. **25**, 205 (1991)].
[25] F. Capasso and F. Beltram, Mater. Res. Soc. Symp. Proc. **104**, 47 (1988).
[26] G. Müller, A. Zrenner, F. Koch, and K. Ploog, Appl. Phys. Lett. **55**, 1564 (1989).
[27] P. Won Yu, W. C. Mitchel, M. G. Mier, S. S. Li, and W. L. Wang, Appl. Phys. Lett. **41**, 532 (1982).

Translated by P. Shelnitz

# Influence of growth conditions on the formation and luminescence properties of InGaAs quantum dots in a Si matrix

A. E. Zhukov,* A. Yu. Egorov, A. R. Kovsh, V. M. Ustinov, N. N. Ledentsov, M. V. Maksimov, A. F. Tsatsul'nikov, B. V. Volovik, P. S. Kop'ev, and Zh. I. Alferov

*A. F. Ioffe Physicotechnical Institute, Russian Academy of Sciences, 194021 St. Petersburg, Russia*
(Submitted September 15, 1998; accepted for publication September 16, 1998)
Fiz. Tekh. Poluprovodn. **33**, 194–197 (February 1999)

The influence of the growth conditions during molecular-beam epitaxy and of the degree of lattice mismatch between the epilayer and the substrate on the formation of InGaAs islands on a Si(100) surface is studied. An increase in lattice mismatch (the InAs mole fraction) leads to an increase in the critical thickness corresponding to the onset of island growth, in contrast to the formation of InGaAs islands on GaAs(100). An increase in the deposition temperature also increases the critical thickness, whereas an increase in the arsenic pressure has the opposite effect. Structures containing an array of InGaAs islands in a Si matrix display a luminescence line in the range 1.2–1.3 $\mu$m, depending on the mole fraction of InAs. © *1999 American Institute of Physics.* [S1063-7826(99)00802-9]

Silicon is still the principal material used in semiconductor microelectronics. Although the electrical characteristics of transistors based on III-V materials are superior to those of silicon metal-oxide-semiconductor (MOS) transistors, the latter are characterized by a significantly lower cost and simpler fabrication. However, the use of silicon in light-emitting devices is hampered by the indirect structure of the energy bands. The integration of logic circuits based on silicon with III-V optoelectronic devices is very promising for device applications.

One of the ways to create such structures involves the use of heterostructures based on direct-gap III-V semiconductor compounds grown on a fairly thin GaAs or InGaAs buffer layer deposited on a Si substrate.[1,2] The main problems are then associated with the formation of a domain structure when the III-V layers are grown on Si, as well as with the formation of misfit dislocations in the buffer layer, which subsequently extend into the active layers and are caused by the great difference between the lattice constants of the buffer layer and the substrate.

An alternative approach is to form optically active, direct-gap islands directly in a silicon matrix.[3] If the lateral dimensions of these islands are sufficiently small (less than 100 nm), they will have a single-domain structure, and there will be no misfit dislocations. In addition, the use of an indirect-gap material as a waveguide layer in a laser structure permits significant reduction of the contribution due to the radiative recombination of nonequilibrium charge carriers in the waveguide region to the threshold current density.[4]

Lattice mismatch can serve as the driving force for forming these islands. It was previously shown in Refs. 5–7 that when a certain critical thickness is achieved during the deposition of a highly stressed InGaAs layer on a GaAs(100) surface, there is a transition from a two-dimensional (layer-by-layer) to a three-dimensional (island) growth regime, which leads to the spontaneous formation of elastically stressed InGaAs islands in the gallium arsenide matrix.

The possibility of creating stressed InGaAs islands in a silicon matrix was reported in Ref. 8. Their dimensions were estimated using tunneling microscopy to be about 20 nm along the base and 4 nm in the vertical direction with a surface density of the order of $5\times10^{11}\,\mathrm{cm}^{-2}$. The formation of islands leads to the appearance of an intense band in the photoluminescence spectra at 1.2–1.3 $\mu$m (77 K). In our study we investigated the influence of the deposition regimes on the process leading to their formation.

The structures investigated were grown in an É P-1203 molecular-beam epitaxy (MBE) system (Russia) on Si substrates oriented in the [100] direction. The substrates were prepared by a standard chemical-etching procedure.[9] Removal of the surface oxide layer in the MBE system at 850 °C led to the appearance of a band $2\times1$ high-energy electron diffraction (HEED) pattern. The transition from the two-dimensional to the island growth regime during the deposition of $In_xGa_{1-x}As$ ($x=0-1$) on a silicon surface was monitored directly during the growth process by observing the transition from a band to a point HEED pattern. The growth rate was 0.3–0.5 monolayers/s. The deposition temperature was varied in the range 250–500 °C. The array of InGaAs islands formed was then covered by a silicon layer of thickness 50 nm, which was grown from a solid-state Si source operating at a temperature close to the melting point of Si, which ensured a growth rate of about 1 nm/min.

The photoluminescence of the samples was investigated at 77 K with excitation by an $Ar^+$ laser (514.5 nm) having a power density of 500 W/cm$^2$ and detection by a Ge photodiode.

The HEED investigations showed that the quantity of $In_xGa_{1-x}As$ deposited that corresponds to island growth depends strongly on both the deposition conditions (the substrate pressure and arsenic pressure) and on the mole fraction of InAs in the material deposited.

The dependence of the effective thickness of $In_xGa_{1-x}As$ deposited at the onset of island growth ($h_c$) on

 

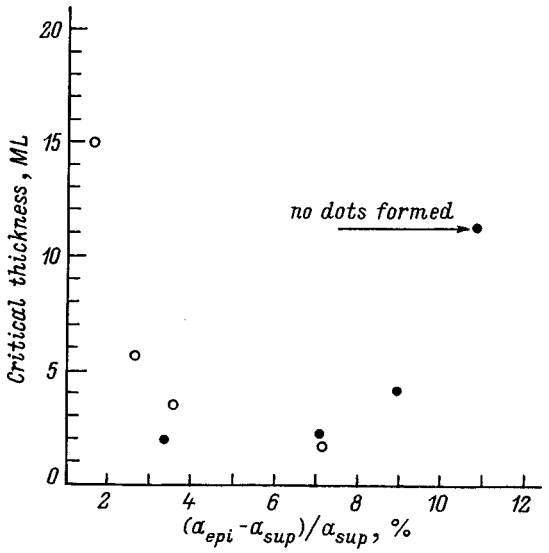


FIG. 1. Dependence of the thickness of deposited $In_xGa_{1-x}As$ corresponding to the onset of island growth ($h_c$) on the degree of lattice mismatch ($\delta$) with respect to the substrate: Si (filled points), GaAs (unfilled points). The deposition temperature was 480 °C.

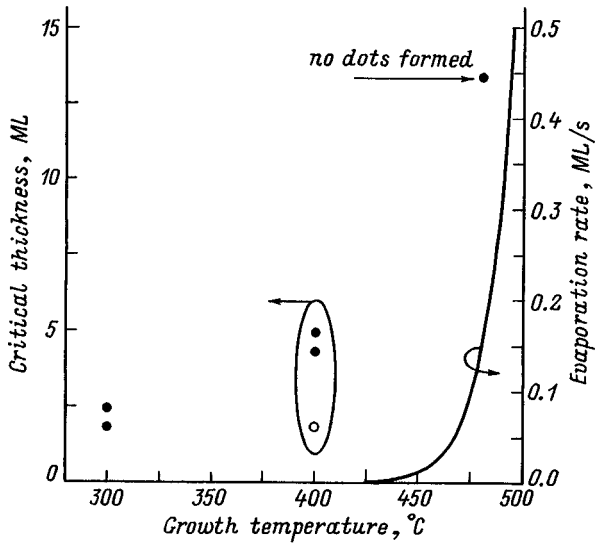


FIG. 2. Dependence of the thickness of deposited InAs corresponding to the onset of island growth during deposition on a Si(100) surface on growth temperature. The arsenic pressure is $1\times10^{-6}$ (filled points) and $3\times10^{-6}$ Pa (unfilled points). Solid curve — temperature dependence of the re-evaporation rate of InAs from the Si surface calculated with consideration of the influence of the mismatch stress.

the degree of lattice mismatch between the epilayer and the substrate ($\delta$) is shown in Fig. 1 for a deposition temperature of 480 °C

$$\delta=(a_{\text{epi}}-a_{\text{sub}})/a_{\text{sub}}, \tag{1}$$

where $a_{\text{epi}}$ and $a_{\text{sub}}$ are the lattice constants of the deposited layer and the substrate, respectively.

It was found that a deposition of a GaAs layer on a Si(100) surface, which corresponds to $\delta\approx4\%$, gives rise to a transition to island growth when 2 monolayers (ML) are completed. An increase in the mole fraction of InAs in the material deposited leads, at first, to a slow increase in $h_c$ and, above $x=0.5$, to a sharper increase in this parameter. When pure InAs was deposited ($\delta=11.5\%$) under the conditions indicated, island formation was not observed at all in the HEED pattern up to 11 ML.

For comparison, Fig. 1 shows our data regarding the dependence of $h_c$ on $\delta$ for a system of $In_xGa_{1-x}As$ islands on a GaAs(100) surface. Since the cause of the transition from the two-dimensional to the three-dimensional growth regime is the stress caused by mismatch of the lattice constants of the epilayer and the substrate, an increase in mismatch should, in general, lead to a decrease in the critical thickness for the transition to the island growth regime, as was observed experimentally in the case of the deposition of InGaAs on GaAs (see also Ref. 10). In contrast to this system, in the case of the deposition of InGaAs on Si the critical thickness for the onset of island growth increases, rather than decreases, as the degree of mismatch increases.

Figure 2 shows the dependence of the effective thickness $h_c$ for the onset of the island growth of InAs on a Si surface on deposition temperature. As can be seen from this plot, while a three-dimensional growth regime is achieved after the deposition of about 2 ML at low temperature (about 300 °C), raising the substrate temperature to 400 °C leads to an increase in the required amount of material to 5 ML, and at 480 °C and higher temperatures the transition to island growth is not observed at all.

A threefold increase in the arsenic pressure during the deposition of InAs at 400 °C permits acceleration of the island formation process. In this case, as is shown in Fig. 2, an island growth regime is achieved after the deposition of 2 ML, which corresponds to the value of $h_c$ at 300 °C and the usual arsenic pressure. However, at both lower (300 °C) and higher (480 °C) temperatures an increase in the As pressure does not have an appreciable influence on the critical thickness.

Thus, there is a certain critical deposition temperature, above which the transition to island growth is not observed. Near that temperature the value of $h_c$ is determined to a significant degree by the arsenic pressure.

According to the theory for the spontaneous formation of a three-dimensional nucleus,[11] a significant influence on this process is exerted by the value of the surface energy, which, in turn, can depend on the deposition conditions. This provides a qualitative explanation for the influence of the substrate temperature and the arsenic pressure on the formation of InGaAs islands on a silicon surface. An increase in the effective thickness of deposited InGaAs, which corresponds to the onset of island growth, can also be caused by the partial re-evaporation of In atoms from the growth surface when the temperature is increased. As we know, the onset of the intense re-evaporation of In during deposition on a GaAs surface corresponds to a temperature of about 540 °C.[12] The larger value of the mismatch stress in the case of the deposition of InAs on a Si surface makes a contribution to the Gibbs free energy and leads to displacement of the point for the onset of intense re-evaporation toward lower temperatures. Figure 2 shows a theoretical plot of the re-evaporation

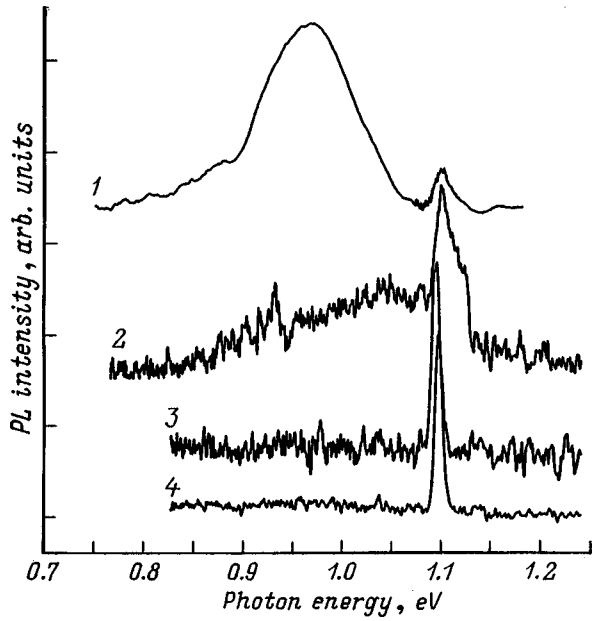


FIG. 3. Photoluminescence spectra recorded at 77 K for structures with $In_xGa_{1-x}As$ islands in a Si matrix [7 ML of InAs at a deposition temperature of 400 °C (*1*) and 3 ML of $In_{0.5}Ga_{0.5}As$ deposited at 480 °C (*2*)]. For comparison, the spectra of a structure with a two-dimensional InAs layer in a Si matrix (3.5 ML of InAs deposited at 400 °C) (*3*), as well as the Si substrate (*4*), are shown.

rate of InAs from a Si surface calculated according to the thermodynamic model in Ref. 13. As is seen, when an InAs growth rate equal to 0.3 ML/s is used in the experiments, re-evaporation can be significant at 460 °C and higher temperatures, but at lower temperatures it has hardly any influence, and it apparently cannot be a decisive factor in the increase in $h_c$ with increasing temperature.

The photoluminescence (PL) spectra of several samples containing arrays of silicon-capped InGaAs islands are shown in Fig. 3. For comparison, the figure also shows the PL spectra of a silicon buffer layer and a sample in which the amount of InGaAs deposited was insufficient for the transition to the island growth regime and, thus, the formation of three-dimensional islands was not observed. In the latter cases only the silicon line at 1.1 eV, which is associated with TO-phonon emission, is observed in the PL spectra. The formation of an array of InGaAs islands leads to the appearance of a new line with a wavelength of about 1.2–1.3 $\mu$m in the PL spectra. An increase in the mole fraction of GaAs in the material forming the islands leads to a regular blue shift of the island emission due to an increase in the InGaAs gap width.

The small electron effective mass and the relative small conduction-band offset on the Si/InGaAs boundary can lead to the absence of a bound electronic state in thin two-dimensional InGaAs layers in silicon.[1] We assume that just this situation is responsible for the absence of emission from InGaAs in samples of subcritical thickness. At the same time, the formation of islands, as in the case of a system of InGaAs quantum dots in a GaAs matrix,[14] leads to lowering of the quantum-well energy and the existence of an electronic level in the islands, causing the appearance of a line in the range 1.2–1.3 $\mu$m. In addition, the absence of this line in the spectra of samples in which islands were not formed proves that it is not caused by point defects on the InGaAs/Si boundary or by impurities in the silicon matrix.

We assume that optimization of the regimes for both growth of the InGaAs islands themselves and their capping by silicon permits raising the luminescence intensity and opens the prospect for the possible employment of self-organized arrays of InGaAs islands in Si as a base for a new generation of silicon-based light-emitting devices.

In summary, we have investigated the influence of the deposition conditions and the degree of lattice mismatch between the epitaxial layer and the substrate on the formation of an array of InGaAs islands on Si(100) during molecular-beam epitaxy. An anomalous dependence of the critical thickness corresponding to the onset of island growth on the degree of mismatch has been discovered; i.e., an increase in the InAs mole fraction leads to an increase in the critical thickness, in contrast with the case of the formation of InGaAs islands on GaAs(100). There is a certain critical deposition temperature, above which the transition to island growth is not observed. Near the critical temperature, raising the arsenic pressure accelerates island formation. Samples containing an array of InGaAs islands in a Si matrix display a line in the luminescence spectra with a wavelength in the range 1.2–1.3 $\mu$m, which depends on the mole fraction of InAs.

This work was carried out with support from INTAS (Grant No. 96-0242) and the Physics of Solid-State Nanostructures Program (Project 97-1090).

*)E-mail: zhukov@beam.ioffe.rssi.re

[1] T. Yamada, M. Tachikawa, T. Sasaki, H. Mori, and Y. Kadota, Appl. Phys. Lett. **70**, 1614 (1997).
[2] T. Egawa, Y. Hasegawa, T. Jimbo, and M. Umeno, Appl. Phys. Lett. **67**, 2995 (1995).
[3] N. N. Ledentsov, in *Proceedings of the 23rd International Conference on the Physics of Semiconductors, Berlin, Germany, July 21–26, 1996*, edited by M. Scheffler and R. Zimmermann, World Scientific, Singapore, (1996), Vol. 1, p. 19.
[4] P. Blood, in *Physics and Technology of Heterojunction Devices*, D. V. Morgan and R. H. Williams (Eds.), P. Peregrinus, London (1991), Chap. 7, p. 231.
[5] L. Goldstein, F. Glas, J. Y. Marzin, M. N. Charasse, and G. Le Roux, Appl. Phys. Lett. **47**, 1099 (1985).
[6] P. M. Petroff and S. P. Den Baars, Superlattices Microstruct. **15**, 15 (1994).
[7] A. Yu. Egorov, A. E. Zhukov, P. S. Kop'ev, N. N. Ledentsov, M. V. Maksimov, and V. M. Ustinov, Fiz. Tekh. Poluprovodn. **28**, 1439 (1994) [Semiconductors **28**, 809 (1994)].
[8] G. E. Cirlin, V. G. Dubrovskii, V. N. Petrov, N. K. Polyakov, N. P. Korneeva, V. N. Demidov, A. O. Golubok, S. A. Masalov, D. V. Kurochkin, O. M. Gorbenko, N. I. Komyak, V. M. Ustinov, A. Yu. Egorov,
A. R. Kovsh, M. V. Maximov, A. F. Tsatsul'nikov, B. V. Volovik, A. E. Zhukov, P. S. Kop'ev, Zh. I. Alferov, N. N. Ledentsov, M. Grundmann, and D. Bimberg, Semicond. Sci. Technol. **13**, 1262 (1998).
[9] A. Ishisaka and Y. Shiraki, J. Electrochem. Soc. **133**, 666 (1986).
[10] D. Leonard, K. Pond, and P. M. Petroff, Phys. Rev. B **50**, 11 687 (1995).

[11] V. A. Shchukin, N. N. Ledentsov, P. S. Kop'ev, and D. Bimberg, Phys. Rev. Lett. **75**, 2968 (1995).
[12] M. McElhinney and C. R. Stanley, Electron. Lett. **29**, 1302 (1993).
[13] A. Yu. Egorov, A. R. Kovsh, A. E. Zhukov, V. M. Ustinov, and P. S. Kop'ev, Fiz. Tekh. Poluprovodn. **31**, 1153 (1997) [Semiconductors **31**, 989 (1997)].
[14] A. Yu. Egorov, A. E. Zhukov, P. S. Kop'ev, N. N. Ledentsov, M. V. Maksimov, V. M. Ustinov, A. F. Tsatsul'nikov, Zh. I. Alferov, D. L. Fedorov, and D. Bimberg, Fiz. Tekh. Poluprovodn. **30**, 1345 (1996) [Semiconductors **30**, 707 (1996)].

Translated by P. Shelnitz

## AMORPHOUS, GLASSY AND POROUS SEMICONDUCTORS

# Optical properties of porous silicon layers processed with a HF:HCl:$C_2H_5OH$ electrolyte

A. I. Belogorokhov

*Institute of Rare Metals, 109017 Moscow, Russia*

L. I. Belogorokhova

*Moscow State University, 119899 Moscow, Russia*

(Submitted December 9, 1997; accepted for publication May 20, 1998)
Fiz. Tekh. Poluprovodn. **33**, 198–204 (February 1999)

The properties of porous silicon samples prepared by adding hydrochloric acid to the usual hydrofluoric-acid electrolyte have been studied. These samples exhibit an intense photoluminescence that does not degrade over time and is unaffected by exposure to intense laser illumination. The peak photoluminescence from these layers of porous silicon occurs at photon energies of 1.85–1.9 eV. The photoluminescence signal from samples prepared in the standard way under the same initial conditions but without HCl in the composition of the electrolyte is two orders of magnitude less intense. Studies of the degradation of these porous silicon samples with time and exposure to various power levels of laser illumination revealed that the samples with the maximum content of HCl in the electrolyte composition emitted photoluminescence that was unaffected by laser illumination. In this work, the infrared spectra of the samples was measured in order to monitor the chemical state of their surfaces. It was found that the abrupt 100-fold increase in the intensity of the photoluminescence signal from samples made according to the method proposed here is associated both with distinctive features of the structure of porous silicon layers and with the presence of a thin crystalline layer of $SiO_2$ on the surface of nanocrystallites.  [S1063-7826(99)00902-3]

Close attention is paid to ongoing studies of the properties of porous silicon. There are several reasons for this, the most important of which is the intense photoluminescence it emits in the visible region of the spectrum.[1,2] This property, which is interesting for engineering applications, remains without a comprehensive physical explanation even today (see Refs. 3 and 4).

Available data indicate that contributions to the photoluminescence can come either from emission by silicon nanocrystallites (NC) that is shifted into the visible region by quantum-well effects[5] or emission by adsorbates such as siloxane $Si_6O_3H_6$, i.e., hydrates of silicon,[6] that form as the porous silicon is grown or as it degrades. A third possible contribution to the photoluminescence is emission from the silicon/adsorbate interface.[7] Banerjee[8] has asserted that photoluminescence in the red region of the spectrum could be connected with the existence of complexes, e.g., a localized hole plus an oxygen ion that is uninvolved in the formation of bridge bonds.[8] Recently, discussions of the origin of this photoluminescence in porous silicon have been increasingly more strongly focused on the nature and mechanisms of degradation of porous silicon layers.[9,10] The intense interest in degradation phenomena is warranted by the possibility that porous silicon may eventually be used extensively in optoelectronics. Several authors have attempted to resolve questions about degradation of porous silicon by varying the exposure time and density of current that passes through the sample during the electrochemical etching reaction.[11,12] The position and shape of the photoluminescence peak can be changed by further processing the porous silicon in various chemical[13,14] or gaseous[15] media. Many authors have assumed that the photoluminescence of porous silicon layers degrades either because of passive or active passivation of the surfaces of nanocrystallites after preparation.[16] In some cases this leads to a shift in the photoluminescence peak towards the blue end of the spectrum,[17] while sometimes, conversely, the shift is toward the red end and is accompanied by decreasing photoluminescence intensity.[18] Cases have been reported of ambiguous behavior of the photoluminescence signal when samples of porous silicon are subjected to additional chemical processing.[19]

In this paper we describe the properties of porous silicon structures that do not degrade with time. We prepared these porous silicon samples by changing the composition of the electrolyte, adding hydrochloric acid (HCl) to its traditional components. The resulting porous silicon layers exhibit intense photoluminescence, almost two order of magnitude higher than the signals from samples made on the same substrates by traditional methods, i.e., without adding HCl to the electrolyte solution. We studied how the photoluminescence properties of these porous silicon structures degrade with time and exposure to laser illumination at various power lev-

 

els. At the same time, we recorded the infrared spectra of the samples, which allowed us to monitor the structure and properties of the state of the porous silicon surface.

## 1. SAMPLE PREPARATION AND EXPERIMENTAL METHOD

As starting material for obtaining porous silicon layers we used single-crystal boron-doped *p*-Si (100) with resistivity $\rho = 1\ \Omega \cdot \mathrm{cm}$. The porous silicon samples were made by electrolytic anodization. The current density passing through the sample and the etch time were $30\ \mathrm{mA/cm^2}$ and 5 min, respectively. The composition of the electrolyte used to obtain sample 1 was standard, i.e., $HF:H_2O:C_2H_5OH$ in the ratios 1 : 1 : 1. The other samples were made with HCl in the electrolytes, specifically 2, 10, 20, and 38 ml of HCl added to 100 ml of solution for samples 2, 3, 4, and 5, respectively. The samples were then washed in a standard solution and dried in a stream of dry air. The thickness of the porous silicon layers, which was in the range 10–20 $\mu$m, was monitored by electron and optical microscopy. The porosity of the porous silicon, which was determined from gravimetric measurement data, could be as large as 70% ± 5%. The microstructure and morphology of the surface of nanocrystallites in the porous silicon was investigated by using a JEOL 840A scanning electron microscope with the LINK element analysis system. In the course of these investigations we recorded the photoluminescence spectra and infrared optical spectra. The spectral dependence of the photoluminescence was obtained by using a DFS-24 double monochromator with a FEU-79 detector to record photoluminescence excited initially by a stabilized argon laser at wavelengths 457.9, 488, and 514.5 nm. The laser power was varied from 0.5 to 100 mW. The laser beam was focused into a spot with area 1.4 $\mathrm{mm^2}$. The average scanning time was about 3 min. Optical spectra were recorded using a fast-scan IFS-113v (Bruker) Fourier spectrometer in the wave number range 300–5000 $\mathrm{cm^{-1}}$ with spectral resolution no worse than 0.5 $\mathrm{cm^{-1}}$. We made some of the samples under study up to a year before the investigations were carried out, and during that entire period we kept them in the open air under normal conditions, periodically recording their photoluminescence and infrared spectra in order to study their degradation with time.

## 2. INVESTIGATION OF POROUS SILICON PHOTOLUMINESCENCE

Figure 1 shows photoluminescence spectra of samples *1–5* obtained at room temperature. The peak position and intensity of the photoluminescence for samples *4* and *5* did not change over the whole storage time (12 months). The photoluminescence peak was located in the energy range 1.85–1.9 eV. The shape of the spectral curves for samples *2–4* could be reproduced by superimposing four Gaussian curves. Figure 2 shows how the positions of the maxima of these Gaussians changed with increasing HCl content in the electrolyte. For sample *5* the shape of the photoluminescence peak is close to classical, i.e., Gaussian. Noteworthy is the fact that the contribution from the peak denoted by ''*1*'' (the long-wavelength peak) to the total photoluminescence spectrum drops off sharply from sample *2* to sample *5* by roughly a factor of 50, whereas the intensity of peaks *3* and *4* increases by more than factor of 2 with increasing content of HCl.

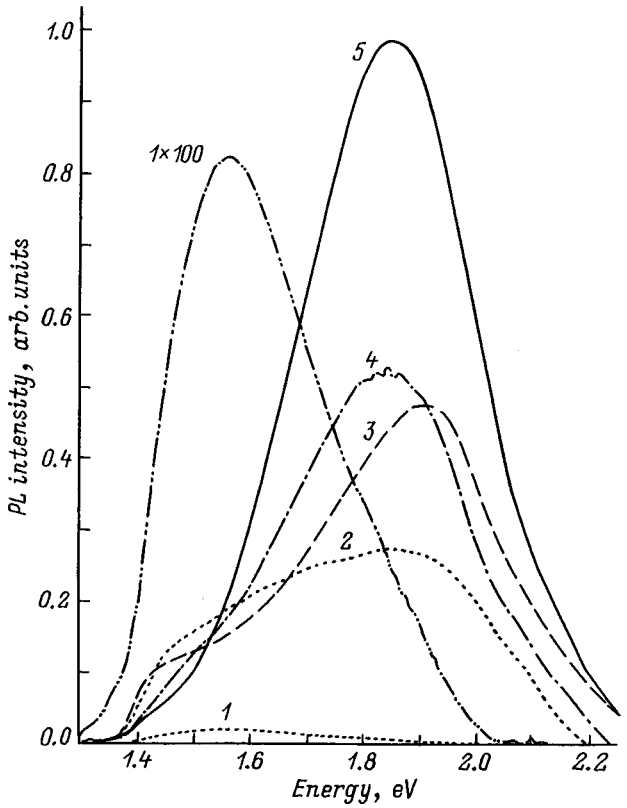


FIG. 1. Photoluminescence spectrum for samples of porous silicon obtained at $T = 295$ K. The photoluminescence spectrum of sample *1* is magnified a hundred times, samples *2* and *3* ten times. The spectra were recorded at a laser wavelength of 488 nm. The laser optical power was 50 mW.

It is easy to trace a fine structure in the low-temperature (1.4 K) photoluminescence spectra of samples *2–5*, consisting of a set of rather low-intensity peaks spaced from one another by 20–21 meV. Based on the distance between these peaks we can estimate the diameter of the nanocrystallites[20] and also their approximate shape, i.e., whether we are dealing with collections of quantum wires or quantum dots. On the basis of calculations given in Refs. 21 and 22 we conclude that the shape of the nanocrystallites in samples *4* and *5* was close to cylindrical. In contrast, the structure of sample *1* is spongy, consisting of a collection of quantum dots with an average diameter of about 3.0 nm. The structures of the porous silicon layer in samples *2* and *3* are distinguished by strong nonuniformity both in the size of the nanocrystallites and their shape. This is the main reason for the appearance of several peaks in their PL spectra. Analysis of the low-temperature PL spectra of similar samples was given in Ref. 23.

## 3. DEGRADATION OF POROUS SILICON SAMPLES UNDER THE ACTION OF LASER RADIATION

Our studies of the degradation of the photoluminescence signal as a function of the intensity of laser light incident on the sample yielded the following results. The intensity of the

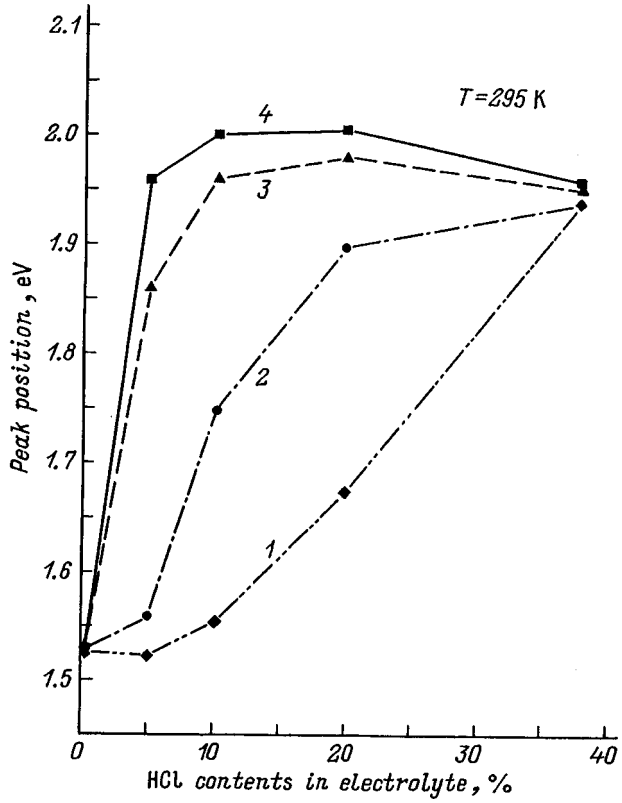


FIG. 2. Dependence of the position of the maxima of Gaussian curves (*1*—*4*) which were used to approximate the shape of the photoluminescence spectra in our samples on the concentration of HCl in the electrolyte.

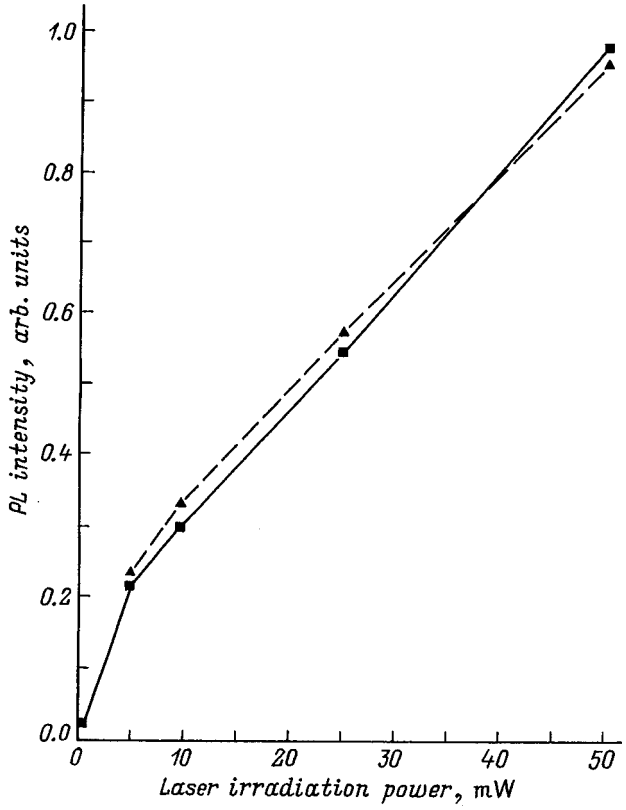


FIG. 3. Dependence of the photoluminescence signal intensity of sample *4* on the power incident on the sample from the laser. The wavelength of the Ar-laser was 488 nm. The solid curve corresponds to data obtained at a temperature of 295 K, the dashed curve at 1.4 K.

signal and shape of the photoluminescence peak for sample *5* were unchanged after continuous laser illumination for at least 1 hour at power levels of 0.5 to 100 mW. In the case of sample *4*, the intensity of the photoluminescence peak decreased exponentially with time, and the rate of change of the photoluminescence signal intensity increased with increasing laser power. Dependences of the photoluminescence signal intensity for sample *4* on the incident laser power obtained at room temperature and liquid-helium temperature, shown in Fig. 3, consist of nearly linear functions. For samples *2* and *3* similar results were obtained. The degradation of the photoluminescence signal for sample *4* over a period of 60 min after the start of the experiment can be seen in Fig. 4.

After each sample had been exposed to laser light for 1 hour, it was placed in darkness for another hour. We then took another photoluminescence spectrum at the same point on the sample. It turned out that the intensity of the photoluminescence signal from sample *4* recovered its original value. For sample *3* the situation turned out to be somewhat more complex: it degraded rapidly under the action of the laser illumination, and we were unable to completely recover its photoluminescence properties. For samples *1* and *2* the degradation process was irreversible in character. As we noted above, the photoluminescence spectrum had a complex form. The process of degradation of the photoluminescence in green and red regions of the spectrum took place differently. The most significant changes in the shape of the photoluminescence peak took place on the high-energy side, whereas the long-wavelength portion of the photoluminescence peak of these samples was practically undisturbed. For sample *1* the degradation was quite rapid (in about 1 min).

In our view, it is natural to associate the change in the photoluminescence signal with time under exposure to laser light with thermal processes that occur in the illuminated portion of the sample. If the layer of porous silicon consists of a rather orderly structure that is oriented in some common direction, then the heat transport in such a layer will be higher than in a layer with a random structure, consisting of nanocrystallites surrounded by regions of silicon dioxide. Our assertion that degradation of the photoluminescence signal is connected with thermal processes in the porous silicon layer is confirmed by the fact that we observed no change in the low-temperature photoluminescence spectrum for samples *1–5*, despite the fact that the laser power and illumination times on the sample were respectively 100 mW and 60 min.

## 4. FTIR SPECTROSCOPY OF POROUS SILICON SAMPLES

Figure 5 shows absorption spectra for samples 1 to 5 in the wave number range from 2000 to 2400 $cm^{-1}$. It is clear from the figure that strong absorption is taking place in sample *1* at bonds of the following types: SiH (2090 $cm^{-1}$), $SiH_2$ (2114 $cm^{-1}$) and $SiH_3$ (2140 $cm^{-1}$) (see Ref. 24), whereas the absorption in the spectrum of sample *5* is primarily due to vibration of atoms at bonds of types $SiH(O_3)$

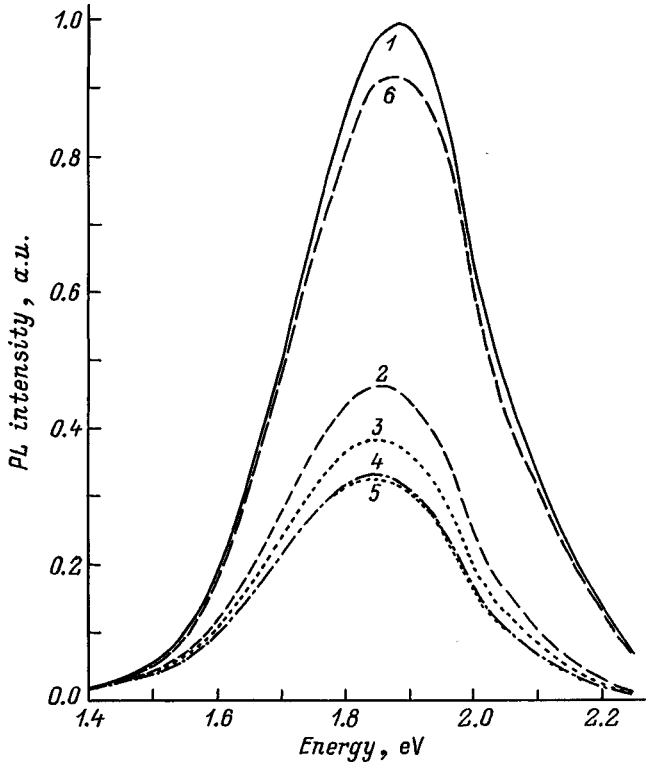


FIG. 4. Time dependence of the photoluminescence signal from sample *4* under the action of CW laser illumination at a power of 10 mW and a wavelength of 488 nm. The photoluminescence spectra were recorded after storage of the sample. Storage time, minutes: *1* — 0, *2* — 15, *3* — 25, *4* — 45, *5* — 60. Curve *6* corresponds to a photoluminescence spectrum obtained after an hour's exposure of the sample to laser radiation and subsequent storage of the sample in the dark for 30 min.

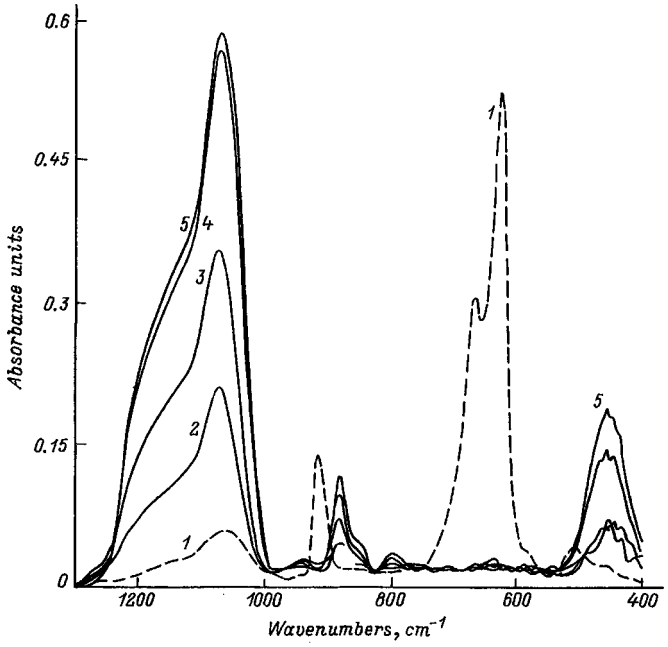


FIG. 6. Infrared absorption spectra of samples *1–5*. The labels on the curve correspond to sample numbers.

($2254\,\mathrm{cm}^{-1}$) and $SiH(SiO_2)$ ($2196\,\mathrm{cm}^{-1}$) (see Ref. 25). For samples *2–5* the absorption at $SiH(O_3)$ bonds increases with increasing HCl content in the electrolyte. The infrared spectroscopy data correlate well with the results of photoluminescence measurements. At the same time, we should point out that this dependence of the absorption on HCl content is nonmonotonic in character. A sharp increase in the absorption intensity is apparent in sample *4* compared to sample *3*. Moreover, there is nearly no evidence of an absorption band due to $SiH(SiO_2)$ bonds in the optical spectra of samples *2* and *3*. This can be understood if we postulate that the surfaces of nanocrystallites in samples *4* and *5* are covered by a thin layer of stoichiometric $SiO_2$.

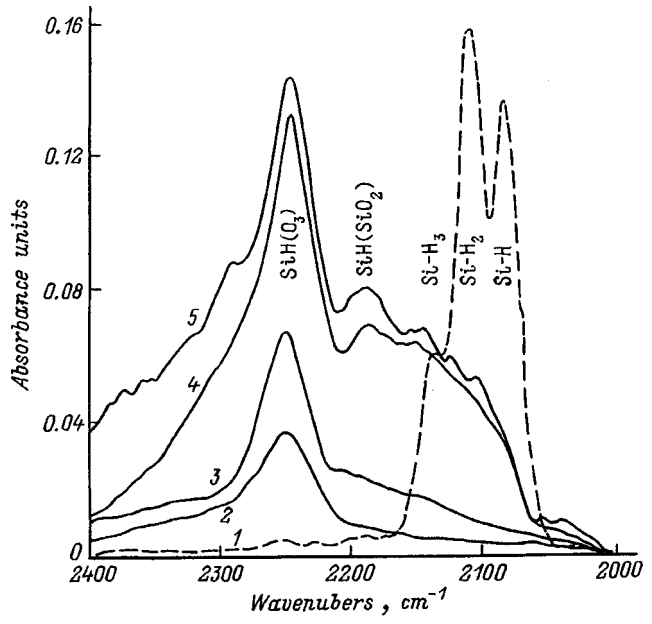


FIG. 5. Infrared spectra of samples *1–5* obtained at $T=295$ K.

Figure 6 shows the spectral dependences of the absorption coefficient for samples *1–5* in the wave number range ($400-1300$) $\mathrm{cm}^{-1}$. The spectrum of sample *1*, represented by a dashed curve, differs considerably from the spectra of the other samples. The intense absorption band in the wave number range ($600-670$) $\mathrm{cm}^{-1}$ corresponds to vibrations of the Si–Si stretch ($615\,\mathrm{cm}^{-1}$), $Si-H_2$ deformation ($628\,\mathrm{cm}^{-1}$), Si–H deformation ($654\,\mathrm{cm}^{-1}$), and $Si-H_2$ wagging ($668\,\mathrm{cm}^{-1}$) types.[26] The peak located at a frequency of 906 $\mathrm{cm}^{-1}$, corresponds to (scissor) vibrations at $Si-H_2$ bonds.[26] In contrast, the spectra of samples *2–5* exhibit virtually none of these modes. In their place we see an intense absorption band in the wave number range ($1000-1210$) $\mathrm{cm}^{-1}$. It has a complicated shape which can nevertheless be successfully reproduced by superimposing four Gaussians with maxima located at the following frequencies in $\mathrm{cm}^{-1}$: 1067, 1119, 1164, and 1201. The results of fitting the absorption spectra of sample 4 in this way are shown in Fig. 7. The second and third of these peaks correspond to the asymmetric stretch vibration mode of Si–O–Si.[27] Based on the theoretical calculations and experimental studies of Olsen and Shimura,[28] we can explain the presence of the first peak as a manifestation of resonance with transverse optical ($TO$) phonons, and the fourth peak as resonance with longitudinal optical ($LO$) phonons, in silicon dioxide. Usually optical phonons in $SiO_2$

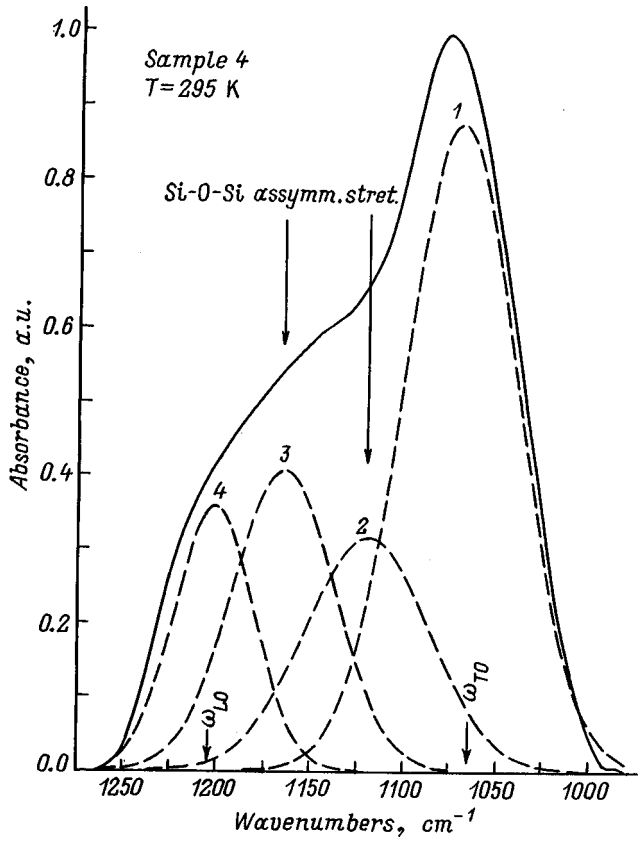


FIG. 7. Absorption spectrum of sample *4*.

are inactive. However, in thin $SiO_2$ layers the selection rules allow the *LO* and *TO* modes to be active in Raman scattering and optical IR spectra.[29,30] The presence of these modes in the spectra can be regarded as proof of the presence of a thin layer of stoichiometric $SiO_2$ at the surface of the nanocrystallites.

Graf *et al.*[31] assumed that this $SiO_2$ layer forms in stages: an initial stage, involving the creation of Si–OH type bonds at the surface of the nanocrystallites, must precede the formation of silicon dioxide. It should be noted that samples *2–5* exhibit an absorption peak accompanied by a shoulder at frequencies 803 and 850 $cm^{-1}$, respectively. This comes from vibrations of O–Si–O (symmetric stretch) type in the thin layer of $SiO_2$. Also noteworthy is an intense absorption band in the spectrum of sample *1* at a frequency of 950 $cm^{-1}$ that is absent from the spectra of the other samples. It is known[32] that when crystalline silicon oxidizes a thin, intermediate layer of $SiO_x$ forms. The peak located at this frequency can be related to bridge-like vibrations of Si–O–Si (stretching) type in just such a thin layer of nonstoichiometric $SiO_x$.[32] The two peaks in the spectra of samples *2–5* at frequencies 460 and 870 $cm^{-1}$, which until now have not been discussed, have intensities that increase with increasing HCl content in the electrolyte, and can be associated with absorption at bonds of Si–O–Si (bending) and $O_2$–Si–H(OH) (stretching) type.[32]

In the previous section we have indicated that samples *4* and *5* degrade the least under the action of laser illumination. Based on infrared data we can conclude that of the various bonds present at the surface of nanocrystallites, those of $SiH(O_3)$, $SiH(SiO_2)$, and $SiH(O_2)$ types are the most stable against laser light, whereas $SiH_2(SiO)$ and $SiH(Si_2O)$ are not stable. This conclusion agrees with the results of Chen *et al.*,[33] with the sole difference that these complexes, which occur at the surface of the nanocrystallites, were obtained by those authors only after a lengthy procedure of thermal oxidation at a temperatures in the range 400–500 °C.

## 5. DISCUSSION OF THE RESULTS

The porous silicon layers obtained by us have a nonuniform structure which consists of a surface layer made up of nanocrystallites with an average diameter of 1.9 to 2.1 nm and an interface layer made up of either dendrites or spongy material. The ratio of thicknesses of these layers changes as the content of HCl in the electrolyte increases, favoring the former. This also can explain the decrease in photoluminescence signal intensity under continuous laser illumination, since the surface and inner sublayers of porous silicon have different heat conductivities. This can lead to considerable local heating of the sample, which then stimulates the process of photo-oxidation of Si–Si bonds. Moreover, the increase in the temperature considerably increases the rate of surface nonradiative recombination. Many authors[34,35] have suggested such a possibility in their papers. However, when heat is transported efficiently away from the part of the porous silicon sample heated by the laser, we can anticipate that the properties of the porous silicon will be stable under exposure to laser illumination. As we showed above, the porous silicon samples made with a maximum content of HCl (*4* and *5*) have a structure that, according to our data, consists of elongated nanocrystallites oriented in a specified direction. Our IR spectroscopy results show that the nanocrystallite surfaces in these samples are covered by a thin layer of stoichiometric $SiO_2$. The addition of hydrochloric acid to the ordinary hydrogen-fluoride electrolyte can significantly change the state of the silicon surface, and also the kinetics of the chemical reaction.[36] The formation of a thin $SiO_2$ layer leads to effective passivation and a considerable decrease in the number of dangling bonds, i.e., centers for nonradiative recombination, at the surface of the nanocrystallites. In our view, this explains the change in the photoluminescence signal under the action of the laser light. Furthermore, we note that Si nanocrystallites separated by an insulator emit more intense photoluminescence.[37]

The introduction of HCl into the electrolyte solution at various concentrations slows the process of electrochemical etching of the silicon. We would like to create conditions such that, on the one hand, effective etching of the silicon takes place in a specified direction, while, on the other hand, nothing hinders the formation of bonds of Si–O and Si–H type on the newly formed nanocrystallite surfaces. When the boundary region of the sample is immediately adjacent to the etch front, the porosity of the newly formed porous layer may be insufficient, which then can prevent a surface layer of stoichiometric $SiO_2$ from forming, because there are simply not enough of the required number of oxygen atoms in that region of the sample at that instant of etching. In short,

an oxide layer of type $SiO_x$ forms at the surface of the nanocrystallites, which is then subjected either to further oxidation or to other structural adjustments, which could be the reason for degradation of the photoluminescence signal. Moreover, nonradiative recombination centers can form on these surfaces in the form of the so-called ''dangling'' silicon bonds. On the other hand, vigorous formation of silicon oxide in the region where the sample is etched can affect the final geometric shape of the nanocrystallites, i.e., the final structure can be either spongelike or relatively ordered, depending on the crystallographic direction at the instant where bonds of type Si–O are being formed. The etch rate vector is directed towards the maximum density of charge carriers. In the past, we have pointed out the fact[12,14] that the kinetics of formation of a porous silicon layer are not the same along different crystallographic directions.

We may have succeeded in finding a successful combination of technological parameters for obtaining porous silicon layers that exhibit both intense photoluminescence (two orders of magnitude higher than that from traditional methods of obtaining porous silicon) and stable optical properties. Nevertheless it is likely that our choice of parameters, though successful, is still far from optimum. In conclusion we note that it is very important to investigate the properties of porous silicon samples obtained by the methods we have proposed here, but starting with films of crystalline silicon with different orientations and different electrical conductivities.

This work was carried out within the framework of Project 02-96-18853 of the Russian Fund for Fundamental Research.

The authors are grateful to S. A. Gavrilov for providing the samples and V. A. Karavanskiĭ for useful discussions.

[1] L. T. Canham, Appl. Phys. Lett. **57**, 1046 (1990).
[2] S. Sawada, N. Hamada, and N. Okubo, Phys. Rev. B **49**, 5236 (1994).
[3] A. G. Cullis, L. T. Canham, and P. D. J. Calcott, J. Appl. Phys. **82**, 909 (1997).
[4] J. L. Gole, F. P. Dudel, D. Grantier, and D. A. Dixon, Phys. Rev. B **56**, 2137 (1997).
[5] Qi. Zhang and S. C. Bayliss, J. Appl. Phys. **79**, 1351 (1996).
[6] H. D. Fuchs, M. Stutzmann, M. S. Brandt, M. Rosenbauer, J. Weber, A. Breitschwerdt, P. Deak, and M. Cardona, Phys. Rev. B **48**, 8172 (1993).
[7] F. Koch, V. Petrova-Koch, T. Muschik, A. Kux, F. Muller, V. Gavrilenko, and F. Möller, in *Proceedings of the 21st International Conference Phys. Semicond.* (World Scientific, Singapore, 1993).
[8] S. Banerjee, Phys. Rev. B **51** 11 180 (1995).
[9] K. N. El'tsov, V. A. Karavanskiy, and V. V. Martynov, JETP Lett. **63**, 119 (1996).
[10] R. Guerrero-Lemus, J. D. Moreno, J. M. Martinez-Duart, M. L. Marcos, J. Gonzales-Velasco, and P. Gomez, J. Appl. Phys. **79**, 3224 (1996).
[11] K. H. Li, C. Tsai, J. Sarathy, and J. C. Campbell, Appl. Phys. Lett. **62**, 3192 (1993).
[12] A. I. Belogorokhov, L. I. Belogorokhova, V. A. Karavanskiĭ, and A. N. Obraztsov, Fiz. Tekh. Poluprovodn. **28**, 1424 (1994) [Semiconductors **28**, 800 (1994)].
[13] T. Ya. Gorbach, G. Yu. Rudko, P. S. Smertenko, S. V. Svechnikov, M. Ya. Valakh, V. P. Bondarenko, and A. M. Dorofeev, Semicond. Sci. Technol. **11**, 601 (1996).
[14] A. I. Belogorokhov, V. A. Karavanskiy, and L. I. Belogorokhova, Fiz. Tekh. Poluprovodn. **30**, 1177 (1996) [Semiconductors **30**, 1208 (1996)].
[15] Y. M. Weng, Z. N. Fan, and X. F. Zong, Appl. Phys. Lett. **63**, 168 (1993).
[16] D. W. Zheng, Y. P. Huang, Z. J. He, A. Z. Li, T. A. Tang, R. Kwor, Q. Cui, and X. J. Zhang, J. Appl. Phys. **81**, 492 (1997).
[17] M. A. Butturi, M. C. Carotta, G. Martinelli, L. Passari, G. M. Youssef, A. Chiorino, and G. Ghiotti, Solid State Commun. **101**, 11 (1997).
[18] N. Rigakis, J. Hilliard, L. Abu Hassan, J. M. Hetrick, D. Andsager, and M. H. Nayfeh, J. Appl. Phys. **81**, 440 (1997).
[19] H. Koyama, N. Shima, and N. Koshida, Phys. Rev. B **53**, R13291 (1996).
[20] N. S. Averkiev, V. M. Asnin, I. I. Markov, A. Yu. Silov, V. I. Stepanov, A. B. Churilov, and N. E. Mokrousov, JETP Lett. **55**, 631 (1992).
[21] C. Delerue, G. Allan, and M. Lannoo, Phys. Rev. B **48**, 11 024 (1993).
[22] T. Takagahara and K. Takeda, Phys. Rev. B **46**, 15 578 (1992).
[23] A. I. Belogorokhov, R. Enderlein, A. Tabata, J. R. Leite, V. A. Karavanskii, and L. I. Belogorokhova, Phys. Rev. B **56**, 10 276 (1997).
[24] A. Venkateswara Rao, F. Ozanam, and J. -N. Chazalviel, J. Electrochem. Soc. **138**, 153 (1991).
[25] D. V. Tsu, G. Lucovsky, and B. N. Davidson, Phys. Rev. B **40**, 1795 (1989).
[26] A. C. Dillon, M. B. Robinson, and S. M. George, Surf. Sci. Lett. **295**, L998 (1993).
[27] W. Kaiser, P. H. Keck, and C. F. Lange, Phys. Rev. **101**, 1264 (1956).
[28] J. E. Olsen and F. Shimura, J. Appl. Phys. **66**, 1353 (1989).
[29] S. M. Hu, J. Appl. Phys. **51**, 5945 (1980).
[30] C. T. Kirk, Phys. Rev. B **38**, 1255 (1988).
[31] D. Graf, M. Grundner, and R. Schilz, J. Vac. Sci. Technol. A **7**, 808 (1989).
[32] G. Lukovsky, J. Yang, S. S. Chao, J. E. Tyler, and W. Czubatyj, Phys. Rev. B **28**, 3225 (1983).
[33] H. Chen, X. Hou, G. Li, F. Zhang, M. Yu, and X. Wang, J. Appl. Phys. **79**, 3282 (1996).
[34] E. Ribeiro, F. Cerdeira, and O. Teschke, Solid State Commun. **101**, 327 (1997).
[35] P. K. Kashkarov, E. A. Konstantinova, S. A. Petrova, V. Yu. Timoshenko, and A. E. Yunovich, Fiz. Tekh. Poluprovodn. **31**, 745 (1997) [Semiconductors **31**, 639 (1997)].
[36] S. A. Gavrilov, I. N. Sorokin, V. A. Karavanskii, M. O. Bashkin, and A. Yu. Trifonov, *Mater. of the 10th International Conference on Thin Films* (Spain, Salamanca, 1996), p. 85.
[37] H. Chen, X. Hou, G. Li, F. Zhang, M. Yu, and X. Wang, J. Appl. Phys. **79**, 3282 (1996).

Translated by Frank J. Crowne

# Conductivity of structures based on doped nanocrystalline $SnO_2$ films with gold contacts

B. A. Akimov, A. M. Gas'kov, S. E. Podguzova, M. N. Rumyantseva, and L. I. Ryabova

*M. V. Lomonosov Moscow State University, 119899 Moscow, Russia*

M. Labeau and A. Tadeev

*Institut National Polytechnique de Grenoble, Boîte Postale 46, 38402 St. Martin d'Hères, France*
(Submitted April 7, 1998; accepted for publication July 1, 1998)
Fiz. Tekh. Poluprovodn. **33**, 205–207 (February 1999)

The conductivity of nanocrystalline Pt-, Pd-, and Ni-doped tin dioxide films on insulating $SiO_2$ substrates is investigated in the temperature range 77–400 K. Doping allows variation of the resistance from $10^4$ to $10^7\Omega$. It is established that, in contrast with a Au/single-crystal $SnO_2$ contact, the gold contacts for the nanocrystalline material are ohmic in the entire temperature range and their contribution to the conductance of all the structures investigated does not exceed 5%. © *1999 American Institute of Physics.* [S1063-7826(99)01002-9]

Nanocrystalline tin dioxide film are used to create sensitive elements for resistive-type gas sensors. In structures with a high-resistivity sensitive element it is fairly difficult to separate the possible effects of the Si substrate and the gold contact on the character of the temperature dependence of the conductance.[1–4] Investigations of a gold contact on single-crystal tin dioxide with an electron concentration $n\sim10^{17}\text{cm}^{-3}$ showed that the contact is nonohmic and that it is characterized by the appearance of a Schottky barrier of height $\varphi_B\sim0.55$ meV.[5] This value essentially coincides with the half-width of the silicon band gap. Therefore, it cannot be ruled out that the activation of conduction with an energy $E_a\sim0.5$ meV, which has been observed, for example, for structures with a $SnO_2$(Cu) sensitive element on a silicon substrate with an insulating $SiO_2$ sublayer,[1–4] can be determined by either the substrate or the contacts.

In the present work we investigated structures in which polished $SiO_2$ served as the substrate. Nanocrystalline Pt-, Pd-, and Ni-doped $SnO_2$ films were obtained by pyrolysis of an aerosol of the corresponding metalorganic compounds at 520 °C. The synthesis method was described in detail in Refs. 6 and 7. The deposition time for all the films was constant and amounted to ~10 min. The film thickness was determined on cleavage surfaces in a Jeol JSM-35 scanning electron microscope and was equal to $\sim1\mu$m. The microstructure and phase composition were studied by x-ray diffraction analysis on a Siemens diffractometer using Cu$K_\alpha$ radiation. The presence of only one phase of $SnO_2$ (cassiterite) was detected for all the films investigated. No phases containing impurities of the metals introduced were found. This can be associated either with the insignificant content of impurities introduced or with the small size of the crystallites formed by impurities in the phases.[7] Table I presents the results of a calculation of the mean grain diameter of the $SnO_2$ crystallites from widths of the x-ray diffraction reflections using the Debye–Scherrer formula. The mean diameter of the $SnO_2$ grains does not vary upon the introduction of impurities to within the estimation accuracy (10−15%). The elemental composition of the films was determined by local x-ray analysis (CAMECA SX50). The composition and characteristics of the films obtained are listed in Table I.

The films obtained by us had a rectangular shape and standard dimensions equal to $2\times7$ mm. Gold contacts in the form of four strips of width 0.5 mm were deposited through special stainless-steel masks in two stages. A thin strip of gold with a thickness of the order of 20 nm was initially deposited by reactive sputtering. The thickness of the contact layer was then increased to 1–2 $\mu$m by thermal sputtering. The layout of the contacts on a film is shown schematically in the inset in Fig. 1.

The introduction of dopants led to significant variation of the resistance of the films in the range from $10^4\Omega$ for undoped film *1* to more than $10^7\Omega$ for film *5*, which was

TABLE I. Characteristics of the test samples.

| Film | Impurity content in the solution, at. % | Impurity content in the film, at. % | Mean grain diameter, nm | $R$, Ω $T=273$ K | $E_a$, meV |
|---|---|---|---|---|---|
| *1* | | | 9 | $7.2\times10^3$ | ··· |
| *2* | 3% Pd | 0.7 | 7 | $2\times10^6$ | 100 |
| *3* | 3% Pt | 0.5 | 8 | $6.4\times10^4$ | 130 |
| *4* | 5.8% Ni | 0.3 | 9 | $1.2\times10^5$ | 60 |
| *5* | 3% Pd, 2.9% Ni | 0.6% Pd, <0.1%Ni | 9 | $1.7\times10^7$ | 210 |

 

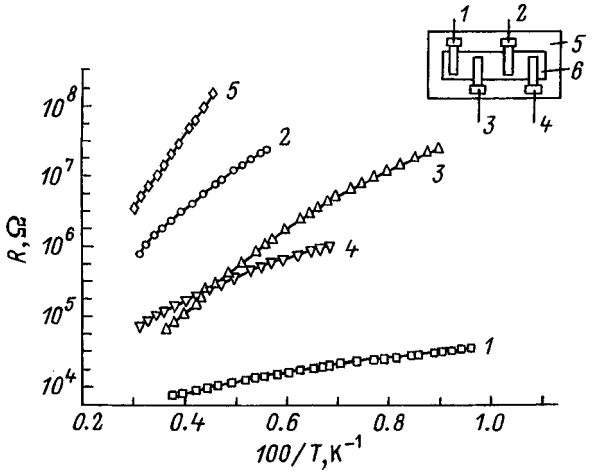


FIG. 1. Temperature dependence of the resistance $R$ of the test samples. The numbers next to the curves correspond to the numbers of the samples in Table I. Inset — schematic representation of the structures investigated: *1–4* — gold contacts; *5* — $SiO_2$ substrate; *6* — $SnO_2$ film.

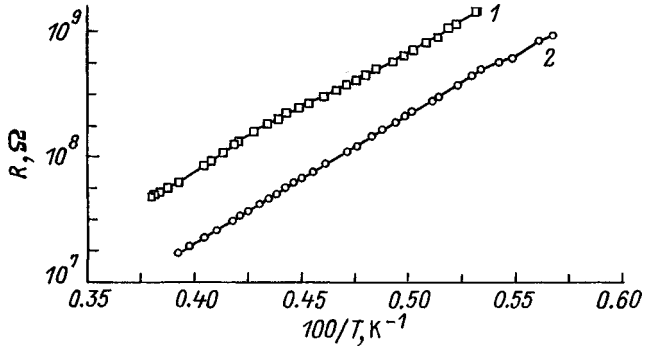


FIG. 2. Temperature dependence of the resistance $R$ of sample *5*. Curve *1* was obtained when the measurements were performed using contacts *1* and *4*, and curve *2* was obtained using contacts *2* and *3* (see the inset in Fig. 1).

doped with Ni and Pd. The temperature dependence of the resistance $R$ was measured at a stabilized voltage $U \leqslant 10$ V in the temperature range $77 \leqslant T \leqslant 400$ K. The current-voltage characteristics were linear in the range indicated above. Figure 1 presents plots of the temperature dependence of $R$ obtained in measurements with contacts separated by a distance of 1 mm. The plots of the temperature dependence of the resistance in $\log R$-vs-$100/T$ coordinates for films *2* and *5*, which have the highest resistivity, are linear (Fig. 1). The values of the activation energy $E_a$ calculated from the relation $R \sim \exp(E_a/kT)$ are presented in Table I. The activation energies listed in Table I for films *3* and *4* were estimated from the slope of the high-temperature portions of the $\log R$-vs-$100/T$ curves.

The contact resistances were determined using the method proposed by Reeves and Harrison[8] (the transmission line model or TLM). The TLM method reduces to measuring the resistance from several pairs of contacts which have identical areas, but are separated by different distances. Similar series of measurements were performed for all the samples indicated in Table I. It was found that the contact resistances do not exceed 5% of the resistance of the film itself, regardless of its original characteristics. For comparison, Fig. 2 presents plots of the temperature dependence of $R$ for film *5*, which were obtained from measurements with different pairs of contacts (curve *1* — contacts *1* and *4*, curve *2* — contacts *2* and *3*; see the inset in the Fig. 1). Thus, the contact resistances neither contribute significantly to the value of the conductance nor affect the temperature dependence of $R$. This behavior can be attributed to features of the microstructure of the films. It has not been ruled out that transition layers with a thickness comparable to the thickness of the depletion layer form and that the contacts do not have cutoff properties when the film and contact fabrication technologies considered here are used.

The activation character of the dependence of the resistance of the doped films investigated is probably due to the formation of intercrystallite barriers. Since the films exhibit *n*-type conduction, the possible acceptor activity of the impurities introduced could lead only to partial compensation of the donor activity of the oxygen vacancies. It is known that the ionization energy of the oxygen vacancy level in $SnO_2$ is $\sim 130$ meV.[5] However, the value of $E_a$ for the samples investigated varies in the range from 60 to 210 meV, and it is close to 130 meV only in the platinum-doped sample. Nevertheless, compensation can have an effect on the height of the intercrystallite barrier because of the change in the position of the Fermi level. On the other hand, the impurity can be distributed nonuniformly in the bulk and at the grain boundaries and can thus influence the magnitude of the band bending on the interfaces.

This work was performed with partial support by Grant 96-15-96500 from the Russian Fund for Fundamental Research.

*)E-mail: mila@mig.phys.msu.su; Fax: +(7)-(095)-932-8876

[1] M. N. Rumyantseva, A. M. Gaskov, L. I. Ryabova, J. P. Senateur, B. Chenevier, and M. Labeau, Mater. Sci. Eng. **41**, 333 (1996).
[2] M. N. Rumyantseva, M. Labeau, G. Delabouglise, L. Ryabova, I. Kutsenok, and A. Gaskov, J. Toxicol. Environ. Health **7**, 1785 (1997).
[3] B. A. Akimov, A. V. Albul, A. M. Gas'kov, V. Yu. Il'in, M. Labeau, M. N. Rumyantseva, and L. I. Ryabova, Fiz. Tekh. Poluprovodn. **31**, 400 (1997) [Semiconductors **31**, 335 (1997)].
[4] B. A. Akimov, A. M. Gas'kov, M. Labeau, M. M. Osipova, M. N. Rumyantseva, and L. I. Ryabova, Vestn. Mosk. Univ., Ser. 3: Fiz. Astron. **5**, 60 (1996).
[5] C. G. Fonstad and R. H. Rediker, J. Appl. Phys. **42**, 2911 (1971).
[6] I. B. Gautheron, M. Labeau, G. Delabouglise, and U. Schmatz, Sens. Actuators B **15–16**, 357 (1993).
[7] M. Labeau, B. Gautheron, F. Cellier, M. Vallet-Regi, E. Garcia, and Gonzalez Calbet, J. Solid State Chem. **102**, 434 (1993).
[8] G. K. Reeves and H. B. Harrison, IEEE Trans. Electron Device Lett. **5**, 111 (1982).

Translated by P. Shelnitz

# Influence of the substrate temperature and annealing on the 1.54-$\mu$m erbium photoluminescence of *a*-Si:H films obtained using a glow discharge

E. I. Terukov, O. I. Kon'kov, V. Kh. Kudoyarova, and O. B. Gusev

*A. F. Ioffe Physicotechnical Institute, Russian Academy of Sciences, 194021 St. Petersburg, Russia*

G. Weiser and H. Kuehne

*Philipps Universität-Marburg, D-35032 Marburg, Germany*

(Submitted July 13, 1998; accepted for publication July 28, 1998)
Fiz. Tekh. Poluprovodn. **33**, 208–210 (February 1999)

Effective Er photoluminescence is observed at room temperature in *a*-Si:H films doped with Er atoms through a gas phase using powdered $Er(TMND)_3$ as a source of Er ions. It is shown that the conditions for deposition of the films and their subsequent annealing influence the photoluminescence intensity and its temperature dependence. The observed behavior is attributed to restructuring of the amorphous silicon matrix within an Auger excitation mechanism involving defects. © *1999 American Institute of Physics.* [S1063-7826(99)01102-3]

Erbium-doped silicon, *a*-Si:H(Er), is of great interest in connection with the prospect of creating light-emitting diodes which are based on silicon electronics and which operate at a wavelength of 1.54 $\mu$m, which corresponds to the minimum of the absorption band of an optical fiber.

We recently reported the observation of the effective room-temperature photoluminescence of erbium ions in *a*-Si:H films obtained in a glow discharge using powdered $Er(TMND)_3$ as a source of Er ions.[1] The photoluminescence (PL) intensity of the samples obtained was comparable in value to the Er PL intensity of the *a*-Si:H(Er) samples with optimized erbium and oxygen concentrations that we previously obtained by dc silane decomposition in a magnetic field.[2]

This paper reports the influence of the substrate temperature and high-temperature annealing on the Er PL of *a*-Si:H(Er) films obtained in a glow discharge using powdered $Er(TMND)_3$ as a source of Er ions. The annealing was performed in a vacuum with a residual pressure $P=10^{-6}$ Torr in the range from room temperature to 500 °C for 1 h. The changes in the film structure during the annealing were investigated by Raman and infrared (IR) spectroscopy. The PL spectra were recorded with excitation by an argon laser at the wavelength $\lambda=514$ nm. The excitation power was 20 mW. The PL detection system included a double grating monochromator and a cooled germanium photodetector. The composition of the films, i.e., the Er and O concentrations and the distribution profiles of these elements across the film thickness, was investigated using Rutherford backscattering with irradiation of the films by accelerated $\alpha$ particles with an energy of 3.17 MeV. According to these data, Er and O were distributed uniformly across the sample thickness, and their concentrations were $2.1\times10^{20}$ and $1.4\times10^{21}\text{cm}^{-3}$ in the test samples.

According to the IR-spectroscopic data, annealing the samples obtained with the substrate at room temperature leads to alteration of the local structure accompanied by changes in the $CH_2$ and $CH_3$ modes and the vibrations of C–C bonds, which, however, does not influence the distribution of the Er and O concentrations across the film thickness.

Figure 1 presents the PL spectra of *a*-Si:H(Er) films obtained with different substrate temperatures. The spectra were recorded at $T=77$ K in an energy range which includes all the possible radiative transitions in the films. As can be seen from the figure, Er photoluminescence is observed in the films at 0.805 eV, regardless of the substrate temperature. The Er PL intensity differed to a slight extent and was 1.5 times greater in the samples prepared with a substrate temperature equal to 200 °C. A significant difference was observed in the behavior of the PL associated with radiative recombination of the matrix. For example, the samples obtained with the substrate at room temperature are characterized by a broad PL maximum in the vicinity of 0.95 eV,

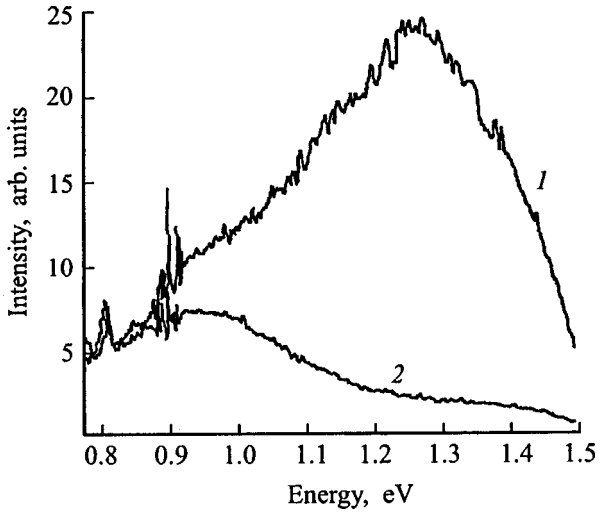


FIG. 1. PL spectra of *a*-Si:H(Er) films obtained with substrate temperatures equal to 200 (*1*) and 20 °C (*2*). The spectra have been normalized to the Er PL maximum at 0.805 eV.

 

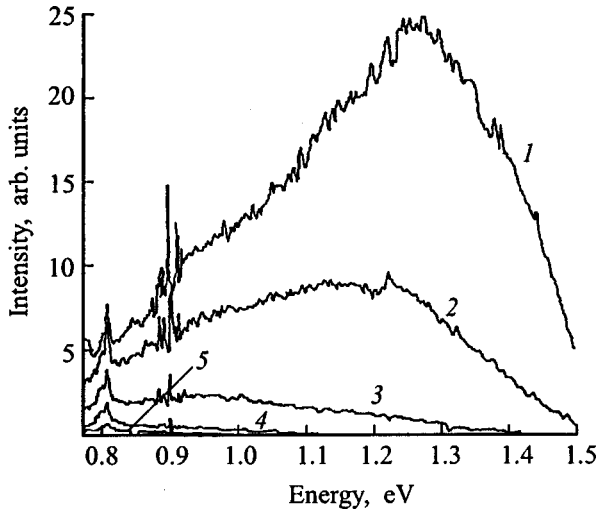


FIG. 2. PL spectrum of an *a*-Si:H(Er) sample obtained with a substrate temperature equal to 200 °C. Measurement temperature $T$, K: *1* — 77, *2* — 130, *3* — 190, *4* — 250, *5* — 310.

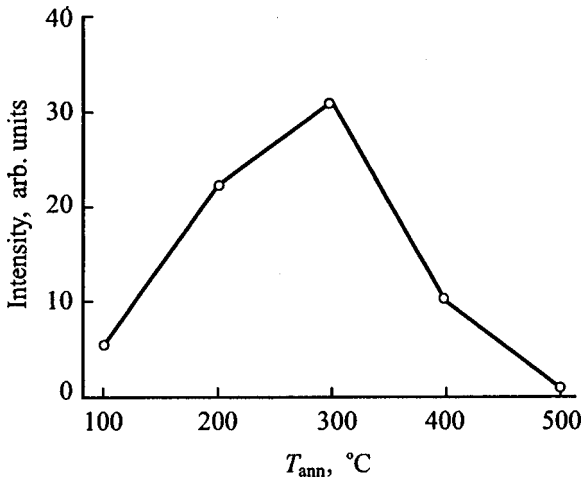


FIG. 4. Influence of the annealing temperature $T_{ann}$ on the Er PL intensity for a sample obtained at 20 °C.

which is characteristic of PL associated with defects. The samples obtained with a substrate temperature equal to 200 °C have a PL maximum near 1.25 eV, which is associated with intrinsic radiative recombination from the density-of-states tails of the conduction band and the valence band.[3] The ''defect'' peak at 0.95 eV is barely noticeable. The set of lines in the PL spectra near 0.9 eV is associated with the influence of the atmosphere.

The temperature dependence of the PL spectra of a sample obtained with a substrate temperature equal to 200 °C is shown in Fig. 2. As the temperature is raised, we see a sharp decrease in the intensity of the intrinsic PL band. At $T>100$ K the band associated with a radiative transition through defects into the middle of the band gap is the dominant feature in the spectra.

Figure 3 are plots of the temperature dependence of the Er PL intensity for samples obtained with different substrate temperatures. When the substrate temperature is increased, enhancement of the thermal Er PL quenching is observed. As a result, at room temperature the PL intensity of the sample prepared with the substrate at room temperature becomes higher than the PL intensity of the sample prepared with a substrate temperature equal to 200 °C. This finding, in our view, is attributable to the influence of the local environment of the Er atom on the process under consideration. It is known that the local environment has a significant influence on the lifetime of the excited state of the Er atom and makes a contribution to the mechanism of thermal Er PL quenching. As we have already noted,[1] the samples obtained with the substrate at room temperature have a polymer-like structure containing both a C–H bond and an O–H group in the local environment of the Er atom. In the opinion of Slooff *et al.*,[4] the latter determine the mechanism of thermal quenching in organic polymers.

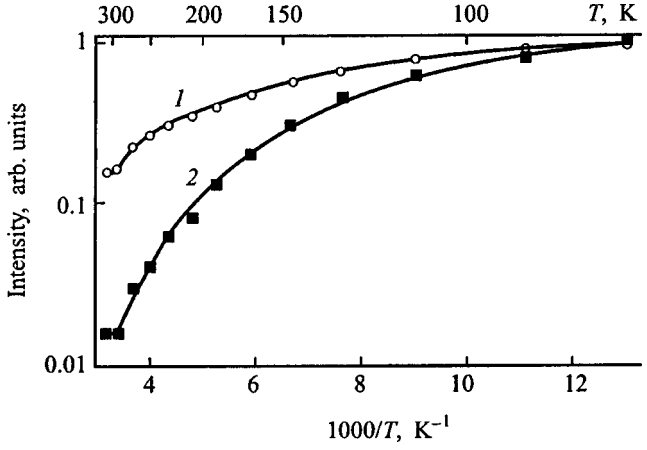


FIG. 3. Temperature dependence of the Er PL intensity for *a*-Si:H(Er) samples obtained with substrate temperatures equal to 20 (*1*) and 200 °C (*2*).

The influence of thermal annealing on the Er PL intensity measured at room temperature is shown in Fig. 4. The most significant change in the Er PL was observed on samples obtained with the substrate at room temperature. Annealing these samples at $T_{ann}\sim 300$ °C led to an almost 30-fold increase in the Er PL intensity, which can be attributed to restructuring of the films. According to the IR-spectroscopic data, annealing in this temperature range leads to a decrease in the intensities of the $CH_2$ and $CH_3$ modes and to the disappearance of bands corresponding to C–C bonds.[1] These changes have essentially no influence on the temperature dependence of the Er PL intensity. This is evidence of the insignificant influence of the local environment on the radiative lifetime, but, on the other hand, it points to an increase in the concentration of optically active Er ions during such restructuring.

Annealing the samples at $T_{ann}>300$ °C leads to a decrease in the Er PL intensity, which is associated, in our view, with further restructuring of the films. When the annealing temperature is raised, the effusion of hydrogen from the films is observed, and variation of the gap width occurs. In all likelihood, this alters the conditions for the pumping of Er PL in *a*-Si:H films, which, according to our interpretation, takes place as a result of an Auger process associated with the trapping of an electron from the conduction band by a

defect in the $D^0$ state with the formation of a $D^-$ state (the $D^0+e\rightarrow D^-$ electronic transition).[5] Energy is subsequently imparted as a result of the Coulomb interaction to the system of $f$ electrons in the erbium ions, in which the $^4I_{15/2}\rightarrow{}^4I_{13/2}$ transition takes place. This process has a resonance character in $a$-Si:H due to the closeness of the energies of these two electronic transitions, and its efficiency decreases with decreasing gap width.

A similar dependence of the Er PL intensity on annealing temperature was also observed on the $a$-Si:H films obtained with a substrate temperature of 200 °C, except that the observed changes were less pronounced. At the optimum annealing temperature of 300 °C the observed increase in the Er PL was only 1.5-fold. The latter is evidence that the structure of these films is more perfectly formed and does not contain a polymeric component, which would be more prone to restructuring during annealing.

Thus, the doping of $a$-Si:H films with Er atoms during plasma deposition using powdered $Er(TMND)_3$ as an erbium source is an effective method for preparing photoluminescent films emitting at 1.54 $\mu$m. Thus, we can hope to fabricate electroluminescent structures based on amorphous layers within this method.

We wish to thank the Ministry of Science of Russia (Project 97-1036), the Russian Fund for Fundamental Research (Grant 96-02-16931-a), and the EC INCO-Copernicus (Grants 977048 and PL978104) for their financial support of this work.

[1] E. I. Terukov, O. I. Kon'kov, V. Kh. Kudoyarova, O. B. Gusev, and G. Weiser, Fiz. Tekh. Poluprovodn. **32**, 987 (1998) [Semiconductors **32**, 884 (1998)].
[2] M. S. Bresler, O. B. Gusev, V. Kh. Kudoyarova, A. N. Kuznetsov, P. E. Pak, E. I. Terukov, I. N. Yassievich, B. P. Zakharchenya, W. Fuhs, and A. Sturm, Appl. Phys. Lett. **67**, 3599 (1995).
[3] R. A. Street, *Hydrogenated Amorphous Silicon*, Cambridge University Press, Cambridge (1991).
[4] L. H. Slooff, A. Polman, M. P. Oude Wolbers, F. C. J. M. van Veggel, D. N. Reinhoudt, and J. W. Hofstraat, J. Appl. Phys. **83**, 497 (1998).
[5] W. Fuhs, I. Ulber, G. Weiser, M. S. Bresler, O. B. Gusev, V. Kh. Kudoyarova, A. N. Kuznetsov, E. I. Terukov, and I. N. Yassievich, Phys. Rev. B **56**, 9545 (1997).

Translated by P. Shelnitz

## SEMICONDUCTOR STRUCTURES, INTERFACES AND SURFACES

# Transport properties and photosensitivity of metal/porous-silicon/*c*-Si structures

D. G. Yarkin

*Institute of Rare Metals, 109017 Moscow, Russia*
(Submitted May 28, 1997; accepted for publication September 15, 1998)
Fiz. Tekh. Poluprovodn. **33**, 211–214 (February 1999)

The current-voltage characteristics, photosensitivity, and impedance of *p*-type Al/porous-silicon/*c*-Si structures with 0.2 to 6-$\mu$m-thick porous layers of 80% porosity are studied. It is shown that at reverse and small forward bias voltages the current is determined by the potential barrier of the *c*-Si substrate at the isotypic porous-silicon/*c*-Si heterojunction. The photosensitivity is determined by the absorption of light in the *c*-Si substrate. The potential barrier of the metal/porous-silicon contact does not influence the photosensitivity or the current-voltage characteristics of the structures. The experimental plots of the dependence of the impedance on applied forward bias, thickness of porous silicon layer, and frequency agree well with the theoretical dependences, if an equivalent circuit including two *RC* circuits connected in series and comprised of the resistance and geometric capacitance of the porous silicon layer and the resistance and capacitance of the potential barrier of the *c*-Si substrate is used.
 [S1063-7826(99)01202-8]

As soon as photoluminescence with an efficiency of several percent at room temperature was discovered in layers of porous silicon (PS), this material became an object of intensive research. Considerable progress has been made in regard to the parameters of electroluminescent structures,[1] but the electroluminescence efficiency is still low. The investigation of the properties of device structures is also being continued. Studies of the photosensitivity of metal/PS/*c*-Si structures have shown that the photosensitivity is caused by the potential barrier at the PS/*c*-Si heterointerface.[2–4] It was concluded from an analysis of current-voltage characteristics (IVC's) in Refs. 5 and 6 that metal/PS/*c*-Si structures can be represented as the following two elements connected in series: the metal/PS contact barrier and the resistance of the PS layer. On the other hand, it was shown in Refs. 7 and 8 that metal/PS/*c*-Si structures can be represented as the following elements connected in series: the resistance of the PS layer and the potential barrier in the *c*-Si layer at the PS/*c*-Si heterointerface. Thus, the role of the metal/PS contact in the transport properties of metal/PS/*c*-Si structures is still not entirely clear.

In this paper we present the results of measurements of the impedance and photosensitivity of metal/PS/*c*-Si structures with a high-porosity PS layer. These results confirm that the potential barrier of the metal/PS contact has no effect on the photosensitivity or the I–V characteristics of the structures.

Al/PS/*c*-Si structures were fabricated on *c*-Si(111) substrates of *p*-type conduction ($10\,\Omega\cdot$cm) with a rear aluminum ohmic contact. Layers of porous silicon of thickness $d=0.2-6\,\mu$m were obtained by anodic etching of the substrates in an HF(48%):$C_2H_5OH=3:5$ solution over the course of 20–600 s at an anodic current density equal to 13 mA/cm$^2$. The aluminum contacts deposited on a porous silicon layer with a total area $A=65$ mm$^2$ consisted of a contact section with an area of 3.8 mm$^2$ (a thick layer of Al) and a semitransparent contact with an area of 2.7 mm$^2$ (50% transmission) for the photoelectric measurements. The measurements were performed two weeks after fabrication of the structures, when their characteristics became stable with time.

It was found from measurements of the optical transmission spectra of a PS layer on a *c*-Si substrate in the infrared range that the refractive index of the PS layer is $n_{IR}=1.35$. This value of $n_{IR}$ corresponds to 80% porosity if the material consists only of *c*-Si and air. The presence of other atoms (O, C) in the skin layer of the nanocrystallites can be disregarded, since the secondary-ion mass-spectrometric measurements performed after two weeks of storage in air gave values for the oxygen and carbon concentrations of the order of $1.5\times10^{20}$ cm$^{-3}$.

Figure 1 shows the current-voltage (I–V) characteristics of Al/PS/*c*-Si structures with 2 and 0.2-$\mu$m-thick PS layers, which were measured in the dark and upon exposure to light from an incandescent lamp at an intensity of 1 mW/cm$^2$. Connecting the *c*-Si substrate to the positive terminal of the power source corresponds to a positive bias. It can be seen that the dark I–V characteristics of structures with PS layers of different thicknesses are very close to one another. This means that the reverse current does not depend on the thickness of the PS layer and that it is determined by the Al/PS barrier or the PS/*c*-Si heterojunction. The forward current at a bias of several volts for the structure with a 2-$\mu$m PS layer is only 1.5 times smaller than the forward current for the structure with a 0.2-$\mu$m PS layer. This indicates that the current at a large forward bias is probably restricted by the

 

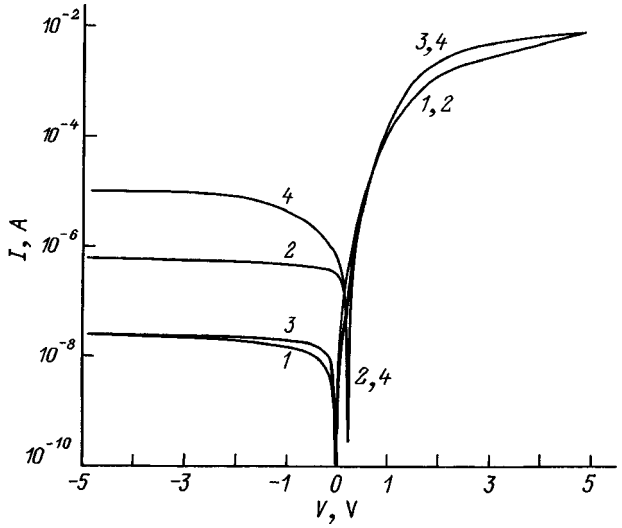


FIG. 1. Current-voltage characteristics of Al/PS/*c*-Si structures with 2-$\mu$m (*1*, *2*) and 0.2-$\mu$m (*3*, *4*) thick PS layers measured in the dark (*1*, *3*) and with illumination (*2*, *4*) by an incandescent lamp.

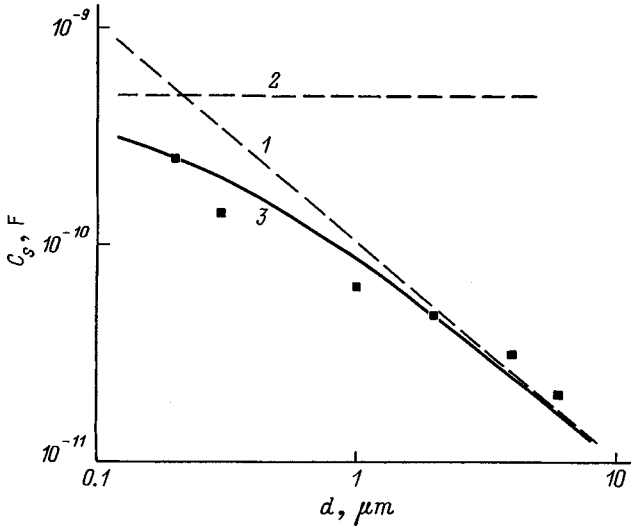


FIG. 2. Dependence of the capacitance $C_S$ of Al/PS/*c*-Si structures on the thickness $d$ of the PS layer. Calculated plots of $C(d)$ for the geometric capacitance of the PS layer (*1*), the barrier capacitance of the *c*-Si substrate (*2*), and the capacitance corresponding to these elements connected in series (*3*).

resistance of the metal/PS resistance, rather than by the resistance of the PS layer. It has been shown in several studies that the forward current in metal/PS/*c*-Si structures is a space-charge-limited current.[9] This is evidenced by the dependence of the current on the thickness of the PS layer, which is close to $I \propto 1/d^3$. We also obtained such a dependence for structures with a thickness of the PS layer equal to $2-6$ $\mu$m.

It can be seen from Fig. 1 that the photocurrent in the Al/PS/*c*-Si structure with a 2-$\mu$m PS layer is roughly an order of magnitude smaller than the photocurrent in the structure with a 0.2-$\mu$m PS layer. It was also found that the photocurrent increases rapidly with temperature. The reason for this increase is the restriction of the photocurrent by the high series resistance of the PS layer (this question was examined in greater detail in Ref. 7). This is confirmed by measuring the illumination-vs-current curves of Al/PS/*c*-Si structures of different thicknesses. At the light intensity used by us the open-circuit voltage $V_{oc}$ is equal to $0.2-0.25$ V for all the structures.

The form of the photosensitivity spectra of all the Al/PS/*c*-Si structures investigated with 80% porosity and the Al/*c*-Si structure was identical. In the case of a less porous PS layer, the short-wavelength photosensitivity cutoff shifted toward longer wavelengths. This confirms the results in Refs. 2–4 and provides evidence that the photogenerated carriers are separated in the space-charge region on the *c*-Si side of the PS/*c*-Si heterojunction. The absence of a photocurrent caused by the barrier at the Al/PS interface, however, is not enough to prove that this barrier is absent or small. Proof that this barrier is small was obtained from the impedance measurements.

The capacitance $C_S$ and the resistance $R_S$ of the Al/PS/*c*-Si structures were investigated in the frequency range $\omega = 10-10^6$ Hz. The measurements were performed using an equivalent circuit with elements connected in series, i.e., it was assumed that the complex resistance of the structure equals $R_S + 1/i\omega C_S$. When the frequency of the ac signal was high, $C_S$ did not depend on frequency. In such a case $C_S$ is probably determined by the barrier capacitance of the *c*-Si substrate $C_{\mathrm{Si}}$ and the capacitance of the PS layer $C_{\mathrm{PS}}$, which are connected in series:

$$C_S = \frac{C_{\mathrm{PS}} C_{\mathrm{Si}}}{C_{\mathrm{PS}} + C_{\mathrm{Si}}}.$$

The experimentally measured dependences of $C_S$ on the thickness of the PS layer and on applied constant reverse bias confirm this hypothesis.

Figure 2 shows the dependence of the capacitance of the Al/PS/*c*-Si structures on the thickness of the porous layer measured at a constant reverse bias equal to $-2$ V and an ac frequency equal to $10^4$ Hz. The figure also shows the calculated values of $C_{\mathrm{PS}}$, $C_{\mathrm{Si}}$, and $C_S$. It was assumed in the calculations that

$$C_{\mathrm{PS}} = \frac{A \varepsilon_{\mathrm{PS}} \varepsilon_0}{d},$$

$$C_{\mathrm{Si}} = A \left[ \frac{e \varepsilon_{\mathrm{Si}} \varepsilon_0 N_a}{2(V_b - V)} \right]^{1/2},$$

where $\varepsilon_{\mathrm{PS}}$ and $\varepsilon_{\mathrm{Si}}$ are the dielectric constants of PS and *c*-Si, respectively, $\varepsilon_0$ is the permittivity of free space, $N_a$ is the concentration of acceptors in the substrate, and $V_b$ is the band bending. The following values were used: $\varepsilon_{\mathrm{PS}} = 1.82$ ($\varepsilon_{\mathrm{PS}} = n_{\mathrm{IR}}^2$), $\varepsilon_{\mathrm{Si}} = 12$, $N_a = 1.5 \times 10^{15}\ \mathrm{cm}^{-3}$, $V_b = V_{oc} = 0.25$ V, and $V = -2$ V. Good agreement between the calculated and experimental plots of $C_S(d)$ can be seen from the figure.

Figure 3 shows plots of the dependence of $1/C_S^2$ on constant bias for structures with 2- and 0.2-$\mu$m-thick PS layers, which were measured at an ac frequency equal to $10^4$ Hz. The figure also shows calculated plots of $1/C_S^2(V)$. Good agreement between the calculated and experimental plots can be seen from Fig. 3. This is especially important, if it is taken

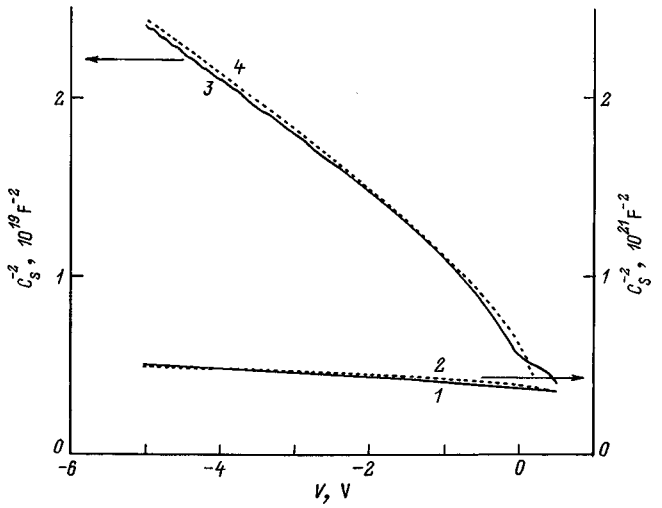


FIG. 3. Experimental and calculated dependences of $1/C_S^2$ on the constant bias $V$ for Al/PS/$c$-Si structures with 2 $\mu$m (*1*, *2*) and 0.2 $\mu$m (*3*, *4*) thick PS layers.

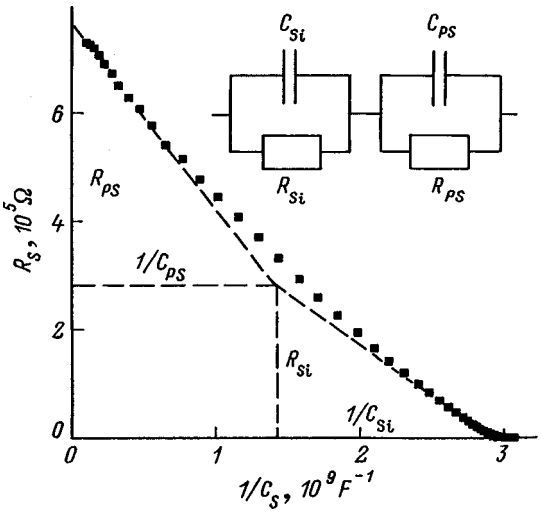


FIG. 4. Dependence of the ac resistance $R_S$ on the capacitance $C_S$ derived from the frequency dependences for an Al/PS/$c$-Si structure with a 0.2-$\mu$m-thick PS layer. The extrapolated values of $R_{PS}$, $C_{PS}$, $R_{Si}$, and $C_{Si}$ are also shown. Inset — equivalent circuit of an Al/PS/$c$-Si structure under reverse and zero bias.

into account that no fitting parameters were actually used to construct the calculated plots. All the quantities appearing in the formulas were determined experimentally. Since it was assumed in constructing each calculated plot that the constant reverse voltage falls entirely on the heterojunction barrier, the agreement between theory and experiment allows us to conclude that the reverse-bias current is restricted by the resistance of that barrier. This provides evidence that the height of the potential barrier of the metal/PS contact is far smaller than the height of the potential barrier at the PS/$c$-Si heterojunction. Apparently, as in the general case of a metal/semiconductor contact,[10] the height of the metal/PS barrier is determined by an interface state. As for the PS/$c$-Si barrier, its presence is evidently caused by the high concentration of defects at the heterojunction.[4] In fact, according to theoretical calculations made under the assumption of the absence of defects, there should be a carrier-enriched region, rather than a potential barrier, at the PS/$c$-Si heterojunction.[9]

At low frequencies the value of $C_S$ depends on frequency. This can be understood by examining the equivalent circuit of an Al/PS/$c$-Si structure in Fig. 4. According to Ref. 11, the impedance of such a circuit is specified by the expressions

$$R_S = R_{Si} + R_{PS} - \left( \frac{\tau_1}{C_{S1}} + \frac{\tau_2}{C_{S2}} \right),$$

$$\frac{1}{C_S} = \frac{1}{C_{S1}} + \frac{1}{C_{S2}},$$

$$\frac{1}{C_{S1}} = \frac{(\omega\tau_1)^2}{C_{Si}[1+(\omega\tau_1)^2]},$$

$$\frac{1}{C_{S2}} = \frac{(\omega\tau_2)^2}{C_{PS}[1+(\omega\tau_2)^2]},$$

$$\tau_1 = R_{Si}C_{Si}, \quad \tau_2 = R_{PS}C_{PS}.$$

Measurements of $R_S$ and $C_S$ in the frequency range from $\omega\tau_1 \ll 1$, $\omega\tau_2 \ll 1$ to $\omega\tau_1 \gg 1$, $\omega\tau_2 \gg 1$ permit determination of the resistance of the PS layer $R_{PS}$ and the resistance of the barrier of the $c$-Si substrate $R_{Si}$, as well as $C_{PS}$ and $C_{Si}$. The results of our measurements show that the conditions indicated above hold in the samples investigated at zero bias when the frequency is varied from $10^2$ to $10^5$ Hz.

Figure 4 shows the dependence of $R_S$ on $1/C_S$ for structures with a 0.2-$\mu$m-thick porous layer measured at zero bias. The experimental points on the curves were obtained from the measured values of $R_S$ and $C_S$ at various frequencies. It can be seen from Fig. 4 that the dependence of $R_S$ on $1/C_S$ consists of two nearly linear segments with different slopes. Extrapolation of these segments to the respective axes and the point of intersection of the extrapolation curves give the values of $P_{PS}$, $C_{PS}$, $R_{Si}$, and $C_{Si}$. The values obtained for the structure with a 0.2-$\mu$m-thick PS layer are: $R_{PS} = 4.9\times10^5\,\Omega$, $C_{PS} = 690$ pF, $R_{Si} = 2.7\times10^5\,\Omega$, and $C_{Si} = 710$ pF. For the structure with a 2-$\mu$m-thick PS layer (not shown in the figure) the second segment is indistinct, since $C_{Si} \gg C_{PS}$. Therefore, we determined only the parameters of the PS layer: $R_{PS} = 4.7\times10^6\,\Omega$ and $C_{PS} = 52$ pF. The results obtained show that the resistance of the porous layer depends almost linearly on its thickness. The resistivity of PS is $\rho = R_{PS}C_{PS}/\varepsilon_{PS}\varepsilon_0 = 2\times10^9\,\Omega\cdot$cm. It is noteworthy that the resistivity of PS itself can depend on frequency, but the value of $\rho$ that we obtained agrees well with the values of the resistivity of highly porous layers obtained from measurements of thick structures ($d > 10\,\mu$m), in which there is no rectification of the current and the I–V characteristic is linear.[12]

Thus, these investigations of the I–V characteristic, the photosensitivity, and the impedance of $p$-type metal/PS/$c$-Si structures have shown that at reverse and small forward biases the dark current is determined by the potential barrier of the $c$-Si substrate at the isotypic heterojunction. The photosensitivity is determined by the absorption of light in the

*c*-Si substrate. The potential barrier of the metal/PS contact does not influence the photosensitivity or the I–V characteristic of the structures. The dependences of the capacitance of the structures on the constant bias and the thickness of the PS layer are completely determined by the geometric capacitance of the PS layer and the capacitance of the space-charge region of the *c*-Si substrate. The impedance of the structures is determined by two parallel *RC* circuits connected in series (the layer of porous silicon and the space-charge region in *c*-Si at the heterojunction).

We express our thanks to A. L. Balagurov and E. A. Petrova for some useful discussions and for supplying the samples.

[1] P. M. Fauchet J. Lumin. **70**, 294 (1996).
[2] J. P. Zheng, K. L. Jiao, W. P. Shen, W. A. Anderson, and H. S. Kwok, Mater. Res. Soc. Symp. Proc. **283**, 371 (1993).
[3] E. V. Astrova, A. A. Lebedev, A. D. Remenyuk, V. Yu. Rud', and Yu. V. Rud', Fiz. Tekh. Poluprovodn. **31**, 159 (1997) [Semiconductors **31**, 121 (1997)].
[4] L. A. Balagurov, D. G. Yarkin, G. A. Petrovicheva, E. A. Petrova, A. F. Orlov, and S. Ya. Andryushin, J. Appl. Phys. **82**, 4647 (1997).
[5] D. Deresmes, V. Marissael, D. Stievenard, and C. Ortega, Thin Solid Films **255**, 258 (1995).
[6] K. Khirouni, J. C. Bourgoin, K. Borgi, H. Maaref, D. Deresmes, and D. Stievenard, Mater. Res. Soc. Symp. Proc. **452**, 619 (1997).
[7] M. Ben Chorin, F. Moller, and F. Koch, J. Appl. Phys. **77**, 4482 (1995).
[8] L. Pavesi, J. Microelectron. **27**, 437 (1996).
[9] C. Peng, K. D. Hirschman, and P. M. Fauchet, J. Appl. Phys. **80**, 295 (1986).
[10] A. G. Milnes and D. L. Feucht, *Heterojunctions and Metal-Semiconductor Junctions* (Academic Press, New York–London, 1972).
[11] L. S. Berman, *Capacitance Methods for Investigating Semiconductors* [in Russian], Nauka, Leningrad (1972).
[12] L. A. Balagurov, N. B. Smirnov, E. A. Kozhukhova, A. F. Orlov, and A. Ya. Polyakov, Izv. Akad. Nauk, Ser. Fiz. **58**, 78 (1994).

Translated by P. Shelnitz

# Gain in injection lasers based on self-organized quantum dots

A. R. Kovsh, A. E. Zhukov, A. Yu. Egorov, V. M. Ustinov, N. N. Ledentsov, M. V. Maksimov, A. F. Tsatsul'nikov, and P. S. Kop'ev

*A. F. Ioffe Physicotechnical Institute, Russian Academy of Sciences, 194021 St. Petersburg, Russia*
(Submitted September 15, 1998; accepted for publication September 16, 1998)
Fiz. Tekh. Poluprovodn. **33**, 215–223 (February 1999)

The analytical form of the dependence of the gain on pump current density for lasers with an active region based on self-organized quantum dots is derived in a simple theoretical model. The proposed model is shown to faithfully describe experimental data obtained for laser diodes based on InGaAs quantum dots in an AlGaAs/GaAs matrix, as well as InAs quantum dots in an InGaAs/InP matrix. The previously observed gain saturation and switching of the lasing from the ground state to an excited state of the quantum dots are studied. The influence of the density of quantum-dot arrays on the threshold characteristics of lasers based on them is examined on the basis of this model. © *1999 American Institute of Physics.* [S1063-7826(99)01302-2]

## 1. INTRODUCTION

One of the principal parameters determining the possibility of the practical employment of a semiconductor laser is the threshold current density $J_{\text{th}}$. The use of quantum wells (QW's) as active regions has led to the creation of laser diodes having a significantly lower value of $J_{\text{th}}$ than traditional double heterostructure lasers.[1] The lowering of $J_{\text{th}}$ is associated primarily with the decrease in the size of the gain medium, where an inverted population must be maintained. It is expected that further lowering of $J_{\text{th}}$ can be achieved when a quantum-dot (QD) array serves as the active region.[2–4] The rapid progress made in the study of the self-organization of surfaces has led to the creation of arrays of self-organized QD's and to the realization of continuous lasing on the ground state of the QD's in lasers based on them with $J_{\text{th}}$ of the order of 60–100 A/cm$^2$ (Ref. 5) at room temperature, which is already comparable to the lowest recorded values for QW lasers.[6]

The low values of $J_{\text{th}}$ indicated above were attained either for stripe diodes with large cavity lengths ($L>1$ mm) or for laser diodes in a geometry with four cleavage faces [a structure with an annular mode ($L\to\infty$)], i.e., for structures with small radiation-extraction losses. However, these diodes are characterized, in principle, by a low differential efficiency, $\eta_D$:

$$\eta_D=\eta_i\frac{\alpha_m}{\alpha_m+\alpha_i}. \tag{1}$$

Here $\alpha_i$ denotes the internal losses, $\eta_i$ is the internal quantum efficiency, and $\alpha_m$ denotes the losses at mirrors, which are, in turn, related to the cavity length ($L$) by the standard equation

$$\alpha_m=\frac{1}{L}\ln\left(\frac{1}{R}\right), \tag{2}$$

where $R$ is the reflectivity of the mirrors.

Most practical applications require relatively high ($>50\%$) values of $\eta_D$ and thus call for the use of either comparatively short diodes (with $L<1$ mm) or a special waveguide design that ensures small internal losses, which is fairly difficult to achieve.[7] As was previously shown, a decrease in the cavity length of lasers with a QD active region leads to a superlinear increase in the threshold current density, attesting to gain saturation.[8,9] Thus, the problem of overcoming gain saturation is crucial to the practical application of QD lasers. Its solution requires an understanding of which parameters of a system with QD's are most significant and determination of the experimentally observed character of the dependence of the gain on pump current density.

Complete theoretical simulation of this dependence is a formidable task, which requires a large number of mathematical calculations and sometimes knowledge of experimentally inaccessible parameters, and such a situation usually leads to some discrepancy between theory and experiment.[10] One of the first attempts to relate experimentally determined values of the gain in QD lasers to the energy and emission characteristics of an ensemble of QD's was undertaken in Ref. 11, but the dependence of the gain on pump current density was not obtained in analytical form. In Ref. 12 a phenomenological equation was proposed for describing experimental data. Its use permits, in particular, prediction of the dependence of the threshold characteristics of actually existing lasers on the density of the QD array.

In this paper we develop a simple model, which describes the threshold characteristics of a laser based on a QD array in analytical form, from the first principles of laser gain. The theoretical model is compared with experiment using experimental data obtained for laser diodes based on two different systems with QD's: (In, Ga)As QD's in an (AlGa)As/GaAs host and InAs QD's in an InGaAs/InP host.

## 2. THEORY

Figure 1 shows schematically the dependences of the gain on pump current density for a double heterostructure,[13]

 

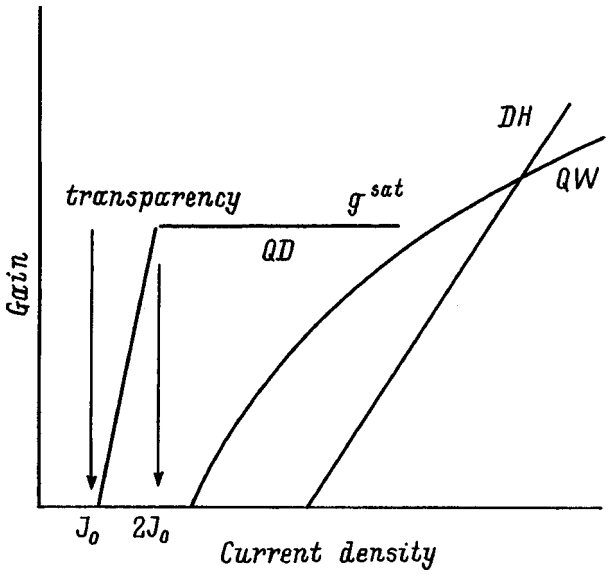


FIG. 1. Schematic representation of the dependence of the gain on pump current density for lasers based on a double heterostructure (DH), a quantum well (QW), and an array of ideal quantum dots (QD).

a structure with a quantum well,[14] and a structure with an ideal QD array. Quantum dots which have identical dimensions and shape (do not produce nonuniform broadening) and a ground energy level sufficiently distant from the higher-lying states are considered ideal.

An ideal QD array is essentially a two-level system, and the dependence of the modal gain ($g_{QD}$) on pump current density ($J_{QD}$) can be obtained from the standard equations[15]

$$J_{QD}=\text{const}\times r_{sp}(E_{12}), \tag{3}$$

$$g_{QD}=\text{const}\times(E_{12})^2\times r_{st}(E_{12}), \tag{4}$$

where $r_{sp}$ is the rate of spontaneous recombination, $r_{st}$ is the rate of stimulated emission, and $E_{12}$ is the energy of the transition of an electron, which is localized in a QD, from the valence band to the conduction band.

Correlated (exciton) trapping takes place at low temperatures, where the time for the binding of an electron and a hole in an exciton is much shorter than the charge-carrier trapping time in a QD. It has not been conclusively established whether exciton trapping of an electron and a hole in a QD also takes place at high temperatures. On the other hand, the condition of local electroneutrality indicates that the trapping process can be treated using the exciton approximation, i.e.,

$$f_2=1-f_1\equiv f_0, \tag{5}$$

where $f_1$ ($f_2$) is the probability that the $E_1$ ($E_2$) state is occupied by an electron or, stated differently, $f_0$ is the probability that a QD is occupied by an exciton. Therefore, the rates of spontaneous and stimulated emission take on the following forms:

$$r_{sp}(E_{12})=\text{const}\times f_0, \tag{6}$$

$$r_{st}(E_{12})=\text{const}\times[(f_1-f_2)]=\text{const}\times(2f_0-1). \tag{7}$$

We can then write Eqs. (3) and (4) in the form

$$J_{QD}=C_1\times f_0, \tag{8}$$

$$g_{QD}=C_2\times(2f_0-1), \tag{9}$$

where $C_{1(2)}$ are constants. Now, solving this system of equations and introducing the notation

$$\frac{C_1}{2}=J_0, \tag{10}$$

$$C_2=g^{sat}, \tag{11}$$

we obtain the following expression, which relates the modal gain ($g_{QD}$) to the recombination current density ($J_{QD}$) on states of an array of ''ideal'' QD's:

$$g_{QD}=g^{sat}\frac{J_{QD}-J_0}{J_0}. \tag{12}$$

Figure 1, which provides a schematic representation of this dependence, reveals the physical meaning of $J_0$ and $g^{sat}$: $J_0$ is the transparency current density which corresponds to zero gain and is needed to create an inverted population. When the pump current density $J_{QD}$ equals $J_0$, there is one exciton in each QD, and an increase in the pump current causes increasingly more QD's to begin to be filled by a second exciton and the gain to increase linearly with current. When the current density equals $2J_0$, the QD array attains its maximum possible gain.

Figure 2 shows schematically the electron (hole) density of states of a real system with QD's. The differences from the ideal case include, first, nonuniform broadening of the density of states due to the spread of sizes of the QD's, which leads to a decrease in the maximum gain, and, second, relative proximity of the higher-lying states (QD excited states, as well as wetting-layer and matrix states), which leads to an increase in the transparency current.

In order to obtain the dependence of the gain on current for QD's in a simple analytical form with allowance for the

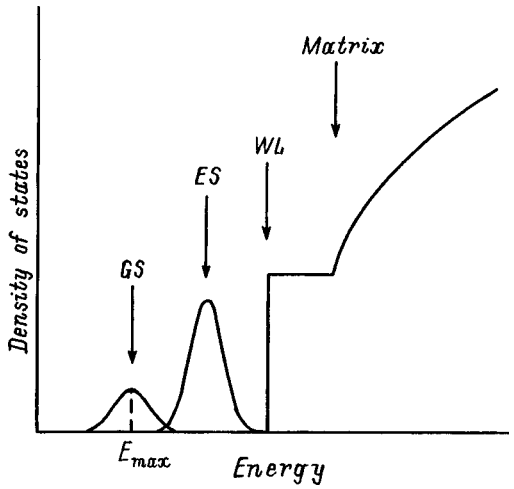


FIG. 2. Schematic representation of the density of states of a structure with an array of self-organized quantum dots having a finite spread of sizes. The density of states contains nonuniformly broadened, quantum-dot ground state (GS) and excited state (ES), wetting-layer states (WL), and matrix states. $E_{max}$ — energy value corresponding to the ground state density maximum.

spread of sizes, we assume equality of the matrix element (or the oscillator strength) for dots of all sizes, and we consider cases in which the thermal distribution function varies only slightly in the range of the nonuniformly broadened density of states (fairly typical cases, in which $kT$ is greater than the nonuniform broadening or in which the Fermi level is located above the QD energy states). Therefore, it can be assumed that the maximum gain is attained at the density-of-states maximum. Disregarding the higher-lying states, we obtain the following analogs of Eqs. (3) and (4):

$$J_{\mathrm{QD}} = \mathrm{const} \times \int r_{\mathrm{sp}}(E)\, dE, \tag{13}$$

$$g_{\mathrm{QD}}^{\max} \equiv g_{\mathrm{QD}} = \mathrm{const} \times (E_{\max})^2 \times r_{\mathrm{st}}(E_{\max}), \tag{14}$$

where $E_{\max}$ is the photon energy, which corresponds to the transition for dots of average size or to the density-of-states maximum. [We note that in Eq. (13) and in the following equations the integration limits are chosen in accordance with the states considered]. Equations (6) and (7) remain the same:

$$r_{\mathrm{sp}}(E) = \mathrm{const} \times f_0(E), \tag{15}$$

$$r_{\mathrm{st}}(E_{\max}) = \mathrm{const} \times [2 f_0(E_{\max}) - 1], \tag{16}$$

since, in contrast to the case of a QW or a bulk material, here integration over all the transitions with a given energy within the electron or hole density of states is not required in calculating the emission rates, since an electron can recombine radiatively only with a hole in the same QD. From the mathematical standpoint, this requirement is analogous to the introduction of a selection rule with respect to $k$ in the treatment of transitions from a continuous density of states.

Assuming, as we have done above, that $f_0$ varies weakly in the energy density range of the ground state, by analogy with (8)–(11), we obtain an equation identical to Eq. (12). The main difference from the case of ideal QD's is that at the same QD density nonuniform broadening leads to a decrease in the value of the maximum gain ($g^{\mathrm{sat}}$), while the value of the transparency current ($J_0$) remains the same, and the dependence of the gain on current maintains the linear form.

Let us now consider the effect of wetting-layer (WL) and matrix states. The expression for the current density utilized for radiative recombination in these states can be written in the form

$$J_{\mathrm{WL+matrix}} = \mathrm{const} \times \int r_{\mathrm{sp}}^{\mathrm{WL+matrix}}(E)\, dE. \tag{17}$$

Under the assumptions of symmetric electron and hole densities of states and equality between the electron and hole masses, which are often employed in such estimates, as well as with allowance for the momentum selection rule, the rate of spontaneous recombination in wetting-layer and matrix states can be written as

$$r_{\mathrm{sp}}^{\mathrm{WL+matrix}}(E) = \mathrm{const} \times E \rho^2(E) f^2(E), \tag{18}$$

$$f(E) = \frac{1}{1 + \exp\left(\dfrac{E-F}{kT}\right)}, \tag{19}$$

where $\rho(E)$ is the electron (hole) density of states of the WL or the matrix as a function of $E$, and $F$ is the quasi-Fermi level for electron (holes). Thus, we have

$$J_{\mathrm{WL+matrix}} = \mathrm{const} \times \int E \times \frac{\rho^2(E)}{\left[1 + \exp\left(\dfrac{E-F}{kT}\right)\right]^2} dE. \tag{20}$$

In order to avoid numerical calculations, we assume that the wetting-layer and matrix states are located above the quasi-Fermi level. We can then go over from a Fermi–Dirac distribution to a Boltzmann distribution, and Eq. (20) takes on the form

$$J_{\mathrm{WL+matrix}} = \mathrm{const} \times \exp\left(\frac{2F}{kT}\right) \times \int E \rho^2(E) \exp\left(-\frac{2E}{kT}\right) dE. \tag{21}$$

The integral over the energy appearing in this expression clearly converges and is equal to a constant, i.e.,

$$J_{\mathrm{WL+matrix}} = \mathrm{const} \times \exp\left(\frac{2F}{kT}\right), \tag{22}$$

$$\mathrm{const} \equiv J_2. \tag{23}$$

On the other hand,

$$f_0 = \frac{1}{1 + \exp\left(-\dfrac{F}{kT}\right)}; \tag{24}$$

therefore,

$$\exp\left(\frac{2F}{kT}\right) = \left(\frac{f_0}{1-f_0}\right)^2. \tag{25}$$

Equation (12), in turn, can be written in the form

$$J_{\mathrm{QD}} = J_0\left(1 + \frac{g_{\mathrm{QD}}}{g^{\mathrm{sat}}}\right), \tag{26}$$

and, using (8) and (10), we find

$$f_0 = \frac{1}{2}\left(1 + \frac{g_{\mathrm{QD}}}{g^{\mathrm{sat}}}\right). \tag{27}$$

Equation (22) finally takes on the form

$$J_{\mathrm{WL+matrix}} = J_2\left(\frac{g^{\mathrm{sat}} + g_{\mathrm{QD}}}{g^{\mathrm{sat}} - g_{\mathrm{QD}}}\right)^2. \tag{28}$$

Thus, we have expressed the current caused by recombination on high-lying states in terms of the gain that can be achieved in a QD. The total pump current density can be represented in the form

$$J = J_{\mathrm{QD}} + J_{\mathrm{WL+matrix}} = J_0\left(1 + \frac{g_{\mathrm{QD}}}{g^{\mathrm{sat}}}\right) + J_2\left(\frac{g^{\mathrm{sat}} + g_{\mathrm{QD}}}{g^{\mathrm{sat}} - g_{\mathrm{QD}}}\right)^2. \tag{29}$$

Thus, the presence of the higher-lying WL and matrix states leads to an increase in the transparency current density and a deviation of the dependence of the gain on current density from its linear course.

At small gains, where $g_{QD} \ll g^{sat}$, the total pump current density takes on the form

$$J = J_0\left(1 + \frac{g_{QD}}{g^{sat}}\right) + J_2\left(1 + 2\frac{g_{QD}}{g^{sat}}\right). \quad (30)$$

Hence, we can obtain an expression for the gain in terms of the current density:

$$g_{QD} = g^{sat}\frac{J - (J_0 + J_2)}{J_0 + 2J_2}. \quad (31)$$

Introducing the notation

$$J_{tr} = J_0 + J_2, \quad (32)$$

we obtain the following formula, which describes the dependence of the gain on pump current density at small gains:

$$g_{QD} = g^{sat}\frac{J - J_{tr}}{J_{tr}}\gamma, \quad (33)$$

where

$$\gamma = \frac{J_{tr}}{J_{tr} + J_2}. \quad (34)$$

Here $J_{tr}$ is the transparency current density, $J_2$ is the fraction of the transparency current density due to radiation recombination on ''parasitic'' WL and matrix states, and the coefficient $\gamma$ specifies the relative contribution of these states

$$\gamma = 1 \quad \text{for} \quad J_2 = 0, \quad (35)$$

$$\gamma = 1/2 \quad \text{for} \quad J_2 \to \infty. \quad (36)$$

An expression such as (33) was first proposed in Ref. 12 to describe a linear gain regime. We have given here the physical meaning of the parameter $\gamma$ and indicated its possible range of variation.

Apart from the ground state, QD's can also contain excited states. As in the treatment of the contribution of the WL and the matrix, we assume that these states lie above the Fermi level. This leads to the appearance of a third term in Eq. (30):

$$J = J_{QD} + J_{QD}^{ex} + J_{WL+matrix}$$
$$= J_0\left(1 + \frac{g_{QD}}{g^{sat}}\right) + J_1\left(\frac{g^{sat} + g_{QD}}{g^{sat} - g_{QD}}\right)$$
$$+ J_2\left(\frac{g^{sat} + g_{QD}}{g^{sat} - g_{QD}}\right)^2, \quad (37)$$

where $J_1$ is the fraction of the transparency current density utilized to pump QD excited states. At small gain values we obtain an equation which is completely identical to Eq. (34), but the transparency current density is now defined by the expression

$$J_{tr} = J_0 + J_1 + J_2, \quad (38)$$

and $\gamma$ remains unchanged. This fact is curious, since it follows from it that the presence of QD excited states does not have any influence on the slope of the dependence of the gain on pump current density, in contrast to the case of the WL and matrix states.

## 3. EXPERIMENT

In order to test the validity of the model described above, we investigated the gain characteristics of two laser structures with QD's. The first structure, which will henceforth be designated as QD-GaAs, was grown on an $n^+$-GaAs(100) substrate. The active region consisted of three planes of InGaAs QD's separated by $Al_{0.15}Ga_{0.85}As$ spacer layers with a thickness of 50 Å and was placed in the middle of an $Al_xGa_{1-x}As$ ($x = 0.45 - 0.15$) waveguide, which was capped by emitter layers, each having a thickness of 1.5 $\mu$m. The second structure, QD-InP, was grown on an $n^+$-InP(100) substrate, which also served as the lower emitter. Three layers of InAs QD's separated by 50-Å InGaAs layers were placed in the middle of a waveguide InGaAs layer with a thickness of 0.6 $\mu$m, which was capped from above by an InAlAs emitter layer with a thickness of 1.5 $\mu$m. The measurements were performed at 300 K for the QD-GaAs structure and at 77 K for the QD-InP structure. The technological regimes used to grow the structures and fabricate the laser diodes, as well as the procedures of the electro- and photoluminescence measurements, were described in greater detail in Ref. 16, 17, and 18, respectively.

## 4. RESULTS AND DISCUSSION

### 4.1. Dependence of the gain on pump current density

The experimental dependence of the gain on current density can be obtained from the condition of equality between the modal gain ($g_{mod}$) and the total losses at the lasing threshold:

$$g_{mod}(J_{th}) = \alpha_m + \alpha_i. \quad (39)$$

The internal losses $\alpha_i$, in turn, can be determined from the experimentally measured external quantum efficiency as a function of the stripe length using Eq. (1).

Figure 3a presents the dependence of the modal gain on current density determined by the method described above for the QD-GaAs laser structure. It is clearly seen that this dependence has two saturated segments. The position of the lasing wavelength as a function of threshold current density is presented in Fig. 3b. A comparison of the figures reveals that the beginning of the second segment on the plot of the gain as a function of current density corresponds exactly to an abrupt blue shift of the lasing wavelength.

We assume that the behavior of the gain and the lasing wavelength just described is attributable to the fact that only the QD ground state is filled at low current densities. An increase in the pump current density leads, on the one hand, to saturation of the gain in the ground state, but, on the other hand, it leads to a gradual increase in the population of the excited state. As a result, at a certain current density the maximum gain attained in the excited state begins to surpass

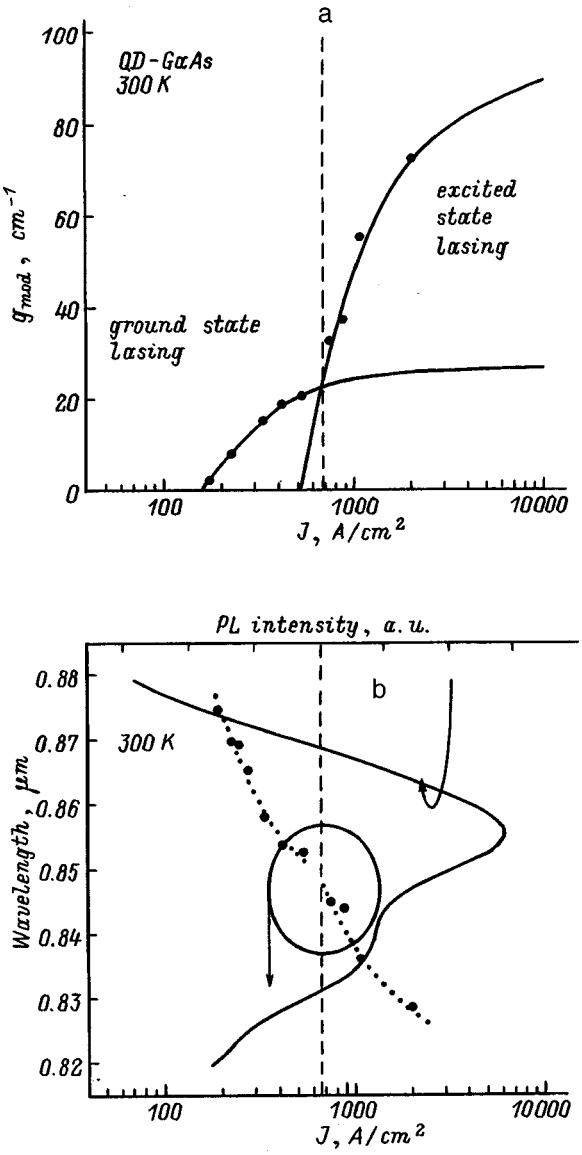


FIG. 3. Experimental plots (points) of the modal gain (a) and the lasing wavelength (b) as functions of pump current density for the QD-GaAs structure at room temperature. The solid curves were calculated in accordance with Eqs. (37) and (29) and the fitting parameters listed in Table I. The photoluminescence spectrum of this structure recorded after removal of the upper contact layer is shown in section b of the figure.

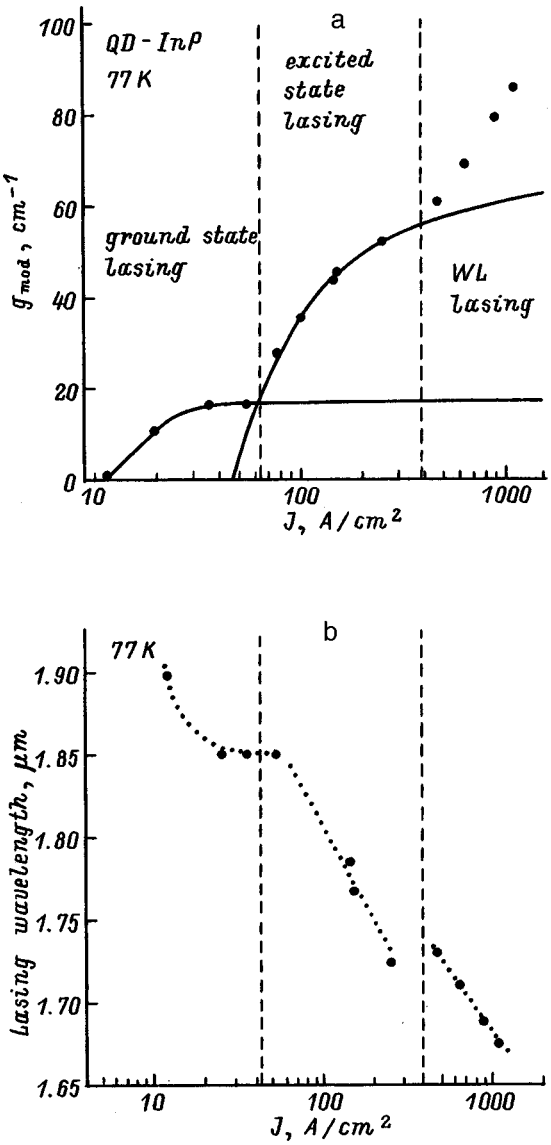


FIG. 4. Dependence of the modal gain (a) and the lasing wavelength (b) for the QD-InP structure at 77 K. The solid lines were calculated in accordance with Eqs. (37) and (29) and the fitting parameters listed in Table I.

the maximum gain for the ground state, i.e., an abrupt blue shift of the lasing wavelength occurs. When the pump current density is raised further, lasing takes place already on the excited state, on which the gain also saturates as the current density rises, but at a significantly higher level in comparison with the ground state.

The photoluminescence spectrum of this structure in Fig. 3b, which was recorded after removal of the upper contact layer, consists of two distinct peaks, of which the long-wavelength peak corresponds to the QD ground state and the short-wavelength peak corresponds to the QD excited state. We note that the lasing wavelength lies within the long-wavelength peak on the first segment and that it lies within the second segment in the case of lasing on the excited state.

The QD-InP laser exhibits similar dependences of the gain and lasing wavelength on pump current density (Fig. 4). Clearly expressed switching of the lasing from the ground state to the excited state is again observed. In addition, at a current density of the order of 400 $A/cm^2$ the lasing switches to states of the two-dimensional wetting layer, and the gain-vs-current curve becomes strictly logarithmic, as is characteristic of QW lasers[14] (see Fig. 1).

For both structures the segment of the gain-vs-current curve, which corresponds to the ground state, is approximated well by the expression (37) with definite values of $J_0$, $J_1$, $J_2$, and $g^{sat}$, and the segment corresponding to the excited state is approximated by Eq. (29), since in this case $J_0$ now refers to the excited state. The values of the parameters for the structures investigated are listed in Table I. The good correspondence between the experimental and theoretical data allows us to state that the proposed approach is valid for a broad range of material parameters, since we investigated two different QD systems.

TABLE I. Parameters of the gain for QD lasers.

| Structure | State | $g^{sat}$ | $J_0$ | $J_1$ | $J_2$ | $\gamma$ |
|---|---|---|---|---|---|---|
| InGaAs QD's | Ground | 27 | 126 | 36 | 0 | 1 |
| in an AlGaAs matrix | Excited | 102 | 480 | ⋯ | 33 | 0.93 |
| InAs QD's | Ground | 17.1 | 10.2 | 0.6 | 0 | 1 |
| in an InGaAs/InP matrix | Excited | 69 | 42 | ⋯ | 3.6 | 0.9 |

It is noteworthy that the relationships between the values of the fitting parameters correspond to their physical meaning. For example, the fraction of the transparency current that is utilized for the recombination of carriers on wetting-layer states ($J_2$) in the case where lasing occurs on the ground state is negligible in comparison with the case of lasing on the excited states. This phenomenon is attributed to the fact that the pump level is considerably higher and, consequently, a larger number of carriers are in the wetting layer in the latter case.

It would be useful to more thoroughly examine the ratios between the values of the saturated gain $g^{sat}$ and the values of $J_0$ attained for lasing on the excited state and the ground state:

$$R_{g^{sat}}=\frac{g^{sat}(\text{excited})}{g^{sat}(\text{ground})}, \tag{40a}$$

$$R_{J_0}=\frac{J_0(\text{excited})}{J_0(\text{ground})}. \tag{40b}$$

The values of these parameters for the two laser structures are listed in Table II.

It follows from the data presented above that the saturated gain attained in the excited state in the QD-GaAs and QD-InP lasers is approximately four times higher than the corresponding gain for the ground state.

In order to explain the closeness of these values to 4, let us consider the energy spectrum of a QD. In the simple hydrogenic atom approximation[19] the spectrum of a QD contains one $1s$ ground state with two degenerate spin states, as well as a $2s$ state and three $2p$ states, which have the same energy. Thus, four times more carriers can accumulate at the excited level; therefore, the ratio between the saturated gains should be of the order of 4, if it is assumed that recombination occurs with the same oscillator strength in the ground state and the excited state. In general, the splitting between the $2s$ and $2p$ states because the QD potential well is not described by a Coulomb potential, as well as the splitting of the $2p$ states themselves because of the aspherical shape of a QD, should lead to removal of the degeneracy of the excited level. However, this splitting is considerably smaller than the nonuniform broadening of the QD density of states associated with the spread of sizes, and the foregoing qualitative arguments remain valid.

TABLE II. Ratios between parameters of the gain for the excited state and the ground state of QD lasers.

| Structure | $R_{g^{sat}}$ | $R_{J_0}$ |
|---|---|---|
| InGaAs QD's in an AlGaAs matrix | 3.8 | 3.8 |
| InAs QD's in an InGaAs/In matrix | 4 | 4.1 |

It can be shown that at zero temperature, at which there is no thermal spreading of the energy distribution function of the carriers, the value of $R_{J_0}$ should be equal to 6, and at an infinitely high temperature, at which the thermal distribution of the carriers does not vary within the QD density-of-states bell-shaped curve, it should be equal to 1. The experimentally determined values of $R_{J_0}$ (see Table II) are 3.8 and 4.1 for the lasers based on GaAs and InP, respectively, and lie in the theoretically predicted ranges. The closeness of the values of this parameter for the two lasers can be attributed to the fact that although the measurement temperature for the QD-GaAs laser was 300 K and the value for the QD-InP structure was 77 K, the value of $R_{J_0}$ is determined not only by the temperature, but also by the energy spacing between the ground state and the excited state, and the latter is roughly three times smaller for the QD-InP laser than for the QD-GaAs laser and compensates for the effect of the temperature. Therefore, $R_{J_0}$ should be roughly the same, as is observed experimentally.

### 4.2. Influence of quantum dots on the characteristics of quantum-dot lasers

Equation (37) enables us to obtain the dependence of the threshold current density on QD density. The total surface density of a QD array can be increased, for example, by the repeated deposition of several rows of dots or by employing special deposition regimes,[16] which permit variation of the QD density in each of the rows. Regardless of how an $N$-fold change in the QD density occurs, it leads to $N$-fold scaling of the saturated gain in Eq. (37), as well as the contributions of the transparency current density governed by the ground state ($J_0$) and the excited state ($J_1$) under the assumption that the electronic structure and emission characteristics of the QD's remain the same. Since the WL states lie below the matrix states, they make the main contribution to the third term in Eq. (37). Then, if an $N$-fold change in the total QD density occurs as a result of a change in the number of QD layers deposited, we can write the following expression on the basis of Eq. (37) in the case of lasing on the QD ground state:

$$J=NJ_0\left(1+\frac{g_{QD}}{Ng^{sat}}\right)+NJ_1\left(\frac{Ng^{sat}+g_{QD}}{Ng^{sat}-g_{QD}}\right)+NJ_2\left(\frac{Ng^{sat}+g_{QD}}{Ng^{sat}-g_{QD}}\right)^2. \tag{41a}$$

In the case where the QD surface density is altered with conservation of the number of planes with QD's deposited, the required equation has the form

$$J=NJ_0\left(1+\frac{g_{\rm QD}}{Ng^{\rm sat}}\right)+NJ_1\left(\frac{Ng^{\rm sat}+g_{\rm QD}}{Ng^{\rm sat}-g_{\rm QD}}\right)+J_2\left(\frac{Ng^{\rm sat}+g_{\rm QD}}{Ng^{\rm sat}-g_{\rm QD}}\right)^2. \quad (41b)$$

The only difference between Eqs. (41a) and (41b) is that in the former case the fraction of the transparency current utilized to pump WL states is scaled with $N$, while in the latter case it is not. We note again that in the case of lasing on the excited state these equations do not contain the second term and $J_0$ refers to the excited state.

In order to experimentally test the validity of the foregoing arguments, we compare the threshold characteristics of two laser structures which differ with respect to the QD surface density in the active region. The first of them, the QD-GaAs laser considered above, has a QD surface density per layer of dots of the order of $2\times10^{11}$ cm$^{-2}$, which is four times higher than the typical value of $5\times10^{10}$ cm$^{-2}$ for InGaAs/AlGaAs QD's, which characterizes the QD-GaAs-LD laser offered for comparison.

In Fig. 5a the points show the experimental dependence of the gain on pump current density for a single layer of QD's in both structures. The solid curves in this figure represent the dependences described by Eqs. (37) and (29) with the fitting parameters determined above for the QD-GaAs laser. At the same time, the dotted curves were obtained from Eq. (41b) with the same values of the parameters and $N=\frac{1}{4}$. There is good agreement between the experimental data and the theoretically predicted behavior of the gain as a function of pump current density for the QD-GaAs-LD structure, which points out the possibility of using this approach to design the active region of a QD laser.

For example, using Eq. (41), we can determine the optimal QD density corresponding to the minimum threshold current density, $J_{\rm th}$, for an assigned threshold gain, which must be attained at the lasing threshold, $G_{\rm th}$:

$$J_{\rm th}(N)=NJ_0\left(1+\frac{G_{\rm th}}{Ng^{\rm sat}}\right)+NJ_1\left(\frac{Ng^{\rm sat}+G_{\rm th}}{Ng^{\rm sat}-G_{\rm th}}\right)+NJ_2\left(\frac{Ng^{\rm sat}+G_{\rm th}}{Ng^{\rm sat}-G_{\rm th}}\right)^2, \quad (42a)$$

$$J_{\rm th}(N)=NJ_0\left(1+\frac{G_{\rm th}}{Ng^{\rm sat}}\right)+NJ_1\left(\frac{Ng^{\rm sat}+G_{\rm th}}{Ng^{\rm sat}-G_{\rm th}}\right)+J_2\left(\frac{Ng^{\rm sat}+G_{\rm th}}{Ng^{\rm sat}-G_{\rm th}}\right)^2. \quad (42b)$$

Figure 5b shows the dependence of $J_{\rm th}$ on QD density described by Eq. (42b) for various levels of the threshold gain. The values of $J_0$, $J_1$, $J_2$, and $g^{\rm sat}$ were obtained from the fitting curves corresponding to the dependence of the gain on current density for a single layer of QD's in the QD-GaAs structure. The QD density was normalized to the value of the QD surface density in this structure ($2\times10^{11}$ cm$^{-2}$). It can clearly be seen that the dependence of $J_{\rm th}$ on

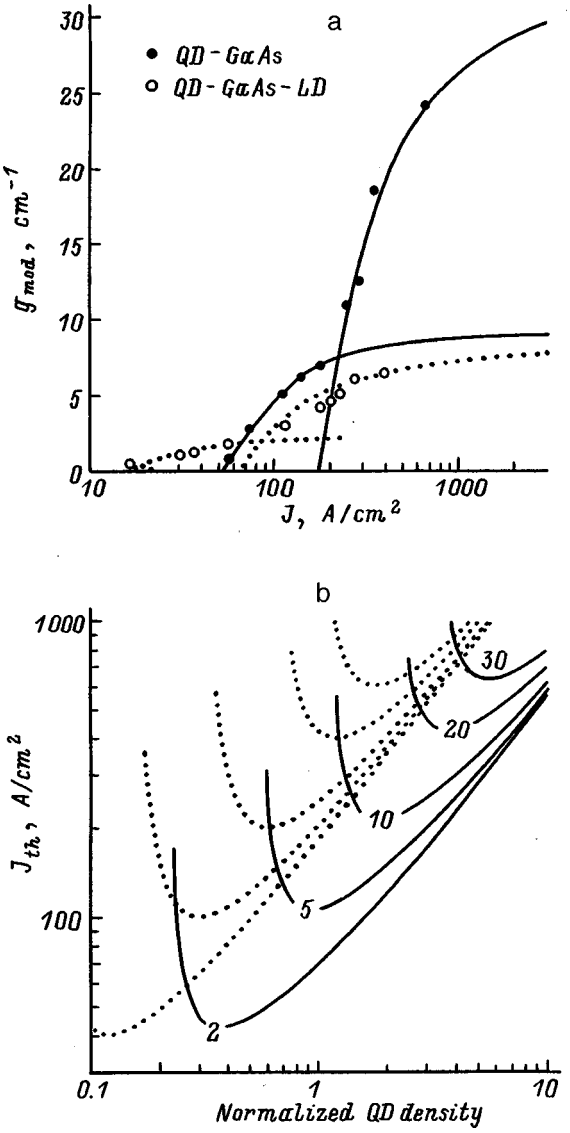


FIG. 5. a — Dependence of the modal gain on pump current density for a single layer of quantum dots in two structures based on InGaAs QD's in an AlGaAs matrix with different QD surface densities. The filled circles correspond to the QD-GaAs structure with a surface density $\sim2\times10^{11}$ cm$^{-2}$, and the open circles correspond to the QD-GaAs-LD structure with a QD surface density $\sim5\times10^{10}$ cm$^{-2}$. The solid lines were calculated in accordance with Eqs. (37) and (29) and the fitting parameters listed in Table I, and the dotted curves were obtained using Eq. (41b) with $N=(1/4)$. b — Dependence of the threshold current density on QD density for lasing in the ground state (solid curves) and excited state (dotted lines). The numbers on the curves correspond to the threshold gain level (cm$^{-1}$). $N$ — the QD density normalized to $2\times10^{11}$ cm$^{-2}$.

QD density is qualitatively the same as the dependence of the threshold current on the number of quantum wells for lasers based on them. There is an optimal QD density ($N_{\rm opt}$), which corresponds to the minimum value of $J_{\rm th}$ for a definite level of the threshold gain. The value of $J_{\rm th}$ decreases with increasing $N$ up to $N_{\rm opt}$, and then it begins to increase. If the necessary threshold gain is excessively large, lasing can become unattainable in the ground state at a definite QD density, but it can be realized in excited states. As was previously noted, lasers with high radiation-extraction losses are used in most practical applications. They must therefore have

a sufficiently high differential efficiency. As follows from Fig. 5b, denser QD arrays are therefore desirable in practice for achieving small threshold currents at a high loss level.

To avoid cluttering the figure, we did not present the dependence of $J_{th}$ on $N$ for the case of variation of the QD density by increasing the number of rows that contain QD arrays [Eq. (42a)]. In this case the plots of $J_{th}$ for the ground state do not vary at all, and in the excited state $J_{th}$ increases slightly for $N>1$ and decreases for $N<1$. We also note that in this case not all the rows with QD's are located at the maximum of the light wave and that the experimental values of $J_{th}$ will consequently be slightly higher.

Differentiating (42) with respect to $N$ and setting $(dJ_{th}/dN)$ equal to zero, we can obtain the dependence of $N_{opt}$ on the threshold gain $G_{th}$. Considering lasing on the ground state, for which, as follows from Table I, the WL contribution can be ignored $(J_2=0)$, we obtain

$$\frac{dJ_{th}}{dN}=J_0+J_1\left(1-\frac{2G_{th}^2}{(N_{opt}g^{sat}-G_{th})^2}\right)=0. \tag{43}$$

It is clearly seen that the dependence of $N_{opt}$ on $G_{th}$, which satisfies Eq. (43), must be a linear function. We note that in the case of lasing on the excited state, in which the WL cannot be ignored, this dependence ceases to be linear.

## 5. CONCLUSIONS

In this paper we have proposed a model which permits derivation of the analytical form of the dependence of the gain on pump current density for QD lasers. Two different systems of self-organized QD's have been considered to compare theory with experiment: InGaAs QD's in an AlGaAs host grown on a GaAs substrate and InAs QD's in an InGaAs host lattice-matched to an InP substrate. It has been shown that the proposed model permits description of the threshold characteristics of QD lasers, including the switching of the lasing from the ground state to the excited state of the QD's. The fourfold degeneracy of the excited state leads to a fourfold increase in the saturated gain in comparison to the QD ground state. The influence of the QD surface density on the threshold characteristics has been studied theoretically. A less dense QD array exhibits a lower value of the transparency current and, consequently, of $J_{th}$ at low threshold gains, while a QD ensemble with a higher density displays a higher value of the saturated gain, which leads to smaller values of $J_{th}$ at large threshold gains. The effects described above are in good agreement with experiment on both the qualitative and quantitative levels.

We express our sincerest thanks to M. A. Odnoblyudov for some useful discussions.

This work was carried out with the support of INTAS Project 96-0467 and the Physics of Solid-State Nanostructure Program (Projects 97-1090 and 98-1096).

[1] J. P. van der Ziel, R. Dingle, R. C. Miller, W. Wiegmann, and W. A. Nordland Jr., Appl. Phys. Lett. **26**, 463 (1975).
[2] Y. Arakawa and H. Sakaki, Appl. Phys. Lett. **40**, 939 (1982).
[3] L. Goldstein, F. Glas, J. Y. Marzin, M. N. Charasse, and G. Le Roux, Appl. Phys. Lett. **47**, 1099 (1985).
[4] P. M. Petroff and S. P. Den Baars, Superlattices Microstruct. **15**(1), 15 (1994).
[5] V. M. Ustinov, A. Yu. Egorov, A. R. Kovsh, A. E. Zhukov, M. V. Maksimov, A. F. Tsatsul'nikov, N. Yu. Gordeev, S. V. Zaitsev, Yu. M. Shernyakov, N. A. Bert, P. S. Kop'ev, Zh. I. Alferov, N. N. Ledentsov, J. Bohrer, D. Bimberg, A. O. Kosogov, P. Werner, and U. Gosele, J. Cryst. Growth **175/176**, 689 (1997).
[6] Zh. I. Alferov, S. V. Ivanov, P. S. Kop'ev, N. N. Ledentsov, M. É. Lutsenko, B. Ya. Mel'tser, M. I. Nemenov, V. M. Ustinov, and S. V. Shaposhnikov, Fiz. Tekh. Poluprovodn. **24**, 152 (1990) [Sov. Phys. Semicond. **24**, 92 (1990)].
[7] L. J. Mawst, A. Bhattacharya, J. Lopez, D. Botez, D. Z. Garbuzov, L. DeMarco, J. C. Connolly, M. Jansen, F. Fang, and R. F. Nabiev, Appl. Phys. Lett. **69**, 1532 (1996).
[8] O. G. Schmidt, N. Kirstaedter, N. N. Ledentsov, M. H. Mao, D. Bimberg, V. M. Ustinov, A. Y. Egorov, A. E. Zhukov, M. V. Maximov, P. S. Kop'ev, and Zh. I. Alferov, Electron. Lett. **32**, 1302 (1996).
[9] S. V. Zaitsev, N. Yu. Gordeev, Yu. M. Sherniakov, V. M. Ustinov, A. E. Zhukov, A. Yu. Egorov, M. V. Maximov, P. S. Kop'ev, Zh. I. Alferov, N. N. Ledentsov, N. Kirstaedter, and D. Bimberg, Superlattices Microstruct. **21**, 559 (1997).
[10] L. V. Asryan and R. A. Suris, IEEE J. Selected Top. in Quantum Electron. **3**(2), 148 (1997).
[11] D. Bimberg, N. Kristaedter, N. N. Ledentsov, Zh. I. Alferov, P. S. Kop'ev, and V. M. Ustinov, IEEE J. Selected Top. in Quantum Electron. **3**(2), 196 (1997).
[12] A. E. Zhukov, A. R. Kovsh, V. M. Ustinov, A. Yu. Egorov, N. N. Ledentsov, A. F. Tsatsul'nikov, M. V. Maximov, Yu. M. Shernyakov, V. I. Kopchatov, A. V. Lunev, P. S. Kop'ev, D. Bimberg, and Zh. I. Alferov, Semicond. Sci. Technol. (in press).
[13] F. Stern, IEEE J. Quantum Electron. **QE-9**, 290 (1973).
[14] P. W. McIlroy, A. Kurobe, and Y. Uematsu, IEEE J. Quantum Electron. **QE-21**, 1958 (1985).
[15] H. C. Casey, Jr. and M. B. Panish, *Heterostructure Lasers* [Academic Press, New York (1978); Mir, Moscow (1981), p. 211].
[16] A. R. Kovsh, A. E. Zhukov, A. Yu. Egorov, V. M. Ustinov, Yu. M. Shernyakov, M. V. Maksimov, A. F. Tsatsul'nikov, B. V. Volovik, A. V. Lunev, N. N. Ledentsov, P. S. Kop'ev, Zh. I. Alferov, and D. Bimberg, Fiz. Tekh. Poluprovodn. **32**, 1114 (1998) [Semiconductors **32**, 997 (1998)].
[17] V. M. Ustinov, A. E. Zhukov, A. Yu. Egorov, A. R. Kovsh, S. V. Zaitsev, N. Yu. Gordeev, V. I. Kopchatov, N. N. Ledentsov, A. F. Tsatsul'nikov, B. V. Volovik, P. S. Kop'ev, Z. I. Alferov, S. S. Ruvimov, Z. Liliental-Weber, and D. Bimberg, Electron. Lett. **34**, 670 (1998).
[18] A. Zh. Zhukov, A. Yu. Egorov, A. R. Kovsh, V. M. Ustinov, S. V. Zaïtsev, N. Yu. Gordeev, V. I. Kopchatov, A. V. Lunev, A. F. Tsatsul'nikov, B. V. Volovik, N. N. Ledentsov, and P. S. Kop'ev, Fiz. Tekh. Poluprovodn. **32**, 892 (1998) [Semiconductors **32**, 795 (1998)].
[19] L. D. Landau and E. M. Lifshitz, *Quantum Mechanics: Non-Relativistic Theory*, 3rd ed. [Pergamon Press, Oxford (1977); Nauka, Moscow (1974), p. 300].
[20] A. E. Zhukov, V. M. Ustinov, A. Yu. Egorov, A. R. Kovsh, A. F. Tsatsul'nikov, M. V. Maximov, N. N. Ledentsov, S. V. Zaitsev, N. Yu. Gordeev, Yu. M. Shernyakov, P. S. Kop'ev, and Zh. I. Alferov, J. Electron. Mater. **27**(3), 106 (1998).

Translated by P. Shelnitz

# Changes in the luminescent and electrical properties of InGaN/AlGaN/GaN light-emitting diodes during extended operation

A. N. Kovalev and F. I. Manyakhin

*Moscow Institute of Steel and Alloys, 117936 Moscow, Russia*

V. E. Kudryashov, A. N. Turkin, and A. É. Yunovich

*M. V. Lomonosov Moscow State University, 119899 Moscow, Russia*

(Submitted April 9, 1998; accepted for publication April 14, 1998)
Fiz. Tekh. Poluprovodn. **33**, 224–232 (February 1999)

Changes in the luminescence spectra and current–voltage and capacitance–voltage characteristics of light-emitting diodes based on InGaN/AlGaN/GaN heterostructures were investigated as functions of operating time during extended use. Sample blue and green light-emitting diodes with InGaN single quantum-well active layers were examined during operating times of $10^2-2\times10^3$ h at currents up to 80 mA. An increase in the efficiency at the working currents (15 mA) was observed in the first stage of aging (100–800 h) followed by a decrease in the second stage. The greatest changes in the spectra were observed at low currents ($<0.15$ mA). Studies of the distribution of charged acceptors in the space-charge region showed that their concentration grows in the first stage and falls in the second. Models explaining the two stages of aging are proposed: 1) activation of Mg acceptors as a result of destruction of residual Mg–H complexes, and 2) formation of N donor vacancies. A model of subthreshold defect formation by hot electrons injected into the quantum wells is discussed.[1)] © *1999 American Institute of Physics.* [S1063-7826(99)01402-7]

## 1. INTRODUCTION

Problems of the aging of GaN-based devices have become of urgent interest in the last two years as the potential for mass-production of light-emitting diodes (LED's) based on GaN heterostructures has become evident (see the review articles in Refs. 3 and 4). The bonds between the metal and N atoms in a hexagonal lattice of III–V type are stronger than the bonds with As or P in a cubic lattice. Therefore, defect formation in an ideal nitride lattice is less probable than in arsenide or phosphide lattices. Nitride devices should be, given present developments, more long-lived. The actual state of affairs is determined by defects in the GaN structures. But already the service life of GaN-based LED's is estimated to be $>10^5$ h (Refs. 4–6). Therefore, the development of techniques for estimating the service life of LED's after a brief period of use under a high load is of current interest.

Studies of the degradation of such LED's under pulsed loads up to 1 A (Refs. 5 and 7) and at elevated temperatures[6] are well known. Catastrophic degradation occurs upon breakdown in strong fields (static or pulsed). One of the reasons for degradation of LED's—migration of metal ions from the contacts at high pulsed currents—has been identified.[5]

Our aim in this study was to investigate aging processes in the LED's whose luminescence and electrical properties were studied elsewhere (see Refs. 7–12). The measurements were carried out under moderately elevated current loads similar to those used under normal conditions. Changes in the spectra and electrical properties of the diodes were detected, and models are proposed explaining these changes.

## 2. EXPERIMENTAL TECHNIQUE

**2.1.** We investigated blue and green LED's which consist of InGaN/AlGaN/GaN heterostructures with an active layer comprised of InGaN single quantum wells of thickness $d\approx3.5$ nm and which were grown by epitaxy from metallo-organic compounds in the laboratory of the firm Nichiya[7]; the properties of these diodes were investigated in Refs. 8–12.

**2.2.** The choice of aging conditions was made as follows. We estimated the rate of variation of the LED characteristics as the current $J$ through the diodes was increased in the interval 10–100 mA. We found that at $J=80$ mA (voltage $V=4.0-4.2$ V) noticeable changes are observed in the spectra and the capacitance–voltage (CaV) and current–voltage (CV) characteristics after a few hundred hours. At $J=80$ mA the temperature of the active region of the LED was $T=360-370$ K and depended on the series resistance of the LED (for the method of determining the temperature $T$, see below in the discussion of the results). For the tests that were to follow, we chose an operating regime with constant current $J=80$ mA. The tests were carried out in a time of 2000 h.

**2.3.** An important part of the test was a study of the distribution of the effective concentration of charged centers in the space-charge region (SCR) during aging which was induced using an original technique.[13]

**2.3.1.** Slowly varying bias voltages $V$, which defined the width of the SCR $W$, and a small variable signal $\Delta V=U_d$

 

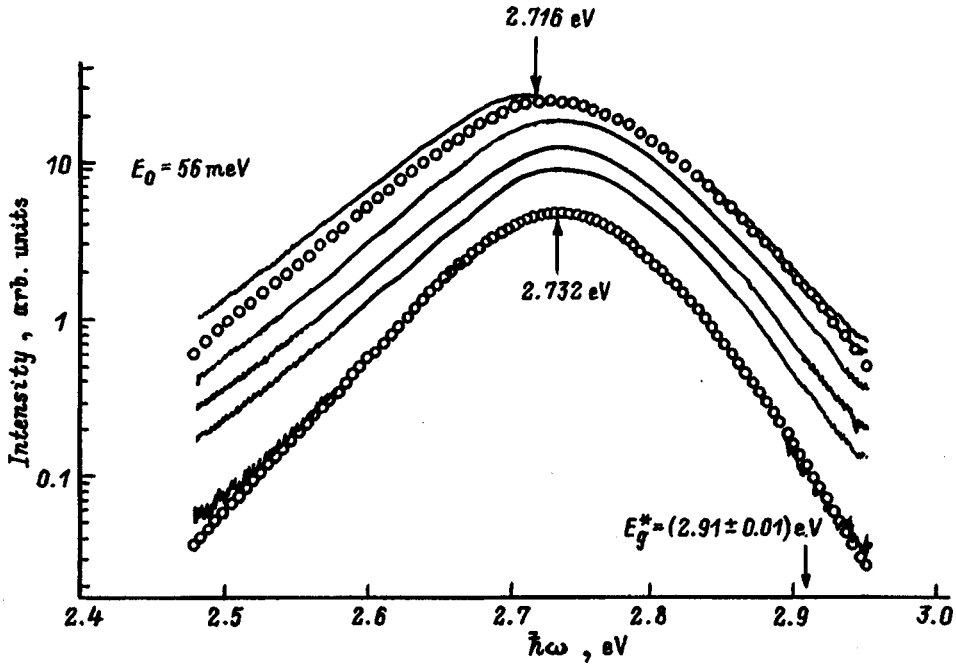


FIG. 1. Electroluminescence spectra of a blue LED at constant current values (from down up) 10, 20, 30, 50, 80, and 100 mA. The points denote spectra calculated according to formula (3) with fitting of the parameters; temperature of the active region: 300 K (lower curve), 358 K (upper curve).

with a period much smaller than the characteristic time of variation of $V$ were applied to the semiconductor structure simultaneously. The width $W$ was modulated by the small variable signal, with modulation width $\Delta W$.

**2.3.2.** If $\Delta Q$ is the variable charge induced in the structure by the voltage $U_d$, $N(W)$ is the effective concentration of charged centers (density of charged centers on the right-hand side of the Poisson equation) on the edge of the SCR (at a distance $W$ from the boundary of the $p$ and $n$ regions), and $C_W=\varepsilon\varepsilon_0 S/W$ is the differential capacitance of the structure ($S$ is the area), then $U_d$ can be represented as a sum of two voltages:

$$U_d=U_W+U_N=(dV/dQ)\Delta Q+(1/2)(d^2V/dQ^2)\Delta Q^2$$
$$=(\Delta Q)(W/\varepsilon\varepsilon_0 S)+(\Delta Q/S)^2/2\varepsilon\varepsilon_0 qN(W). \quad (1)$$

The equivalent circuit of the barrier capacitance in this case can be represented by two capacitors connected in series: $C_W$ and $C_d=2\varepsilon\varepsilon_0 S/\Delta W$, the dynamic capacitance due to small changes in the SCR; here $U_W \gg U_N$.

**2.3.3.** A small variable charge $\Delta Q$ with constant amplitude, which is the sum of two harmonic signals with similar frequencies $\omega_1$ and $\omega_2$, was imposed on the structure. This made it possible to separate $U_W$ and $U_N$ by their frequencies: the signal $U_W$ was measured at the frequency $(\omega_1+\omega_2)/2$, and the signal $U_N$ at the frequency $(\omega_1-\omega_2)$. The constant amplitude of $\Delta Q$ was assigned by passing a current through the structure connected in the feedback circuit of an operational amplifier; at the input of this amplifier a variable voltage with amplitude $U_0 \approx 100$ mV was applied through a reference capacitance $C_0 \gg C_W, C_d$ (Ref. 13). The dependence $N(W)$ in this circuit is given by

$$N(W)=(C_0U_0/S)^2/2q\varepsilon\varepsilon_0 U_N; \quad W=\varepsilon\varepsilon_0 SU_W/C_0U_0. \quad (2)$$

Smooth variation of $V$ ensured continuous recording of the values of $N(W)$ with the concentration values $N(W)$ averaging to $\sim 10^{18}$ cm$^{-3}$ across the layer $\Delta W \approx$ nm.

## 3. EXPERIMENTAL RESULTS

### 3.1. Changes in the electroluminescence spectra

**3.1.1.** Figure 1 plots the electroluminescence (EL) spectra at currents $J=10-100$ mA (Refs. 8–11 presented spectra up to 30 mA). Figure 1 also shows a fit to the spectra using formulas of the model described in Refs. 8 and 9, which takes into account the two-dimensional density of states $N^{2D}(\hbar\omega-E_g^*,E_0)$ in a rectangular quantum well ($E_g^*$ is the effective width of the band gap) with exponential decay of its long-wavelength part ($E_0$ is the exponential parameter due to the fluctuation potential). The short-wavelength decay of the spectrum is described in the model by filling functions at the edges of the conduction band and the valence band $f_c(\hbar\omega-E_g^*,F_n,m,kT)$ and $1-f_v(\hbar\omega-E_g^*,F_p,1-m,kT)$ (here the fitting parameters are $m$ and the Fermi quasilevels for the electrons and holes are $F_n$ and $F_p$):

$$I(\hbar\omega)\sim N^{2D}(\hbar\omega-E_g^*,E_0)f_c(\hbar\omega-E_g^*,F_n,m,kT)$$
$$\times[1-f_v(\hbar\omega-E_g^*,F_p,1-m,kT)]. \quad (3)$$

By varying the fitting parameters we determined the temperature of the active region for $J=80$ mA (the value used in the tests): $T=360-370$ K.

**3.1.2.** The intensity of the EL spectra at 15 mA increased by 10–40% over the first 50–100 h of operation (at 80 mA) for the blue LED's and in a time of $\sim$800 h for the green LED's. During the subsequent period, for times $>1000$ s, the luminescence intensity fell for both the blue and green LED's (Fig. 2). The interference structure, which was quite noticeable before aging, was smeared out after aging. The main emission band was broadened on its long-wavelength side; the energy parameter $E_0$ increased. Large changes in the spectra were observed for the blue LED's at small currents, $J \leqslant 0.15$ mA, where the tunneling and injection components of the currents are of the same order of magnitude. The

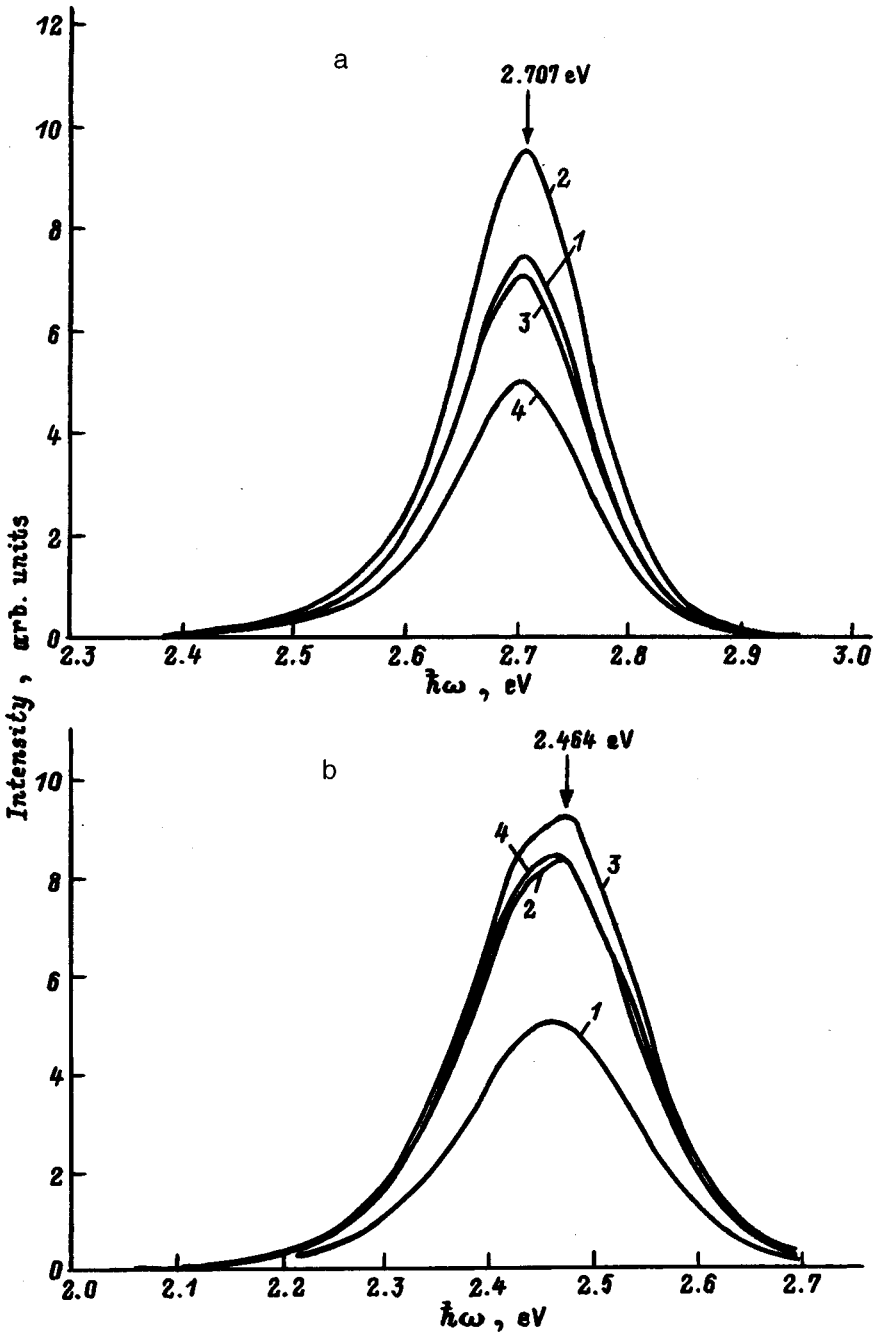


FIG. 2. Electroluminescence spectra of blue (a) and green (b) LED's after passing a direct current of $J=80$ mA through them. a — operating time $t$, h: *1* — 0, *2* — 72, *3* — 800, *4* — 1000. b — operating time $t$, h: *1* — 0, *2* — 480, *3* — 800, *4* — 1000.

luminescence intensity decreased, but the fraction of tunneling radiation[10,11] increased threefold (Fig. 3).

The intensity of the breakdown luminescence[12] decreased with aging, and in this case the relative fraction of the yellow band (2.1–2.3 eV) increased (Fig. 4). It is well known that the yellow band is due to complexes with defects of the structure;[4] this is evidence of the formation, upon passage of a direct current, of defects at the boundaries of the space charge region, where recombination occurs subsequent to impact ionization.

### 3.2. Changes in the electrical properties

**3.2.1.** Changes in the current–voltage (J-V) characteristics as a result of aging are shown in Fig. 5. The tunneling component of the direct current at low voltages grew for the blue and the green diodes. Extended aging led to growth of the series resistance of the diodes $R_s$, whose role is manifested at large currents. Conditions of defect formation depend on the value of $R_s$ (see the discussion of results below).

**3.2.2.** The effective concentration of charged centers in the $p$ region grew during the first aging period for the blue diodes by 10–15%; and in the second period, ~1000 h, the concentration of charged acceptors in the $p$ region decreased 6–8 fold (Fig. 6). The width of the space charge region grew in this case by only ~30%. For the green LED's the effective concentration of charged centers grew slowly for 600–800 h by ~10% and then fell insignificantly (Fig. 6). Note that the change in the concentration of charged accep-

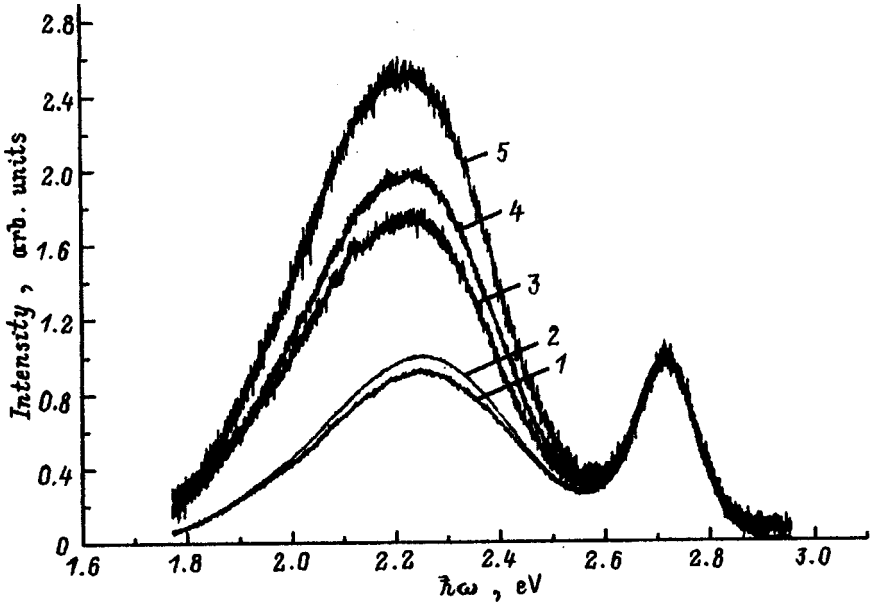


FIG. 3. Electroluminescence spectra of blue LED's for $J=0.15$ mA after aging. Operating time $t$, h: *1* — 0, *2* — 72, *3* — 558, *4* — 800, *5* — 1000.

tors occurred at distances $W\approx 40-80$ nm, i.e., at distances of the order of the mean free path $l_{fp}$ (estimate given below).

## 4. DISCUSSION OF RESULTS

### 4.1. Models of growth and decay of luminescence efficiency

**4.1.1.** The most important step in the creation of efficient LED's based on GaN was realized because of an understanding of the mechanism of Mg compensation: formation of Mg–H complexes during epitaxy. Either means of activation—bombardment with an electron beam or heating in an $N_2$ atmosphere—destroys the Mg–H complexes and allows hydrogen to escape from the lattice.[14,15] Obviously, some fraction of these complexes remains in the finished structures. The changes in the properties of the LED's during the first aging period, namely growth in the intensity of the main band and growth of the effective acceptor concentration, can be explained by additional activation of Mg acceptors in the $p$ space charge region.

The model of the first stage is as follows: for injective excitation of the active region the residual Mg–H complexes can be destroyed, hydrogen escapes from the complexes, and the charge of the $Mg^-$ ions should be compensated for by the holes:

$$Mg-H \Rightarrow Mg^- + (+) + H. \tag{4}$$

**4.1.2.** In the second stage of the process, formation of donor defects that compensate the acceptors predominates. These defects increase the probability of nonradiative recombination and the probability of emission in the yellow band which manifests itself in tunneling and breakdown lumines-

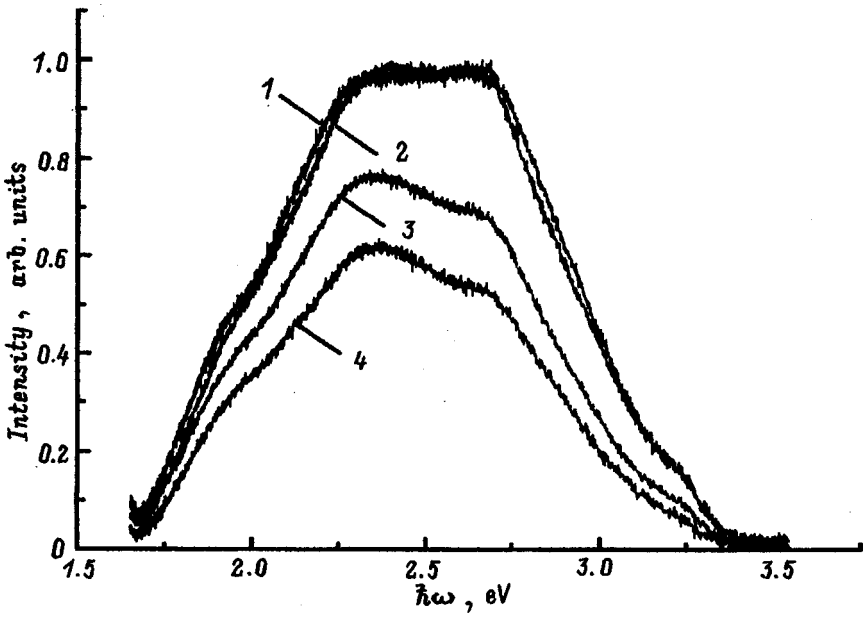


FIG. 4. Breakdown luminescence of blue LED's for $J=4$ mA after aging. Operating time $t$, h: *1* — 0, *2* — 72, *3* — 800, *4* — 1000.

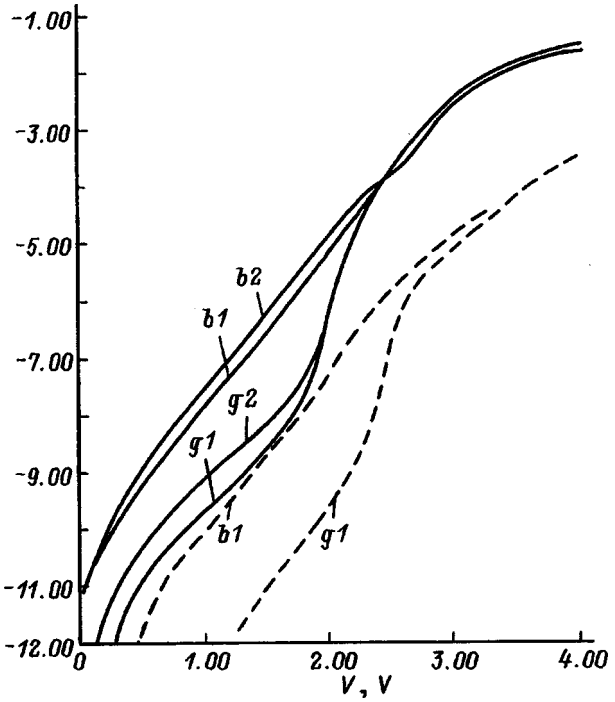


FIG. 5. Current–voltage characteristics of blue ($b1$, $b2$) and green ($g1$, $g2$) LED's before ($b1$, $g1$) and after ($b2$, $g2$) passing a direct current of 80 mA through them for 800 h. Solid curves — $T=300$ K, dashed curves — $T=80$ K.

cence. Native defects of this kind can be nitrogen vacancies $V_N$, whose probability of formation is significantly greater than for Ga vacancies:[16,17]

$$\mathrm{GaN} \Rightarrow \mathrm{Ga} + V_N^+ + (-) + \mathrm{N}. \tag{5}$$

The charge states in this equation should be taken as nominal, which is not a certainty. However, this model explains the second stage of the aging process. In addition, defect migration takes place along the grain boundaries and growth columns: The defects accumulate at ''weak points,'' at which the electric field is maximum. Thus it is possible to explain the growth of the tunneling component of the current and the tunneling emission in the spectra.

#### 4.2. Model of subthreshold injective defect formation

**4.2.1.** To explain why formation of structural defects in GaN is possible at a comparatively low temperature $T \approx 370$ K, it is necessary to invoke the model of defect formation in $p-n$ heterostructures by hot electrons. This model, developed for GaAs-based structures, was used successfully to explain aging processes in $n$-AlGaAs/$p$-GaAs heterojunctions.[18] Here it was assumed that the atoms are displaced upon transfer to them of the kinetic energy of the hot electrons, which acquire this energy by intersecting a heterojunction with a conduction band discontinuity. This assumption is based on the experimental observation that defects are formed at a depth on the order of the mean free path $l_{fp}$ from the boundary of the heterojunction. In contrast to this mechanism, defects are formed during multiphonon scattering at the diffusion depth $L_n \gg l_{fp}$.

**4.2.2.** In heterostructures, electrons injected into a narrow-gap layer from a wide-gap $n$-barrier have energy $\Delta E \gg kT$ relative to the bottom of the conduction band $E_c$:

$$\Delta E = E - E_c > \Delta E_c = E_{c2} - E_{c1} \gg kT. \tag{6}$$

The electrons should give back this energy at the other edge of the well—at the $p$-boundary (Fig. 7); for a voltage on the order of the contact potential, $V \approx \varphi_k$, the mean energy of the electrons remains the same as at the $n$-boundary (Fig. 7c). In the investigated structures, there are compensated layers on both sides of the quantum well.[8–12] For $V > \varphi_k$ a large part

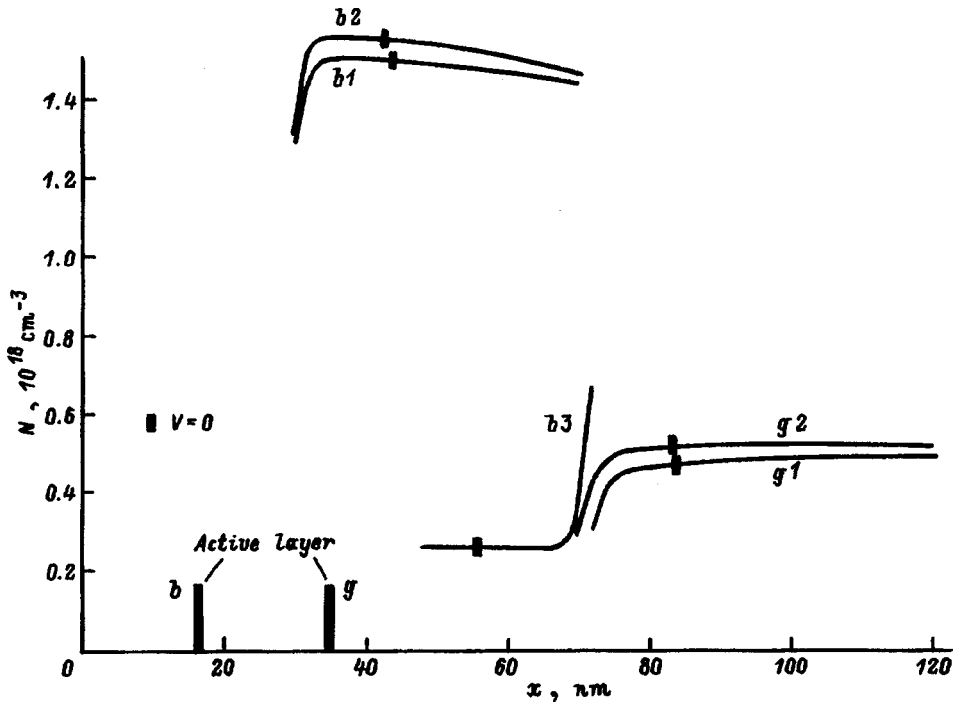


FIG. 6. Distribution of the effective concentration of charged centers ($N$) with depth $x$ in the space-charge region of blue (b) and green (g) LED's before and after passing a direct current of 80 kA through them. Operating time $t$, h: $b1$, $g1$ — 0; $b2$, $g2$ — 250; $b3$ — 1000.

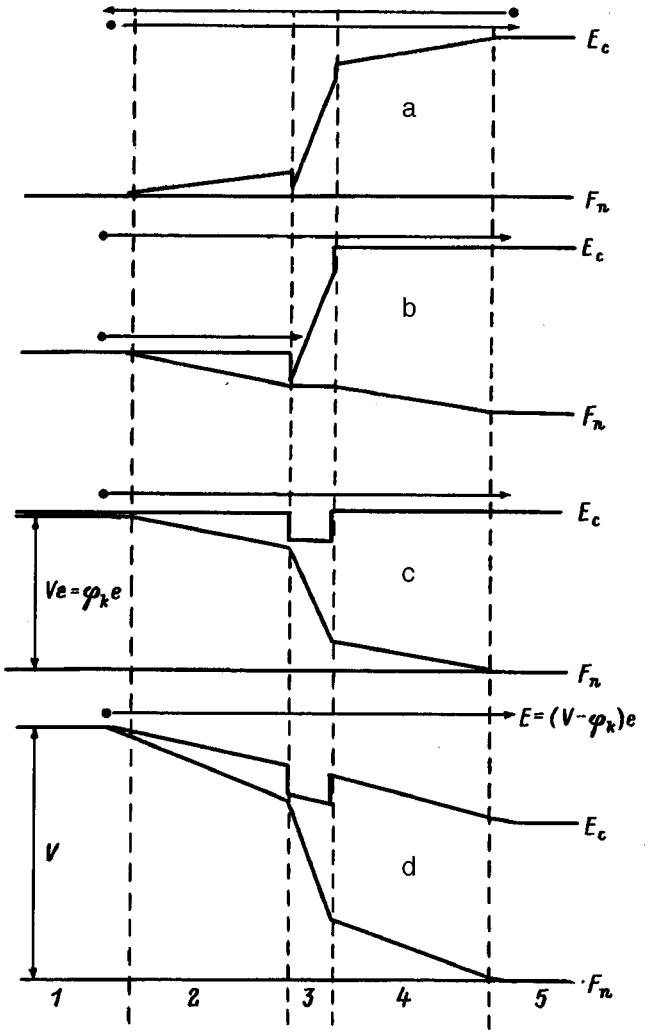


FIG. 7. Schematic representation of electron transitions from the emitter to the base region in the presence of a compensating layer. a — $V=0$; b — $V<\varphi_k$; c — $V\approx\varphi_k$; d — $V>\varphi_k$. *1* — *n*-AlGaN; *2, 4* — *i*-AlGaN (compensated layers); *3* — *i*-InGaN (active layer), *5* — *p*-AlGaN.

of the direct voltage falls in the quantum well and in these layers since the *p* and *n* contact regions are heavily doped. Electrons, as they drift in the electric field of the compensated layers, acquire additional energy and traverse a path on the order of the mean free path $l_{fp}$ (Fig. 7d). The critical energy of the electrons for a large current density can be transferred to the lattice during a time on the order of the relaxation time on a length $\sim l_{fp}$ not only because of scattering on phonons, but also because of subthreshold defect formation. This should occur either in compensated layers adjoining the active layer or in the *p* space charge layer.

**4.2.3.** If the electrons transfer energy to the Mg–H complexes, then the reaction of breaking the complex bond and activation of the Mg acceptor will proceed with a high probability according to formula (4). This mechanism operates mainly at the boundary of the active region and *p*-AlGaN. The threshold defect formation energy $E_d$ (Mg–H bond breaking energy) is greater than the Frenkel' thermodynamic energy; estimates give $E_d\approx 4$ eV.

It is well known that during high-temperature heat treatment nitrogen escapes from the GaN lattice as the gas $N_2$, forming nitrogen vacancies $V_N$ (Refs. 16 and 17). If hot electrons transfer energy to the lattice, thereby breaking Ga–N bonds, then the defect formation reaction (5) will take place at low temperatures. Note that the calculated probability for the formation of the equilibrium concentration of donor vacancies $V_N$ is greater in *p*-type GaN.[19]

Processes of Mg activation and $V_N$ formation are simultaneous. In the first stage Mg activation predominates, but it is limited by the low Mg–H concentration. In the second stage $V_N$ formation predominates and is not limited: N atoms are basic to the lattice. At extended times this process saturates due to dynamic-equilibrium recombination of $V_N$ with N atoms.

**4.2.4.** In the theoretical analysis of subthreshold defect formation during hot electron injection to follow, we will proceed by analogy with theories of radiation solid-state physics, which treat the interaction of atoms of the crystal with fast particles.[20] The difference is that the energy of the hot electrons, $\Delta E$, is much smaller than the threshold energy of displacement of the atoms $E_d$, and the interaction process goes through excitation of the electron subsystem (see Refs. 20 and 21). Displacement of a lattice atom by electrons with kinetic energy $\Delta E$ can occur with probability

$$w(\Delta E)\sim\exp(-E_d/\Delta E),$$

where $E_d$ is the threshold displacement energy. The effective probability of displacement, integrated over all energies $\Delta E$ and velocities $v_x$, is

$$\xi=\int w(\Delta E)v_x\exp(-v_x)dv_x\int\exp(-v_y)dv_y \times\int\exp(-v_z)dv_z\Big/\int\int\int v_x f_0 dv_x dv_y dv_z,$$

where $v_i=m_n^* v_i^2/2kT$, $f_0$ is the electron distribution function in the wide-gap *n*-emitter, and $v_i$ are the components of the thermal velocity of the electron.

We assume that diffusion of the generated defects is small, and we disregard the electric field in the region under consideration. Thus, the concentration of the displaced native atoms $\Delta N_0$ varies with time *t* and distance *x* according to the formulas

$$\Delta N_0=G(x)\tau_0(T)\{1-\exp[-t/\tau_0(T)]\},$$
$$G(x)=N_0\gamma_0(x),\quad \gamma_0(x)=(3/2)(j/q)\xi_0 a(x)\sigma_0,$$
$$a(x)=\exp(-x/l_{fp})[1-\exp(-x/l_{fp})]\exp(-x/L_D), \quad (7)$$

where $N_0$ is the concentration at the time $t=0$, $a(x)$ is the spatial distribution of the rate of point defect generation, $G(x)$ is their generation rate, $j$ is the current density, $q$ is the charge of the electron, $\tau_0$ is the characteristic relaxation time of defect displacement, $L_D$ is the diffusion length, and $\sigma_0$ is the cross section of interaction of the hot electrons with an atom. With the passage of time, this dependence saturates with a time constant $\tau_0(T)$.

**4.2.5.** For Mg–H complexes, whose concentration is significantly lower than the concentration of native atoms, $N_k \ll N_0$, the variation of the concentration $\Delta N_k$ is given by

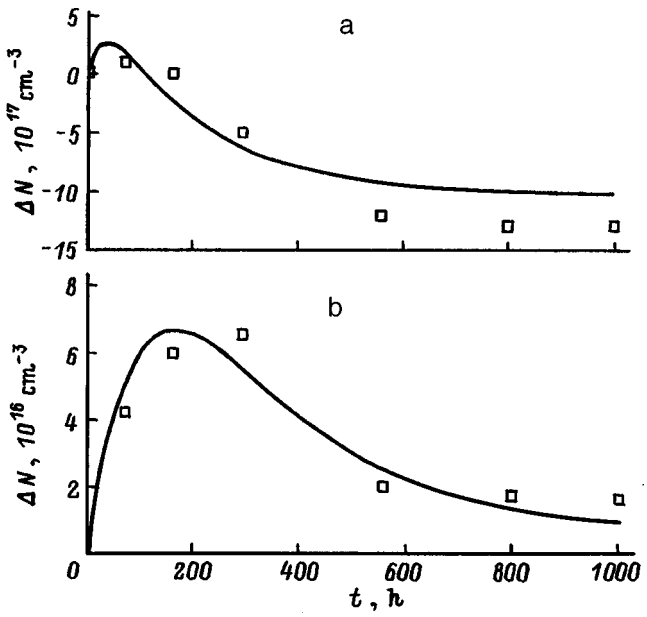


FIG. 8. Variation with time of the effective concentration of charged centers in the space-charge region of blue LED's for $x=0.67l_{fp}$ (a) and green LED's for $x=3l_{fp}$ (b). The points are the experimental data, and the solid curves were calculated according to formulas (7)–(9).

$$N_k(x,t)=N_{k0}\{\gamma_k(x)\tau_k(T)/[\gamma_k(x)\tau_k(T)+1]\}\times\{1-\exp[-t[\gamma_k(x)\tau_k(T)+1]/\tau_k(T)]\}, \quad (8)$$

where $\gamma_k(x)$ and $\tau_k(T)$ are quantities analogous to $\gamma_0(x)$ and $\tau_0(T)$ in formula (7), but for complexes. As a result of the relatively low concentration $N_{k0}$ and high probability of escape of hydrogen from the lattice for large values of $\tau_k(T)$, the dependence $\Delta N_k(x,t)$ takes the form

$$\Delta N_k(x,t)=N_{k0}\{1-\exp[-\gamma_k(x)t]\}. \quad (9)$$

**4.2.6.** The mean free path $l_{fp}$, which enters into the expression for $a(x)$, for values of the electron mobility $400-600\ \mathrm{cm^2/(V\cdot s)}$ has the order-of-magnitude value $l_{fp}\approx 3\times10^{-6}$ cm and is determined mainly by scattering on native atoms. We define the effective interaction cross section as $\sigma_0=(N_0 l_{fp})^{-1}\approx 9\times10^{-17}\ \mathrm{cm^2}$. Taking the values $J=80$ mA ($j\approx 80\ \mathrm{V/cm^2}$) and $t\approx\tau_0\approx 10^2-10^3$ h from our experiments for blue LED's, we can estimate the threshold energy ($E_d$) and effective probability of displacement of the atoms ($\xi_0$) in formulas (7): $E_d\approx 7-8$ eV; $\xi_0\approx 2\times10^{-14}$. The estimate of the effective probability of displacement of the atoms of the Mg–H complexes to explain the observed changes in the concentrations of charged impurities $\Delta N_0$, $\Delta N_k$ in the described experiments gives the following parameter values: $E_d\approx 3-4$ eV, $\gamma_k\approx 10^{-5}$, and $\xi_k\approx 8\times10^{-10}$.

The curve in Fig. 8 plots the dependence $\Delta N(t)$ calculated according to formulas (8) and (9) using the above parameter estimates. The points are the corresponding measured values, plotted in Fig. 6 for the blue and green LED's. It can be seen that the effective concentration of charged centers varies in accordance with the calculations.

The above analysis estimates the orders of magnitude of the parameters. It demonstrates the possibility of subthreshold formation of point defects in GaN heterostructures by electrons acquiring excess kinetic energy in the electric field of the compensated regions, and can explain aging effects in GaN-based LED's.

## 5. CONCLUSIONS

It has been shown that the luminescence spectra and electrical properties of blue and green LED's based on InGaN/AlGaN/GaN heterostructures with single quantum wells vary noticeably over the course of 100–2000 h of operation at a current of 80 mA.

The growth of the luminescence intensity at currents $\sim$15 mA and the increase in the concentration of charged acceptors in the space-charge region during the first period of aging are explained by additional activation of Mg acceptors due to escape of H atoms from residual Mg–H complexes. The slow decay of the luminescence intensity and the decay of the concentration of charged acceptors during the second period can be explained by the formation of donor defects as a result of extended injection of hot electrons into the quantum well. The first period for the blue diodes (70–100 h) is shorter than for green diodes (800–1000 h) because of the greater compensation of acceptors and weaker electric fields in the green diodes.

The proposed model of injection-stimulated subthreshold defect formation can explain aging effects (breaking of Mg–H bonds or Ga–N bonds by hot electrons injected into the quantum well).

We are grateful to Dr. Sh. Nakamura for providing LED's to Moscow State University for study and to Prof. V. S. Vavilov for a discussion of the results. Two of us (A. É. Yunovich and V. E. Kudryashov) are grateful to the Soros Program for financial support.

[1)]This work was presented in part at the Second International Conference on Semiconductor Nitrides (Tokushima, October 1997, Ref. 1) and at the Fall Meeting of the Materials Research Society (Boston, December 1997, Ref. 2).

[1] A. N. Kovalev, V. E. Kudryashov, F. I. Manyakhin, A. N. Turkin, and A. E. Yunovich, in *Proceedings of the Second International Conference on Nitride Semiconductors* (Tokushima, Japan, 1997), Paper P1–6, p. 46.
[2] A. N. Kovalev, V. E. Kudryashov, F. I. Manyakhin, A. N. Turkin, and A. E. Yunovich, *Abstracts of the 1997 Fall Meeting of the Materials Research Society* (Boston, USA, 1997), Abstract D17.3, p. 130.
[3] A. É. Yunovich, Svetotekhnika, No. 6, 2 (1996).
[4] F. A. Ponce and D. P. Bour, Nature (London) **386**, 351 (1997).
[5] M. Osinski, P. Perlin, P. G. Eliseev, G. Liu, and D. Burton, MRS Symp. Proc. **449**, 179 (1997).
[6] T. Egawa, H. Ishikava, T. Jimbo, and M. Umeno, MRS Symp. Proc. **449**, 1191 (1997).
[7] S. Nakamura, M. Senoh, N. Iwasa, S. Nagahama, T. Yamada, and T. Mukai, Jpn. J. Appl. Phys. **34**, Pt. 2, No. 10b, L1332 (1995).
[8] K. G. Zolina, V. E. Kudryashov, A. N. Turkin, A. É. Yunovich, and S. Nakamura, MRS Int'l. J. Nitride Semicond. Res., 1/11 (1996).
[9] K. G. Zolina, V. E. Kudryashov, A. N. Turkin, and A. É. Yunovich, Fiz. Tekh. Poluprovodn. **31**, 1055 (1997) [Semiconductors **31**, 850 (1997)].
[10] A. E. Yunovich, A. N. Kovalev, V. E. Kudryashov, F. I. Manyakhin, A. N. Turkin, and K. G. Zolina, MRS Symp. Proc. **449**, 1167 (1997).
[11] V. E. Kudryashov, K. G. Zolina, A. N. Kovalev, F. I. Manyakhin, A. N. Turkin, and A. É. Yunovich, Fiz. Tekh. Poluprovodn. **31**, 1304 (1997) [Semiconductors **31**, 1265 (1997)].

[12] F. I. Manyakhin, A. N. Kovalev, V. E. Kudryashov, A. N. Turkin, and A. E. Yunovich, MRS Int'l. J. Nitride Semicond. Res., 2/11 (1997).
[13] N. N. Goryunov, F. I. Manyakhin, and R. Yu. Osipov, Inform. Technol. Proekt., No. 2, 51 (1997).
[14] H. Amano, M. Kito, K. Hiramatsu, and I. Akasaki, Jpn. J. Appl. Phys. **28**, L2112 (1989).
[15] S. Nakamura, T. Mukai, and M. Senoch, J. Appl. Phys. **76**, 8189 (1994).
[16] C. B. Vartuli, S. J. Pearton, C. R. Abernathy *et al.*, J. Vac. Sci. Technol. B **14**, 2523 (1996).
[17] J. Leitner, J. Steikal, and P. Vonka, Mater. Lett. **28**, 197 (1996).
[18] F. I. Manyakhin, Izv. VUZov, Ser. Mater. Élektron. Tekhn., No. 1, 63 (1997).
[19] C. G. Van De Walle, C. Stampfl, and J. Neugebauer, in *Proceedings of the Second International Conference on Nitride Semiconductors* (Tokushima, Japan, 1997), Paper W1–1, p. 386.
[20] V. S. Vavilov, A. E. Kiv, and O. R. Niyazova, *Mechanisms of Defect Formation and Migration in Semiconductors* (Nauka, Moscow, 1981).
[21] V. S. Vavilov, Usp. Fiz. Nauk **167**, 4, 407 (1997).

Translated by Paul F. Schippnick

# Mechanisms of radiative recombination in InGaAsSb/InAsSbP lasers operating in the 3.0 to 3.6-$\mu$m spectral range

M. Aĭdaraliev, N. V. Zotova, S. A. Karandashev, B. A. Matveev,*) M. A. Remennyĭ, N. M. Stus', and G. N. Talalakin

*A. F. Ioffe Physicotechnical Institute, Russian Academy of Sciences, 194021 St.Petersburg, Russia*
(Submitted April 21, 1998; accepted for publication) April 23, 1998)
Fiz. Tekh. Poluprovodn. **33**, 233–238 (February 1999)

It is shown that type-I or type-II heterojunctions can be formed at heterojunction boundaries, depending on the composition of the active region and/or bounding layers. This is governed by differences in the mechanisms of radiative recombination, the temperature dependence of the radiation wavelength, the polarization type of the radiation, and the current–voltage characteristics. © *1999 American Institute of Physics.*
[S1063-7826(99)01502-1]

Diode lasers based on narrow-gap III–V semiconductors emitting in the middle infrared (IR) are of interest because of the possibility of using them in molecular spectroscopy, pollution monitoring, and in fiber-optic communications based on fluorite glasses with low optical losses.

This paper is a continuation of research on mesa-strip lasers based on InGaAsSb / InAsSbP, double heterostructures (DH) which emit in the spectral range 3.0–3.6 $\mu$m and which were grown on *n*-InAs (111) substrates.[1,2] In this paper we show that type-I and type-II heterojunctions can be formed at heterojunction boundaries, depending on the composition of the active region and/or the bounding layers. This is governed by differences in the mechanisms of radiative recombination, the temperature dependence of the radiation wavelength, the polarization type of the radiation, and the current–voltage characteristics.

## 1. OBJECTS OF STUDY AND EXPERIMENTAL TECHNIQUE

Double heterostructures were grown by liquid-phase epitaxy on a *n*-InAs (111) A substrate with electron density $n=(1-2)\times 10^{16}\,\mathrm{cm}^{-3}$ and consisted of three layers: two wide-gap bounding layers of $InAs_{1-v-w}Sb_vP_w$ ($0.05\leqslant v \leqslant 0.10$; $0.09\leqslant w\leqslant 0.18$) of *n*- and *p*-type conductivity, respectively, and the active layer of the laser with composition $n$-$In_{1-x}Ga_xAs_{1-y}Sb_y$ ($0\leqslant x\leqslant 0.1$; $0\leqslant y\leqslant 0.1$). The thicknesses of the wide-band layers were 4–6 $\mu$m, and of the active layer 1–4 $\mu$m. Mesa-strip lasers with strip widths 10 and 20 $\mu$m and cavity length 150–600 $\mu$m were fabricated using photolithography. Similar structures, grown on InAs (100) substrates, were investigated earlier in Refs. 3 and 4.

Photoluminescence at $T=77$ K and electroluminescence in the temperature range $T=77$–160 K were recorded by a cooled InSb photodiode using a synchronous detection scheme. To excite photoluminescence (PL), we used an LPI-14 diode laser (wavelength $\lambda=0.8$ $\mu$m, power $\sim$50 W, pulse duration $\tau=5$ $\mu$s, frequency $f=500$ Hz), whose emission was directed onto a *P*-InAsSbP wide-gap emitter. The signal was recorded in ''reflection'' geometry. The luminescence was analyzed with a DFS-12 spectrometer. Measurements were performed in the pulsed ($\tau=5$ $\mu$s, $f=500$ Hz) and continuous (cw) regime.

The composition of the layers, determined by a CAMEBAX micro-x-ray analyzer, and the parameters of the investigated structures are given in Table I. The widths of the band gaps $E_g$ of the layers were determined from the maxima of the photoluminescence spectra (77 K) and coincided with the $E_g$ values calculated from the composition of the solid solution.[5] The band discontinuities at the heterojunction boundaries were determined by interpolation using the technique of Ref. 6.

In the table the double heterostructures are divided into three groups, depending on the material of the active region. The first group includes structures with an InAs active region, the second group includes structures with an InGaAsSb active region, and the third group includes structures with an InAsSb active region. The double heterostructures of group 1 realize type-II heterojunctions, the double heterostructures of group 2 realize heterojunctions of both types, and the double heterostructures of group 3 realize type-I heterojunctions.

## 2. EXPERIMENTAL RESULTS AND DISCUSSION

Figure 1 shows typical photoluminescence spectra at $T=77$ K for the three groups of samples. The short-wavelength decay of the intensity $I_{\mathrm{PL}}$ is similar for all three groups and is described by an exponential dependence with activation energy $\varepsilon_0\sim kT\sim 10$ meV, which suggests that the composition of the active regions is homogeneous. The half-widths of the spectra are equal to $\sim$25 meV, which indicates that the electron density in the active region is low ($n\sim 5\times 10^{16}\,\mathrm{cm}^{-3}$).

The lasers had threshold currents $I_{\mathrm{th}}$ from 15 (current density $j_{\mathrm{th}}=200\,\mathrm{A/cm}^2$) to 100 mA and output power up to 2 mW from the face (at a current $I=20\,I_{\mathrm{th}}$) at 77 K. The single-mode lasing regime was realized in the current interval $(1-2)\,I_{\mathrm{th}}$. Minimum threshold currents were observed for cavity lengths $\sim$300 $\mu$m. In the lasers with strip width

 

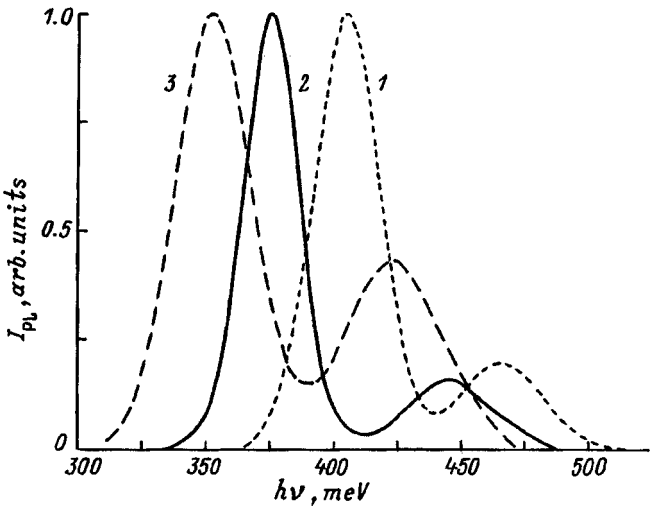


FIG. 1. Photoluminescence spectra of three groups of samples at 77 K. Structures: 217 (*1*), 209 (*2*), 216 (*3*) (see table).

10 $\mu$m the longitudinal spatial mode ($m=0$) was usually observed.

Figure 2 shows typical curves of the threshold current $I_{\text{th}}$ and differential quantum efficiency $\eta_{\text{diff}}$ as functions of the temperature (Fig. 2a), of the output power $P$ as a function of the current $I$ (Fig. 2c), and emission spectra for $I=I_{\text{th}}, 2I_{\text{th}}$ (Fig. 2b).

The temperature dependence of the threshold current is fitted by two exponential segments with characteristic temperatures $T_0=55-88$ K in the interval $T=77-120$ K (the region in which radiative recombination predominates) and $T_0=16-21$ K for $T>120$ K, where nonradiative Auger recombination with participation of the spin–orbit detached band predominates.[7] The temperature dependence of the differential quantum efficiency has two similar segments. Note the nonmonotonicity of the slope of the curve $\eta_{\text{diff}}(T)$ near $T=120-140$ K. In Ref. 8 it was shown that in InAs and in solid solutions similar to it in composition the probability of intraband absorption (IA) by holes followed by their transition to the spin–orbit detached band is great since the spin–orbit decoupling energy $\Delta$ is close to the width of the band gap $E_g$. In InAs and in solid solutions similar to it in composition, a situation is realized near 140 K, where the photon energy $h\nu\approx\Delta$ and intraband absorption is maximized. As the temperature is raised, so that the photon energy becomes less than $\Delta$, intraband absorption decreases, causing the appearance of an inflection point in the temperature dependence of $\eta_{\text{diff}}$.

The current–power characteristic has a sublinear dependence. With growth of the current, the differential quantum efficiency decreases due to heating of the laser. In addition, intraband absorption leads to growth of the concentration of nonequilibrium carriers, which lowers the refractive index of the active region and leads to a weakening of optical confinement and escape of radiation into the passive regions.

Figure 3 plots the dependence of the photon energy of the laser radiation $h\nu$ on temperature (*a*), the degree of polarization $\alpha$ of the laser mode on the current (*b*), the current–voltage ($I-U$) characteristic (*c*), and the energy band diagram (*d*) for samples of group 1, for which a type-II heterojunction is formed (see Table I).

The energy of the photons emitted in lasers of group 1 is $405-408$ meV (77 K), which is less than the width of the InAs band gap (410 meV) and larger than the band–acceptor transition energy (395 meV). A value similar to ours was obtained in an analogous structure with optical pumping.[9] Unusual here is the absence of any dependence (or weak dependence) of the laser peak energy on the temperature. The emitted radiation has TM polarization. The degree of polarization $\alpha=(I_{\text{TE}}-I_{\text{TM}}/(I_{\text{TE}}+I_{\text{TM}})$, where $I_{\text{TM}}$ and $I_{\text{TE}}$ are the intensities of the radiation for TM- and TE-polarized light, reaches 97%. The current–voltage characteristic (Fig. 3c) in the forward direction has an *S*-shaped dependence.

Let us consider the energy band diagram (Fig. 3d). On the $N-n$ heteroboundary there exist self-consistent pockets for holes on the wide-gap layer ($N$) side, and for electrons on the narrow-gap active region ($n$) side. Estimates show that for the same electron density in the $N$ and $n$ layers ($N\sim n\sim 5\times10^{16}$ cm$^{-3}$) and pocket width $\sim$200 Å the depth of the pockets is $\sim(1/2)\Delta E_c$ for the electrons and $\sim(1/2)\Delta E_v$ for

TABLE I. Laser structure parameters.

| Group of samples | Material of active region | Number of structure | Composition of active region $x$ | Composition of active region $y$ | Composition of bounding layers $InAs_{1-v-w}Sb_vP_w$ $v$ | Composition of bounding layers $w$ | $E_g$, meV active region | $E_g$, meV bounding layers | $\Delta E_g$ meV | $\Delta E_c$, meV | $\Delta E_v$, meV | Type of HJ | Laser mode energy, meV | $I_{\text{th}}$, mA | Type of polarization |
|---|---|---|---|---|---|---|---|---|---|---|---|---|---|---|---|
| 1 | InAs | 217 | 0 | 0 | 0.095 | 0.16 | 410 | 475 | 65 | 114 | −49 | II | 405 | 45 | TM |
| 2 | $In_{1-x}Ga_xAs_{1-y}Sb_y$ | 209 | | | | | | | | | | | 376 | 16 | |
| | | 212 | 0.09 | 0.1 | 0.05 | 0.11 | 385 | 468 | 83 | −32 | 115 | II | 380 | 100 | TE,TM |
| | | 215 | | | | | | | | | | | 380 | 50 | |
| | | 208 | 0.1 | 0.07 | 0.07 | 0.1 | 363 | 441 | 80 | 44 | 36 | I | 361 | 50 | TE |
| 3 | $InAs_{1-y}Sb_y$ | 213 | | | | | | | | | | | 356 | 50 | |
| | | 214 | 0 | 0.075 | 0.07 | 0.1 | 355 | 443 | 88 | 50 | 38 | I | 360 | 115 | TE |
| | | 216 | | | | | | | | | | | 355 | 100 | |

*Note:* $\Delta E_g$ is the difference in the band gaps of the materials of the bounding regions and the active region; $\Delta E_c$ and $\Delta E_v$ are the energy gaps of the conduction band and the valence band at the heterojunction.

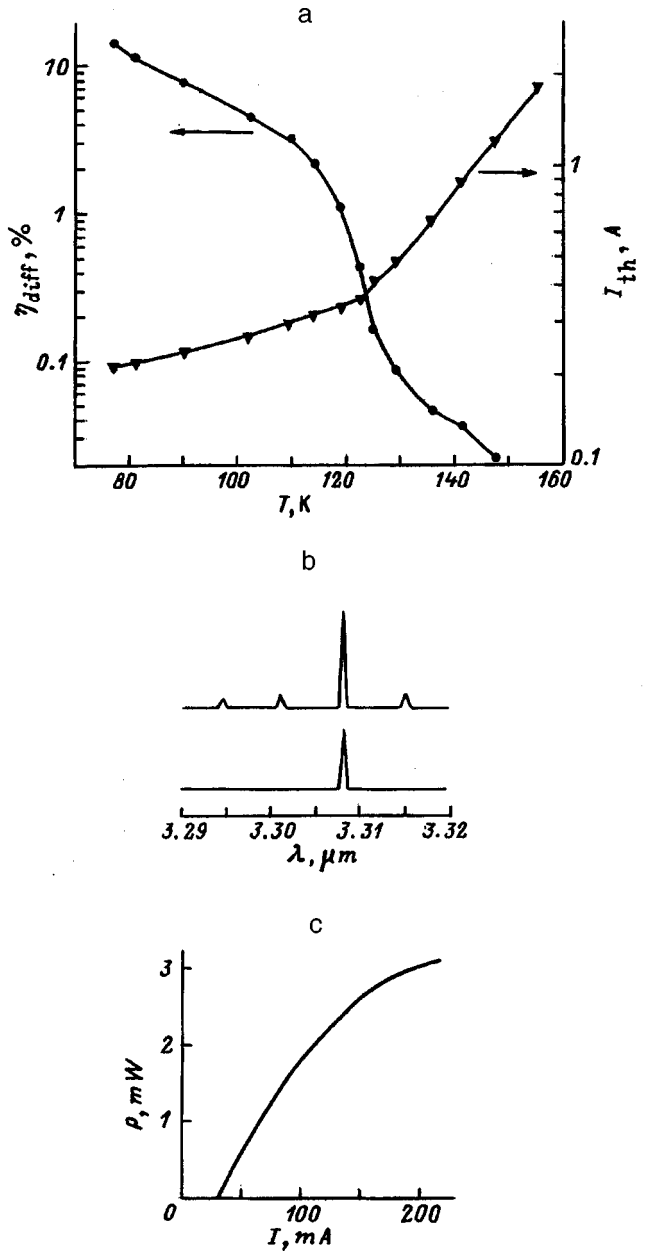


FIG. 2. Dependence of the differential quantum efficiency $\eta_{\text{diff}}$ and threshold current $I_{\text{th}}$ on the temperature (a). Laser emission spectra for $I=I_{\text{th}}=30$ mA (lower curve) and $I=2\,I_{\text{th}}=60$ mA (upper curve) (b) and current–power ($P-I$) characteristic (c). Structure 209.

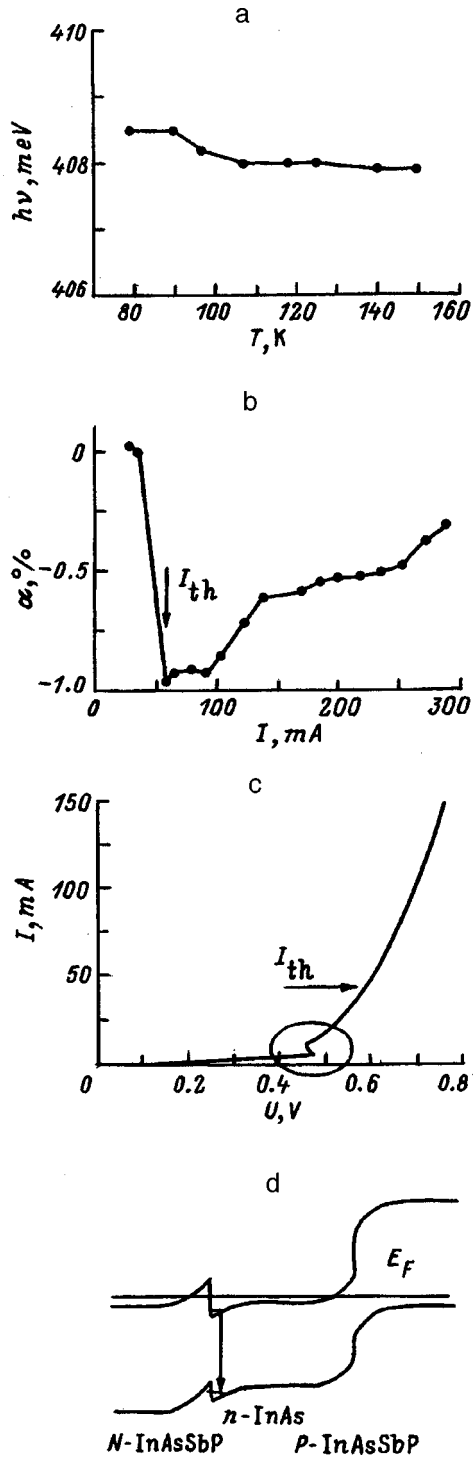


FIG. 3. Dependence of the photon energy $h\nu$ on temperature $T$ (a) and of the degree of polarization of the radiation $\alpha$ on the current $I$ (b). Current–voltage ($I-U$) characteristic (c) and energy band diagram (d) for samples of the first group. Structure 217. $E_F$ is the Fermi level.

the holes, i.e., 57 and 25 meV, respectively. The large discontinuity in the conduction band, ~114 meV, provides good electron confinement, which creates conditions for quantization and radiative recombination of the electrons and holes located at levels in the pockets with carrier tunneling through the heterojunction.

In view of the discussion above, we assume that in lasers of group 1 recombination occurs primarily near the type-II $N-n$ heterojunction, and not in the volume of the active region. Radiation is created as a result of recombination of electrons and holes located in the self-consistent quantum wells on either side of the heterojunction boundary, with tunneling of light holes into the narrow-gap region of the double heterostructure. In this case, the radiation has TM polarization,[10] and the temperature dependence of the laser photon energy is due to competition of temperature narrowing of the band gap and filling of the pockets, whose depth is determined by the band discontinuities $\Delta E_c$ and $\Delta E_v$, which are independent of temperature.

Figure 4 plots the dependence of the photon energy $h\nu$ on temperature (a), the degree of polarization $\alpha$ on the cur-

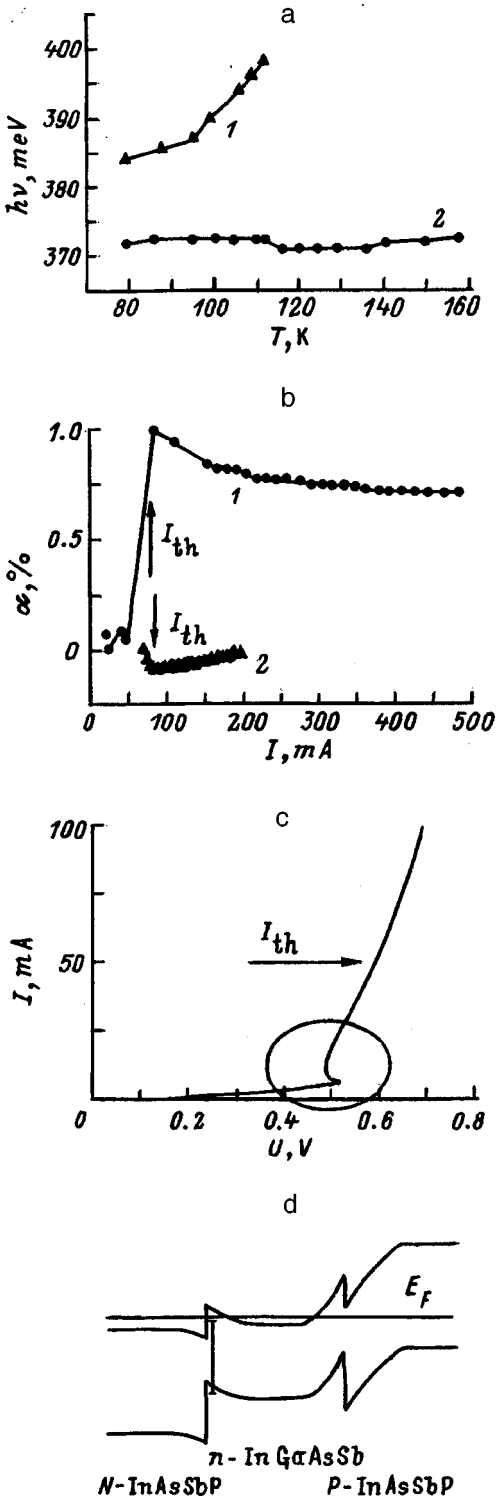


FIG. 4. The same as in Fig. 3, but for samples of the second group for the case of a type-II heterojunction. Structures: a — 209 (*1*) and 215 (*2*); b — 212 (*1*) and 215 (*2*); c — 215.

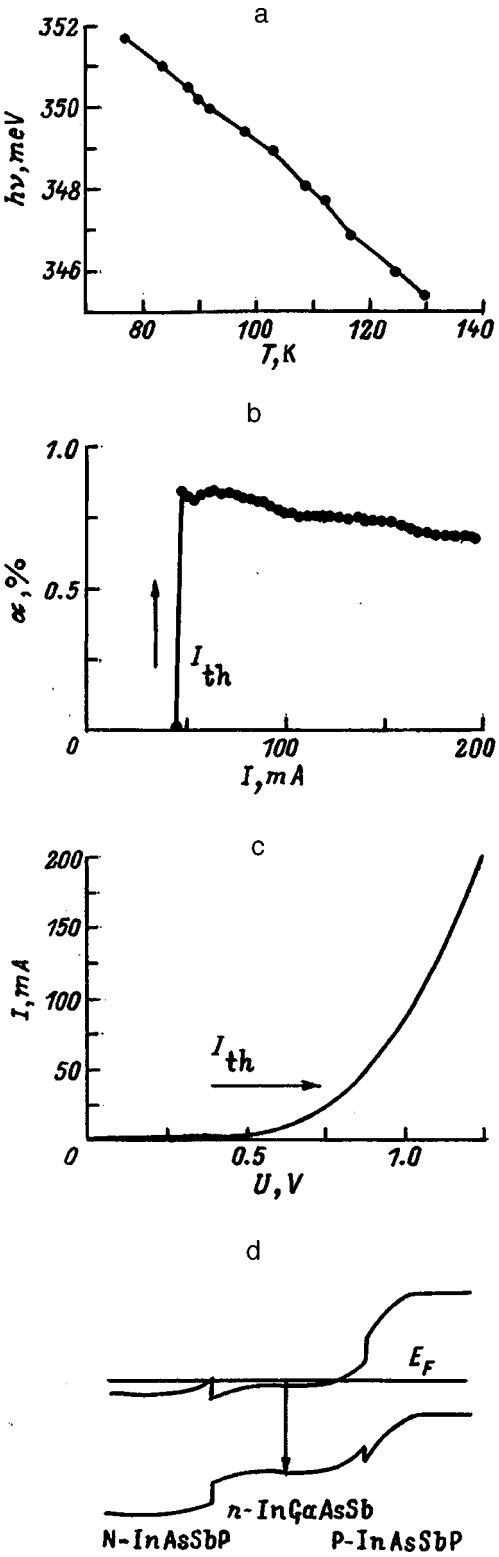


FIG. 5. The same as in Figs. 3 and 4, but for samples of the second group for the case of a type-I heterojunction. Structure 208.

rent (b), and the current–voltage characteristic (c) and also shows the energy band diagram (d) for group-2 samples with an InGaAsSb active region in the case in which a type-II heterojunction is formed.

These lasers, like the lasers of group 1, are characterized by an anomalous temperature dependence and an *S*-shaped current–voltage characteristic. As the temperature is raised, a short-wavelength (''blue'') shift of the radiation wavelength is observed; this shift is probably associated with filling of the pockets as a result of an increase in the threshold concentration of current carriers due to an increase in losses with increasing temperature.

In the given double heterostructures, the discontinuity in

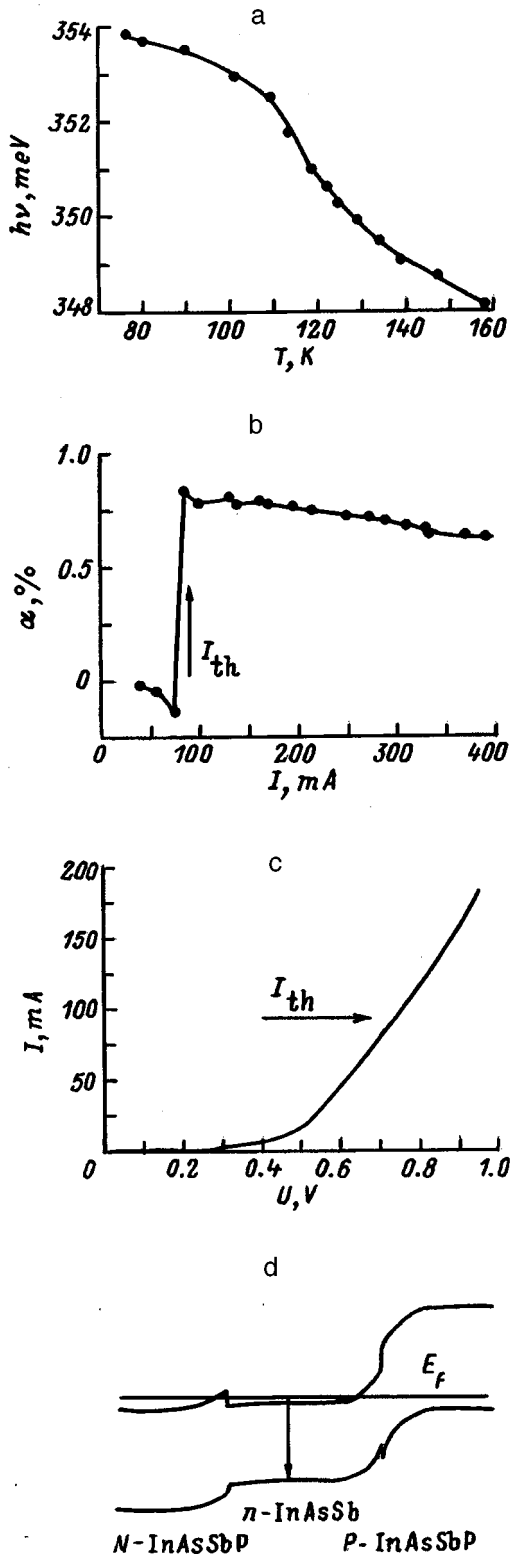


FIG. 6. The same as in Figs. 3–5, but for samples of the third group. Structures 216 (a,b) and 213 (c).

the valence band is significantly greater than in the conduction band, which ensures good hole containment. In most of the lasers, TE polarization of the laser radiation was observed; therefore, the main contribution to the radiation probably comes from recombination of a tunneled-in electron with a heavy hole (Fig. 4d).

In lasers based on type-II heterojunctions a large spread in the degree of polarization was observed (this can be seen from Fig. 4b, but for the structures shown in Fig. 3 it is not seen), which probably reflects the influence of imperfection of the heterojunction and, consequently, transformation of heavy holes into light holes, or the coexistence of processes of recombination of a tunneled-in electron with a heavy hole and a tunneled-in light hole with an electron.

In lasers of group 2 with an $In_{0.9}Ga_{0.1}As_{0.93}Sb_{0.07}$ active region a type-I heterojunction was realized. The laser photon energy essentially coincides with the width of the band gap of the active region and decreases with temperature in accordance with temperature narrowing of the band gap (''red'' shift). The radiation has TE polarization ($\alpha = 85\%$). The lasers have the usual current–voltage characteristic (Fig. 5).

Type-I heterojunctions are always realized in lasers of group 3. The current–voltage characteristic, the temperature dependence of the photon energy of the laser radiation $h\nu$, and the degree of polarization $\alpha$ are plotted in Fig. 6, which also shows the energy band diagram. The photon energy $h\nu$ essentially coincides with the width of the band gap of the active region. All the dependences have the usual form for radiative recombination in the volume of the active region.

Thus, in double heterostructures in which type-I heterojunctions are formed, interband radiative recombination takes place in the volume of the active region with the characteristic ''red'' temperature shift of the laser peak energy, TE polarization of the laser radiation, and the usual current–voltage characteristic.

In double heterostructures in which type-II heterojunctions are realized, radiative recombination occurs between the electrons and holes located in self-consistent quantum wells in a narrow region near the heterojunction upon tunneling of one of the charge carriers. Such recombination is accompanied by a ''blue'' temperature shift of the laser peak energy, an *S*-shaped current–voltage characteristic, and polarization type dictated by the tunneling particle.

We wish to thank N. D. Il'inskiĭ for technical assistance.

This work was supported under the program ''Optics and Laser Physics'' by the Ministry of Scientific and Technical Programs of the Russian Ministry of Science, Project No. 4.14.

*)E-mail: bmat@iropt3.ioffe.rssi.ru; Fax: (812) 2474324

[1] N. V. Zotova, S. A. Karandashev, B. A. Matveev, M. A. Remennyĭ, N. M. Stus', and G. N. Talalakin, Pis'ma Zh. Tekh. Fiz. **23**, 72 (1997) [Tech. Phys. Lett. **23**, 41 (1997)].

[2] M. Aĭdaraliev, N. V. Zotova, S. A. Karandashev, B. A. Matveev, M. A. Remennyĭ, N. M. Stus', and G. N. Talalakin, Pis'ma Zh. Tekh. Fiz. **24**, 12 (1998) [Tech. Phys. Lett. **24**, 47 (1998)].

[3] B. N. Baranov, T. N. Danilova, O. G. Ershov, A. N. Imenkov, V. V. Sherstnev, Yu. P. Yakovlev, Pis'ma Zh. Tekh. Fiz. **18**, 6 (1992) [Tech. Phys. Lett. **18**, 62 (1992)].

[4] T. N. Danilova, A. P. Danilova, O. G. Ershov, A. N. Imenkov, M. V. Stepanov, V. V. Sherstnev, and Yu. P. Yakovlev, Fiz. Tekh. Poluprovodn. **31**, 1392 (1997) [Semiconductors **31**, 1200 (1997)].

[5] T. H. Glisson, J. R. Hauser, M. A. Littlejohn, and C. K. Williams, J. Electron. Mater. **7**, 1 (1978).

[6] S. Adachi, J. Appl. Phys. **58**, R1 (1985).

[7] M. Aĭdaraliev, G. G. Zegrya, N. V. Zotova, S. A. Karandashev, B. A. Matveev, N. M. Stus', and G. N. Talalakin, Fiz. Tekh. Poluprovodn. **26**, 246 (1992) [Sov. Phys. Semicond. **26**, 138 (1992)].
[8] N. A. Gun'ko, G. G. Zegrya, N. V. Zotova, Z. N. Sokolova, N. M. Stus', and V. B. Khalfin, Fiz. Tekh. Poluprovodn. **31**, 1396 (1997) [Semiconductors **31**, 1242 (1997)].
[9] O. B. Gusev, M. S. Bresler, N. V. Zotova, and N. M. Stus', Fiz. Tekh. Poluprovodn. **26**, 735 (1992) [Sov. Phys. Semicond. **26**, 415 (1992)].
[10] O. V. Konstantinov, V. I. Perel', and B. V. Tsarenkov, Fiz. Tekh. Poluprovodn. **3**, 1039 (1969) [Sov. Phys. Semicond. **3**, 873 (1970)].

Translated by Paul F. Schippnick

# High-power light-emitting diodes operating in the 1.9 to 2.1−$\mu$m spectral range

T. N. Danilova, B. E. Zhurtanov, A. L. Zakgeĭm, N. D. Il'inskaya, A. N. Imenkov, O. N. Saraev, M. A. Sipovskaya, V. V. Sherstnev, Yu. P. Yakovlev

*A. F. Ioffe Physicotechnical Institute, Russian Academy of Sciences, 194021 St. Petersburg, Russia*
(Submitted May 14, 1998; accepted for publication May 20, 1998)
Fiz. Tekh. Poluprovodn. **33**, 239–242 (February 1999)

Light-emitting diodes (LED's) operating in the spectral range 1.9−2.1 $\mu$m have been fabricated by liquid-phase epitaxy on the basis of AlGaAsSb/GaInAsSb double heterostructures with a high Al (64%) content in the wide-gap regions. The design of the LED makes it possible to locate the active region near the heat-removal elements of the housing, and pass the light through the GaSb substrate, which is completely unshielded by the contact. The LED's are investigated in the quasi-continuous (CW) regime and pulsed regime at room temperature. The optical power of the LED's possesses a linear current dependence over a wide range of currents. A CW optical power as high as 4.6 mW and a peak optical power of 190 mW in the pulsed regime were achieved at room temperature. It is shown that the transition from linear to sublinear current dependence of the optical power is governed by Auger recombination in the pulsed regime at pulse durations as low as 5 $\mu$s. © *1999 American Institute of Physics.* [S1063-7826(99)01602-6]

**1**. The spectral range 1.9−2.1 $\mu$m encompasses absorption lines of water vapor, $CO_2$, and other gases, which makes radiation sources in this spectral range promising for the construction of gas-analyzers. Devices for measuring humidity are widely used in technological applications, particularly for process monitoring.[1] Radiation sources in this spectral range can also be used in medicine, for example, to measure the sugar level in blood.

Despite the fact that lasers in this spectral range work at room temperature,[2–5] in a number of practical applications not requiring high spectral resolution, light-emitting diodes (LED's) and even thermal radiation sources are used. Lasers are, on the one hand, more expensive and, on the other, aligning the narrow laser line with the absorption lines complicates the measurement setup when precision temperature control is employed. In comparison with thermal radiation sources, LED's have the advantage that they emit a rather narrow spectral line and therefore do not require the use of optical filters, and, additionally, allow one to use electrical modulation instead of mechanical.

The present paper is a continuation of our papers on the fabrication and testing of LED's based on GaInAsSb/AlCaAsSb heterostructures that emit in the spectral range 1.8−2.2 $\mu$m.[6–9] Our aim in this study was to develop an LED design and then fabricate and test LED's with minimized thermal resistance, which makes it possible to increase the external quantum yield and current interval in which the radiation intensity is proportional to the current.

**2**. The investigated LED's were fabricated by liquid-phase epitaxy (LPE) on the basis of GaInAsSb/AlGaAsSb heterostructures grown on a *n*-GaSb (100) substrate tellurium-doped to a free electron concentration of $(8-9)\times10^{17}\,\mathrm{cm}^{-3}$. The LED's had a structure (Fig. 1a) in which the narrow-gap active layer is sandwiched between two wide-gap emitters. The advantage of the structure of LED's

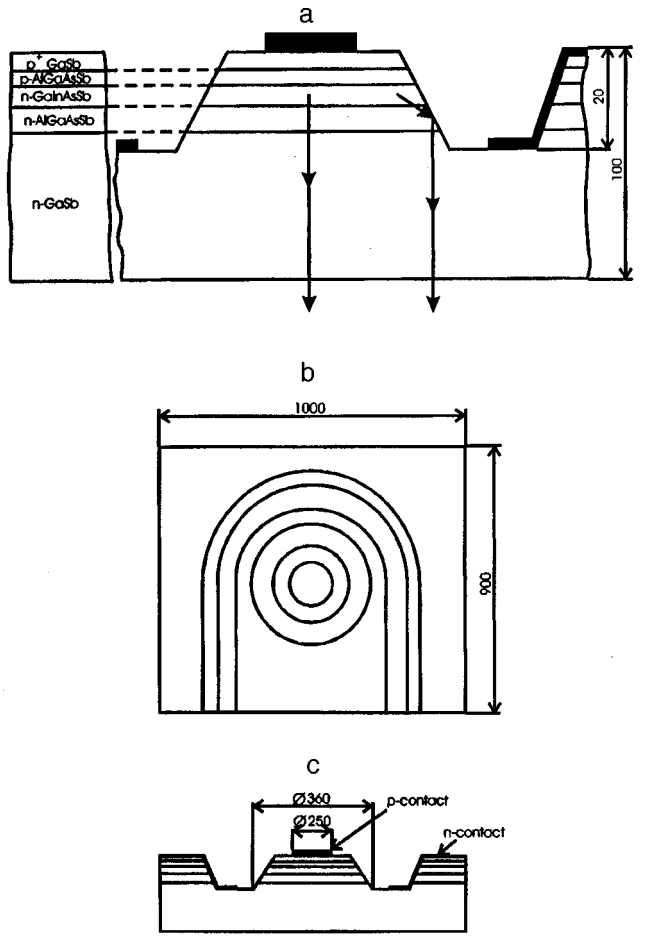


FIG. 1. Design of the light-emitting diode: a — arrangement of layers of the structure; b — front view of the contact surfaces; c — cross-sectional view. Linear dimensions are given in microns. The arrows indicate the direction by which light leaves the structure.

 

with two wide-gap emitters in comparison with one wide-band emitter was demonstrated in Ref. 8. All of the grown layers were isoperiodic with the substrate. The lattice mismatch between the substrate and the narrow-gap layer was $\Delta a/a=(8-9)\times10^{-4}$, and between the substrate and the wide-band layer $1.37\times10^{-3}$. A narrow-gap layer of composition $Ga_{1-x}In_xAsySb_{1-y}$, where $x\sim0.1$, and $y\sim0.08$, was doped with tellurium to a free electron concentration of $(7-8)\times10^{16}\,cm^{-3}$. The thickness of the narrow-gap layer was $2\,\mu m$. The wide-gap layers were grown with a greater Al content than in the wide-gap layers of the LED's studied previously,[5–9] and had the composition $Al_{0.64}Ga_{0.36}As_{0.44}Sb_{0.956}$. The wide-gap *N*-layer was doped with tellurium to a free electron concentration of $6\times10^{17}\,cm^{-3}$. The wide-gap *P*-layer was doped with germanium to a free hole concentration $\sim10^{18}\,cm^{-3}$. The thickness of the *N*-layer was $1.5\,\mu m$. The thickness of the *P*-layer was $1.7\,\mu m$. With the aim of creating a low-resistance contact, the wide-gap *P*-layer was coated with a layer of $P^+$-GaSb with a high level of doping and a free hole concentration in it $\sim10^{19}\,cm^{-3}$. The thickness of this layer was $\sim3\,\mu m$.

The calculated value of the width of the band gap at room temperature in the narrow-gap region was $E_g\sim0.64\,eV$, and in the wide-gap region, $E_g=1.23\,eV$.

The LED design shown in Fig. 1 was optimized to lower the thermal resistance and increase the radiation yield. Accordingly, circular mesa-diodes are first created using photolithography with deep etching into the substrate from the grown epitaxial structures. Contacts are then deposited on the diode structure in such a way that the *n* and *p* contacts are located on one surface. A view of the LED looking down on the contact areas is shown in Fig. 1b. A silicon wafer possessing good thermal conductivity serves as electrical insulation for the contacts. Contact layers were deposited on this wafer by photolithography. The contact layers of the LED were then soldered to them by first aligning and then heating them. An overall cross-sectional view of the LED is shown in Fig. 1c. In this design the active region is located closer to the heat-transfer element than in the case where it lies on a thick substrate. Light from the active region leaves the structure, as shown by the arrows in Fig. 1a, through the substrate, which is completely unshielded by the contact.

On the outer surface of the LED an epoxy compound is deposited in the form of a lens of height $\sim2.4\,mm$, expanding the radiation flux to a divergence of $16-20°$ at half-maximum.

For the investigated LED's we measured the emission spectra, the dependence of the optical output power on the current, the quantum yield, and the current–voltage characteristic.

The spectral characteristics of the LED's were investigated with the aid of a standard synchronous detection scheme, an MDR-2 monochromator, and a GaInAsSb-based photodiode as the receiver.[10] The optical power was recorded by an IMO-2M power meter. The measurements were performed with the LED's powered in the quasi-continuous regime by current pulses of meander type with a pulse repetition rate of 400 Hz and in the pulsed regime by current pulses with duration ($\tau$) 5, 10, and 20 $\mu$s with pulse repetition rate equal to 1 kHz. The LED's were investigated at room temperature.

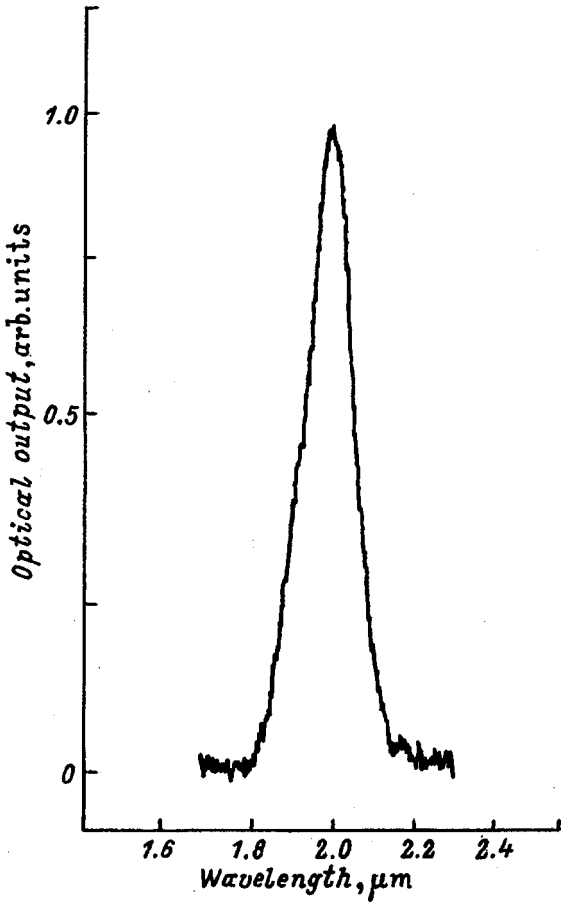


FIG. 2. Emission spectrum of an E-41 N 21 LED, quasi-continuous power supply, current 100 mA, room temperature.

**3**. The emission spectra at room temperature contain one band (Fig. 2). The dependence of the peak wavelength on the composition of the solid solution in the active region is essentially linear and varies from 1.9 to $2.1\,\mu m$. The half-width of the emission band, i.e., the full width at half-maximum (FWHM), is $0.17\,\mu m$ at a current of 50 mA and $0.18\,\mu m$ at a current of 200 mA. As the current is increased from 50 to 200 mA, the peak shifts toward longer wavelengths by $0.015-0.017\,\mu m$.

The optical power ($P$) and its dependence on the injection current ($I$) of the investigated LED's in the quasi-continuous regime is plotted in Fig. 3. The maximum value of the optical power, 4.6 mW, was obtained at a current of 200 mA. In the current interval $50-200$ mA the dependence $P(I)$ is essentially linear. At large currents the measurements were made in the pulsed power regime, but the pulse durations were limited to microseconds (Fig. 4). As can be seen , in this case the dependence $P(I)$ is essentially linear up to currents $\sim520$ mA. The dependence then becomes sublinear for all three pulse durations $\tau=5$, 10, 20 $\mu$s represented in the figure. The maximum achieved peak optical power was 190 mW at a current of 1.4 A for a pulse duration of 5 $\mu$s and pulse repetition rate of 1 kHz.

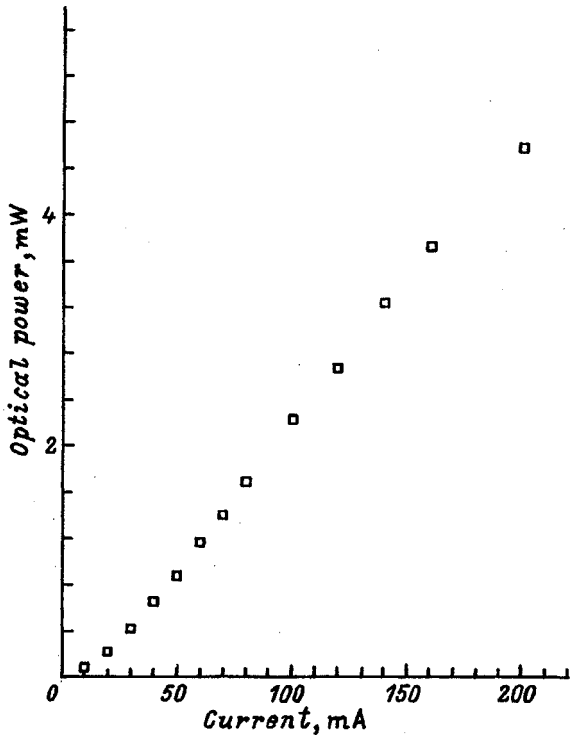


FIG. 3. Dependence of optical power on current in the quasi-continuous regime at room temperature for an E-41 N 21 LED.

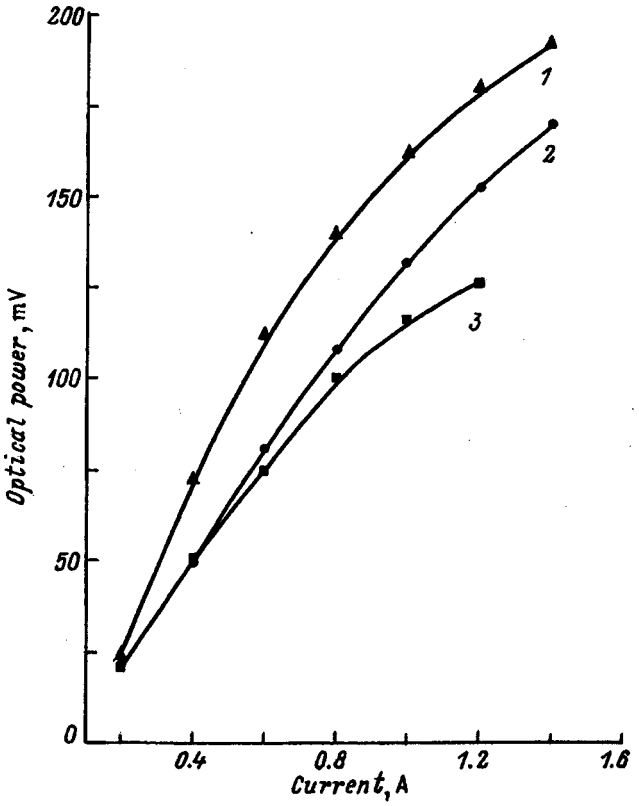


FIG. 4. Dependence of optical power on current in the pulsed regime at room temperature for a T-41 N 21 LED. Pulse duration $\tau$, *1* — 5, *2* — 10, *3* — 20. Pulse repetition rate 1 kHz.

The measured external quantum yield of the investigated LED's was ~4% at room temperature.

Measurement of the current–voltage characteristics of the investigated LED's showed that at room temperature for forward bias they have a rectilinear segment, giving a cutoff of 0.5 V and a slope corresponding to a residual resistance in the range $2.2-2.8\,\Omega$.

**4**. Let us discuss the results which we obtained.

The LED's which we investigated had some improvements over the LED's fabricated and investigated by us earlier.[6–9] First, they have wider-gap emitters with Al content ~64%, and second, the design of these LED's makes it possible to locate the active region closer to the heat-transfer part of the housing and lead the radiation out through the substrate, which is unshielded by the contact.

It should be noted that the Al content of the AlGaAsSb wide-gap layers obtained by liquid-phase epitaxy (~64%) is a record.

The values of the series resistances of the LED's show that despite the increase in the width of the band gap of the emitter layers, the use of a heavily doped $P^+$ layer in the pre-contact region proved to be sufficient to keep the series resistances from growing in comparison with the series resistances of the previous LED's.[9] Nevertheless, the current heating of the active region of the investigated LED's was considerable since the maximum of the emission spectrum shifts toward longer wavelengths and some broadening of the emission band also takes place as the current is increased from 50 to 200 mA in the quasi-continuous regime. However, this heating is rather moderate and the dependence $P(I)$ in this current interval remains essentially linear (Fig. 3). The dependence $P(I)$ also remains linear as the current is increased to ~520 mA in the pulsed regime when using microsecond pulses (Fig. 4). The appearance of a sublinear dependence in $P(I)$ with further increase of the current may be due to two factors—heating of the active region and increase in current losses due to Auger recombination. If we represent the dependence $P(I)$ as a power law, $P\sim I^n$, then in the case where its sublinearity is governed by Auger recombination, $n$ should be 2/3. Analysis shows that in the pulsed regime for $I>0.520$ A and $\tau=5\ \mu$s $n=2/3$, for $\tau=10\ \mu$s $n=11/21$, and for $\tau=20\ \mu$s $n=2/7$. This implies that for a pulse duration of 5 $\mu$s the sublinearity of the dependence $P(I)$ is governed by Auger recombination. Decreasing the pulse duration below 5 $\mu$s does not lead to an extension of the segment of the dependence $P(I)$ at currents $I>0.520$ A. For the pulse durations $\tau=10$ and 20 $\mu$s the sublinearity of the dependence $P(I)$ is governed not only by Auger recombination, but also by heating.

The peak optical power of 4.6 mW in the quasi-continuous regime and 190 mW in the pulsed regime are significant values for spontaneous emission sources in the wavelength region ~2 $\mu$m.

In summary, the use of a symmetric double heterostructure with high Al content (64%) in the wide-gap regions and the development of a design, which can be used to locate the active region near the heat-removal base of the housing and lead the light flux out through the substrate unshielded by the contact has made it possible to obtain LED's that emit at higher optical power levels: 4.6 mW at a current of 200 mA

in the quasi-continuous regime, and a peak power of 190 mW at a current of 1.4 A in the pulsed regime. It has been shown that for a pulse duration of 5 $\mu$s the transition of the dependence $P(I)$ from linear to sublinear is governed not by heating of the active region, but by processes of Auger recombination in it.

This work was supported in part by a contract with INCO–Copernicus [Contract No. 1C15-CT97-0802 (DG12-CDPF)] and by a grant of the Russian Ministry of Science under the program ''Optics and Laser Physics.''

[1] A. N. Baranov, Yu. P. Yakovlev, A. N. Imenkov, M. P. Mikhaĭlova, A. I. Klimentenok, and V. L. Shutov, Bumazh. Promst., No. 9, 20 (1989).
[2] L. M. Dolginov, L. V. Druzhinina, I. V. Kryukova, A. N. Lapshin, E. V. Matveenko, and M. G. Mil'vidskiĭ, Kvant. Elektron. **5**, 26 (1978) [Sov. J. Quantum Electron. **8**, 18 (1978)].
[3] A. N. Baranov, B. E. Dzhurtanov, A. N. Imenkov, Yu. M. Shernyakov, and Yu. P. Yakovlev, Pis'ma Zh. Tekh. Fiz. **12**(9), 557 (1986) [Tech. Phys. Lett. **12**, 228 (1986)].
[4] H. K. Choi, S. J. Eglasch, and M. K. Conners, Appl. Phys. Lett. **63**, 3271 (1993).
[5] D. Z. Garbuzov, R. H. Martinelli, H. Lee, R. J. Menna, P. K. York, L. A. DiMareo, M. G. Marvey, R. J. Matarese, S. Y. Narayan, J. C. Connoly, Appl. Phys. Lett. **70**, 2931 (1997).
[6] A. Andaspaeva, A. N. Baranov, A. A. Guseĭnov, A. N. Imenkov, N. M. Kolchanova, E. A. Sidorenkova, Yu. P. Yakovlev, Pis'ma Zh. Tekh. Fiz. **15**(18), 71 (1989) [Tech. Phys. Lett. **15**, 734 (1989)].
[7] A. A. Andaspaeva, A. N. Baranov, A. A. Guseĭnov, A. N. Imenkov, N. M. Kolchanova, Yu. P. Yakovlev, Fiz. Tekh. Poluprovodn. **24**, 1708 (1990) [Sov. Phys. Semicond. **24**, 1067 (1990)].
[8] A. A. Popov, V. V. Sherstnev, Yu. P. Yakovlev, Pis'ma Zh. Tekh. Fiz. **23**(18), 12 (1997) [Tech. Phys. Lett. **23**, 701 (1997)].
[9] A. A. Popov, V. V. Sherstnev, and Yu. P. Yakovlev, Pis'ma Zh. Tekh. Fiz. **23**(20), 19 (1997) [Tech. Phys. Lett. **23**, 16 (1997)].
[10] I. A. Andreev, A. N. Baranov, M. A. Afrailov, V. G. Danil'chenko, M. P. Mikhaĭlova, and Yu. P. Yakovlev, Zh. Tekh. Fiz. **12**(21), 1311 (1986) [Tech. Phys. Lett. **12**, 542 (1986)].

Translated by Paul F. Schippnick

# Rapid tuning of the generation frequency of InAsSb/InAsSbP diode lasers ($\lambda = 3.3\,\mu$m) due to nonlinear optical effects

A. P. Danilova, T. N. Danilova, A. N. Imenkov, N. M. Kolchanova, M. V. Stepanov, V. V. Sherstnev, and Yu. P. Yakovlev*)

*A. F. Ioffe Physicotechnical Institute, Russian Academy of Sciences, 194021 St. Petersburg, Russia*
(Submitted May 28, 1998; accepted for publication June 1, 1998)
Fiz. Tekh. Poluprovodn. **33**, 243–248 (February 1999)

A study has been made of wavelength tuning in double heterostructure InAsSb/InAsSbP-based diode lasers. A simple mathematical model, which takes into account the spatially homogeneous injection and the dependence of the dielectric constant on the charge carrier density, is discussed. The wavelength can be increased or decreased, depending on the pump current and diode structure parameters, as is observed experimentally. The process of wavelength tuning proceeds with virtually zero delay time since it is determined by the photon lifetime in the cavity and in part by the lifetime of nonequilibrium charge carriers.
 [S1063-7826(99)01702-0]

**1**. A key element of high-resolution diode-laser spectrometers is a tunable diode semiconductor laser. Previously, the generation frequency of the laser was usually varied by heating of the active region.[1–6] This limited the response time of the laser spectrometers to a few milliseconds.

It has recently been discovered how to tune the generation frequency of a diode laser by varying the current with a speed exceeding the thermal relaxation rate.[7,8] The wavelength of the radiation decreases when the current exceeds a threshold value by less than 40%, and at higher currents it increases. The decrease in the wavelength was linked with an increase in the concentration of nonequilibrium charge carriers in the active region, and the increase was linked with self-focusing of the radiation. In a subsequent work,[9] on the basis of a comparison of the tuning characteristics of the lasers with collocated and separated electron and optical confinement it was shown that the dependence of the wavelength on the current is enhanced when the spreading of the injection current over the area of the active region is reduced.

In this paper we report the results of an ongoing experimental study of current tuning of the radiation wavelength initiated by us earlier.[7–9] We will also establish an experimental and theoretical basis for wavelength tuning due to nonlinear optical effects.

**2**. For this study we fabricated lasers based on $N$-$InAsSb_{0.17}P_{0.35}/n$-$InAsSb_{0.05}/P$-$InAsSb_{0.17}P_{0.35}$ double heterostructures (Fig. 1) with a high level of homogeneity of their electrical and optical properties and pump density over the area of the active medium. The structures were obtained by liquid-phase epitaxy on InAs substrates oriented in the [100] crystal plane. The narrow-gap $n$-InAsSb active layer was intentionally left undoped. The carrier density in it was $n = 10^{16}\,\mathrm{cm}^{-3}$. InAsSbP wide-gap layers served for both electron and optical confinement. The $N$-InAsSbP layer was doped with tin to an electron concentration of $2\times10^{18}\,\mathrm{cm}^{-3}$, the $P$-InAsSbP layer was obtained by doping it with zinc to a hole concentration of $1\times10^{18}\,\mathrm{cm}^{-3}$. The thickness of the active region was 1 $\mu$m and the strip width varied in the limits $15-20\,\mu$m. Laser diodes with length of the Fabry–Perot internal cavity $275-350\,\mu$m were obtained by cleaving. The tuning processes were investigated at 78 K. The laser was investigated both in the pulsed power regime

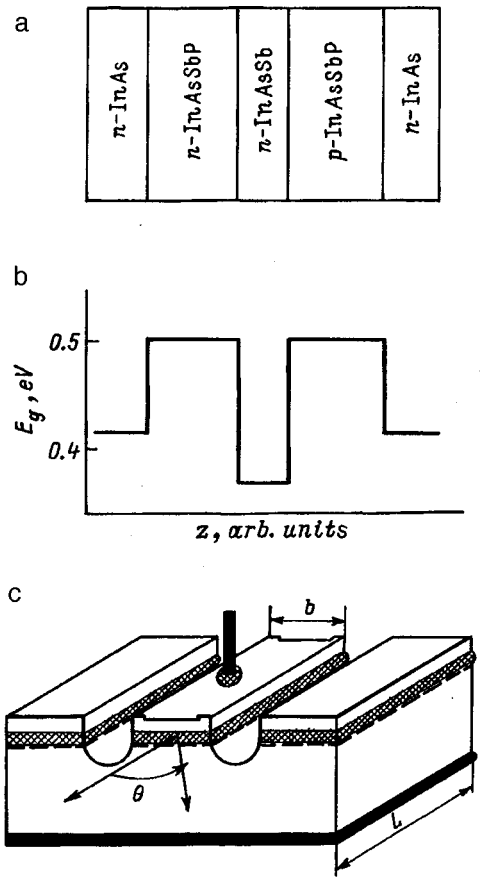


FIG. 1. Structure of the investigated diode laser: a — arrangement of epitaxial layers, b — layer-by-layer profile of the width of the band gap, c — design of a mesa-strip laser.

 

and in the constant current regime, on which a sawtooth current was superimposed. The constant current was set equal to the threshold current $I_{th}$. The amplitude of the sawtooth term was chosen such that the laser generated primarily one spectral mode over the entire interval of variation of the current. The frequency of the sawtooth current was set from $10^2$ to $10^4$ Hz. The pulse duration in the pulsed power regime was varied from 10 $\mu$s to 4 ms, and the pulse duty factor was set at 100. Tuning of the frequency of the the generated radiation was investigated by passing the output laser light through an external Fabry–Perot optical cavity with varying optical length. As cavities we used silicon wafers of thickness 47 and 11.2 mm. The optical signal was detected by an InSb-based photodetector and was amplified by a differential amplifier. Variation of the optical ray path through the silicon Fabry–Perot cavity delivered a resolution of the laser wavelength of $2\times10^{-2}$ Å. In addition, we investigated the spectral makeup of the radiation and the dependence of the directivity diagram on the pump current in the plane perpendicular to the $p-n$ junction and in the plane parallel to it.

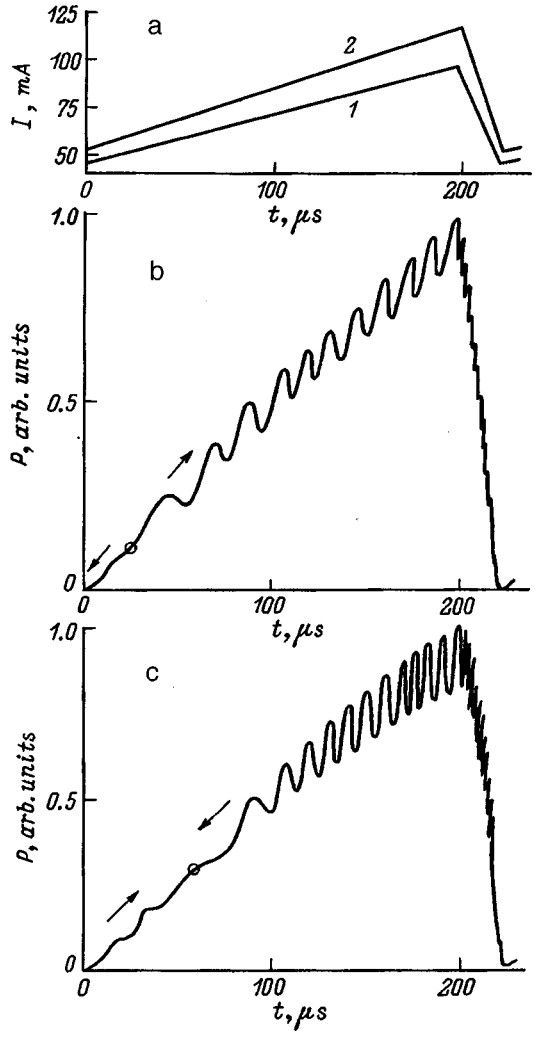


FIG. 2. Oscilloscope traces of the feed current ($I$) for a structure with strip width 16 (*1*) and 20 $\mu$m (*2*) (a) and the intensity ($P$) of the laser emission of a structure with strip width 16 $\mu$m after passing through an external Fabry–Perot resonator of length 47 mm (b), and of a structure with strip width 20 $\mu$m after passing through a cavity of length 11.2 mm (c). The arrows indicate the direction of movement of the sinusoidal waves.

**3**. Let us consider the experimental results. When the laser was driven by a sawtooth current $I(t)$ (Fig. 2a), the intensity of the radiation passed through the external cavity, $P(t)$, had a sawtooth shape and was modulated by a sine wave (Figs. 2b and 2c). The modulation arises as a result of variation of the laser radiation wavelength $\lambda$ with the current, whereupon it traverses the transmission interference bands of the outer cavity.

Let us consider the operation of the external cavity. The condition for interference maxima of the radiation that passes through the cavity is

$$2ln_r\cos r = m\lambda, \tag{1}$$

where $m=1,2,\ldots$ is the order of the interference maximum, $l$ is the length, $n_r$ is the refractive index of the external cavity, and $r$ is the angle between the normal to the plane of the cavity and the direction of propagation of the ray in it. From Eq. (1) we obtain the variation of the radiation wavelength between maxima:

$$\Delta\lambda = \frac{\lambda^2}{2\lambda(n_r-\lambda dn_r/d\lambda)\cos r}. \tag{2}$$

Experimentally, $\Delta\lambda$ was found to be 0.36 Å for $l=47$ mm and 1.5 Å at $l=11.2$ mm for $\lambda=3.3$ $\mu$m. By varying the angle $r$ it is possible to determine the direction of variation of the radiation wavelength $\lambda$ with the current since according to Eq. (1) $\lambda$ decreases as $r$ increases for fixed $m$. Thus, if $\lambda$ decreases with growth of the current, the sine waves on the oscilloscope screen will move to the right as $r$ is increased. The opposite dependence is also valid. Experimentally, the sine waves on the oscilloscope screen are observed to move to the right and to the left as $r$ is increased (Figs. 2b and 2c). As a rule, in lasers with a small strip width (16 $\mu$m) the radiation wavelength at first increases slightly as the current is raised, and then decreases (Fig. 2b). The positive shift reaches 0.3–1 Å when the current exceeds the threshold by 5–15%, and the negative shift reaches 3–5 Å when the current exceeds the threshold by a factor of 2 (Fig. 3a). These lasers emit the longitudinal spatial mode with half-width $\Delta\theta\approx13-14°$ (Fig. 3b).

In the lasers with a somewhat greater strip width (20 $\mu$m), following the decrease of the wavelength with growth of the current it was observed to increase (Fig. 2c).

The decrease of the wavelength reached $\Delta\lambda=3-5$ Å at currents 20–30% greater than the threshold current (Fig. 3a). The subsequent positive shift reached 16 Å when the threshold was exceeded by more than a factor of 2. The longitudinal mode also predominates spatially. When the current exceeded the threshold by less than 30%, the half-width of the directivity diagram was $\Delta\theta=10-11°$; it then increased with increasing current and reached 20° when the threshold was exceeded by a factor of 2.

The tuning intervals on the positive and negative sides remain constant when the sawtooth pulse repetition frequency was varied by a factor of 100 (Fig. 4). The amplitude of the sine waves in the oscilloscope trace decreased somewhat with increase of the sawtooth repetition frequency be-

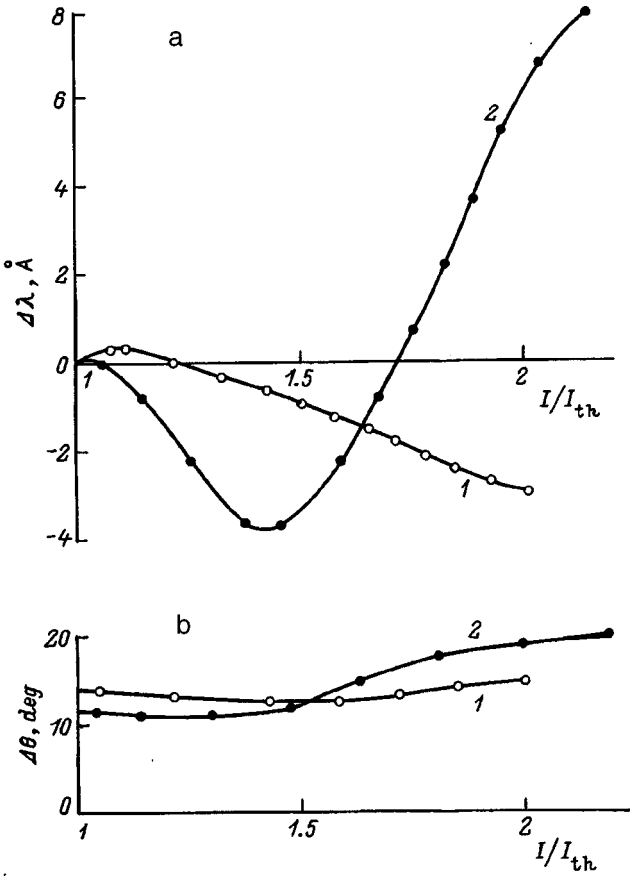


FIG. 3. Dependence of the change in the laser radiation wavelength $\Delta\lambda$ (a) and of the half-width of the directivity diagram $\Delta\theta$ (b) on the ratio of the feed current to the threshold current $I/I_{\text{th}}$ for lasers with strip width 16 (*1*) and 20 $\mu$m (*2*).

cause of a decrease in the photodetector gain. The frequency of the sine waves reached $1.5\times10^5$ Hz. This corresponds to a response time no worse than 1 $\mu$s.

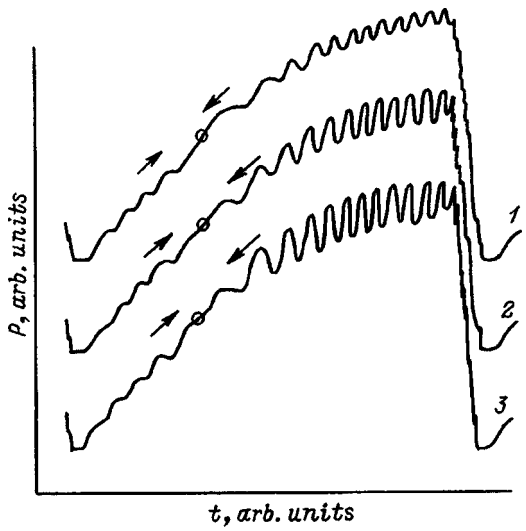


FIG. 4. Oscilloscope traces of radiation that has passed through an external cavity of length 47 mm, for the 20-$\mu$m strip width laser driven by a sawtooth current with a period (in milliseconds) equal to *1* — 0.16, *2* — 1.6, *3* — 16.

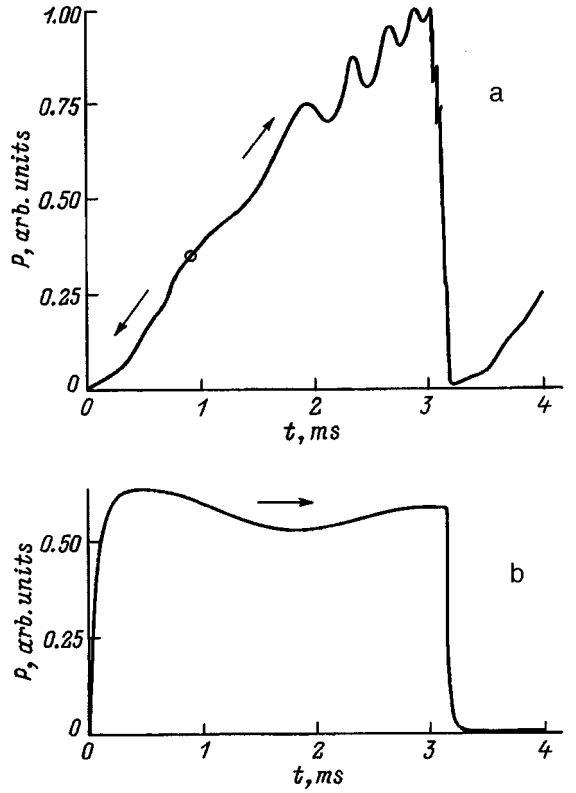


FIG. 5. Oscilloscope traces of radiation that has passed through an external cavity of length 47 mm, for the 20-$\mu$m strip width laser driven by a sawtooth current (a) and a pulsed current (b).

The variation of the laser radiation wavelength during one growth period of the sawtooth current proved to be significantly greater than for a rectangular pulse with duration equal to the period of the sawtooth current (Fig. 5). This proves that the main reason for variation of the radiation wavelength during current growth is not laser heating due to the current.

The experimental results reduce to the following.

1) In *N*-InAsSbP / *n*-InAsSb / *P*-InAsSbP laser structures it is possible to obtain significant current tuning of the radiation wavelength both in the direction of increase and decrease.

2) The time constant of current tuning was not found experimentally to exceed 1 $\mu$s.

3) Variation of the wavelength was not due to heating or cooling of the laser.

**4**. Let us analyze the experimental results. From the experimental data given above it follows that current tuning of the radiation wavelength is not controlled by changes in the temperature of the material of the active region of the laser. In Ref. 7 we suggested that the short-wavelength shift of the radiation wavelength is connected with an increase in the concentration of nonequilibrium charge carriers, and the long-wavelength shift is connected with self-focusing of the radiation. This was based on the previously[10] established fact that the intensity of spontaneous emission increases with the current above threshold, on the self-focusing effect which we observed at currents exceeding the threshold current by more than 40%, and on the decrease in the dielectric constant of

the semiconductor as a result of an increase in the concentration of nonequilibrium charge carriers.

The concentration of nonequilibrium charge carriers at the edges of the strip can significantly exceed its threshold value since the laser radiation intensity here is equal to zero due to the arrangement along the edges of the strip of nodes of the electromagnetic wave; as a result, only spontaneous recombination occurs here. Far from the edges of the strip the carrier concentration can be even less than threshold due to the high rate of induced recombination. Therefore, the dielectric constant in a working laser decreases toward the edges of the strip, thereby creating conditions for self-focusing. This effect increases with increasing homogeneity of the pumping, i.e., with decreasing dispersal of carriers over the area of the $p-n$ junction. The propagation constant of the electromagnetic wave along the strip ($\tilde{\varepsilon}$), which characterizes the propagation velocity of the laser radiation along the strip, has a value intermediate between the dielectric constant on the edge of the strip and at its center. It can be both less than or greater than its value at the threshold of lasing in the absence of laser radiation.

Let us calculate the propagation constant $\tilde{\varepsilon}$. In their earlier studies, Eliseev and Bogatov[11] showed that self-focusing is caused by the dependence of the dielectric constant $\varepsilon$ on the amplitude of the electromagnetic wave. This has to do with the nonlinearity of the optical medium of the laser. However, the question of the propagation constant of the electromagnetic wave, $\tilde{\varepsilon}$, which governs its wavelength, remains open.

We consider a mathematical model in which the current density does not vary over the area of the laser and there is no spreading, i.e., the pump is spatially homogeneous. We start with the existence of a concentration dependence of the dielectric constant

$$\varepsilon=\varepsilon_i+2n\frac{dn}{dN}(N-N_0), \tag{3}$$

where $\varepsilon_i$ is the dielectric constant at the inversion threshold, $n$ is the refractive index of the active medium, and $N_0$ is the concentration of the charge carriers at the inversion threshold. The conditions of constancy in time of the concentration of charges of the nonequilibrium current carriers $N$ and photons $N_\Phi$ have the usual form:[11]

$$\frac{dN}{dt}=G-\frac{N}{\tau}-\beta N_\Phi(N-N_0)=0, \tag{4}$$

$$\frac{dN_\Phi}{dt}=\beta N_\Phi(N-N_0)-\frac{N_\Phi}{\tau_\Phi}=0, \tag{5}$$

where $N_\Phi=u^2n^2/\hbar\omega 8\pi$, $\tau$ is the lifetime of the nonequilibrium charge carriers, $\beta$ is the differential gain, $G$ is the pump density of nonequilibrium charge carriers, $\tau_\Phi$ is the local photon lifetime, $u$ is the amplitude of the electromagnetic wave, and $\hbar\omega$ is the photon energy. We assume the pump density $G$ to be independent of the coordinates. From Eq. (4) we obtain

$$N-N_0=\frac{N_{\text{th}}-N_0}{1+\beta\tau N_\Phi}\left(\frac{G_\tau-N_{\text{th}}}{N_{\text{th}}-N_0}+1\right), \tag{6}$$

where $N_{\text{th}}$ is the nonequilibrium carrier concentration at the lasing threshold. Using Eq. (6), we can write an expression for the dielectric constant $\varepsilon$ in terms of the dielectric constant at the inversion threshold $\varepsilon_i$ and the photon density $N_\Phi$:

$$\varepsilon=\varepsilon_i+\delta\varepsilon_0\frac{1}{1+\beta\tau N_\Phi}\left(\frac{G\tau-N_{\text{th}}}{N_{\text{th}}-N_0}+1\right), \tag{7}$$

$$\delta\varepsilon_0=2n\frac{dn}{dN}(N_{\text{th}}-N_0).$$

Using Eq. (7), we write the Helmholtz wave equation in the form

$$\frac{d^2u}{dy^2}+\left(\frac{2\pi}{\lambda}\right)^2(\varepsilon_i-\tilde{\varepsilon})u+\left(\frac{2\pi}{\lambda}\right)^2\delta\varepsilon_0\frac{i+1}{1+u^2/D}u=0, \tag{8}$$

where $D=\hbar\omega 8\pi/\beta\tau n^2$, and $i=(G\tau-N_{\text{th}})/(N_{\text{th}}-N_0)$ is the relative excess of the current above threshold. A change in $\tilde{\varepsilon}$ leads to a change in the laser wavelength:

$$\Delta\lambda=\frac{\lambda}{2\varepsilon}\Delta\tilde{\varepsilon}. \tag{9}$$

Note that Eq. (8), in contrast to the analogous Eq. (7.4) in Ref. 11, contains the quantity $i$ in its third term. Since $\tilde{\varepsilon}$ depends on $u^2$, Eq. (8) reflects the nonlinearity of the optical medium of the laser.

In the case in which there is an inflection point in the curve $u=f(y)$ Eq. (8) allows one to express $\tilde{\varepsilon}$ in terms of the wave amplitude at this point $u_1$,

$$\varepsilon=\varepsilon_i+\delta\varepsilon_0\frac{i+1}{1+u_1^2/D}. \tag{10}$$

From Eqs. (4) and (5) we calculate the local lifetime of a photon in the cavity $\tau_\Phi$,

$$\tau_\Phi=\frac{(1+\beta\tau N_\Phi)}{(N_{\text{th}}-N_0)}\frac{1}{(1+i)}\frac{1}{\beta}. \tag{11}$$

On the other hand, the photon lifetime in the cavity is

$$\tilde{\tau}_\Phi=\frac{n}{c}\frac{1}{\alpha_\Sigma}, \tag{12}$$

where $\alpha_\Sigma$ is the effective absorption which corresponds to the sum of all radiation losses. To hold the radiation flux constant, we must satisfy the condition

$$\int_{-b/2}^{b/2}\frac{N_\Phi}{\tau_\Phi}dy=\frac{1}{\tilde{\tau}_\Phi}\int_{-b/2}^{b/2}N_\Phi dy. \tag{13}$$

This condition expresses the possibility of an overflow of radiation generated in one region where $\tau_\Phi(y\simeq 0)$ is smaller into another region where $\tau_\Phi$ is larger ($y\simeq\pm b/2$), i.e., from the edges toward the center. This condition along with the dependence of $\tilde{\varepsilon}$ on the radiation intensity is a manifestation

of the nonlinearity of the optical medium of the laser. For a known distribution $N_\Phi = f(y)$ Eq. (13) can be used to relate the radiation intensity to the current.

Let us determine the nature of the dependence of $\tilde{\varepsilon}$ on $i$. For a small excess of the current above the lasing threshold, where the influence of the radiation on the dielectric constant is still insubstantial, optical confinement is governed by the jump in the dielectric constant at the boundary between the crystal and the external medium. The distribution of the amplitude of the electromagnetic wave over the width of the strip for the zeroth spatial mode in this case is a cosine. The zeroth spatial mode is the most probable one because of the weak optical confinement in the direction perpendicular to the plane of the $p-n$ junction. Such a distribution corresponds to the value $\tilde{\varepsilon} = \varepsilon_{\text{th}} - (\lambda/2b)^2$. A more detailed treatment shows that $\tilde{\varepsilon}$ increases weakly with the current because of the excess value of the dielectric constant in the center of the strip. When the decrease in the dielectric constant at the edges of the strip reaches the value $(\lambda/2b)^2$, the inflection point of the curve $u = f(y)$ turns out to be inside the strip. Equation (10) can be used to determine $\tilde{\varepsilon}$. It is used when the current exceeds the lasing threshold

$$\frac{\Delta I}{I_{\text{th}}} = \left(\frac{\lambda}{2b}\right)^2 \Big/ \left(2n\frac{dn}{dN}N_{\text{th}}\right) = 0.08 \tag{14}$$

for $b = 16\,\mu$m, $n = 3.6$, $dn/dN = 0.3\times10^{-18}\,\text{cm}^3$, and $N_{\text{th}} = 6\times10^{16}\,\text{cm}^{-3}$. This is manifested experimentally in our case in the moderate growth of $\lambda$ with the current when it exceeds its threshold value by less than 10% (Fig. 3a, curve *1*).

Equation (10) implies the following. First of all, for $i \ll 1$ and $u_1^2/D \ll 1$ the inequality $\tilde{\varepsilon} < \varepsilon_{\text{th}}$ is satisfied. Note that $\varepsilon_{\text{th}} = \varepsilon_i + \delta\varepsilon_0$, $\delta\varepsilon_0 < 0$. The quantity $\tilde{\varepsilon}$ decreases sublinearly with growth of $i$. An approximate solution of Eq. (8) for $b \gg \lambda$ shows that the decrease of $\tilde{\varepsilon}$ should give way to an increase at $i \simeq 1.5$, i.e., when the current exceeds its threshold value by

$$\frac{\Delta I}{I_{\text{th}}} = 1.5\frac{N_{\text{th}} - N_0}{N_{\text{th}}}. \tag{15}$$

The decrease in $\tilde{\varepsilon}$ is $\Delta\tilde{\varepsilon}_- = 0.1|\delta\varepsilon_0|$. In the structure corresponding to curve *2* in Fig. 3a, this happens when $\Delta I/I_{\text{th}} = 0.4$. Using Eq. (15), we can evaluate the quantity $(N_{\text{th}} - N_0)/N_{\text{th}}$ for the given laser; we find it to be equal to 0.27. Correspondingly, $\delta\varepsilon_0$ is equal to $3.5\times10^{-2}$, and the wavelength decrease is $\Delta\lambda_- = 4.5$ Å. The calculated and experimental values of $\Delta\lambda$ are of the same order of magnitude.

Second, for $i \gg 1$, when $u_1^2/D > 1$, because of self-focusing, we find that $\tilde{\varepsilon} > \varepsilon_{\text{th}}$ and it increases with increasing current $i$. These two segments of dependence of $\tilde{\varepsilon}$ on $i$ should be joined smoothly by a curve with a positive slope. The increment of $\tilde{\varepsilon}$ can exceed $|\Delta\tilde{\varepsilon}_-|$ and, correspondingly, $\Delta\lambda_+$ can exceed $|\Delta\lambda_-|$. It should be noted that the above estimates correspond to strictly homogeneous pumping. Spreading of the charge carriers over the surface of the strip will substantially increase the intervals of variation of the current, and an increase in $N_{\text{th}} - N_0$ will increase the intervals of variation of $\Delta\tilde{\varepsilon}$ and $\Delta\lambda$. An increase in $\lambda$ is observed only in the lasers with a wide strip ($20\,\mu$m), where self-focusing takes place (Fig. 3a, curve *2*), and here $\Delta\lambda_+$ exceeds $|\Delta\lambda_-|$ by a factor of 4.

To estimate the delay time of the process of current tuning, it is necessary to allow for the fact that the dielectric constant depends on the concentration of nonequilibrium charge carriers, which in turn depends on the rates of induced and spontaneous recombination. The dependence on spontaneous recombination is attributable to a more rapid increase in the carrier concentration at the edges of the strip than its decrease at the center of the strip. This is the main reason for growth of the spontaneous emission with growth of the current above its threshold value.

In reality, post-threshold growth of the charge carrier concentration is at least three times slower than its pre-threshold growth. Consequently, the effect on the laser wavelength of spontaneous recombination is weaker than the effect of induced recombination. The photon lifetime in the cavity is $\sim10^{-12}$ s, and the lifetime of the charge carriers for spontaneous recombination is $\sim10^{-8}$ s. The response time of current tuning probably has an intermediate value. Such rapid tuning from the standpoint of laser spectroscopy is nearly instantaneous.

In summary, by using a simple mathematical model, which takes into account the spatially homogeneous pumping and the dependence of the dielectric constant on the charge concentration, it is possible to qualitatively explain the available experimental results. The arising laser medium is optically inhomogeneous. This leads to a change in the laser wavelength with variation of the current toward larger and smaller values. As follows from a theoretical analysis, for a small current excess above its threshold value the wavelength is expected to increase and then decrease. With further increase of the current the wavelength can again increase. The magnitude of the wavelength shift depends on the quality of the structure and the cavity parameters. The variation of the laser wavelength with the current is due to quantum effects and, to some extent, the spontaneous lifetime. Such tuning from the standpoint of laser spectroscopy is nearly instantaneous.

This work was supported in part by contract with INCO-Copernicus [Contract No. 1C15-CT97-0802 (DG12-CDPF)] and by a grant from the Russian Ministry of Science under the program ''Optics and Laser Physics.''

*)E-mail: yak@iropt.ioffe.rssi.ru; Fax: (812) 247 0006

[1] V. G. Avetisov, A. N. Baranov, A. N. Imenkov, A. I. Nadezhdinskiĭ, A. N. Khusnutdinov, and Yu. P. Yakovlev, Pis'ma Zh. Tekh. Fiz. **16**, 66 (1990) [Tech. Phys. Lett. **16**, 70 (1990)].
[2] V. G. Avetisov, A. N. Baranov, A. N. Imenkov, A. I. Nadezhdinskiy, A. N. Khusnutdinov, and Yu. P. Yakovlev, Proc. SPIE **1724**, 83 (1992).
[3] A. N. Baranov, T. N. Danilova, O. G. Ershov, A. N. Imenkov, V. V. Sherstnev, and Yu. P. Yakovlev, Pis'ma Zh. Tekh. Fiz. **18**, 6 (1992) [Tech. Phys. Lett. **18**, 28 (1992)].

[4] A. N. Baranov, A. N. Imenkov, V. V. Sherstnev, and Yu. P. Yakovlev, in *Proceedings of the Fifth International Conference on InP and Related Materials* (Paris, 1993) p. 19.
[5] Yu. P. Yakovlev, A. N. Baranov, A. N. Imenkov, V. V. Sherstnev, M. V. Stepanov, and A. Ya. Ponurovskiĭ, Kvant. Élektron. **20**, 839 (1993) [Quantum Electron. **23**, 726 (1993)].
[6] A. A. Popov, Yu. P. Yakovlev, A. N. Baranov, A. N. Imenkov, and V. V. Sherstnev, Proc. SPIE **2112**, 50 (1994).
[7] T. N. Danilova, O. I. Evseenko, A. N. Imenkov, N. M. Kolchanova, M. V. Stepanov, V. V. Sherstnev, and Yu. P. Yakovlev, Pis'ma Zh. Tekh. Fiz. **22**, 7 (1996) [Tech. Phys. Lett. **22**, 268 (1996)].
[8] T. N. Danilova, O. I. Evseenko, A. N. Imenkov, N. M. Kolchanova, M. V. Stepanov, V. V. Sherstnev, and Yu. P. Yakovlev, Fiz. Tekh. Poluprovodn. **31**, 662 (1997) [Semiconductors **31**, 563 (1997)].
[9] T. N. Danilova, O. I. Evseenko, A. N. Imenkov, N. M. Kolchanova, M. V. Stepanov, V. V. Sherstnev, and Yu. P. Yakovlev, Pis'ma Zh. Tekh. Fiz. **24**, 77 (1998) [Tech. Phys. Lett. **24**, 157 (1998)].
[10] P. G. Eliseev and V. P. Strakhov, Pis'ma Zh. Éksp. Teor. Fiz. **16**, 606 (1972) [Sov. Phys. JETP **16**, 428 (1972)].
[11] P. G. Eliseev and A. P. Bogatov, Trudy FIAN **166**, 15 (1986).

Translated by Paul F. Schippnick

# Long-wavelength photodiodes based on $Ga_{1-x}In_xAs_ySb_{1-y}$ with composition near the miscibility boundary

I. A. Andreev, E. V. Kunitsyna, M. P. Mikhaĭlova, and Yu. P. Yakovlev

*A. F. Ioffe Physicotechnical Institute, Russian Academy of Sciences, 194021 St.Petersburg, Russia*
(Submitted June 8, 1998; accepted for publication June 9, 1998)
Fiz. Tekh. Poluprovodn. **33**, 249–253 (February 1999)

The possibility of using liquid-phase epitaxy to obtain $Ga_{1-x}In_xAs_ySb_{1-y}$ solid solutions isoperiodic with GaSb near the miscibility boundary is investigated. The effect of crystallographic orientation of the substrate on the composition of the solid solutions grown in this way is examined, and the indium concentration is observed to grow from 0.215 to 0.238 in the $Ga_{1-x}In_xAs_ySb_{1-y}$ solid phase in the series of substrate orientations (100), (111)A, (111)B. A change in the composition of the solid solution leads to a shift of the long-wavelength edge of the spectral distribution of the photosensitivity. The use of a GaSb (111)B substrate made it possible, without lowering the epitaxy temperature, to increase the indium content in the solid phase to 23.8% and to create long-wavelength photodiodes with spectral photosensitivity threshold $\lambda_{th}=2.55\,\mu$m. The primary characteristics of such photodiodes are described, along with aspects of their fabrication. The proposed fabrication technique shows potential for building optoelectronic devices (lasers, LED's, photodiodes) based on $Ga_{1-x}In_xAs_ySb_{1-y}$ solid solutions with red boundary as high as $2.7\,\mu$m. © *1999 American Institute of Physics.* [S1063-7826(99)01802-5]

## 1. INTRODUCTION

The spectral range $1.8-3.0\,\mu$m is of interest for problems of laser diode spectroscopy of gases and molecules,[1] laser ranging systems,[2] medical applications,[3] and problems of ecological monitoring. The use of the spectral window $2.2-2.4\,\mu$m is especially attractive for problems of gas analysis since in this spectral range such atmospheric pollutants as $CH_4$, CO, $NO_2$, and $H_2CO$ have strong absorption lines while the absorption bands of water vapor and carbon dioxide are weak.[4]

The most promising materials for fabrication of optoelectronic devices in the spectral range $1.8-3.0\,\mu$m are multicomponent solid solutions based on gallium antimonide (GaSb). However, for $Ga_{1-x}In_xAs_ySb_{1-y}$ solid solutions there exists a wide range of compositions that are inaccessible for liquid-phase epitaxy (LPE), the so-called immiscibility region.[5] The solid solution $Ga_{1-x}In_xAs_ySb_{1-y}$ can be prepared by LPE on a GaSb substrate, such that it is isoperiodic with GaSb only in the range $0<x<0.29$ (the band gap $E_g\simeq 0.72-0.50$ eV), i.e., similar to GaSb in composition, and in the range $0.74<x<1$ ($E_g\simeq 0.30-0.24$ eV), i.e., similar to InAs in composition.[6]

Baranov *et al.*[7] reported the first long-wavelength laser structures on a GaSb substrate based on the solid solutions $Ga_{1-x}In_xAs_ySb_{1-y}$ near the boundary of the immiscibility region (wavelength $\lambda=2.5\,\mu$m). However, the photodiodes based on such solutions that have been described in the literature so far have been photodiodes operating at room temperature with threshold wavelength[1)] $\lambda_{th}$ not exceeding $2.3-2.4\,\mu$m.[8–10]

In this paper we report for the first time the fabrication, with use of liquid-phase epitaxy, of long-wavelength photodiodes with threshold wavelength $\lambda_{th}=2.55\,\mu$m based on the solid solutions $Ga_{1-x}In_xAs_ySb_{1-y}$/GaSb with composition near the miscibility boundary. Aspects of the fabrication and the distinguishing characteristics of such photodiodes are described.

## 2. PECULIARITIES OF LIQUID-PHASE EPITAXY OF $Ga_{1-x}In_x$ $As_ySb_{1-y}$/GaSb SOLID SOLUTIONS NEAR THE MISCIBILITY BOUNDARY

The production process of growth of the quaternary solid solutions $Ga_{1-x}In_xAs_ySb_{1-y}$ near the miscibility boundary has several peculiarities which complicate the preparation of such compounds. Figure 1a plots as functions of the temperature $T$ two independent constraints on the preparation of GaInAsSb solid solutions isoperiodic with GaSb—the constraint of spinodal decay (curve *1*) and the constraint proceeding from the condition of molecularity (curve *2*).[6] The first constraint follows from the conditions of solid (I)–solid (II) phase equilibrium. In the spinodal decay region the solid solutions are diffusionally unstable. The second constraint follows from the conditions of melt–solid phase equilibrium. As can be seen from Fig. 1a, to increase the In content in such solid solutions it is necessary to lower the epitaxy temperature. As the melt is enriched with indium and arsenic, a significant supercooling of the system (by more than 10 K) is required to suppress the growing tendency of the GaSb substrates to dissolve.[11] Such supercooling leads to an increase in the fraction of bulk crystallization in the melt. Consequently, the lattice constant of the growing epitaxial layer changes. Therefore, we have attempted to exploit the possi-

 

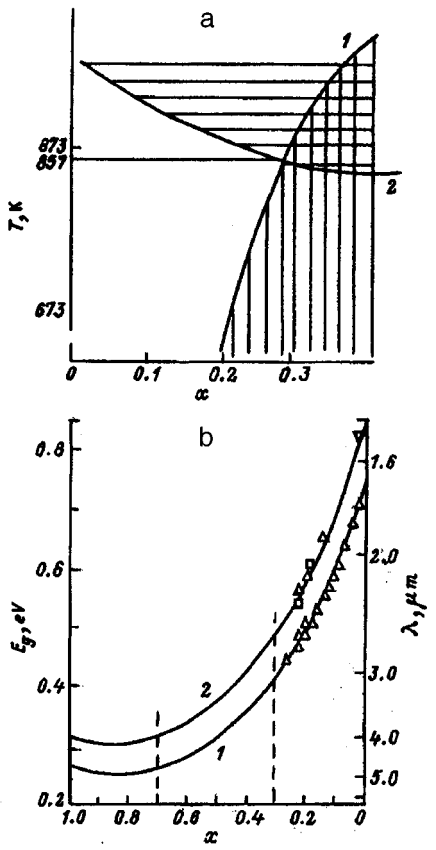


FIG. 1. a — Existence domain of isoperiodic solid solutions $Ga_{1-x}In_xAs_ySb_{1-y}$/GaSb ($y \approx 0.9x$), bounded by spinodal decay (*1*) and by the condition of molecularity (*2*). b — dependence of the band gap of the solid solution $Ga_{1-x}In_xAs_ySb_{1-y}$ on the In content in the solid phase, $x$, at 300 (*1*) and 77 K (*2*).

bility of increasing the In content in such solid solutions by only varying the orientation of the substrate without varying the epitaxy temperature.

To calculate the phase equilibrium diagrams, we employed the method based on an original thermodynamic model proposed in Ref. 12.

The band gap $E_g$ of $Ga_{1-x}In_xAs_ySb_{1-y}$ solid solutions isoperiodic with GaSb ($y \sim 0.9x$) was calculated as a function of the In content in the solid phase $E_g = f(x)$ at 300 K according to the interpolation formula[13]

$$E_g(x) = 0.725(1-x) + 0.29x - 0.6x(1-x). \quad (1)$$

As can be seen from the curves in Fig. 1b calculated from formula (1), increasing the indium content of the solid solution leads to a decrease of $E_g$. Consequently, to shift the threshold wavelength $\lambda_{th}$ of a photodetector toward longer wavelengths it is necessary to use $Ga_{1-x}In_xAs_ySb_{1-y}$ solid solutions in the active region that are as indium-enriched as possible, i.e., with composition near the miscibility boundary.

The investigated structures were grown by LPE on GaSb substrates with *n*-type conductivity. They were doped with tellurium (Te) to a concentration of $(1-5)\times 10^{17}\,cm^{-3}$ and had different orientations: (100), (111)A, and (111)B. As ingredients of the starting mixture for the epitaxial layers $Ga_{1-x}In_xAs_ySb_{1-y}$ we used the binary compounds InSb, GaSb, and InAs. The intentionally undoped solid solution $Ga_{1-x}In_xAs_ySb_{1-y}$ usually has *p*-type conductivity; therefore, to obtain epitaxial layers with *n*-type conductivity and concentration $\sim 10^{15}-10^{16}\,cm^{-3}$, which were then used to prepare the photodiode structures, doping was achieved using tellurium contained in the GaSb starting portion. The layers were grown in a hydrogen atmosphere in a high-purity graphite cassette of cylindrical form in a horizontal reactor. Layer growth was initiated by supercooling the melt before pouring it onto the substrate. The epitaxy temperature at which it is possible to obtain isoperiodic solid solutions ($T_e = 597\,°C$) was determined experimentally.

X-ray diffraction studies revealed a high quality of the grown layers which were isoperiodic with GaSb. The lattice mismatch of the layer and substrate was small ($\Delta a/a < 8\times 10^{-4}$). The chemical composition of the solid solutions was determined on a JXA-5 ''Camebax'' x-ray microanalyzer.

We observed the interesting effect of the influence of the crystallographic orientation of the substrate on the composition of the solid solutions. Our results reveal that the indium concentration grows from 0.215 to 0.238 in the solid phase $Ga_{1-x}In_xAs_ySb_{1-y}$ as one runs through the series of orientations of the GaSb substrate (100), (111)A, (111)B while holding constant the composition of the liquid phase and all conditions for preparation of the layers. Such a trend in the composition of the solid solution leads to a shift of the long-wavelength edge of the photosensitivity spectral distribution as we observed for the three types of $Ga_{1-x}In_xAs_ySb_{1-y}$-based structures grown from liquid phase of the same molecular composition on substrates with different orientations at $T_e = 597\,°C$ (Fig. 2a). This trend is similar to the effect of varying the In content in the liquid phase (Fig. 2b). For $Ga_{1-x}In_xAs_ySb_{1-y}$ solid solutions grown on GaSb (100) substrates at $T_e = 597$–$600\,°C$ we were not able to obtain structures with threshold wavelength $\lambda_{th}$ greater than 2.4 $\mu$m while the use of a GaSb (111)B substrate allowed us to achieve $\lambda_{th} = 2.55\,\mu m$.

The observed effect of the influence of the crystallographic orientation of the substrate can be explained in terms of the free energy by the greater difficulty of formation of nuclei on (100) faces since the surface energy $\gamma$ of the principal faces of the substrate for III–V semiconductors satisfies the relation[14]

$$\gamma(111) = \gamma(100)/\sqrt{3}. \quad (2)$$

Correspondingly, the work of formation of the nuclei during epitaxial growth is greater for a (100) face than for a (111) face. In addition, the polarity of the properties of the substrate in the (111) direction has an effect on the structure of the layers, which is explained by peculiarities of the structure of the (111)A and (111)B planes and nucleus formation on them.

### 3. PHOTODIODES WITH A RED SPECTRAL SENSITIVITY BOUNDARY AT 2.55 $\mu$m

To build a high-efficiency, long-wavelength photodiode based on the solid solution $Ga_{1-x}In_xAs_ySb_{1-y}$ with maxi-

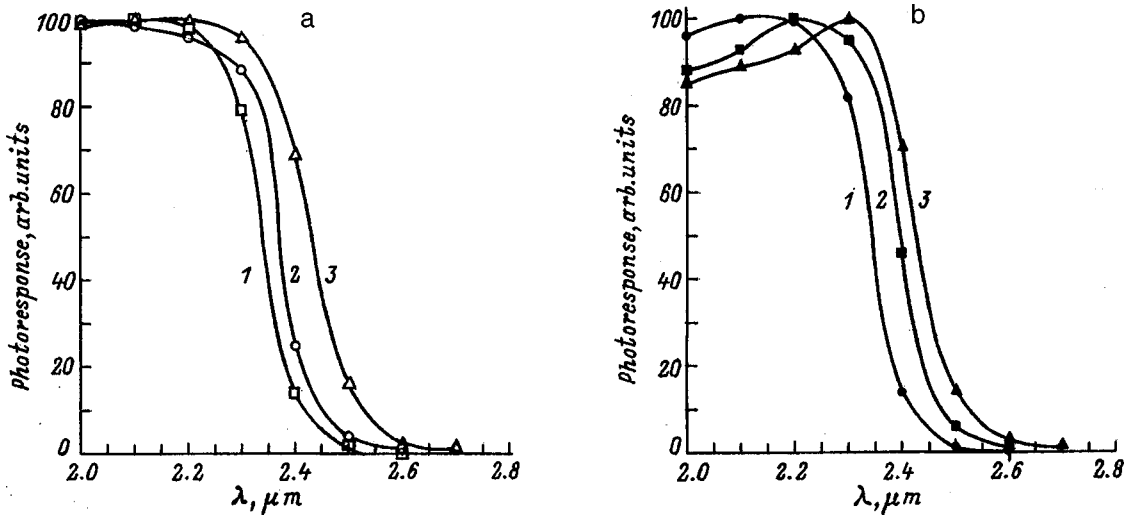


FIG. 2. Spectral distribution of photosensitivity of structures based on the solid solutions $Ga_{1-x}In_xAs_ySb_{1-y}$, grown at $T_e=597$ °C. a — growth from liquid-phase with the same composition on GaSb substrates with orientation *1* — (100), *2* — (111)A, *3* — (111)B; indium content in the solid phase $x=0.212$ (*1*), 0.226 (*2*), 0.238 (*3*). b — growth from liquid phase of different compositions on GaSb (111)B substrates; indium content in the solid phase $x=0.216$ (*1*), 0.225 (*2*), 0.235 (*3*).

mum In content, it was necessary in addition to solve a number of technological problems, such as how to grow a GaAlAsSb ''wide-gap'' window for efficient delivery of radiation into the structure and how to lower the concentration of majority carriers in the active region in order to obtain devices with good response time.

We prepared and investigated in detail photodiodes based on $n$-GaSb/$n$-$Ga_{1-x}In_xAs_ySb_{1-y}$/$P^+$-$Ga_{1-x}Al_xAs_ySb_{1-y}$ heterostructures grown on a substrate with (111)B orientation. As the active medium we used the solid solution $Ga_{0.765}In_{0.235}As_{0.21}Sb_{0.79}$ ($E_g=0.51$ eV, thickness 2.5 $\mu$m), and as the wide-gap window we used the solid solution $Ga_{0.66}Al_{0.34}As_{0.025}Sb_{0.975}$ ($E_g=1.2$ eV, thickness 1.5 $\mu$m). On the basis of the layers grown using standard photolithography we prepared samples of mesa-photodiodes with diameter of the sensitive element 1.0 mm.

The spectral distribution of the sensitivity of a typical photodiode is plotted in Fig. 3 for three different temperatures. As can be seen from the figure, the threshold wavelength is equal to 2.55 $\mu$m at room temperature. The temperature coefficient of variation of the band gap, defined in the temperature range $T=90-295$ K, is $\alpha=-3.3\times10^{-4}$ eV·K$^{-1}$. We estimated the temperature coefficient of the shift of the long-wavelength edge of the spectral sensitivity at half-maximum ($\lambda_{(1/2)\max}$) as 1.6 nm·K$^{-1}$. The monochromatic current sensitivity at the maximum of the spectrum ($\lambda_{\max}=2.2-2.4$ $\mu$m) was $S_\lambda=1.1-1.2$ A/W, which corresponds to a quantum efficiency of 0.6–0.7. This can be taken as a good result since we did not use any special anti-reflection coatings.

Measurement of the current–voltage characteristic showed that the impurity distribution in the heterostructure was sharp, and that the concentration of majority carriers in the active region was small, $n=(3-5)\times10^{15}$ cm$^{-3}$. The capacitance of the photodiode with total diameter 1.2 mm at zero reverse bias is 450 pF. The response time of the photodiode was determined in our case by its $RC$ component and when operating with a load $R_l=50\,\Omega$ did not exceed 50 ns, which is a good result for photodiodes with the stated diameter of the working element. Note that the above value of the capacitance is 4–5 times lower than was reported, for example, in an advertisement published by EPITAXX Corp., which describes photodiodes based on the solid solution $Ga_{0.82}In_{0.18}As$/InP with red limit $\lambda_{th}=2.55$ $\mu$m, fabricated by hydride gas-phase epitaxy.[15] With a diameter of 1.0 mm, EPITAXX photodiodes have a capacitance of 1400–1800 pF.

In addition, there are requirements on the reverse dark current ($I_d$) of the photodetector (that it be low) since the sensitivity of the photodetector is determined by the dark current $I_d$ (photodiode regime) or the shunt resistance

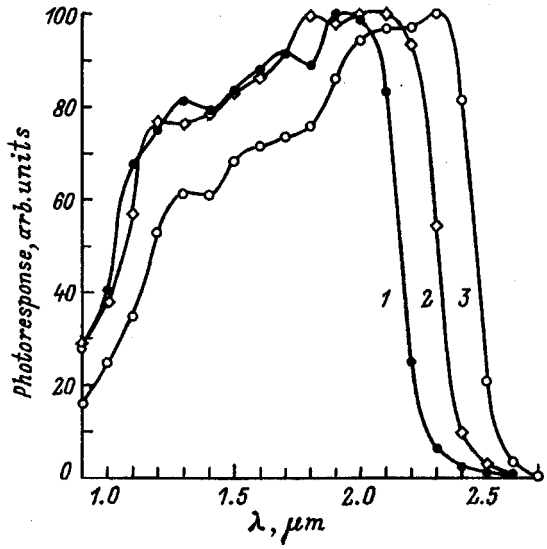


FIG. 3. Spectral distribution of the photosensitivity of a GaSb/GaInAsSb/GaAlAsSb long-wavelength hetero-photodiode at temperatures $T=90$ (*1*), 215 (*2*), and 295 K (*3*).

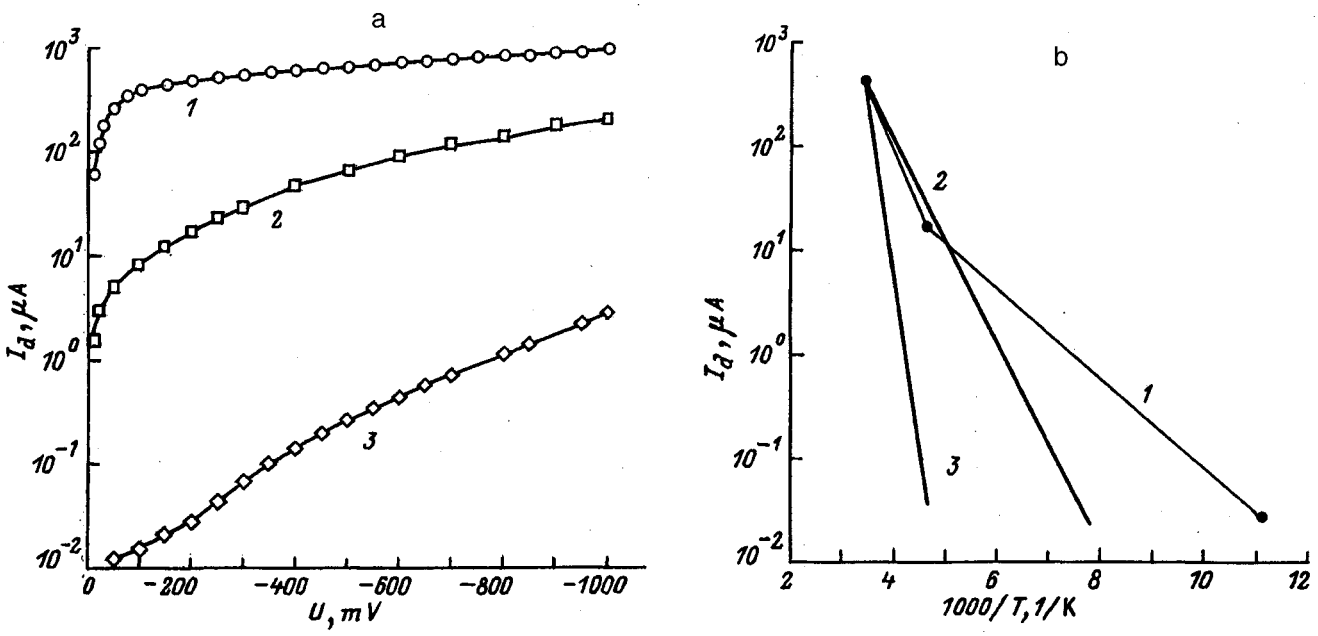


FIG. 4. a — Dependence of the dark current $I_d$ on the reverse bias voltage $U$ of a GaSb/GaInAsSb/GaAlAsSb long-wavelength hetero-photodiode at temperatures $T=295$ (*1*), 215 (*2*), 90 K (*3*). b — temperature dependence of the dark current: *1* (points) — experiment, *2* — theoretical curve for the generation–recombination current, *3* — theoretical curve for the diffusion current.

$R_0=(dU/dI)_{U=0}$ (photovoltaic regime). Both parameters depend strongly on the band gap ($E_g$) of the utilized solid solution and the mechanism of the dark current

$$I_d \sim \exp(-E_g/nkT), \tag{3}$$

where $k$ is the Boltzmann constant, $T$ is the absolute temperature, and $n$ is a parameter that is determined by the threshold dark current and varies from $n=1$ (mechanism of interband recombination) to $n=2$ (generation–recombination mechanism). Consequently, it is necessary to examine the mechanism of the dark current in the structure $n$-GaSb/$n$-$Ga_{1-x}In_xAs_ySb_{1-y}$/$P^+$-$Ga_{1-x}Al_xAs_ySb_{1-y}$. We investigated the direct and reverse current–voltage characteristics at different temperatures. Typical curves of the dark current as a function of the reverse bias at three temperatures are plotted in Fig. 4a. Figure 4b plots the temperature dependence of the reverse current for the bias $U=-0.2$ V (filled circles). Figure 4b also shows the calculated temperature dependence for the generation–recombination (GR) mechanism and the diffusion (D) mechanism of the dark current. Obviously, the experimental data agree better with the dependence for the generation–recombination current. This kind of current has a temperature dependence of the form $I\sim T^{3/2}\exp(-E_g/2kT)$. The activation energy for this dependence is $E_A=0.3$ eV, which is close to half the value of the band gap of the material of the active region of the photodiode [GaInAsSb, $E_g(0)\simeq 0.6$ eV]. The deviation of the experimental dependence from the calculated dependence for the generation–recombination current is due to growth of the effect of the tunneling component of the dark current,[16] which has a weaker temperature dependence and which is decisive in narrow-gap materials at high voltages and low temperatures.

At room temperature for reverse biases higher than 0.2 $-0.5$ V the weak dependence $I(U)$ ($I\sim W\sim U^{1/2}$) is described by the following relation for the generation–recombination current:

$$I=qn_iWA/\tau_{\text{eff}}, \tag{4}$$

where $q$ is the charge of the electron, $A$ is the surface area of the $p-n$ junction, $W$ is the width of the space charge layer, $n_i$ is the intrinsic charge-carrier concentration, and $\tau_{\text{eff}}$ is the effective lifetime of the minority charge carriers. For $n_i=4\times10^{14}$ cm$^{-3}$ and $W\sim1$ $\mu$m the experimental value of the current yields $\tau_{\text{eff}}=7\times10^{-7}$ s, which is close to the radiative lifetime for GaInAsSb solid solutions. The reverse dark current density for typical diodes is $j=(0.8-5)\times10^{-2}$ A/cm$^2$ for $U=-(0.2-0.5)$ V.

Analysis of the forward branches of the CVC shows that the current can be analytically represented by the dependence $I\sim\exp(qU/nkT)$, where $n$ increases as the temperature is lowered from $n=1.9$ to $n=2.8$. This indicates a shift of the mechanism of the dark current from generation–recombination to tunneling. The reverse dark current density is larger than expected. A further decrease of the dark current can be achieved by improving the conditions of fabrication of the photodiode structures, e.g., by using rare-earth elements in the active region to lower the impurity concentrations[17] or by using a neutral solvent (Pb) when growing the GaInAsSb.[18] In addition, as we showed in Ref. 19, a reduction of the surface leakage currents, which contribute significantly to the total current, can be achieved by passivating the structures in aqueous sulfide solutions.

## CONCLUSIONS

We developed a reproducible technique for growing the quaternary solid solutions $Ga_{1-x}In_xAs_ySb_{1-y}$ on a GaSb substrate near the miscibility boundary. Using a GaSb (111)B substrate makes it possible to increase the indium content in the solid phase to 23.8% without lowering the epitaxy temperature and create long-wavelength photodiodes whose sensitivity threshold is $\lambda_{th}=2.55\ \mu$m and falls gradually to $\lambda=2.7\ \mu$m. Preliminary studies show that the proposed fabrication technique may be promising for building optoelectronic devices (lasers, LED's, photodiodes) based on $Ga_{1-x}In_xAs_ySb_{1-y}$ solid solutions with sensitivity red limit as high as $2.7\ \mu$m.

[1)]It is customary to take the threshold wavelength $\lambda_{th}$ as the wavelength at which the sensitivity is 10% of maximum.

[1] A. I. Nadezhdinski and A. M. Prokhorov, *Applications of Tunable Diode Lasers* [SPIE, **1724** (1992), p. 2].
[2] M. Kavaya, Laser Focus World , No. 1, 27 (1991).
[3] J. Lucas, Infrared Phys. **25**, No. 1/2, 227 (1985).
[4] R. H. Pierson and A. N. Fletcher, Anal. Chem. **28**, 1218 (1956).
[5] A. N. Baranov, A. N. Imenkov, O. P. Kapranchik, A. M. Litvak, N. A. Charykov, and Yu. P. Yakovlev, Pis'ma Zh. Tekh. Fiz. **16**, 19 (1990) [Tech. Phys. Lett. **16**, 121 (1990)].
[6] A. N. Baranov, A. A. Guseĭnov, A. M. Litvak, A. A. Popov, N. A. Charykov, V. V. Sherstnev, and Yu. P. Yakovlev, Pis'ma Zh. Tekh. Fiz. **16**(5), 33 (1990) [Tech. Phys. Lett. **16**, 177 (1990)].
[7] A. N. Baranov, E. A. Grebenshchikova, B. E. Dzhurtanov, T. N. Danilova, A. N. Imenkov, and Yu. P. Yakovlev, Pis'ma Zh. Tekh. Fiz. **14**(20), 1839 (1988) [Tech. Phys. Lett. **14**, 798 (1988)].
[8] J. C. DeWinter, M. A. Pollack, A. K. Srivastava, and J. L. Zyskind, J. Electron. Mater. **14**, No. 6, 729 (1985).
[9] I. A. Andreev, M. A. Afrailov, A. N. Baranov, V. G. Danil'chenko, M. A. Mirsagatov, M. P. Mikhaĭlova, and Yu. P. Yakovlev, Pis'ma Zh. Tekh. Fiz. **12**(21), 1311 (1986) [Tech. Phys. Lett. **12**, 542 (1986)].
[10] E. Tournie, J.-L. Lazzari, E. Villemain, A. Joullie, L. Gouskov, M. Karim, and I. Salesse, Electron. Lett. **27**, No. 14, 1237 (1991).
[11] A. É. Bochkarev, L. M. Dolginov, L. V. Druzhinina, and Z. B. Kapanadze, in *Semiconductors and Hetero-Junctions*, edited by A. I. Rozental' (Valgus, Tallinn, 1987), p. 3.
[12] A. M. Litvak and N. A. Charykov, Zh. Fiz. Khim. **64**, No. 9, 2331 (1990).
[13] F. Karota, H. Mani, J. Bhan, Fen Jia Hua, and A. Joullie, Rev. Phys. Appl. **22**, No. 11, 1459 (1987).
[14] U. M. Kulish, *Growth and Electrical Properties of Semiconductor Films (Liquid-Phase Epitaxy)* [in Russian], Kalm. Kn. Izdat., Élista, 1976.
[15] *Adverstisement of EPITAXX Corp.: High Sensitivity 2.5 μm Cutoff Wavelength InGaAs Photodiodes.*
[16] J. L. Moll, in *Physics of Semiconductors* (McGraw-Hill, New York, 1964).
[17] N. T. Bagraev, A. N. Baranov, T. I. Voronina, Yu. N. Tolparov, and Yu. P. Yakovlev, Pis'ma Zh. Tekh. Fiz. **11**(1), 47 (1985) [Tech. Phys. Lett. **11**, 135 (1985)].
[18] A. N. Baranov, A. M. Litvak, and V. V. Sherstnev, Izv. Akad. Nauk SSSR, Neorg. Mater. **25**, No. 6, 205 (1989).
[19] I. A. Andreev, E. V. Kunitsyna, V. M. Lantratov, T. V. L'vova, M. P. Mikhaĭlova, and Yu. P. Yakovlev, Fiz. Tekh. Poluprovodn. **31**, 35 (1997) [Semiconductors **31**, 29 (1997)].

Translated by Paul F. Schippnick

## ERRATA

# Erratum: Effect of the diameter of the photoexcited region on the picosecond relaxation of bleaching in a thin layer of GaAs [Semiconductors 32, 484–487 (May 1998)]; Stimulated-emission spectrum arising from interband absorption of a picosecond optical pulse in a thin layer of GaAs [Semiconductors 32, 479–483 (May 1998)]

I. L. Bronevoĭ and A. N. Krivonosov

*Institute of Radio Engineering and Electronics, Russian Academy of Sciences, 103907 Moscow, Russia*
Fiz. Tekh. Poluprovodn. **33**, 119 (January 1999)

[S1063-7826(99)02501-6]

On page 484, in the abstract, line 5 from the top should read ''rate of superluminescence recombination.''
On page 484, left-hand column, line 2 of the second paragraph should read ''intensity of superluminescent emission.''
On page 485, in Eq. (1), $\mu_e = \mu_h \approx E_g$ should read $\mu_e - \mu_h \approx E_g$.
On page 485, right-hand column, line 12 from the bottom should read ''in Ref. 1.''
On page 480, right-hand column, line 15 from the bottom should read ''when $F = 0.2$ mm.''

Translated by M. E. Alferieff

 

# Erratum: Study of GaN thin layers subjected to high-temperature rapid thermal annealing [Semiconductors 32, 1048–1053 (October 1998)]

N. I. Katsavets

*Private Joint-Stock Company ''Semiconductor Devices,'' 192281 St. Petersburg, Russia*

G. M. Laws, I. Harrison, E. C. Larkins, and T. M. Benson

*Department of Electrical and Electronic Engineering, University of Nottingham, Nottingham NG7 2RD, England*

T. S. Cheng and C. T. Foxon

*Department of Physics, University of Nottingham, Notthingham NG7 2RD, England*
Fiz. Tekh. Poluprovodn. **33**, 120 (January 1999)

[S1063-7826(99)02701-5]

On page 1048, the first sentence of Sec. 2 should read ''RHTA was performed in a quartz reactor at 1000 °C for 30 s in a stream of $N_2$ or Ar.''

Translated by M. E. Alferieff

 